Probing the antiferromagnetism of Ni_xMn_{100-x} with ferromagnetic Ni in exchange-biased bilayers and trilayers on $Cu_3Au(001)$

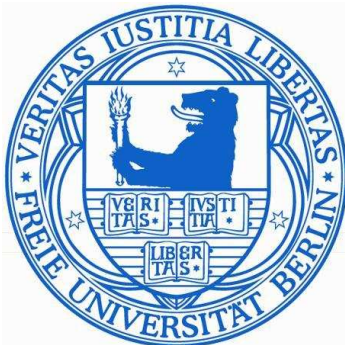

zur Erlangung des

DOKTORGRADES DER NATURWISSENSCHAFTEN (DR. RER. NAT.)

im Fachbereich Physik

der Freien Universität Berlin

vorgelegt von

Muhammad Yaqoob Khan

aus Karak,
K.P.K, PAKISTAN

im Juli 2012

D I S S E R T A T I O N

Erstgutachter: Prof. Dr. Wolfgang Kuch
Zweitgutachter: Prof. Dr. Robert Bittl

Datum des Promotionskolloquiums: 11.07.2012

Abstract

In this thesis the antiferromagnetism of Ni_xMn_{100-x} thin films in contact with ferromagnetic Ni film(s) in exchange-biased bilayers and trilayers on $Cu_3Au(001)$ is investigated by means of magneto-optical Kerr effect (MOKE). Ni_xMn_{100-x} ultrathin films ($10 \leq x \leq 77$) grow in layer-by-layer mode on $Cu_3Au(001)$ with face-centered tetragonal structure similar to its bulk form. Ni_xMn_{100-x} can couple to out-of-plane (OoP) as well as in-plane (IP) magnetized Ni films, the latter stabilized by Co under-layer deposition. The antiferromagnetic (AFM) ordering temperature (T_{AFM}) of Ni_xMn_{100-x} films coupled to IP magnetized Ni increases significantly with decreasing x from $\sim$50 to $\sim$20%, whereas only a slight change in T_{AFM} is observed for bilayers with OoP magnetized Ni as a function of x. The blocking temperature (T_b) is always higher for the IP case than for the OoP except for $Ni_{50}Mn_{50}$, where the reverse is true. The critical thickness of Ni_xMn_{100-x} for the onset of exchange bias (EB) decreases significantly for both coupling directions when decreasing x. These results suggest that for decreasing x, the non-collinear $3Q$-like spin structure of Ni_xMn_{100-x} deviates, driven by composition-dependent strain, from a more-OoP to a more-IP configuration with an associated increase in magnetic anisotropic energy to establish EB at smaller Ni_xMn_{100-x} thicknesses.

Trilayers of $Ni/Ni_xMn_{100-x}/Ni$ ($17 \leq x \leq 25$) on $Cu_3Au(001)$ are studied in detail, while manipulating the easy axis of magnetization of one or both of the FM Ni layers by the deposition of an adjacent Co layer. For the trilayers the exchange bias field H_{eb} is found to be always smaller than in the corresponding bilayers at similar temperatures. This difference of H_{eb} increases as the thickness of the Ni_xMn_{100-x} layer decreases. At reduced thickness (27 ML) of Ni_xMn_{100-x}, along with a significant reduction in H_{eb}, a markedly reduced T_b of $\sim$150 K and $\sim$90 K for trilayers with IP-IP and OoP-OoP configurations of the FM layers, respectively, is observed compared to the bilayer. These results are attributed to some pinned magnetic moments located inside the bulk of the AFM layer which are equally shared by both interfaces. For the perpendicular configuration of the two FM layer magnetizations in trilayers, H_{eb} and T_b are similar as in the bilayers. This indicates a $3Q$-like AFM spin structure where the IP and the OoP spin components independently couple to the adjacent FM layer. Further two important observations are a training-induced positive EB shift, and a temperature-dependent sign reversal of H_{eb} in trilayers when both FM layers are IP as well as OoP magnetized. The former is attributed to interlayer exchange coupling, and the latter to a competition between interlayer and interfacial coupling. Some signs of perpendicular interlayer coupling are also observed, which can be attributed to thickness fluctuations of the Ni_xMn_{100-x} film.

Deutsche Kurzzusammenfassung

In dieser Arbeit wird der Antiferromagnetismus dünner Ni_xMn_{100-x}-Filme in Kontakt mit ferromagnetischem Ni in Exchange-Bias-Doppel- und -Dreifachschichten auf $Cu_3Au(001)$ mittels magneto-optischem Kerr-Effekt untersucht. Ultradünne Ni_xMn_{1-x}-Filme ($10 \leq x \leq 77$) zeigen epitaktisches lagenweises Schichtwachstum auf $Cu_3Au(001)$ in einer flächenzentriert-tetragonalen Struktur, ähnlich der Volumenphase. Ni_xMn_{1-x}-Filme koppeln sowohl zu senkrecht zur Filmebene magnetisierten Ni-Filmken (out-of-plane, OoP) als auch zu in der Filmebene magnetisierten Ni-Filmen (in-plane, IP), wobei letztere durch Aufbringen einer Co-Unterlage stabilisiert werden. Die antiferromagnetische (AFM) Ordnungstemperatur (T_{AFM}) von Ni_xMn_{1-x}, gekoppelt an IP-magnetisiertes Ni, steigt signifikant an wenn x von $\sim$50 auf $\sim$20% reduziert wird, während mit OoP-magnetisiertem Ni nur eine geringe Variation beobachtet wird. Die Blockingtemperatur (T_b) ist außer bei $Ni_{50}Mn_{50}$ im IP-Fall größer als im OoP-Fall. Die kritische Ni_xMn_{1-x}-Schichtdicke für das Auftreten von Exchange-Bias (EB) nimmt für beide Magnetisierungsrichtungen für geringer werdendes x signifikant ab. Diese Ergebnisse legen nahe, dass bei Erniedrigung von x die nichtkollineare $3Q$-artigen Spinstruktur von Ni_xMn_{1-x} aufgrund von konzentrationsabhängigen Verspannungen von einer mehr OoP- hin zu einer mehr IP-artigen Konfiguration verzerrt wird, was mit einer Erhöhung der magnetischen Anisotropieenergie einhergeht, wodurch EB bereits bei kleineren Ni_xMn_{1-x}-Schichtdicken auftritt.

$Ni/Ni_xMn_{1-x}/Ni$ ($17 \leq x \leq 25$)-Dreifachschichten auf $Cu_3Au(001)$ werden im Detail untersucht, wobei die leichte Magnetisierungsrichtung einer der beiden oder beider Ni-Schichten durch das Aufbringen einer nebenliegenden Co-Schicht manipuliert wird. Das Exchange-Bias-Feld H_{eb} der Dreifachschichten ist bei ähnlicher Temperatur immer kleiner als das der entsprechenden Doppelschichten. Dieser Unterschied in H_{eb} wächst mit abnehmender Dicke der Ni_xMn_{1-x}-Schicht an. Bei geringeren Ni_xMn_{1-x}-Schichtdicken (27 ML) wird zusammen mit einer signifikanten Abnahme von H_{eb} auch ein im Vergleich zu den Doppelschichten klar verringertes T_b von $\sim$150 bzw. $\sim$90 K für Dreifachschichten mit IP-IP- bzw. OoP-OoP-Konfiguration der FM-Schichten beobachtet. Diese Ergebnisse werden auf gepinnte magnetische Momente im Inneren der AFM-Schicht zurückgeführt, die gleichermaßen von beiden Grenzflächen her beansprucht werden. Bei senkrechter Anordnung der Magnetisierungen der beiden FM-Schichten sind H_{eb} and T_b ähnlich wie in den entsprechenden Doppelschichten. Dies deutet auf eine $3Q$-artige Spinstruktur hin, bei der die IP- und OoP-Komponenten unabhängig voneinander an die jeweiligen FM-Schichten koppeln. Zwei weitere wichtige Beobachtungen sind ein trainingseffekt-induzierter positiver EB und ein temperaturabhängiger Vorzeichenwechsel von H_{eb} wenn beide FM-Schichten entweder IP- oder OoP-Magnetisierung aufweisen. Ersterer Effekt wird auf Zwischenschicht-Austauschkopplung, zweiterer auf den Wettstreit zwischen Zwischenschichtkopplung und Kopplung an der Grenzfläche zurückgeführt. Es werden weiterhin auch gewisse Anzeichen für senkrechte Zwischenschichtkopplung beobachtet, die auf Schichtdickenfluktuationen der Ni_xMn_{1-x}-Schicht zurückgeführt werden können.

Contents

Chapter 1

Introduction

Nanotechnology is one of the leading research topics in the field of science and engineering. Amongst many potential applications of nanotechnology, one of the most promising ones is in data storage, particularly the hard disk drives (HDD). The HDD is not only the dominant secondary mass storage device for computers but also in the near future very likely for most of home electronic products. The HDD relies on the integration of many key technologies. The read head is one of them, which has experienced the most changes during the last two decades including some revolutionary ones in terms of both the operating principle and the structural design and fabrication processes. It evolved from a thin-film inductive head to an anisotropic magnetoresistive (AMR) head, and recently, the giant magnetoresistive spin-valve (GMR SV) head.

The physical size of the recording bits of a HDD is already in the nanometer regime and is continuously shrinking due to the ever-increasing demand for higher recording densities. Very soon the dimension of the recording bit will reach the sub-10 nm regime. At this level, if not impossible, both the writing and reading processes will become extremely challenging. This poses formidable challenges to the read sensors as the sensor must be made smaller or at least comparable to the bit size, and at the same time, its sensitivity must be improved continuously so as to compensate the loss in signal-to-noise ratio due to the decrease in the bit size. The bit size fundamentally relies on the advance of nanotechnology, and the sensitivity of the sensor on an emerging field called spintronics [1, 2, 3, 4]. The combination of these two fields has played an important role in advancing the areal density of magnetic recording from a few gigabits/in^2 to the current level of more than 100 Gbits/in^2 [5]. In addition to hard disk drives, the technologies developed have also been applied to magnetic random access memories (MRAMs) [6, 7, 8, 9].

Electrons possess both charge and spin. The motion of charges forms the current. The formation of functional devices based on electronic components such as diodes and transistors, is possible due to the ability to control or modulate the charge transport. This is so far only possible in semiconductors instead of metals. The metals have too many electrons per unit volume; any variation of charge distribution is limited to a few atomic layers at the surface that can hardly cause any measurable change in the conductance of the metal. Therefore, with dimensions larger than the mean-free path of electrons, functional electronic devices have not been realized in pure metals. However, belonging to the same family of metals, metallic magnetic materials have an additional degree of freedom—the spin of electrons, which can be used to vary their electronic transport properties. The spin of electrons in magnetic materials

can be easily manipulated using an external magnetic field; it is possible to alter the conductivity of magnetic materials without changing the carrier distribution inside the material. This forms the basis of GMR-based electronics or sometimes is also called magnetoelectronics [5]. It is a sub-field of spintronics or spinelectronics [1, 2, 3, 4]. The spintronics in its broader sense contains all types of electronics that make use of both charge and spin [5].

With the availability of ultra high vacuum technology in the second half of the 1970s, researchers developed a technique which allows growing ultrathin films with extraordinary accuracy in thickness control. The evaporated molecules or atoms form beams and impinge directly on the surface of the substrate to initiate the growth. Therefore, the technique is generally called molecular beam epitaxy (MBE) [10]. The word *expitaxy* was used because MBE had been mainly employed to fabricate semiconductor materials which are normally single crystalline materials grown epitaxially on the substrates. It was realized that besides semiconductors, MBE can also be used to grow layered structures of different materials. This opened an important field in materials science where the layers are a few atomic layers thick, and form a so-called super-lattice structure [11]. Being inspired by the work carried out by the semiconductor community, researchers in the surface-science community started to use the same technique to study surface magnetism and magnetic interactions across an ultrathin antiferromagnetic or nonmagnetic spacer [12]. These research activities led to the discovery of giant magnetoresistance in Fe/Cr super lattices [13, 14].

The principle of a typical GMR/TMR spin valve sensor in its simplest form, as illustrated in Fig. 1.1, consists of two ferromagnetic (FM) layers separated by a nonmagnetic spacer and an antiferromagnetic (AFM) layer in contact with one of the ferromagnetic layers. The thickness of the spacer is chosen such that there is a little exchange coupling between the two FM layers. The magnetization of one of the FM layers which is in direct contact with the AFM layer is *pinned* by the latter, and thus this FM layer is commonly called a *pinned* or *reference* layer. On the other hand, the magnetization of the other FM layer is *free* to rotate to respond to an external field, and thus it is called a *free* or *sensor* layer.

Depending on its parallel or antiparallel spin configuration relative to the pinned reference layer, the resistance of the device changes on the order of 10%. The GMR effect is larger by almost an order of magnitude than the AMR effect, and it is routinely used today to detect the weak magnetic stray fields of the small domains written on magnetic recording media, and this detection has been found on time scales of 100 ps [15]. In practice, a spin valve structure serves as a read head in a disk drive. As the recording disk, with its written magnetic bits rotates underneath the read head, the stray fields of the bits cause the magnetization of the sensor layer to change. The induced change in the GMR signal can therefore be used to read the bit pattern. The typical material for the FM layer is NiFe or CoFe, while that for the spacer is generally copper. The choice of AFM is an issue of high complexity due to many practical considerations.

Like a transistor which needs some bias to work properly, the spin valve also needs a proper magnetic bias so as to achieve a linear response with minimized asymmetry, if any [16, 17, 18, 19]. One of the main tasks of magnetic design of spin valves is to set the magnetization of the pinned layer as rigid as possible and to maintain thermal stability at elevated temperatures under normal operation conditions. The basic energies involved at the AFM/FM interface are exchange and anisotropy, where the former

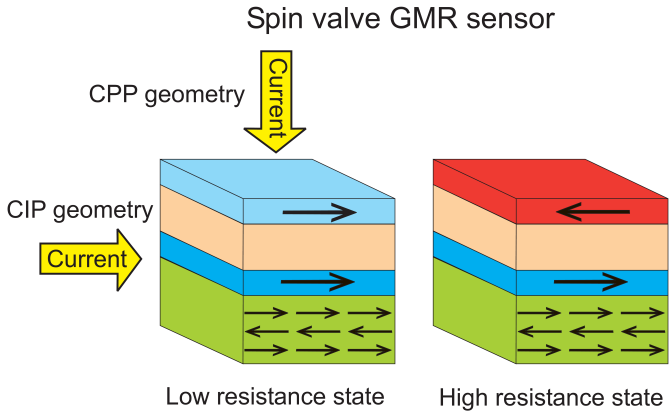

Figure 1.1: Principle of a spin valve. The magnetization of the lower FM layer is pinned by an AFM layer via exchange. The upper FM layer is separated by a nonmagnetic but conducting spacer layer, and its magnetization can be changed by relatively small fields. For a metallic spacer layer (Cu), the current direction is typically in the plane of the films, called the "current in plane"or CIP geometry. For the current direction perpendicular to the plane of the films, one speaks of a "current perpendicular (to) plane"or CPP geometry. In CPP (TMR) geometry, the conducting spacer layer is replaced by an insulating layer such that the current is passed via tunnelling, rather than scattering which is used in CIP (GMR) sensors. [15].

controls magnetic ordering and the latter controls the preferred orientation. A ferromagnet usually has a large exchange parameter but a relatively small anisotropy. This helps a ferromagnetic material to maintain its magnetic order at high temperatures but this is not the case with its preferred orientation, particularly if the dimensions are in nanometre regime. Many AFMs have mostly (but not necessarily) large anisotropies and consequently very stable preferred orientations. In spin valves, exchange coupling between the FM and AFM can produce a ferromagnetic behaviour with stable order and high anisotropy where the anisotropy could be a unidirectional feature not found in ferromagnets. This phenomenon is called exchange bias (EB) because the hysteresis loop associated with the FM/AFM structure can be centred about a non-zero magnetic field. This biasing (exchange bias), which is the main topic of the thesis, is employed to *pin* the magnetization of the FM layer as rigid as possible.

The EB effect arising from the FM/AFM interface, has been discovered more than half a century ago [20]. An AFM layer provides a reference magnetization direction to the ferromagnetic layer in magneto-electronic devices, e.g., hard-disk read heads [1], and magnetic random-access memories [8]. In an EB effect a FM and an AFM material couple to each other, mostly by direct exchange interaction, whereby not only the coercivity of the FM is enhanced, but the hysteresis loop is also shifted along the magnetic field axis below a certain blocking temperature [20, 21]. Although it is accepted that for the EB, the spin-spin interaction at the FM/AFM interface is necessary, EB is influenced by several effects: interface roughness, crystalline and magnetic structure, chemical order, composition, magnetic proximity effects etc. The EB is a very complex issue. Therefore the behaviour of the EB effect varies from system to system and material to material, and it is often stated that despite its high technological importance and tremendous work done on the subject, EB is not yet generally well understood [21, 22, 23, 24]. A number of theoretical models have been proposed to account for

the experimental data, which include, but are not limited to: (1) the coherent rotation model [20], (2) the Néel model [25], (3) the random interface model [26], (4) the AFM domain wall model [27], (5) the interface spin canting model [28], (6) the random and compensated interface model, and so on [29, 30, 31, 32]. Some of these models, which we use to discuss our results, will be briefly presented in the next chapter.

1.1 Why to study Ni_xMn_{100-x} and its magnetic proximity effects?

For a reliable operation of the spin valve, the AFM material has to be chosen such that it meets the following criteria. **1. High exchange bias field (H_{eb}):** To avoid asymmetry and degradation of the output signal due to thermal fluctuations, the pinning field, called exchange-bias field (H_{eb}) must be sufficiently high (>300 Oe) to make the reference layer "rigid"under a moderate external field. **2. High blocking temperature (T_b):** The H_{eb} usually decreases with temperature and the temperature at which it vanishes is called blocking temperature (T_b). A high T_b (>250 °C) is required to ensure that the sensor functions even at elevated temperatures. This is important because the temperature of the active region of the sensor may rise to 60–120 °C during normal operation [5]. **3. Large resistivity of the AFM layer:** As the AFM layer itself does not contribute to the MR effect, a high resistivity material is desirable for suppressing the current-shunting effect. For this purpose, the ideal AFM material should be an insulator. Unfortunately, most of the oxide-based AFM materials like NiO can hardly satisfy other requirements, and thus are unsuitable as AFM materials for practical device applications [5]. **4. Small critical thickness:** The H_{eb} increases with the thickness of an AFM layer. This thickness dependence is different for different AFM materials, but at some sufficient thickness, the H_{eb} is saturated, i.e., it does not depend any more on AFM thickness. The onset thickness for this saturation is called the critical thickness. Considering the temperature dependence of the exchange field, the thickness of the AFM must be chosen well beyond the critical thickness in practical devices. However, a large AFM thickness will make the total thickness of the sensor larger, which is undesirable. Therefore, AFM materials with smaller critical thickness are required for spin-valve applications. **5. Good corrosion resistance:** AFM materials with good corrosion resistance are suitable for practical applications.

The AFM materials mainly studied so far consist of (i) Mn-based alloys, (ii) Cr-based alloys and (iii) Fe, Co or Ni-based oxides [33, 34]. Mn-based alloys are studied the most due to their technological importance. They can be roughly divided into two groups with respect to their crystalline structure and magnetic properties. The one group consists of FeMn, IrMn, RhMn, RuMn and has a fcc crystalline structure. The other group has an fct (CuAu-I) crystal structure and contains NiMn, PtMn, PdMn and some of their ternary alloys. FeMn is the most widely studied AFM material amongst all of them due to several reasons, i.e., its good exchange bias, low critical thickness, no post-deposition annealing requirement [34], easily attainable Néel temperature (490 K) [21] and because its bulklike single-crystalline atomic and spin structure can be obtained on Cu(001) [35, 36, 37]. However, its relatively low blocking temperature and poor corrosion resistance make it unsuitable for read sensor applications. Another member of this Mn-based first group is IrMn which does not require thermal annealing and has better corrosion resistance and smaller critical thickness as compared to FeMn,

but its moderate blocking temperature limits its application in devices [33, 38, 39]. The second group of the above mentioned Mn-based alloys, though it requires an annealing process to get antiferromagnetic phase after deposition, yet it provides much higher blocking temperature, better corrosion resistance, and higher exchange bias field and thus is very suitable to be used in real devices. The major drawback of this group is its larger critical thickness, which could limit its application in very high density recording applications [5]. NiMn plays a leading role in the second group having the highest ordering temperature (T_{AFM}) (as high as 1070 K) in its bulk form [40, 41] as well as blocking temperature (as high as 723 K) in its polycrystalline thin film form [5] amongst all Mn-based alloys in bulk form.

The motivation for probing the antiferromagnetism of equiatomic NiMn on top of Ni/(Co/)Cu_3Au(001) is two-fold. Firstly, it is interesting to see which spin structure NiMn exhibits in thin films on Cu_3Au(001), where it may grow with bulk-like lattice parameters due to lattice matchment with Cu_3Au(001). In bulk form, NiMn has collinear in-plane spin structure [42]. Epitaxial FeMn on Cu(001) has proven to couple to both IP and OoP magnetized FM layers [43, 44] and shows a non-collinear spin structure [35, 36]. In the thin film form, NiMn may not have the same collinear spin structure as is reported for its bulk form [42, 45]. In the bulk AF I-type spin structure of $L1_0$ NiMn, the nearest-neighbor Mn atom's moments are antiparallely aligned and oriented normal to the c-axis of the fct lattice. The Mn and Ni atoms constitute alternating sheets with magnetic moments per atom of 3.8 μ_B and approximately 0 μ_B, respectively [42, 46, 47]. The second motivation is the high Néel or ordering temperature and blocking temperature of NiMn: if $Ni_{50}Mn_{50}/Cu_3Au$(001) can be prepared epitaxially along its c-axis in single-crystalline form like that of its bulk counterpart, it may sustain a very high T_{AFM} and T_b. Furthermore, since EB is an interface phenomenon, its investigation can be more appropriately addressed using single-crystalline materials than polycrystalline ones.

One of the basic requirements to obtain EB is that the magnetic anisotropy energy of the AFM should be larger than the interfacial exchange energy [21]. In most of the theoretical models describing EB, one of the key assumptions is the collinear spin configuration of the AFM layer at the interface, however practically, there are several AFM materials which have non-collinear spin structures. For instance, FeMn (in bulk as well as in thin film form) [35, 36] and $Ni_{28}Mn_{72}$ (only in bulk form) [48] are reported to have non-collinear three-dimensional spin structures which can give rise to EB in both in-plane and out-of-plane directions when coupled to an FM layer in the respective magnetization directions. Nogués *et al.* reported that the exchange bias depends strongly on the spin structure at the interface, especially on the angle between the ferromagnetic and antiferromagnetic spins [49]. Also it has been experimentally demonstrated that in EB systems the spin configuration of an FM as well as of an AFM layer near the interface may significantly deviate from that in the bulk or its intrinsic state in thin film form [50, 51]. Therefore, it could not only be the different orientations of the FM magnetization which, due to exchange interaction at the FM/AFM interface may change the non-collinear spin structure and thus magnetic properties of an AFM, but also the chemical composition of the AFM alloy. The elusive nature of EB is partly due to the a little understanding of the AFM and FM layer's contribution to the exchange interaction at the interface of both layers. An important parameter from AFM alloy films that could affect the interfacial spin structure or the exchange interaction at the interface is its chemical composition, whereas from the FM film, it could be

different magnetization orientations or *magnetic proximity effect*. A systematic study showing the impact of both above stated parameters (i.e., chemical composition of AFM alloy film and magnetization direction of FM film) on interfacial spin structure, especially the second one, is rarely studied at least for the single crystalline form of the exchange bias system. The magnetic proximity effect has been studied very seldom for Mn-based alloys. For equiatomic FeMn AFM thin films coupled with Ni, the T_{AFM} for OoP coupling was reported to be up to 60 K higher than IP coupling [43]. But these results may not be the same when changing the chemical composition of the AFM.

Because conventional methods such as neutron diffraction or susceptibility data cannot be acquired with sufficient signal to obtain the ordering temperature of AFM thin films directly due to lack of material, therefore an indirect way is adopted by observing the influence of FM thin film on an AFM with the help of more sensitive and sophisticated technique such as magneto-optical Kerr effect (MOKE). But for an AFM having complicated three-dimensional non-collinear spin structure, doing so would mean to measure only one, out of two components, of the AFM spin. That is to look at the one face of the picture! To have a complete look at the picture, it is necessary to couple such kind of AFM layer with an adjacent FM of which magnetization could be manipulated in both IP and OoP directions.

1.2 Previous studies on Ni_xMn_{100-x}

Chemically ordered equiatomic NiMn (Ni∼45%–56%) shows an $L1_0$ structure with lattice parameters $a = b = 3.74$ Å and $c = 3.52$ Å, and the chemical ordering results in alternating atomic planes of Ni and Mn along the c-axis, with a contraction perpendicular to these planes [45, 52]. The preparation of equiatomic NiMn films with $L1_0$ structure is not trivial. Often this requires long post-deposition annealing procedures to induce chemical ordering, treatments that may result in strong inter-diffusion at the FM/AFM interface and, therefore, in a complex thermal treatment-dependent magnetic behavior [53, 54, 55, 56]. For films grown by sputtering, annealing up to 40 h at 280 °C is necessary to induce chemical ordering [54]. In this sense, since EB is an interface effect, the study of EB-systems based on FM/AFM bilayers prepared starting from spontaneously ordered $L1_0$ NiMn films obtained by epitaxial growth is of strong interest. Recent studies show that chemically ordered equiatomic NiMn can be grown epitaxially on Cu(111) [57], as well as on Cu(100) [58, 59, 60]. In the case of Cu(111), chemical order was obtained only after annealing at 250 °C in an applied magnetic field of 250 Oe for 16 h. Tieg *et al.* proposed for equiatomic $c(2\times2)$ NiMn/Cu(001) a bulk-like $L1_0$ crystal structure, which is characterized by an in-plane orientation of the bulk c-axis ("a-axis growth") [58].

The dependence of EB on different crystallographic orientations of the AFM in the same FM/AFM system is an open issue in exchange bias. In the case of MnPd, one of the high Néel temperature $L1_0$ AFM model systems, different works have shown that MnPd(001) can be grown epitaxially with either the c-axis or the a-axis along the film normal (c-axis or a-axis growth, respectively), depending on the substrate, growth temperature, or surface morphology [61, 62]. For $L1_0$ NiMn, while the use of Cu(001) as substrate leads to an a-axis epitaxy [58, 59, 60], the use of Cu_3Au(001) as substrate may lead to c-axis epitaxy since Cu_3Au(001) has a lattice constant a = 3.75 Å [63, 64], a value that matches the lattice constant the a- and b-axis of $Ni_{50}Mn_{50}$ [52]. Such an approach could possibly allow for the study of the influence of different

crystallographic orientations (and also different spin structures relative to the film surface) on the magnetic coupling at the interface for the same EB system.

Like other Mn-based alloys, NiMn has been mostly studied in its polycrystalline form prepared by magnetron sputtering. No study of single-crystalline NiMn thin films has been reported until the last few years. For epitaxially grown NiMn thin films, studies have been recently made on Cu(111) [57], and Cu(001) [58, 59, 60]. Ni/NiMn/Cu(111) needed annealing in the presence of a magnetic field and then showed a complex temperature-dependent exchange bias for a thickness of 35 Å[57]. Tieg *et al.* showed antiferromagnetism of equiatomic NiMn in the bilayer system Co/NiMn/(Co/)Cu(001), where NiMn grows with its *a*-axis along the surface normal. The enhancement of coercivity of Co was attributed to the interface magnetic coupling due to the antiferromagnetic character of NiMn above 8 ML thickness at 300 K [58]. Reinhardt *et al.* not only confirmed these findings for a similar system afterwards, but also found stronger coupling in $Co/Ni_{35}Mn_{65}/Cu(001)$ as compared to $Co/Ni_{50}Mn_{50}/Cu(001)$ [59]. In a combined experimental and theoretical investigation, Gao *et al.* have shown by spin-polarized scanning tunneling microscopy that the surface spin density of NiMn/Cu(001) films is non-collinear [60], contrary to what was expected. This was assigned to the broken symmetry at the surface, and explained by the analysis of low energy electron diffraction (LEED) patterns [60]. The magnetic properties (like the antiferromagnetic ordering temperature T_{AFM}, the blocking temperature for exchange bias T_b, and the exchange bias field H_{eb}) of NiMn single-crystalline thin films have never been reported in contact to OoP magnetized FM layers on any substrate including $Cu_3Au(001)$. For NiMn in contact to an IP magnetized FM layer, only a few thickness and temperature-dependent MOKE measurements have been performed on Cu(001) [58, 59], limited to exploring its T_{AFM}.

Previously, it has been found that bulk NiMn has a different crystal structure for different chemical compositions of its constituents. It has a face-centered tetragonal crystal structure with a constant lattice ratio of $c/a < 1$ for nearly equiatomic concentration [42, 45] whereas its crystal structure is found to be very sensitive to the Ni concentration (13–40%); an fcc cubic lattice undergoes a tetragonal distortion, either $c/a < 1$ or $c/a > 1$, or an orthorhombic distortion at lower temperatures [65]. In literature, one can find some work indicating a connection between the bulk Ni_xMn_{100-x} crystal structure and its spin structure. It was shown experimentally that for equiatomic concentration, bulk NiMn has an $L1_0$-type crystal structure with a spin structure in which Mn spins points along a direction perpendicular to the *c*-axis (along [100] direction), whereas the possibility of the Mn moments to lie along [110] direction could not be excluded [42]. For bulk $Ni_{28}Mn_{72}$, the spin structure is non-collinear and three-dimensional [48]. Mitsumata *et al.* have been theoretically obtained similar results for equiatomic and lower concentration of Ni in Mn-based alloys including Ni_xMn_{100-x} where smaller AFM thicknesses are required for the onset and saturation of EB for the non-collinear spin structure compared to the collinear ones [66] due to smaller AFM domain wall width in the former case than in the latter [67]. Recently, Mitsumata *et al.* have generalized their work and theoretically proved that the case of an AFM material might not be considered equivalent to that of the FM ones, and that the AFM domain wall width could possibly be significantly smaller than the domain wall widths of the FMs [68]. Hence, the AFM thickness required to establish EB could be about $1/\sqrt{3}$ times smaller for any kind of AFM material having non-collinear spin structure as compared to the ones with collinear spin structure [68]. However, little

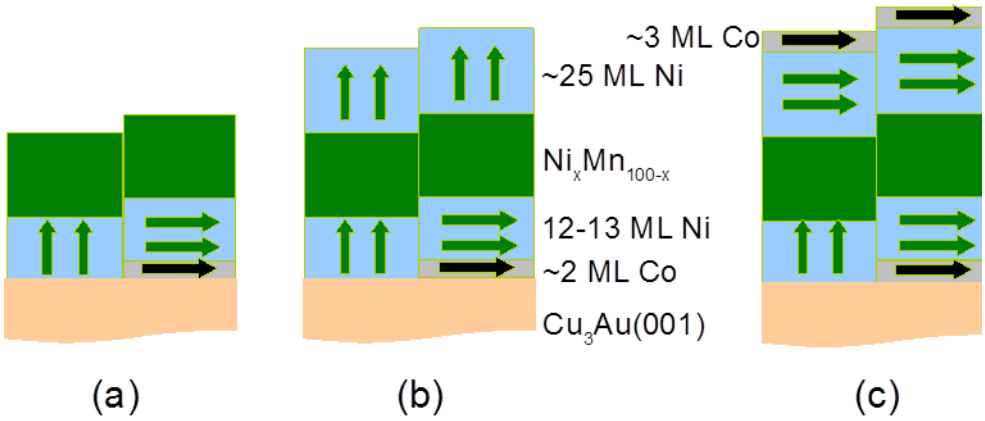

Figure 1.2: Schematic illustration of the samples used to study antiferromagnetic Ni_xMn_{1-x} layers coupled to in-plane as well as out-of-plane Ni layers in bilayers (a) and trilayers (b) and (c). The magnetization of ∼12 ML Ni/Cu_3Au(001) (∼25 ML Ni/Ni_xMn_{1-x}/∼12 ML Ni/(∼2 ML Co/)Cu_3Au(001) is out-of-plane and can be directed in-plane by under(over)-deposition of ∼2 (∼3) ML Co.

experimental work has been done regarding the spin structure of Ni_xMn_{100-x} in thin film form.

1.3 Aim of this thesis

As mentioned above that bulk NiMn has face-centred-tetragonal (fct) crystal structure, and has highest T_{AFM} (1070 K) [40], whereas polycrystalline NiMn thin films have highest H_{eb} as well as highest T_b amongst all Mn-based AFM alloys [5]. We wanted to know whether it is possible to prepare bulk-like Ni_xMn_{1-x} ultra-thin films on Cu_3Au(001) due to the matching lateral lattice constants of the film and the substrate. If yes, then it might maintain its superior magnetic properties, suitable to be used at elevated temperatures in real devices such as magnetic read-heads which are based on GMR/TMR sensors where NiMn as an AFM layer could pin the magnetization of an adjacent FM reference layer through the EB effect. Also, the magnetic properties at the interface are dominated by the AFM layer spin structure which is not known for NiMn in thin film form. In bulk form, the NiMn spin structure is IP collinear [42] and for $Ni_{28}Mn_{72}$, it is non-collinear [48]. The aim of this thesis was to explore the magnetic properties of the Ni_xMn_{1-x} in contact with an adjacent FM Ni layer the magnetic easy axis of which could be manipulated in in-plane or out-of-plane direction by under (over)-deposition of an ultra-thin Co layer. Therefore, for a reliable comparative study of the magnetic behaviour, the very same Ni_xMn_{1-x} film can be used, simultaneously contacted to a FM Ni layer magnetized in IP and OoP direction. A sketch of the bilayers and the trilayers used in thesis is given in Fig. 1.2. The magnetic easy axis of Ni on Cu_3Au(001) [69] and Ni on Ni_xMn_{1-x}/Cu_3Au(001) is OoP in certain thickness range, and can be turned to IP by under(over)-deposition of ∼2–3 ML Co. Ni_xMn_{1-x} could couple to adjacent Ni in both directions if it has 3-dimensional spin structure. As stated before, the magnetic properties in EB system are dominated by the interfacial spin structure which could not only be changed by different magnetization direction of the FM layer but also by changing the AFM spin

structure which could be a function of its composition, in case an AFM is an alloy like NiMn. For further exploring the magnetic properties, especially the spin structure of Ni_xMn_{1-x}, it can be sandwiched between two Ni layers with magnetic easy-axis tunable from OoP to IP direction. The 3-dimensional spin structure of sandwiched Ni_xMn_{1-x} could exhibit interesting magnetic properties of the trilayer system which could help in understanding the elusive nature of exchange bias by looking for location of pinned uncompensated moments within Ni_xMn_{1-x} which is usually supposed to be at the FM/AFM interface. Longitudinal and polar MOKE geometries can be used to investigate the magnetic properties of Ni_xMn_{1-x} such as T_{AFM}, T_b, H_{eb}, and some speculations about its spin structure can be made based on the experimental results.

1.3.1 Outline of the thesis

This thesis is composed of five next chapters. The second chapter is about the theoretical background and contains a brief introduction to the EB phenomenon and some models to explain the origin of the EB effect. The third chapter explains the experimental aspects of the work. The fourth chapter contains experimental results in three sections: the first section presents results for the growth and structure of Ni_xMn_{100-x}/Cu_3Au(001) and epitaxial growth of Ni, the second section deals with thickness-dependent magnetic properties of equiatomic NiMn/Ni/(Co/)Cu_3Au(001) bilayers, and the third section presents thickness-, and concentration-dependent magnetic properties of Ni_xMn_{100-x}/Ni/(Co/)Cu_3Au(001) bilayers. The fifth chapter covers the study of (Co/)/Ni/Ni_xMn_{100-x}/Ni/(Co/)Cu_3Au(001) trilayers to further explore the Ni_xMn_{100-x} spin structure via the magnetic proximity effect and study the interlayer exchange coupling between the two FM layers through the AFM layer as well to get some information about the NiMn frozen or uncompensated spins which are responsible for exchange bias. The sixth chapter finally summarizes the results and conclusions presented in the fourth and fifth chapters.

Chapter 2

Interaction between ferromagnetic/antiferromagnetic thin films and exchange bias

2.1 Unidirectional anisotropy or exchange bias

The unidirectional anisotropy or exchange bias as defined in the following, is quite remarkable. Ferromagnetic materials, alone have two equally favourable magnetic directions, which are collinear and lie along the "easy axis". Therefore two equally stable magnetization directions have the same energy, and same magnitude of an external magnetic field is required to switch the magnetization from one easy direction to the other. In Fig. 2.1(a), the magnetization loop is therefore symmetric about zero field. When an FM is brought into contact with an AFM, usually, the exchange coupling between the two films leads to an increased coercivity of the ferromagnet (Fig. 2.1(b)). This is attributed to magnetic moments in the AFM which are "dragged"around by the external field along with the FM spins. However, the ferromagnetic hysteresis loop is still symmetric, indicating two equivalent easy directions.

The reasoning for the enhancement of coercivity is easy to accept. If, on the other hand, the FM/AFM system is grown in a magnetic field or is cooled down after growth from above its Néel or AFM ordering temperature in the presence of a magnetic field, the hysteresis loop can become asymmetric and shifted from zero field (Fig. 2.1(c)). This unidirectional shift is called exchange bias and reflects the fact that there is now a preferred easy magnetization direction for the FM. In other words, the magnetization **M** of the ferromagnet is pinned by the AFM into this direction. This, at the first look, seems puzzling since at the same time AFM film's interfacial spins are rotating along with FM spins as well as pinning the FM spins.

After the following section will show how this can be understood in terms of simple intuitive picture as well as a theoretical model.

2.2 Discovery of exchange bias

In 1956 when the EB effect was discovered by Meiklejohn and Bean [70] while studying Co (FM) particles covered by their native oxides CoO (AFM), they very rightly recognized that this effect arises from the FM/AFM interface due to the exchange in-

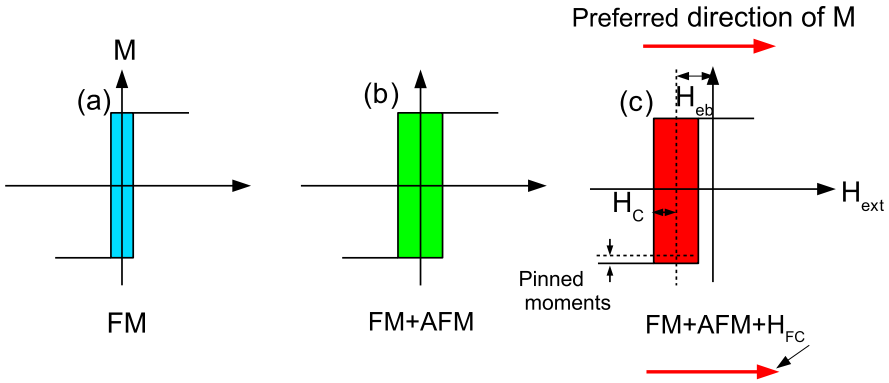

Figure 2.1: Easy-axis magnetization loop of (a) an FM film, (b) an FM film grown on top of an AFM, and (c) an FM/AFM bilayer after field-cooling in the presence of external magnetic field H_{FC}. In (a) and (b), the anisotropy is *uniaxial*, whereas in (c), it is *unidirectional* as the FM is biased with a bias field H_{eb}. The H_{eb} points to the left, while the preferred direction of **M** points to the right, since the structure switches easier into this direction. The cooling field (H_{FC}) is the field applied during cooling from the temperature above the ordering temperature of an AFM and below the Curie temperature of FM. Note that the loop may also be asymmetric vertically because some pinned moments do not rotate into the direction of H_{eb}, i.e., they remain aligned along the preferred direction of **M**. This leads to the vertical asymmetry, as indicated by a slight downward shift of loop shown in (c).

teraction between the FM and the AFM spins. Being an interfacial effect, it has been mostly studies in thin films.

Fig. 2.2 shows the original figures from Ref. [70, 71]. When the system Co-CoO particles is cooled from room temperature down to 77 K through the Néel temperature of CoO (291 K), a symmetric hysteresis loop along the field axis is obtained (Fig. 2.2(a) dashed loop). However, when the sample was cooled down in the presence of a positive magnetic field, the hystersis loop was found shifted along the negative field axis. This is shown by the continuous line loop of Fig. 2.2(a). This shifted loop could not be made centred along the axis even by the application of very strong fields (i.e. 7 T).

By using a self-made torque magnetometer, the authors studied the behaviour of anisotropy above and below the Néel temperature of CoO. It consists of a spring connected to a sample placed in an external magnetic field. Usually, the torque magnetometry is considered a good method for measuring the magnetocrystalline anisotropy (MCA) of single crystal ferromagnets. The torque on the sample is measured as a function of the angle θ between certain crystallographic directions and the applied magnetic field. In strong external magnetic fields, when the magnetization of the sample is parallel to the applied field such that the FM is saturated, the torque is:

$$T = -\frac{\partial E(\theta)}{\partial(\theta)} \tag{2.1}$$

where $E(\theta)$ is the MCA energy. For Co having a hexagonal lattice structure, the torque of the c-axis follows a $\sin(2\theta)$ function as given in Fig. 2.2(b). The torque and the energy, respectively, can be written as:

$$T = -K_1 sin(2\theta) \tag{2.2}$$

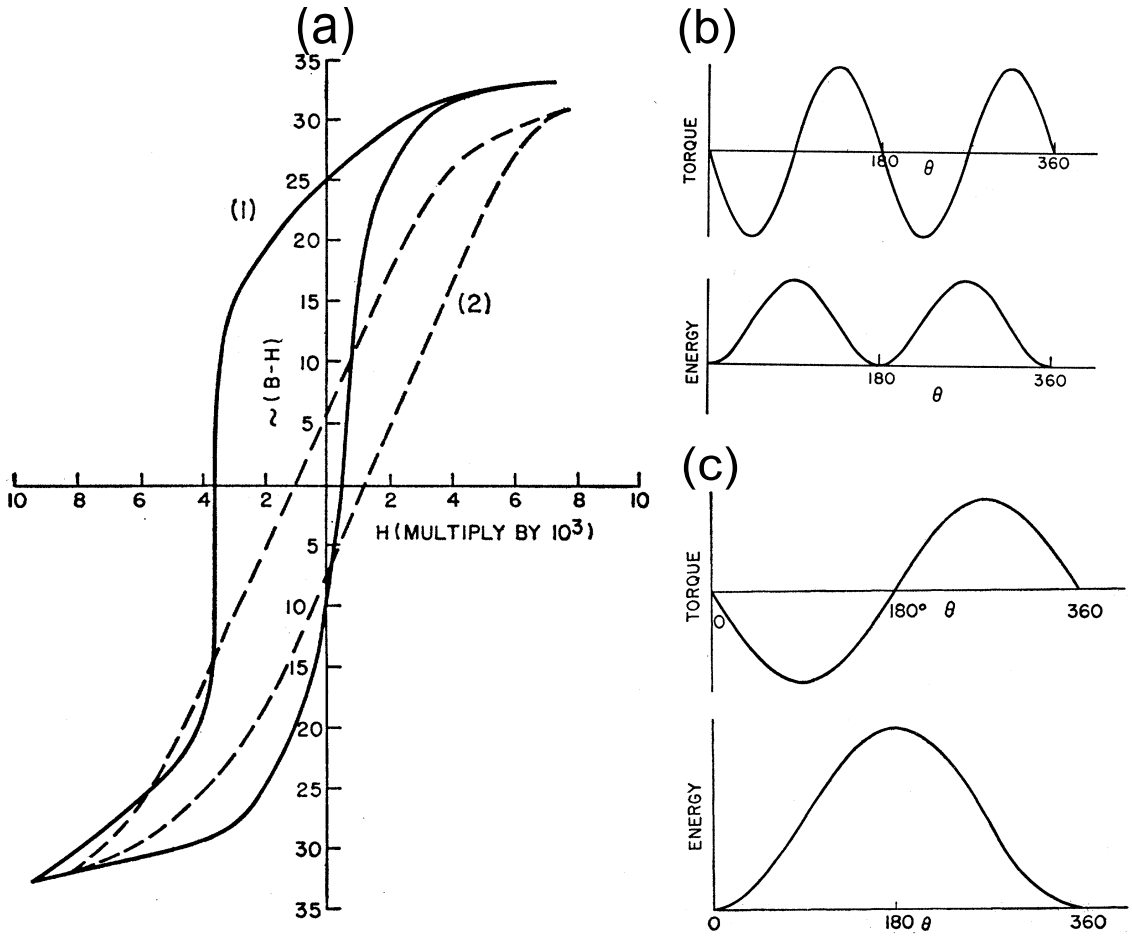

Figure 2.2: (a) Hysteresis loops of Co-CoO particles taken at 77 K. The dashed line shows the loop after cooling in zero field. The solid line is the hysteresis loop measured after cooling the system in a field of 10 kOe, (b) torque and energy curves for Co particles at 300 K showing uniaxial anisotropy corresponding to dashed-loop in (a), (c) torque and energy curves of Co-CoO particles taken at 77 K showing the unusual unidirectioal anisotropy corresponding to solid loop in (a), from Ref. [70, 71].

$$E = \int K_1 sin(2\theta) d\theta = K_1 sin^2(\theta) + K_0 \tag{2.3}$$

where K_1 is the MCA energy and K_0 is an integration constant. From the energy expression, it is clear that at $\theta = 0^o$ and $\theta = 180^o$, the system is in equilibrium (stable). This is typical for FM materials and is observed for Co particles above room temperature where the CoO was in the paramagnetic state. However, the torque curve is completely different below the Néel temperature of CoO (291 K). It follows a sinθ function. The torque and the energy terms can be expressed respectively, as:

$$T = -K_u sin(\theta) \tag{2.4}$$

$$E = \int K_u sin(\theta) d\theta = -K_u cos(\theta) + K_0 \tag{2.5}$$

The K_u in Eq. 2.4 and Eq. 2.5 represents the unidirectional anisotropy. From Eq. 2.5 one concludes that for only one position, that is θ=0°, the Co/CoO system is in equilibrium. Moving the system to any other direction, it comes back to this stable (equilibrium) position. That is why the system is said to have a unidirectional anisotropy which is along the field cooling direction.

One can check whether the same unidirectional anisotropy observed by torque magnetometry is responsible for the loop shift. For that let us consider the Stoner-Wohlfarth (SW) model [72] which makes use of the simplest possible expression for the free energy of a single domain ferromagnetic thin film and calculates the magnetic hysteresis loops. It is assumed that all the spins are confined in the film plane and the film has a uniaxial anisotropy. By the application of sufficient alternating magnetic field, the response of the magnetization is then uniform resulting in a coherent rotation of the FM spin.

For an FM film in single domain form the total energy per unit area is given by

$$E(\theta) = \mu_0 M_{FM} t_{FM} H cos(\theta) + K_{FM} t_{FM} sin^2(\theta) \tag{2.6}$$

where the first term is the contribution from the Zeeman energy and the second term is the uniaxial anisotropy energy. The parameters used are: M_{FM} saturation magnetization of the ferromagnet, H the applied external magnetic field, K_{FM} the uniaxial anisotropy constant of the FM, t_{FM} the thickness of the FM, and θ is the angle enclosed by M and H with the easy axis of magnetization. For simplicity, it is assumed that M and H both have the same angle θ with the easy axis. The hysteresis loop is the magnetization component $Mcos(\theta)$ along the direction of the applied field specified by H and θ which is obtained by solving Eq. 2.6 numerically.

Minimizing the free energy with respect to the angle θ

$$\frac{\partial E(\theta)}{\partial \theta} = 0 \tag{2.7}$$

provides an expression for the coercive field of the FM film:

$$H_C = \frac{2K_{FM}}{\mu_0 M_{FM} t_{FM}} \tag{2.8}$$

The unidirectional anisotropy term in Eq. 2.5 can be added to the above Eq. (2.6).

$$E = \mu_0 H M_{FM} t_{FM} cos(\theta) + K_{FM} t_{FM} sin^2(\theta) - K_u cos(\theta) \tag{2.9}$$

A very similar solution to that of Eq. 2.8 is obtained for this equation by substituting an effective field: $H' = H_C - \frac{K_u}{M_{FM}t_{FM}}$. This makes the loop shifted by $H = \frac{K_u}{M_{FM}t_{FM}}$. This means that the loop shift is equivalent to a unidirectional anisotropy, and this was the conclusion of Meiklejohn and Bean as well.

2.3 Intuitive picture and Meiklejohn and Bean (MB) Model

For a qualitative understanding of EB, an intuitive picture of the (FM/AFM) system is presented in Fig. 2.3. When an FM/AFM system is heated above the Néel or ordering temperature (T_N or T_{AFM}) of the AFM but below the Curie temperature (T_C) of the FM, and a magnetic field is then applied, all the FM spins are aligned along the field direction whereas the AFM spins are disordered as it is in the paramagnetic state (Fig. 2.3(i)). Cooling the system to T_{AFM} in the presence of the field, the interfacial spins of the AFM next to the FM align along the FM spins in such a way that all the next AFM spin planes follow to achieve magnetically neutral structure (Fig. 2.3(ii)). When the field is reversed, the FM spins start to switch back but not the AFM ones because of their larger magnetic anisotropy (Fig. 2.3(iii)). The interfacial interaction between the FM and AFM spins at the interface wants to couple both the FM and the AFM spins at the interface. Or one can say that the interfacial AFM spins exert a kind of torque on the FM spins to keep them aligned along their original position (Fig. 2.3(iii)). Therefore the FM spins favour to have a single stable configuration (the FM anisotropy becomes unidirectional). The field required to switch completely the FM spins will be larger being contacted with an AFM to overcome the microscopic torque (Fig. 2.3(iv)). But when the field is switched back towards its initial direction, the FM spins will be rotated with smaller field as if they would see an internal biasing from the AFM spins, because now the AFM exerts a torque in the direction of the field (Fig. 2.3(v)). Therefore the FM hysteresis loop is shifted along the field axis, that is, exchange bias occurs [21].

The initial theory put forward by Meiklejohn and Bean [70, 71] suggested that a plane of uncompensated spins at the FM/AFM interface was responsible for the effect. An uncompensated spin is defined as a microscopic structure which has a non-zero net magnetic moment, but which exists in an antiferromagnet whose macroscopic magnetic moment is zero. An example of compensated and uncompensated spins at the interfaces is shown in Fig. 2.4. The understanding of EB in MB model is based largely on the assumption of idealized planar compensated or uncompensated interfaces. If the first AFM plane next to the interface is compensated, that is, if the AFM sublattice structure is such as to give equal numbers of the two opposite spin directions at the interface, then the net field exerted on the ferromagnet by an assumed ferromagnetic exchange; across the interface is zero Fig. 2.4(a). On the other hand, if the first AFM plane is uncompensated, as shown in Fig. 2.4(b) with the same direction of all intefacial spins, there is an interfacial energy difference (per unit area) favouring one ferromagnetic orientation over the other to give rise to EB predicted in MB model. Some uncompensated moments at the interface can give rise to frustration as shown in Fig. 2.4(c).

Meiklejohn and Bean might have a similar intuitive picture in their minds as given in Fig. 2.3 and Fig. 2.4, while deriving their theoretical model for EB. In this model,

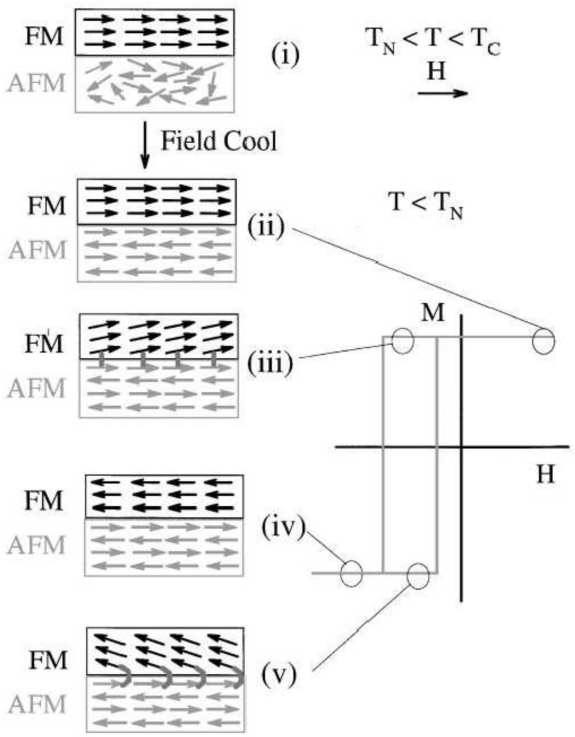

Figure 2.3: Schematic diagram of the spin configuration of an FM/AFM bilayer at different stages (i)-(v) of an exchange-biased hysteresis loop [21].

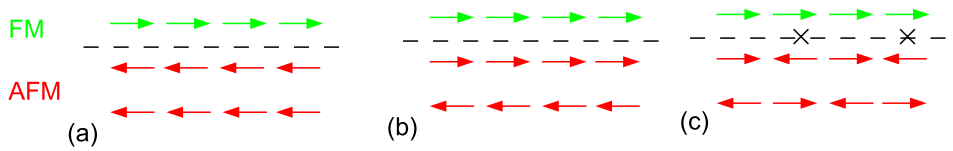

Figure 2.4: Schematic side view of possible atomic moment configurations in a ferromagnetic-antiferromagnetic bilayer with a planar ferromagnetically coupled interface indicated by the dashed line. (a) Compensated, and (b) uncompensated spins, and (c) frustrated spins are indicated by crosses.

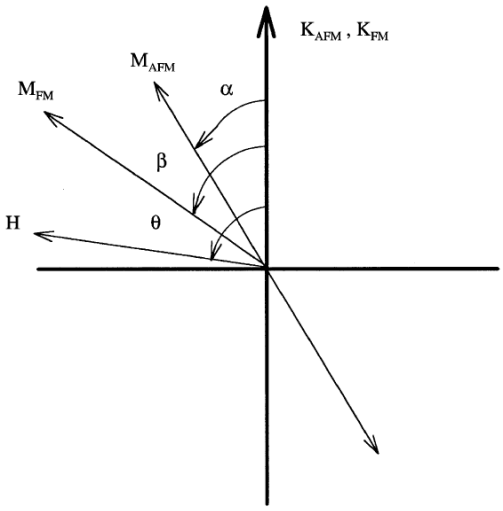

Figure 2.5: Schematic diagram of angles involved in an exchange bias system. Note that the AFM and FM anisotropy axes are assumed collinear and that the AFM sublattice magnetization M_{AFM} has two opposite directions, from Ref. [21].

a plane of uncompensated spins at the FM/AFM interface was assumed for the effect. Assuming coherent rotation of the magnetization, the energy per unit area of an exchange bias system, can be written [21, 73] as

$$E = -HM_{FM}t_{FM}cos(\theta-\beta)+K_{FM}t_{FM}sin^2(\beta)+K_{AFM}t_{AFM}sin^2(\alpha)-J_{INT}cos(\beta-\alpha) \tag{2.10}$$

where H is the applied field, M_{FM} the saturation magnetization, t_{FM} the thickness of the FM layer, t_{AFM} the thickness of the AFM layer, K_{FM} the uniaxial anisotropy of the FM layer, K_{AFM} the anisotropy of the AFM layer, and J_{INT} the interface coupling constant. β, α and θ are the angles between the magnetization and the FM anisotropy axis, the AFM sublattice magnetization (M_{AFM}) and the AFM anisotropy axis, and the applied field and the FM anisotropy axis (Fig. 2.5) [21, 73]. It is usual to assume collinear FM and AFM anisotropies as shown in Fig. 2.5. The first term in the above energy equation holds for the Zeeman energy, the second term accounts for the FM anisotropy, the third term for the anisotropy of the AFM, and the last term is for the interfacial coupling between the FM and AFM.

To make the situation further simplified, the FM anisotropy is considered to be negligibly small [73]. Experimentally this condition is usually met [21]. Therefore, Eq. 2.10 can be written as

$$E = -HM_{FM}t_{FM}cos(\theta-\beta)+K_{AFM}t_{AFM}sin^2(\alpha)-J_{INT}cos(\beta-\alpha) \tag{2.11}$$

The loop shift can be found by minimizing the energy with respect to α and β [73]:

$$H_{eb} = \frac{J_{INT}}{M_{FM}t_{FM}} \tag{2.12}$$

To observe EB, another condition $K_{AFM}t_{AFM} \geq J_{INT}$ should be fulfilled while minimizing the energy Eq. 2.11 [73]. α can be kept at minimum value by meeting the condition of $K_{AFM}t_{AFM} \gg J_{INT}$. But if the reverse condition is true that is $J_{INT} \gg K_{AFM}t_{AFM}$, then the angle $(\beta-\alpha)$ should be smaller, i.e., then the AFM spins will rotate together

with the FM spins to increase only the coercivity without exhibiting any loop shift. The exchange bias magnitude predicted by these calculations is several orders of magnitude larger than the experimental result. This discrepancy is mainly due to several reasons which are not taken into account in this simple model, for instance, (i) AFM domains, (ii) the AFM/FM interface roughness, (iii) a non-collinear spin structure of the AFM, and (iv) a limited number of uncompensated pinned AFM spins. Therefore, actually it is not the presence of a bias field but the small size of it that is puzzling!

A few years ago, Ohldag *et al.* observed experimentally not only the existence of the uncompensated spins at the interface of FM/AFM system [74], but also remarkably found for several different AFM/FM samples that the size of the exchange bias field can be understood in terms of a simple extension of the early Meiklejohn and Bean model, which quantitatively explains the determined bias fields by the number of pinned interfacial moments and their size [75]. It is found that there is in fact only a very small percentage (4%) of moments at the AFM interface which are pinned [75] as shown in Fig. 2.1(c) by a vertical shift in the loop. The rest of the moments rotate rigidly with the ferromagnet. Only these pinned moments contribute to the expression above, so that the predicted bias fields are reduced by a factor of 0.04, which leads to realistic values for the exchange bias. However, the nature (its origin and magnitude) of the pinning is not known.

Amongst several theoretical models to account for the experimentally observed small EB, two of them based on the formation of AFM domains are the most important: (i) the Mauri planar domain-wall model, and (ii) the Malozemoff perpendicular domain-wall (or the random interface) model. These are the most relevant as well to the work of this thesis. Therefore, a brief introduction to these models is being presented below.

2.4 Mauri domain-wall model

In 1987, Mauri presented a simple domain-wall model [27] to account for experimentally observed EB value which are an order of magnitude smaller than predicted by the MB model. A more reasonable estimate for EB field comes from allowing a planar domain-wall to form at the interface with the unfavourable ferromagnetic orientation (Fig. 2.6). If the AFM has an in-plane uniaxial anisotropy energy K_{AFM} and exchange stiffness $A_{AFM} = J_{AFM}/a$, the AFM domain-wall energy has the well known value $\sqrt{A_{AFM}K_{AFM}}$ [26, 28, 76], provided the AFM is assumed to be infinitely thick. The corresponding H_{eb} is then:

$$H_{eb} = \frac{2}{M_{FM}t_{FM}}\sqrt{A_{AFM}K_{AFM}} \tag{2.13}$$

This prediction is significantly smaller than the previous estimate provided by MB model, and for the first time, offers a possible micromagnetic origin for unidirectional anisotropy.

The scheme for the spin configuration within the Mauri model that shows the details of interfacial AFM rigid spins which develop a domain-wall parallel to the interface, is given in Fig. 2.7. For simplicity, the AFM two sublattice spins are shown coupled by two opposite arrows. An FM film of thickness t is separated by an interface of thickness ξ from a thick AFM below. The uniaxial anisotropy of the AFM is along the x axis. The uncompensated interfacial spins and the FM spins are coupled parallel. When an external magnetic field **H** is applied at an angle β with respect to the x axis, the FM

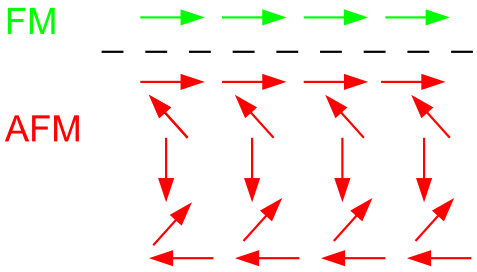

Figure 2.6: The antiferromagnetic layer can reduce its energy by forming a planar domain wall during the hysteresis loop measurement.

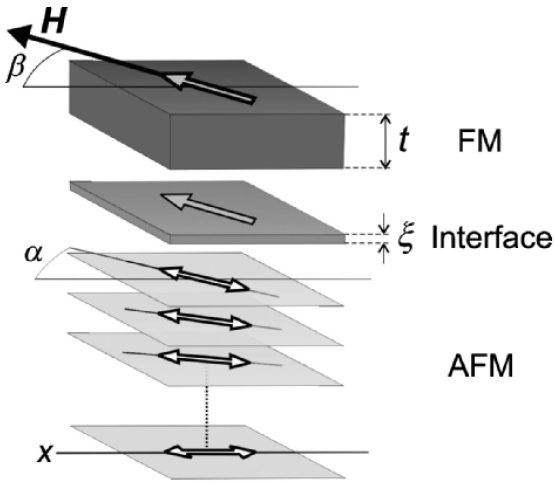

Figure 2.7: Simple model (Mauri model) for exchange bias. A ferromagnetic film of thickness t is separated by an interface of thickness ξ from a thick antiferromagnet below. The uniaxial anisotropy of the AFM is along x. Parallel coupling is assumed between the uncompensated interfacial moments and the FM moments. The external magnetic field **H** is applied at an angle β with respect to x and the FM moments are aligned parallel to **H**. Near the interface the AFM axis is allowed to rotate and form a domain-wall. The rotation of the AFM axis in the domain-wall is given by $\alpha \leq \beta$, from Ref. [15].

spins are aligned parallel to **H** for sufficiently high fields. At and near the interface the AFM spins might rotate along with the FM spins during the magnetization reversal and thus form a planar domain-wall. The AFM spins rotation in the domain-wall depends on the magnetocrystalline anisotropy of the AFM and is given by $\alpha \leq \beta$.

Like in the MB model, coherent rotation of the FM layer magnetization is considered during the magnetization reversal. Therefore the energy per unit area of the system can be expressed as:

$$E = -HM_{FM}t_{FM}cos(\theta-\beta)+K_{FM}t_{FM}sin^2(\beta)-J_{INT}cos(\beta-\alpha)-2\sqrt{A_{AFM}K_{AFM}}(1-cos(\alpha)) \tag{2.14}$$

All the first three terms are the same as in Eq. 2.10, only the anisotropy of the AFM layer is replaced by the AFM domain-wall energy as a last term. The EB is determined by three main parameters. (i) The pinned interfacial spin density S_{AFM} /(ξa), where S_{AFM} is the magnitude of the pinned interfacial spins, and ξ and a are the interface thickness and the in-plane atomic separation, respectively. (ii) The inter-

ficial coupling energy per unit area (E_{INT}), and (iii) the domain-wall energy (E_W). The (ii) is expressed as $E_{INT} = JS_{FM}S_{AFM}/(\xi a)$, where S_{FM} is the magnitude of the FM spins, and J is the interfacial exchange coupling constant. If $E_W > E_{INT}$, the AFM is rigid, preventing the formation of a domain-wall in the AFM. Maximum bias is then obtained, given by $H_{eb} = JS_{AFM}S_{FM}/(\xi aMt)$, where t and M are the thickness and magnetization of the FM. This is exactly what was determined by the MB model (Eq. 2.12, where J_{INT} is replaced by $JS_{AFM}S_{FM}/(\xi a)$). If $E_W < E_{INT}$, the bias field is determined by the formation of a planar domain-wall and is given by $H_{eb} = E_W/(Mt)$. The relatively weak bias field is due to smaller (from ideal) magnetocrystalline anisotropy of the AFM. This model has been experimentally verified by Scholl *et al.* [77] by observing an exchange spring of AFM NiO in the $Co/NiO(001)$ system.

The Mauri domain-wall model is found to be in good agreement with some of the experimental results but only for samples with sufficiently thick AFM films which can accommodate a planar domain-wall within itself. This model does not provide any explanation for the presence of EB in AFM/FM systems with thinner AFM layers. Therefore, there must be some thing lacking in this model; for instance, roughness of the interface has not been taken in to account and throughout the interface, a parallel alignment of the FM and AFM spins is considered.

2.5 Malozemoff random interface or perpendicular domain-wall model

Even for a very thin AFM film in contact with an FM film, where a Mauri DW wall is not possible, still bias field could be observed, which needs an explanation. Malozemoff considered the effect of random interface roughness and predicted that it is energetically favourable to form domains on the antiferromagnet interface side [26, 78]. These domains were found to reduce the H_{eb} by two orders of magnitude compared to the ideal MB model, a similar reduction as that found by Mauri. Also, formation of these domains is not restricted by the thickness of the AFM film, as the domain-wall is formed in perpendicular direction and the domain itself is formed along the lateral direction of the interface (opposite to the Mauri model). Another difference is that in the Malozemoff model, domains are permanently formed, whereas in the Mauri model, domains are only temporarily induced during the magnetization reversal of the FM film.

Fig. 2.8 shows how the spin configuration changes if a single mono-atomic bump is added at the interface. The energy associated with this bump can be found by counting the number of reversed spin pairs induced by the bump. A single bump at the interface induces a unidirectional exchange energy of $\pm z_i J$, where z_i is of the order unity and depends on the lattice details around the bump, and J is the atomic exchange energy between FM and AFM atomic moments. In Fig. 2.8(a), the energy difference in the units of J is -6—one ferromagnetically oriented nearest-neighbour pair across the interface is now replaced by five AFM-aligned pairs, for a net antiferromagnetic deviation of 6 away from perfect compensation. When the bump is shifted by 1 lattice site (Fig. 2.8(b)), the difference in energy (according to $\pm z_i J$) is +6 —a net ferromagnetic deviation of 6 away from perfect compensation. Positive (negative) sign is used for the frustrated spin pair where the spins are coupled ferromagnetically (antiferro-

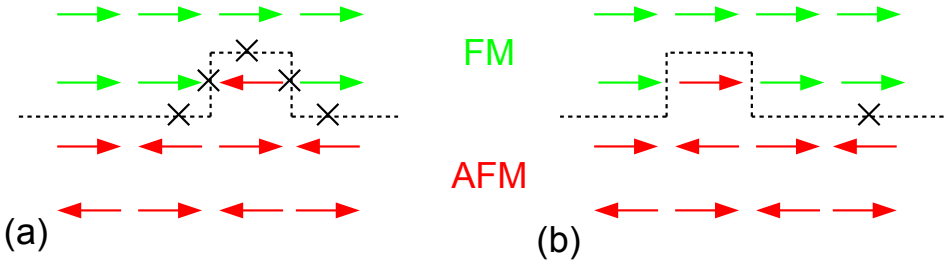

Figure 2.8: (a, b) Schematic demonstration to show how a single bump at the interface can lead to a unidirectional exchange between the ferromagnet and an antiferromagnet at a compensated interface.

magnetically). Thus a net energy difference of $z_i J$=12, acts as the interface, favouring one domain orientation over the other.

Due to the presence of these bumps, it is energetically favourable for an AFM film to break up in lateral domains with perpendicular walls. Keeping the same notation used in this chapter, the expression for the loop shift used by Malozemoff [26] can be written as:

$$H_{eb} = \frac{2}{M_{FM} t_{FM}} \sqrt{A_{AFM} K_{AFM}} \tag{2.15}$$

Comparing this equation (Eq. 2.15) with the one derived by MB (Eq. 2.12), by considering the exchange stiffness at interface equals to that at the AFM, i.e. $A_{INT} \approx A_{AFM}$, where A=J/a with J and a being exchange and lattice constant, respectively, one can see that the MB H_{eb} value is reduced by a factor of $\sqrt{A_{AFM}/K_{AFM}}/2$. Here the term in the denominator $\sqrt{A_{AFM}/K_{AFM}}$ can be immediately recognized to be the AFM domain-wall width (d_w). (Note that the expression for the domain-wall width is exactly the same whether used for FM or AFM.) In other words, the several order of magnitude larger value of EB suggested by MB [73] is now reduced by a factor which is inversely proportional to the AFM domain-wall width i.e. $H_{eb} \propto 1/d_w$. Besides experimental findings which confirm its validity, this model seems quite reasonable based on realistic assumptions.

2.6 Do AFM domains really exist?

Do AFM domains really exist, have they been observed experimentally? The answer is YES! To confidently say yes to this question is possible particularly due to the significant effort made during the last decade by J. Stöhr *et al.* The AFM domains have been observed in several systems containing AFM materials either alone or coupled with FM films, for example in NiO/MgO(100) [79], in epitaxial thin films of $LaFeO_3/SrTiO_3$(001) [80], in Co/$LaFeO_3/SrTiO_3$(001) [50, 81], in Co/NiO(001) [51, 77], and in Co/NiO/MgO(001) [74]. Kuch *et al.* have also provided the proof of the presence of single crystalline FeMn domains in the system Co/FeMn [82].

Ferromagnetic domains arise from the minimization of stray-field energy. If the stray-field energy is larger than the energy required to form domain-walls, the FM will break up into domains. On the other hand, an AFM does not have a macroscopic magnetization (no stray field exists), and thus domain formation in a perfect AFM is

not expected. However, imperfections and defects are the factors which can force the AFM to form domains.

To show the role of AFM domain-walls in EB, X-ray Magnetic Circular Dichroism (XMCD) and X-ray Magnetic Linear Dichroism (XMLD) have been used to image the magnetic ordering near the interface of FM Co on AFM $LaFeO_3$, showing a direct link between the FM domains and AFM domains [50]. A clear correlation at the interface has been observed and it was suggested that this correlation indicates a direct coupling between FM and uncompensated spins in AFM domains. However, due to the limited resolution of XMLD microscopy, it was not possible to directly image the uncompensated spins within the domains. Therefore, for this purpose, a much more sensitive technique like spin-polarized scanning tunneling microscopy (SP-STM) is required. By using SP-STM, a direct image of the AFM structure with atomic resolution has been obtained which contained AFM domain-walls with uncompensated spins [83].

Although the limited resolution of XMC(L)D can be overcome by SP-STM, as discussed above, at the same time SP-STM is only sensitive to the top layer of the AFM without any FM in contact. Therefore an explicit link between EB and the uncompensated spins at the AFM domain-walls can not be observed directly. This leaves unspecified the role of some other effects, such as magnetic defects, surface roughness, and grain size towards the creation of uncompensated spins. The lack of a very powerful technique capable of directly seeing spins at the interface of the AFM/FM bilayer with atomic resolution is actually the main challenge to completely understand the EB phenomenon.

2.7 AFM spin orientation and exchange bias

In some early important models [26, 27], including the one presented by the discoverer of the EB effect [71, 73], one of the basic requirements to get EB is that the magnetic anisotropy energy of the AFM should be larger than the interfacial exchange energy [21], i.e., $K_{AFM}t_{AFM} \geq J_{INT}$ where $J_{INT} = JS_{FM}S_{AFM}cos(\theta)$ and J is the exchange constant, S_{FM} and S_{AFM} are respectively the FM and AFM spins and θ is an angle between them. In most of the theoretical models describing the EB effect, one of the key assumptions is the collinear spin configuration of the AFM layer at the interface, however practically, there are several AFM materials which have non-collinear spin structures. For instance; FeMn in thin films as well as in bulk form [35, 36, 136] and $Ni_{28}Mn_{72}$ in bulk form [48], are reported to have non-collinear three dimensional spin structures which can give rise to EB in both IP and OoP directions when coupled to an FM layer in the respective magnetization directions. Nogués *et al.* reported that the exchange bias depends strongly on the spin structure at the interface, especially on the angle between the ferromagnetic and antiferromagnetic spins [49]. Depending on whether the anisotropy of the AFM layer is higher or lower, the AFM spins can align FM spins toward/along their own direction or the AFM spins can be aligned by the FM's spins along the FM magnetization direction. One example is XMCD images of thin ferromagnetic Co films grown on antiferromagnetic $LaFeO_3$ which imply that the alignment of the ferromagnetic spins is determined, domain by domain, by the spin directions in the underlying antiferromagnetic layer [50]. Another example is Co/NiO(001). Upon Co deposition a spin reorientation near the NiO interface occurs, with the antiferromagnetic spins rotating in plane, parallel to the spins of the Co layer

[51]. The direct observation of the alignment of FM spins by AFM spins, probably due to the larger anisotropy of the $LaFeO_3$, in the first example, and the reorientation of the AFM spins along the FM spins in the second one, most likely due to the weaker anisotropy of the NiO, demonstrate that the spin configuration of FM as well as that of an AFM within different FM/AFM systems near the interface may significantly deviate from that in the bulk or the intrinsic antiferromagnet. Therefore, for a realistic EB model, the AFM spin direction at the interface along with its anisotropy should be taken into account. In case an AFM is a binary alloy, concentration can play a key role in changing both of these inter-dependent parameters, i.e., AFM anisotropy and AFM spin structure. Also, the AFM anisotropy and spin structure can be changed if the AFM thin layer is sandwiched between two FM layers. These are the main topics of interest of this thesis.

2.8 Some other parameters involved in exchange bias

Blocking temperature: The temperature at which EB vanishes is called blocking temperature (T_b), and the temperature at which the antiferromagnetic order vanishes (AFM becomes paramagnetic), is called Néel or antiferromagnetic ordering temperature (T_N or T_{AFM}). Within references listed in Ref. [21], it has been experimentally observed that for thick enough single crystalline AFM films $T_b \approx T_{AFM}$, whereas for much thinner AFM films $T_b < T_{AFM}$. Two main reasons can be speculated for these observations; (i) the connection between T_{AFM} and T_b through the finite size effect, and (ii) the magnetic anistropy of the AFM. A very small fraction of the uncompensated spins is pinned at the interface which produces EB [75], and is not as evenly well distributed at the interface as the unpinned spins, therefore they need some support to feel the effect of each other. This support can be provided by the strength of the AFM order which itself follows a finite size effect. In terms of magnetic anisotropy of the AFM, as a second reason, a necessary condition in some early important models for EB to occur is $K_{AFM} t_{AFM} \geq J_{INT}$ [26, 27]. Like the spin-spin interaction within the AFM (which determines T_{AFM}), the spin-orbit interaction within the AFM (which determines the strength of K_{AFM}) also decreases with increasing temperature and decreasing dimensions of the AFM. The temperature and AFM dimensions dependence of T_{AFM} and K_{AFM} could be different. If K_{AFM} decreases faster than T_{AFM} by increasing temperature, then smaller EB field will be observed because, as discussed above, a smaller anisotropy implies smaller exchange bias and consequently $T_b < T_{AFM}$.

Training effect: For many exchange bias systems, it is well known that with the consecutive number of hysteresis loop measurements, the H_{eb} is decreased, called *Training effect* [21]. The very first empirical expression [84] for training was suggested to depend on the inverse of the square root of the consecutive number of measurements, i.e., $H_{eb}^n - H_{eb}^\infty \propto 1/\sqrt{n}$. This expression follows well the experimental dependence of the EB field for n>2, however, the agreement becomes poor when the very first point is included to the fit. More recently, Binek [85] has been provided a better expression that fits well to all points: $(H_{eb}^{n+1}\text{-}H_{eb}^n) \propto (H_{eb}^n\text{-}H_{eb}^\infty)^3$. This effect could be related to partial reorientation of the AFM domains with each FM magnetization reversal where AFM spins try to find energetically favourable configurations after each cycle.

Positive EB: When a very large magnetic field is applied upon an EB system

during the field-cooling from $T > T_{AFM}$, a positive EB can be observed. In the very first experimental observation of positive EB, an explanation of antiparallel FM/AFM interfacial coupling has been speculated [86]. The very large field-cooling energy overcomes the interfacial exchange energy and the AFM spins at the interface follow the large applied field during FC. This gives rise to positive EB.

2.9 Coupling across an AFM layer in FM/AFM/ FM trilayer

The discovery of GMR and TMR effects has not only triggered research into the field of FM/AFM interfacial exchange interaction responsible for the EB effect, but also focussed the interest to the interlayer exchange coupling, as both of these phenomena are the integral part of the above-mentioned effects used in spin valve sensors (read heads). Due to its technological relevance, a remarkable amount of work has been done on interlayer exchange coupling of FM/spacer/FM, where "spacer" could be either non-magnetic but conducting (in GMR effect) or insulating (in modern TMR effect). However, less attention has been paid to the study of interlayer exchange coupling where a technologically important AFM layer is used as the spacer layer, although Cr and Mn have been notably reported for this study, both of which as an AFM material have less technological significance. The study of FM/AFM/FM is important to explore the physics behind the EB effect which is still not fully understood.

In FM/AFM/FM trilayers the interlayer coupling is different from the other spacer layers because here the magnetic state of the AFM layer especially at the interfaces has to be considered. For an antiferromagnetic material as a spacer layer, each atom has a magnetic moment which is exchange coupled to other AFM atoms and across the interface to the ferromagnet. When an AFM material is used as the spacer layer, it can no longer be considered a "passive" medium transmitting the indirect exchange coupling. Rather it very actively participates in the coupling through exchange coupling at the interface as well as exchange coupling within itself. The interlayer and interfacial coupling may or may not always favour each other. There could be a case where both of the mentioned couplings oppose each other and a competition between them could finally lead to the situation where some of the nearest-neighbour spins within the system are not in their minimum energy state: they are magnetically frustrated. Besides the dipolar [87] and Ruderman-Kittel-Kasuya-Yosida (RKKY) coupling [88, 89, 90] (the coupling mechanisms in trilayers with non-magnetic spacer), an additional but fundamental direct exchange coupling through the AFM spacer makes the FM/AFM/FM trilayer system difficult but interesting to study.

2.9.1 Interface roughness affects spin configuration: an intuitive picture

In FM and AFM layered systems, the interface roughness can affect the spin configuration of the system. To understand this, an intuitive picture showing roughness-induced spin frustration in FM/AFM bilayers is given in Fig. 2.9 where a layer-wise AFM structure is assumed. For ideally perfect interfaces, a parallel (antiparallel) spin configuration is preferred within the spin pairs of the FM (AFM) layer (Fig. 2.9(a)). At the interface, the preferred spin alignment could be either parallel or antiparallel

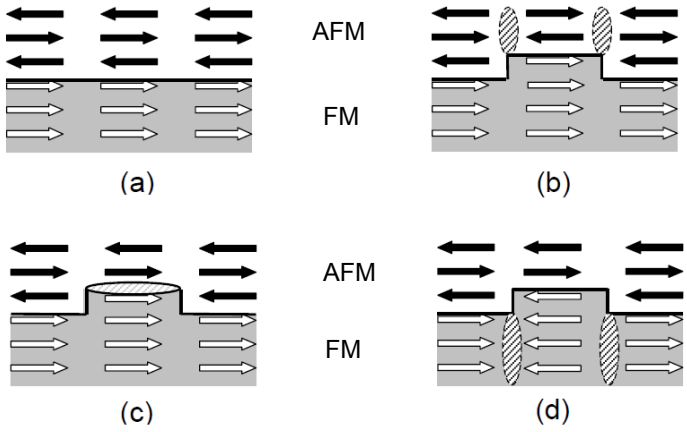

Figure 2.9: Relieving spin frustration at an FM/AFM interface. (a) Perfect interface, no frustration. (b) Frustration caused by a step is relieved by walls in the AFM layer. (c) Frustration relieved at the interface. (d) Frustration relieved by walls in the FM layer, from Ref. [91].

depending on which spin configuration gives minimum energy state. (In the example of Fig. 2.9, it is assumed that antiparallel spin alignment is the minimum energy state at the interface.) But in reality even in epitaxially grown thin films, the interface has roughness either due to the substrate or due to partially filled atomic layers at the interface as shown in Fig. 2.9(b)–(d). Therefore it is not possible to keep the preferred alignment for all spin pairs.

Some of the pairs will not be in their minimum energy configuration, that is, the coupling will be 'frustrated'. For the same structure there could be many plausible spin configurations that are local minima of the energy [92, 93, 94]. The AFM/FM interactions in Fig. 2.9(b)–(c) are frustrated in the AFM layer at the position of the steps at the interface. In Fig. 2.9(d) the frustration of the AFM/FM interaction is released in the FM layer. The relative sizes of several length scales such as the thickness of the FM and AFM layers and the vertical and lateral extent of the interfacial defects as well as the relative strength of the exchange energies are the decisive parameters on which the energy minimization depends and which determine where the frustration should occur. Typically the bulk Néel temperature of an AFM is much lower than the FM Curie temperature. This roughly suggests that the exchange interaction in the FM is stronger than in the AFM. Thus, generally it will cost less energy for the interface frustration region to be in the AFM (Fig. 2.9(b)) than in the FM (Fig. 2.9(d)) which will allow the AFM moments to twist as reported for the Fe/Cr system in Ref. [95]. The frustration will here be relieved by making domain-walls perpendicular to the interface. In this case, regions of thickness in the AFM film that differ by one atomic layer favour coupling in opposite directions, and the twist leads to a non-collinear coupling of subsequent FM layers as described by Slonczewski's *torsion* or *proximity* model [96]. This model will be discussed shortly.

As an alternative to occur in domain-walls perpendicular to the interface, the frustration could be taken up in domain-walls parallel to the interface, as shown in Fig. 2.9(c). The domain-walls parallel to the interface in the AFM like in Fig. 2.9(c) essentially decouple AFM moments from the FM moments [97, 98]. These walls connect the FM steps as illustrated schematically by the thick lines in Fig. 2.10. The resulting coupling between FM layers in an FM/AFM/FM trilayer in that case would be small

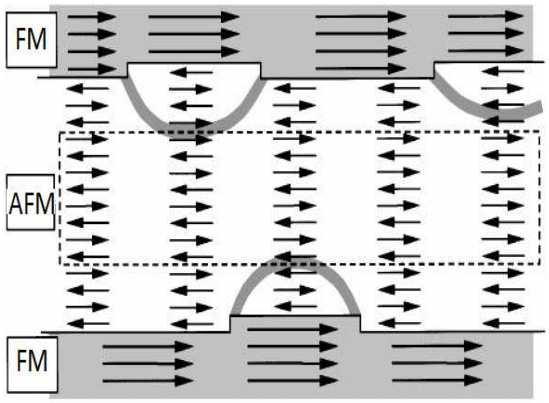

Figure 2.10: A representation of the possible relief of spin frustration in antiferromagnetic AFM (Cr) spacers in superlattices. The heavy lines schematically indicate domain-walls terminated at interfacial steps. The spin frustration is relieved by these walls near the interface leaving a region, shown by the dashed lines, from Ref. [97]

as reported for the Fe/Cr(001) system [94, 99]. Whether domain-walls parallel or perpendicular to the interfaces are favoured depends on different properties of the samples including the temperature and the average step spacing.

From conventional to Slonczewski torsion model

In the conventional model a paramagnetic spacer layer is assumed. To explain certain experimental observations, the total energy per unit area can be phenomenologically expressed as [100, 101]:

$$E_c = -J_1(\hat{m}_1.\hat{m}_2) - J_2(\hat{m}_1.\hat{m}_2)^2 = -J_1 cos(\theta) - J_2 cos^2(\theta) \tag{2.16}$$

The first term in this equation is the Heisenberg-like exchange term and is called bilinear term. The coupling depends on the dot product of the magnetization unit vectors $(\hat{m}_1.\hat{m}_2)$, i.e. it is bilinear in magnetization direction. Depending on the sign of J_1, the magnetization direction of the two FM layers, given by unit vectors $\hat{m}_1$ and $\hat{m}_2$, will be parallel or antiparallel. The second term is called biquadratic coupling term since it is biquadratic in $\hat{m}_1$ and $\hat{m}_2$. It describes canted or non-collinear coupling. Minimization of energy E_c with respect to angle θ in Eq. 2.16 gives the angle of the canted coupling: $cos(\theta) = -J_1/2J_2$.

As an alternative to the conventional model, when the average bilinear coupling J_1 becomes very small due to the thickness fluctuation of the spacer layer, the minimum energy state of the trilayer system could have the situation where the FM layer's magnetizations turn canted or even perpendicular to each other. This is the basis of the *Slonczewski* or *torsion* model [96]. A strong FM/AFM interaction is assumed here. For an odd or even number of AFM layers, the minimum energy state has the FM layers coupled with magnetization directions parallel or antiparallel, respectively. When there are thickness fluctuations which gives both odd and even monolayers of AFM thicknesses, the energy is minimized by the AFM moments in the region with an odd number of layers winding like a torsion spring with one sense, and regions with an even number of layers with the opposite sense, to reach the same average direction of

the top FM layer [96]. The coupling energy per unit area is then given by:

$$E_c = J_{odd}(\theta)^2 + J_{even}(|\theta| - \pi)^2 \tag{2.17}$$

where$-\pi < \theta < \pi$ and J_{odd} and J_{even} are the coupling functions associated with areas where the number (n) of AFM layers is odd and even, respectively [96, 102, 103]. For n odd, Eq. 2.17 is minimized for $\theta = 0$ and the FM layers are ferromagnetically coupled. For equal regions of odd and even layers, $\theta = \pi/2$. The general case of AFM thickness fluctuations in this model leads to non-collinear coupling. Another consequence of this model is that for any small thickness fluctuations there are both odd and even thicknesses present. In this case, the magnetization angle is neither 0 nor π for all applied fields, giving tilted hysteresis curves (with a gradual approach to saturation).

Summarizing both models, one can say that in the conventional model, it is assumed that for ideal interfaces, the energy as a function of the angle of the moments varies as $-J_1 cos(\theta)$, with the sign of J_1 depending on whether parallel or antiparallel alignment is preferred. In the torsion model, more thickness fluctuations are taken into account due to interface roughness, and the coupling energy is assumed to vary as $J(\theta)^2$ or $(|\theta| - \pi)^2$ depending on whether parallel or antiparallel alignment is favoured, respectively. The correct model will have to make use of both models.

Chapter 3

Experimental Aspects

All the experiments were performed under ultra-high vacuum conditions, and a pressure of $\sim 10^{-10}$ mbar could be maintained during the preparation of the films. The chamber was equipped with Ar^+ ion sputtering, annealing, e-beam evaporators, medium energy electron diffraction (MEED), low energy electron diffraction (LEED), Auger electron spectroscopy (AES), and magneto-optical Kerr effect (MOKE) in polar and longitudinal geometries.

3.1 Auger electron spectroscopy (AES)

The sample was cleaned by Ar^+ ions with an energy of 1 keV, and the cleanliness of the sample was then checked by AES. An AES utilises the emission of electrons in the Auger process and is one of the most commonly employed surface analytical techniques for determining the composition of the surface layers of a sample. Auger electrons are emitted from atoms during relaxation of the core level holes. The energy of Auger electrons are determined by the electronic structure of the elements which is unique for each element so that the Auger electrons give the fingerprints of all the elements except H and He [104]. The AES system comprises of a cylindrical mirror analyser with an integral electron gun set to 3 keV energy during operation. A typical spectrum obtained from the clean $Cu_3Au(001)$ is shown in Fig. 3.1, where the three prominent peaks of the *LMM* Auger transitions at 776 eV, 848 eV, and 920 eV can be recognized for copper. For gold, the most prominent peak is at 69 eV. The presence of surface contaminants is below the detection limit of the Auger system ($\sim$ 2% of a ML).

3.2 Low energy electron diffraction (LEED)

After sputtering and AES, the sample was annealed at 800 K for $\sim$10 minutes to order the surface. The temperature was controlled through a computer program and was monitored by a K-type thermocouple attached to the sample holder. LEED is the principal technique for the determination of surface structures, and can be used qualitatively as well as quantitatively. In the qualitative use, the diffraction pattern is recorded and analysis of the spot positions yields information on the size, symmetry and rotational alignment of the thin film unit cell with respect to the substrate unit cell. Two factors make LEED very sensitive for the crystal surface study: the small

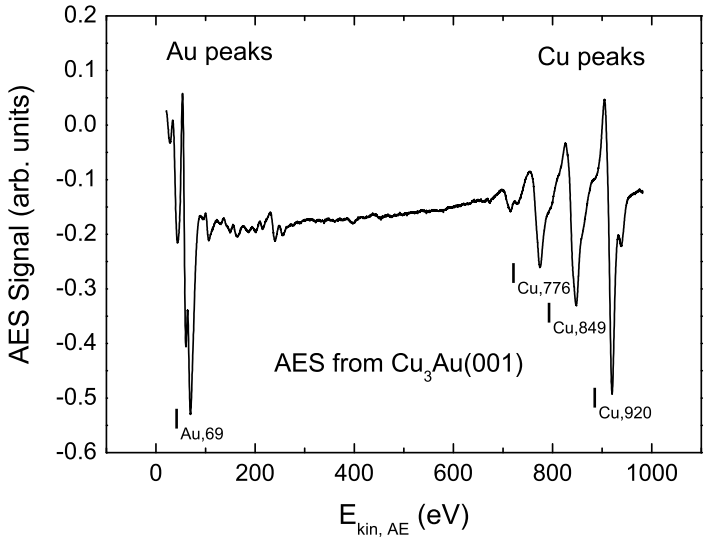

Figure 3.1: Auger spectrum from clean $Cu_3Au(001)$. The number in the subscript along with the element name represents the relevant AES peak energy in electron volts (eV).

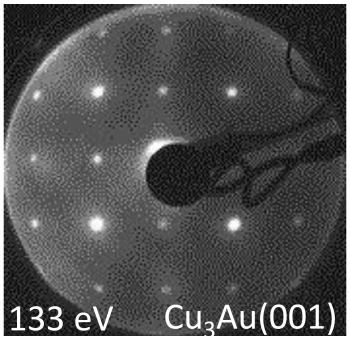

Figure 3.2: LEED pattern of the clean fcc $Cu_3Au(001)$ substrate for 133 eV electron energy. The c(2×2) superstructure indicates the chemical order of the alloy substrate.

mean free path of low energy electrons in solids (around 5 to 10 Å), and the electron's de Broglie wavelength (1.22 Å for 100 eV electron energy) which is comparable to the typical inter-atomic distances. The LEED experiment uses a beam of electrons of a well-defined low energy (typically in the range 20–200 eV) incident normally on the sample. The sample itself must be a single crystal with a well-ordered surface structure in order to generate a back-scattered electron diffraction pattern. Only the elastically-scattered electrons contribute to the diffraction pattern; the lower energy (secondary) electrons are removed by energy-filtering grids placed in front of the fluorescent screen that is employed to display the pattern. An example of the diffraction pattern of the $Cu_3Au(001)$ clean substrate for 76 eV electron energy is displayed in Fig. 3.2. The LEED images are recorded on a computer via a CCD camera attached opposite to the LEED screen.

LEED can also be used quantitatively: for example, the intensity of the (00) spot diffracted beam is recorded as a function of the incident electron beam energy to generate the so-called I(V) curves [105], which provide accurate information about the vertical lattice constant of the crystal under study. The kinematic theory is based on

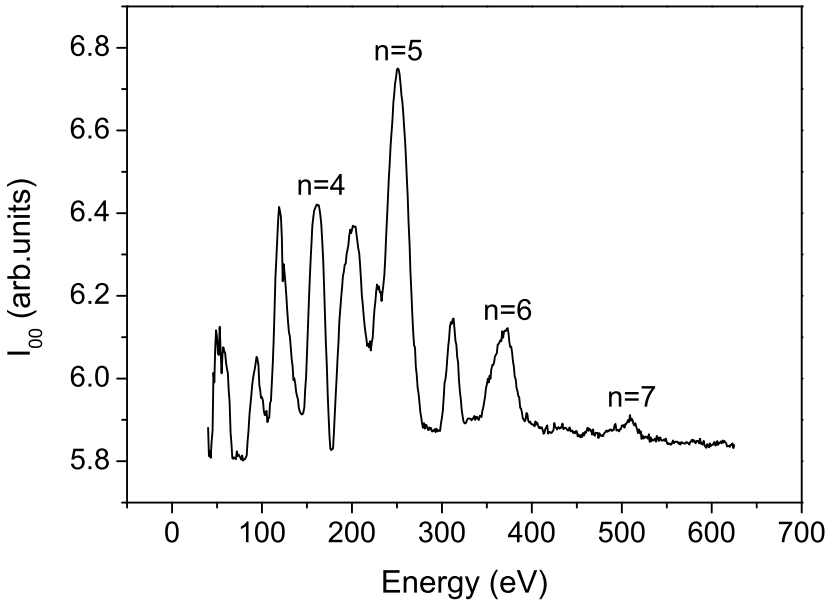

Figure 3.3: Room temperature LEED I(V) curve for the clean ordered $Cu_3Au(001)$ substrate.

the approximation that only single scattering of the incident electron occurs. Using this theory, the perpendicular (vertical) interlayer distance d_p can be expressed as

$$d_p = \frac{n\pi\hbar}{sin(\theta)\sqrt{2m_e(E_{kin}(n) + (-V_0))}} \tag{3.1}$$

where the integer n is the order of the corresponding interference peak, E_{kin}(n) the primary kinetic energy of the electrons of that peak, V_0 the additional energy shift due to the average inner potential in the crystal, m_e the electron mass, and θ the incident angle with respect to the sample surface. An example of the I(V) curve for the $Cu_3Au(001)$ clean surface is shown in Fig. 3.3. This I(V) curve was obtained with a special program (Ee2000) which measures the intensity of the (0,0)-spot for different acceleration voltages, i.e., different electron energies E_{kin}. During the measurement the program automatically increases the acceleration voltage for the specified range, in our case, from 40 to 650 eV in steps of 1 eV. The peaks in this curve occur at energies for which the Bragg condition for $\theta \sim 85^o$ is fulfilled. The corresponding order of the peak is noted on the respective peak (Fig. 3.3). The other peaks come from multiple scattering which is not taken into account by the kinematic approximation used here. Resolving Eq. 4.1 for the electron energy yields:

$$E_{kin} = \frac{n^2h^2}{8sin^2(\theta)m_ed_p^2} + V_0 \tag{3.2}$$

The slope $s = \frac{h^2}{8m_e sin^2(\theta)d_p^2}$ of this linear relation between the electron energy E_{kin} and the square of the diffraction order n^2 gives the vertical lattice constant d_p (Fig. 3.4). With the experimental value of $\theta \sim 85^o$, Eq. 4.1 provides the average interlayer distance for $Cu_3Au(001)$ to be $d_p = 1.88 \pm 0.01$ Å, in agreement with the bulk value of 1.87 Å [106, 107]. The point of intersection of the linear fit with the vertical axis, which corresponds to V_0 at (-12.3 ± 2.8) eV. This is in accordance with the expected value for V_0, from -5 to -15 eV, and therefore indicates that the choice for n is correct.

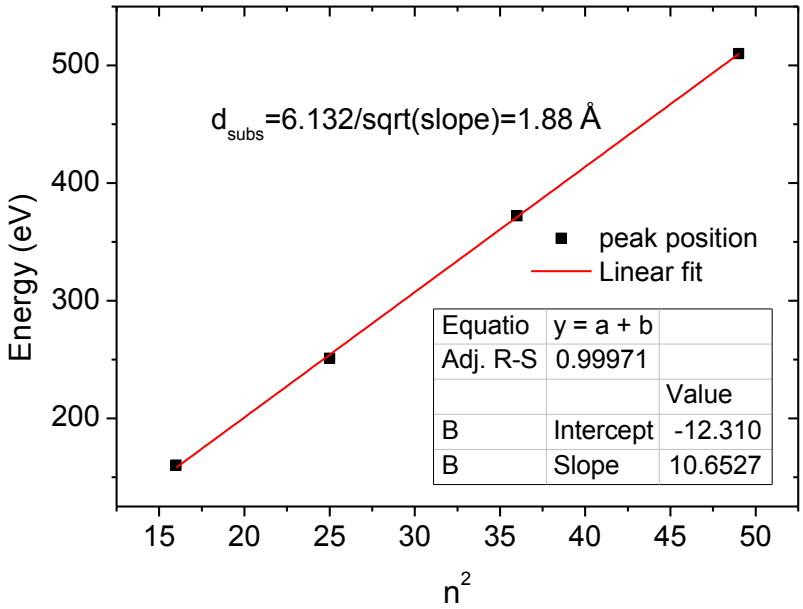

Figure 3.4: Electron beam energy dependence on n^2 for the LEED (00) spot of $Cu_3Au(001)$ substrate. The vertical interlayer distance $d_\perp$ is extracted from the slope of the linear fit.

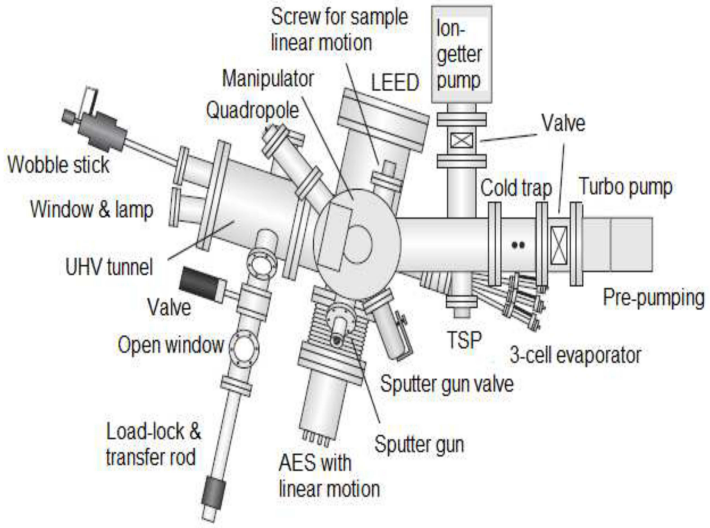

Figure 3.5: UHV MOKE chamber (top view), showing different parts of the system including AES and LEED. For the sample motion inside the chamber, one of the five movable dimensions (x, y, z, θ and ϕ) is possible to show, i.e. screw for sample linear motion (along y-axis). The lower part of the chamber containing MOKE set up can not be shown here.

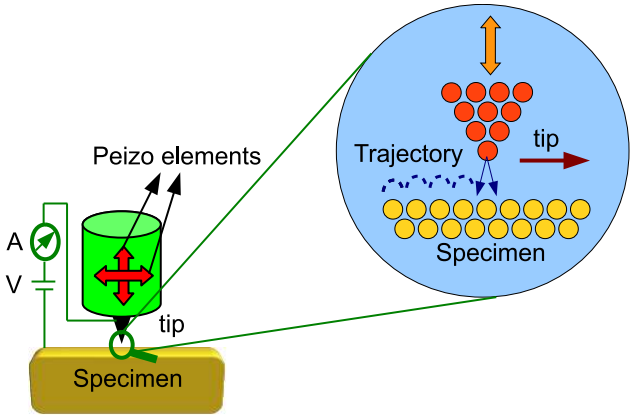

Figure 3.6: A schematic for an STM operation.

A top view of the UHV system with different parts of the chamber including AES and LEED, is shown in Fig. 3.5. The details of the side view of the lower part of the chamber will be described when discussing Fig. 3.14.

In three-dimensional space, primitive translation vectors $\vec{a}_1$, $\vec{a}_2$ and $\vec{a}_3$ make primitive lattice cell (minimum volume cell) such that any translational vector $\vec{T} = n_1\vec{a}_1 + n_2\vec{a}_2 + n_3\vec{a}_3$ leaves the system unchanged, where n_1, n_2, and n_3 are any integers. Performing a Fourier transformation, the corresponding vectors in reciprocal space gives:

$$\vec{a}_i^{\star} = 2\pi \frac{\vec{a}_j \times \vec{a}_k}{\vec{a}_i . \vec{a}_j \times \vec{a}_k}, \tag{3.3}$$

In analogy to the translation vector $\vec{T}$ in real space, in reciprocal space one defines the lattice vector $\vec{G} = n_1\vec{a}_1^{\star} + n_2^{\star}\vec{a}_2 + n_3^{\star}\vec{a}_3$. The importance of the reciprocal lattice becomes evident from the fact that the diffraction pattern of a crystal not only provides precise information about the lateral lattice constant but also the perpendicular lattice constant as outlined above. However, directly mapping the crystal structure in real space needs extremely powerful (sensitive) technique; for example, scanning tunnelling microscope (STM).

3.3 Scanning tunnelling microscope (STM)

An STM is an instrument that can image a conducting surface at the atomic level. It has been developed in 1981 by Gerd Binnig and Heinrich Rohrer. The principle of the STM is remarkably simple, it uses a sharp needle, referred to as 'tip', to interrogate the topography of the surface without touching it. This is done by the method indicated in Fig. 3.6.

A voltage is applied between the metallic tip and the specimen, typically between a few mV and a few V. The STM operates in the regime of extremely small distances between the tip and the surface of only 0.5 to 1.0 nm, i.e., 2 to 4 atomic diameters. At these distances, the electrons can *tunnel* from the tip to the surface or vice versa across the vacuum barrier, hence the name of this microscope—tunnelling microscope. STM usually operates at tunnelling currents between a few pA and a few nA. This current depends on the tip-surface distance d, on the bias voltage V, and on the energy

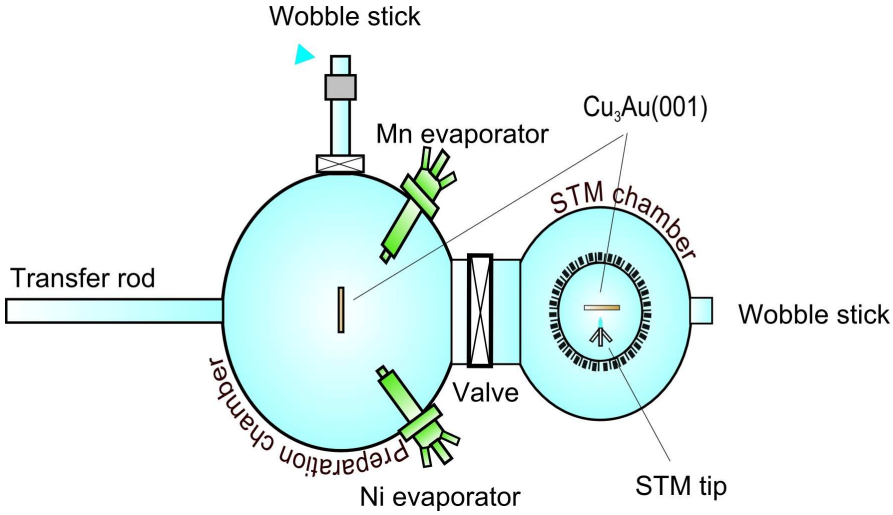

Figure 3.7: (a) A schematic of the STM chamber set up showing the preparation and scanning part. The sample can be transferred from one part to another with the help of two wobble sticks (one in preparation part and one in STM part), and a long transfer rod.

required to escape from the surface, the so called work function ϕ:

$$I(d) = const.(eV)e^{-2\sqrt{2m\phi}d/\hbar} \propto e^{-const.\sqrt{\phi}d} \tag{3.4}$$

The other quantities in the equation are constants, i.e., the electron charge e and mass m, and Planck's constant. For a typical value of the work function ϕ of 4 eV, the tunnelling current reduces by a factor 10 for every 0.1 nm increase in d. This means that over a typical atomic diameter of 0.3 nm, the tunnelling current changes by a factor 1000! This is what makes the STM so sensitive. The tunnelling current depends so strongly on the distance that it is dominated by the contribution between the last atom of the tip and the nearest atom in the specimen. Information is acquired by monitoring the current as the tip's position scans across the surface, and is usually displayed in image form. STM can be a challenging technique, as it requires extremely clean and stable surfaces, sharp tips, excellent vibration control, and sophisticated electronics.

A simple schematic of STM chamber (Omicron) is shown in Fig. 3.7. It consists of two parts: preparation chamber, and STM chamber, both separated by a valve. The sample can be prepared in preparation chamber by using two separate evaporators of Ni and Mn, where co-evaporation is possible. For scanning, the sample is then transferred to the STM chamber with the help of a wobble stick to a transfer rod, then from the transfer rod to scanning position (STM stage) by another wobble stick. To avoid/minimize noise, the STM stage is suspended by four springs and magnetically damped in vacuum during the scanning. Also, both of the turbo pumps are switched off for the same purpose. The valve between the two chambers is closed, and an ultra-high vacuum with pressure of lower than 5×10^{-10} mbar can be maintained with the help of ion-getter pumps in both of the chambers.

In this work, the tip was prepared from tungsten wire by an electrochemical etching method. Using this tip, a topographic image of the substrate ($Cu_3Au(001)$) is obtained, as shown in Fig. 3.8(a). Fig. 3.8(b) shows the upper right part of Fig. 3.8(a). The line scan profile in Fig. 3.8(b) indicates the presence of both monolayer and bilayer

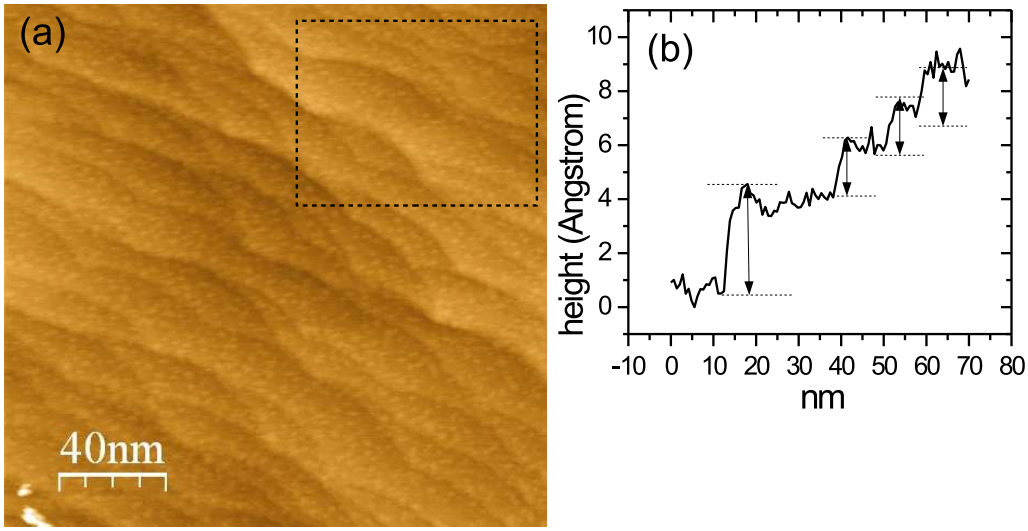

Figure 3.8: STM constant-current image for $Cu_3Au(001)$ substrate, and (b) line profile of the upper right side indicated by a dashed square rectangle.

steps. Two surface terraces separated by a bilayer step should have the same chemical configuration (either a pure Cu or a CuAu surface), and those separated by a monolayer step are expected to have different surfaces. It is to be noted that in the crystal structure of $Cu_3Au(001)$, the Au atoms sit at the corners whereas the Cu atoms occupy the faces of an fcc unit cell.

3.4 Film growth and medium energy electron diffraction (MEED)

The films were grown on the clean substrate by electron-beam-assisted thermal evaporation of high purity material (Co and Ni: 99.99%, Mn: 99.95%). The electron beam is focussed on the tip of a rod of 2 mm diameter which is set to positive high voltage and held in a water-cooled system. The Ni_xMn_{100-x} films were prepared by the simultaneous evaporation of Ni and Mn on $Cu_3Au(001)$. The alloy film composition x was varied by adjusting the individual deposition rates. The growth rate of the films was typically from 0.5 to 2 ML per minute, and was checked by counting the oscillations in the (00)-spot MEED intensity recorded during evaporation. In the MOKE chamber set-up (Fig. 3.5), the AES system is mounted face-to-face to the LEED screen. This allows diffraction experiments in a grazing incidence geometry with primary electron kinetic energy of 2 keV, using the electron gun of the AES system and the fluorescent screen of the LEED system. As examples, the MEED intensity for the growth of Ni and $Ni_{50}Mn_{50}$ on $Cu_3Au(001)$ are shown in Fig. 3.9 and the inset of Fig. 3.9, respectively, with growth rates of 58 sec/ML and 36 sec/ML. The (00)-spot intensity is plotted as a function of time. The shutter, in front of the evaporating source, is opened after one minute, which corresponds to a drop in the MEED intensity. The MEED intensity displays oscillations showing the layer-by-layer growth of the film under the assumption that the maximum in the intensity corresponds to a filled integer monolayer. The film evaporation rate and thus the film thickness can be extracted from the slope of the linear fit obtained from the time versus numbering of the maxima in the MEED

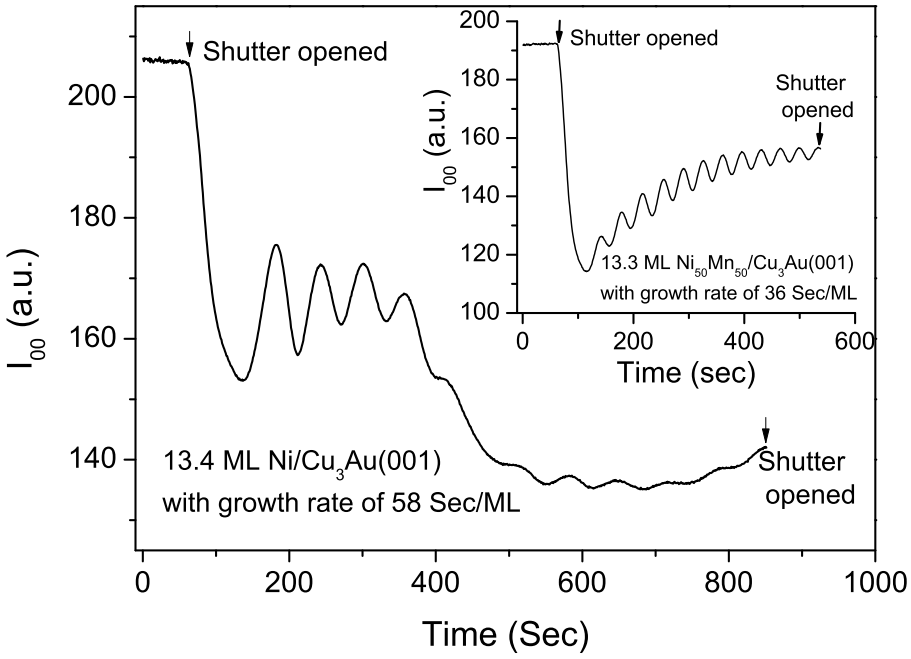

Figure 3.9: MEED curve of the (00)-spot recorded during the deposition of 13.4 ML Ni/Cu_3Au(001), and in the inset, 13.3 ML $Ni_{50}Mn_{50}$/Cu_3Au(001) at T=300 K.

intensity curve.

Preparing the samples for the magneto-optical Kerr effect (MOKE) measurements (discussed in the last section of this chapter), in most of the cases, another shutter was positioned as close as possible (∼3 mm) in front of the substrate, covering the lower half and ∼2 ML Co were evaporated on the upper half (see Fig. 1.2 of introduction). Previously, for a wedged Co sample, in the system Co/Ni/FeMn/Ni/Cu(001), it was shown by magnetic domain images that with a Co thickness of higher than 0.5 ML, the magnetization of 15 ML Ni changed from OoP to IP direction [44]. After removing the shutter, 12−13 ML Ni were evaporated on the entire sample which then has OoP magnetization at the lower half, and IP magnetization at the upper half of the sample due to the underlying ∼2 ML Co. At the lower half of the sample (without Co), the (00) MEED spot intensity versus time during the Ni evaporation was observed on the fluorescent screen as outlined above. The typical growth rate of Ni was 1 ML per minute. For Ni/Cu_3Au(001), we found IP magnetization for thicknesses between 4 to 8 ML, OoP magnetization from 8 to 17 ML, and then again IP for higher thicknesses. All films were deposited at room temperature.

3.5 Ni_xMn_{100-x}/(Ni/)Cu_3Au(001) composition and thickness

AES was used to obtain the Ni (Mn) composition in the Ni_xMn_{100-x} alloy films whether grown on Cu_3Au(001) or on Ni/Cu_3Au(001). In the latter case, immediately after Ni evaporation, Mn and Ni are co-evaporated to obtain Ni_xMn_{1-x} films. Ni_xMn_{1-x} does not grow layer-by-layer on Ni/Cu_3Au(001), so its thickness cannot be directly inferred from MEED. Instead, AES was first utilized to determine the concentration of Ni_xMn_{100-x}. The thickness of Ni_xMn_{100-x} can then be determined since the evaporation

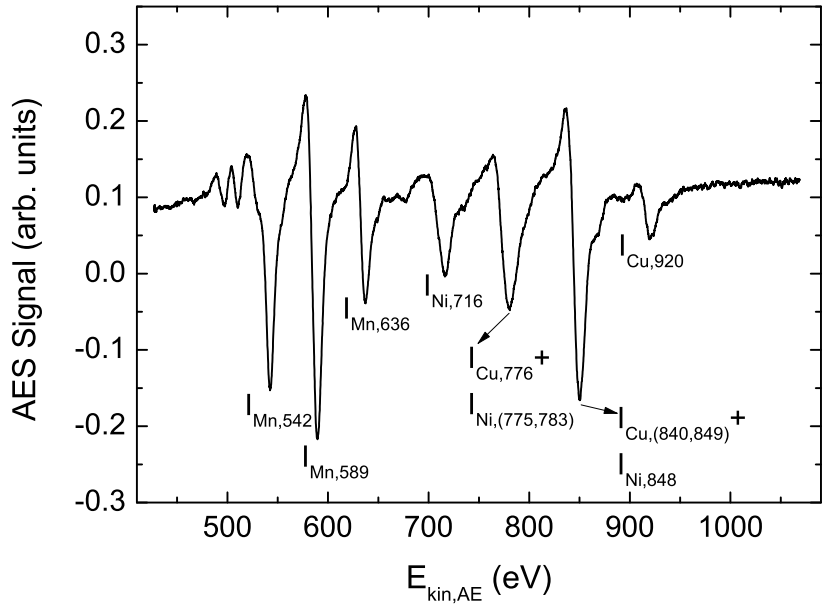

Figure 3.10: Auger spectrum from 9.4 ML $Ni_{53}Mn_{47}$ film grown on Cu_3Au(001) at T=300 K. The number in the subscript along with the element name represents the relevant AES peak energy in electron volts (eV).

rate of Ni was fixed to be the same for Ni and Ni_xMn_{100-x} preparation. In the general case of a film (F) grown on a substrate (S), the Auger intensities of the substrate and the film of thickness d_F can be written, respectively, as:

$$I_S = I_0 S_S \exp^{-d_F/\lambda_S} \tag{3.5}$$

$$I_F = I_0 S_F (1 - \exp^{-d_F/\lambda_F}) \tag{3.6}$$

It is approximated that the attenuation of the Auger electrons within a material is determined by the mean distance the electrons can travel before an inelastic scattering event occurs. The quantities S_i ($i = S, F$) are the sensitivities of the Auger transition, λ_i are effective attenuation lengths of the Auger electron in the materials, and I_0 represents the intensity of the primary beam. From an Auger spectrum, I_S and I_F can be measured, and the thickness of the film can be determined once the parameters S_i and λ_i are known.

The situation is not that easy in the case of a binary alloy film, since now both the constituents of the alloy reduce the Auger signal from the substrate. Fig. 3.10 shows an Auger spectrum of a 9.4 ML $Ni_{53}Mn_{47}$ film grown on Cu_3Au(001). The thickness is determined by MEED. All the Mn Auger peaks are clearly separated from Ni and Cu peaks; the last two peaks of Ni and the first two of Cu are overlapped. Therefore, for the sake of clarity, we used the following Auger electron intensities: $I_{Mn,589}$, $I_{Ni,716}$, and $I_{Cu,920}$, where the number in the subscript along with the element name defines the corresponding peak energy in eV. The ratio between the Auger intensities for Cu and Ni (Mn) as a function of the thickness and the concentration of the alloy film can be experimentally obtained ($R_{Mn} = I_{Cu}/I_{Mn}$, $R_{Ni} = I_{Cu}/I_{Ni}$). For Ni_xMn_{100-x}/Cu_3Au(001), the ratio between equation 3.5 and 3.6 can be written for Ni

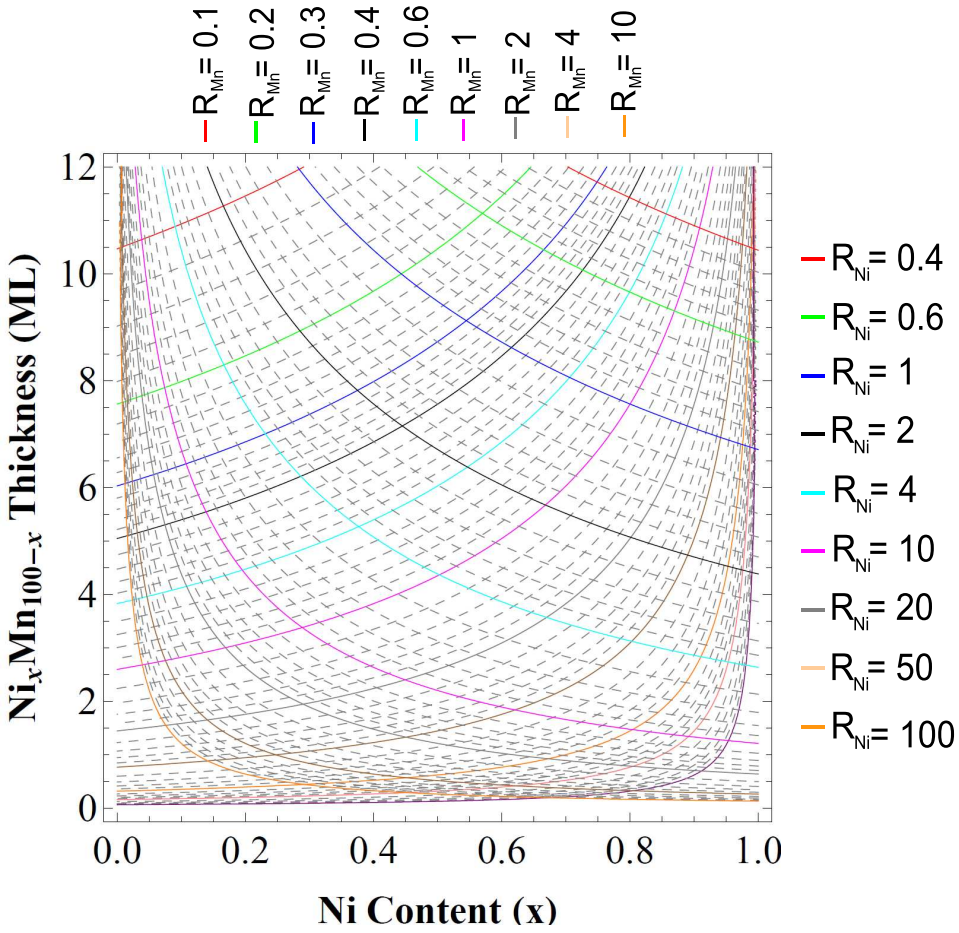

Figure 3.11: The use of Eq. 3.7 (falling lines), and Eq. 3.8 (rising lines) for different values of R_{Ni} and R_{Mn}.

and for Mn respectively, as:

$$R_{Ni} = \frac{S_{Cu}.\exp^{-d/\lambda_{Cu}}}{S_{Ni}.x.(1-\exp^{-d/\lambda_{Ni}})} \tag{3.7}$$

$$R_{Mn} = \frac{S_{Cu}.\exp^{-d/\lambda_{Cu}}}{S_{Mn}.(1-x).(1-\exp^{-d/\lambda_{Mn}})} \tag{3.8}$$

where d is the total film thickness in ML, x the Ni concentration, and (1-x) is the Mn concentration. The x and (1-x) can be statistically interpreted as the fraction of the substrate covered by Ni and Mn, respectively. The values of S_i and λ_i (i=Ni, Mn, and Cu) are known from the work of Ref. [108]. Therefore, using equations 3.7 and 3.8, the values of d and x can be determined. In a plot of d versus x, the solution of these two equations form lines that are monotonically falling (3.7) or rising (3.8), as shown in Fig. 3.10. The cross of these two lines for R_{Ni} and R_{Mn} yields d and x. For NiMn films of thickness smaller than 15 ML and grown on Ni/Cu_3Au(001), the signal contains some contribution from Ni below. To take into account this contribution for the exact calculation of Ni concentration and Ni_xMn_{100-x} thickness, we used the following formula:

$$R = \frac{I_{Mn}}{I_{Ni}} = \frac{S_{Mn}}{S_{Ni}} \frac{(1-\exp^{-d/\lambda_{Mn}}(1-x))}{(1-\exp^{-}d/\lambda_{Ni})x + (1-\exp^{-}d_{Ni}/\lambda_{Ni})\exp^{-}d/\lambda_{Ni}} \tag{3.9}$$

The last term of second part in the denominator of the right hand side is added to the otherwise standard equation which shows the contribution from the underneath Ni film which is attenuated by NiMn above it. If NiMn is grown on the pure substrate then equation 3.9 is without the last term of the denominator and the term $\frac{1-exp^{-d/\lambda_{Ni}}}{1-exp^{-d/\lambda_{Mn}}}$ can be neglected being equal to unity and one is left with the simple relation $R = \frac{I_{Mn}}{I_{Ni}} = \frac{S_{Mn}(1-x)}{S_{Ni}x}$.

3.6 Magneto-Optical Kerr Effect (MOKE)

As the name suggests, magneto-optical Kerr effect is an interaction between magnetic field and light. It can be defined simply as 'when a beam of linearly polarised light reflects off a magnetised surface, the plane of polarisation of the light slightly rotates'. MOKE was discovered by Rev. John Kerr in 1877 [109, 110] while examining the polarization of light reflected from a polished electromagnet pole. The effect is similar to the Faraday effect (1845) [111], where for the first time a relationship between magnetic field and light was provided, however, there the same slight rotation occurs with the linearly polarized light after it is transmitted through a magnetic material. In 1898, Kerr was presented with the Royal Medal and the presenter said, it was a wonder that Kerr learned so much with the "comparatively simple and ineffectual apparatus at his disposal". Kerr responded, "simple it may be, but not ineffectual; rude, but not crude"[112, 113]. This statement represents the simple nature of the technique. Along with its scientific importance and high sensitivity to the magnetisation within the skin depth region, typically 10-20 nm in most metals [114], simplicity is another main reason that this technique has been widely used in the field of surface science since 1985. The Kerr rotation is proportional to the magnetisation in a specific material and therefore magnetic hysteresis loops can be observed for thin films by monitoring the rotation as a function of applied field.

Light is a transverse electromagnetic wave which can be manipulated optically into different polarization states, i.e., a plane, a circularly or an elliptically polarised state. Generally, the plane which contains the electric field **E** and the direction of propagation of the light wave is called the plane of polarization. If the electric field is polarised perpendicular to the plane of incidence on a sample, then it is referred to as *s*-polarised light as shown in Fig. 3.12. Conversely, if the electric field is polarised in the plane of incidence, it is referred to as *p*-polarised light (Fig. 3.12). The plane of incidence is also known as the scattering plane—the plane which contains the incident and reflected light beam. Circularly polarised light can be further referred to as L-circularly polarised and R-circularly polarised light, where L and R signify the electric field rotating in either a clockwise (left) or an anticlockwise (right) direction with respect to the direction of propagation.

Origin and formalism of the magneto-optic effect

The physical origin of the magneto-optic effect can be understood by looking into the classical picture of photon-electron interaction within the atom/material. When an oscillating incident electric field vector **E** hits a magnetized sample, electrons in the sample start to vibrate by a force exerted by the electric field vector **E** according to $\mathbf{F}_E$=q$\mathbf{E}_E$. Due to the magnetization of the sample, there will be an additional Lorentz

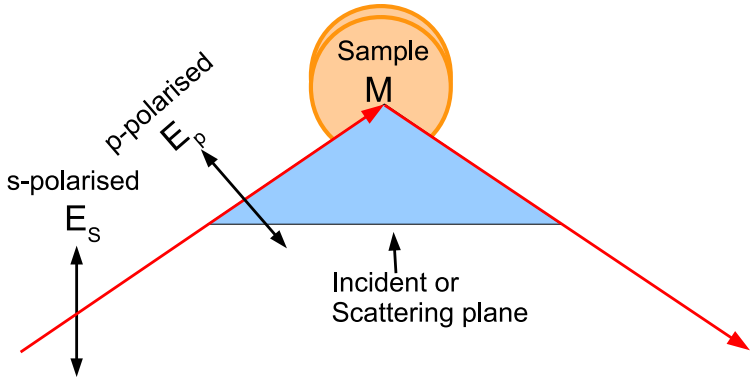

Figure 3.12: Illustration of s-polarised and p-polarised light.

force acting on each electron as well:

$$\mathbf{F} = \mathbf{F}_E + \mathbf{F}_B = q\mathbf{E} + (q\mathbf{V} \times \mathbf{B}) = q(\mathbf{E} + (\mathbf{V} \times \mathbf{B})) = q(\mathbf{E}_E + \mathbf{E}_B) \tag{3.10}$$

The electric field vector $\mathbf{E}_B$ is very small in magnitude, and is perpendicular to both incident electric field vector $\mathbf{E}_E$ (or velocity of electron $\mathbf{V}$) and the magnetic field $\mathbf{B}$. It ($\mathbf{E}_B$) is also called Kerr vector ($\mathbf{E}_K$) and is proportional to the magnetization of the material under study. After reflection, the reduced reflected electric field vector $\mathbf{E}'$ (as some light is transmitted to the sample) and $\mathbf{E}_K$ are combined together, resulting in the Kerr rotation θ_K and Kerr ellipticity ϵ_K with respect to the original electric field vector $\mathbf{E}$. The reflection coefficient, which is material dependent, plays an important role in the MOKE technique. In the absence of magnetization, the reflection coefficient of the material is simply the ratio of the reflected ($|\mathbf{E}^r|$) to the incident electric field amplitude ($|\mathbf{E}^i|$): r=$|\mathbf{E}^r|/|\mathbf{E}^i|$. For s- and p-polarised light, the corresponding electric field coefficients are: r_{ss}=$|\mathbf{E}_s{}^r|/|\mathbf{E}_s{}^i|$; and r_{pp}=$|\mathbf{E}_p{}^r|/|\mathbf{E}_p{}^i|$. The matrix representation will be:

$$\begin{pmatrix} \mathbf{E}_s^r \\ \mathbf{E}_p^r \end{pmatrix} = \begin{pmatrix} r_{ss} & 0 \\ 0 & r_{pp} \end{pmatrix} \begin{pmatrix} \mathbf{E}_s^i \\ \mathbf{E}_p^i \end{pmatrix} = \begin{pmatrix} r_{ss}\mathbf{E}_s^i \\ r_{pp}\mathbf{E}_p^i \end{pmatrix}$$

where the $\mathbf{E}_i$ (i=s and p) represent the s-, or p-polarised electric field vectors of the incident light. When $s(p)$-polarized incident light hits the magnetized sample, a small $p(s)$-polarized light is generated as an additional electric field vector ($\mathbf{E}_K$ vector) after reflection from the magnetized sample (Fig. 3.13).

Therefore, the new two reflection coefficients can be expressed as: r_{sp}=$\mathbf{E}_s{}^r/\mathbf{E}_p{}^i$, and r_{ps}=$\mathbf{E}_p{}^r/\mathbf{E}_s{}^i$. And the resulting new matrix is:

$$\begin{pmatrix} \mathbf{E}_s^r \\ \mathbf{E}_p^r \end{pmatrix} = \begin{pmatrix} r_{ss} & r_{sp} \\ r_{ps} & r_{pp} \end{pmatrix} \begin{pmatrix} \mathbf{E}_s^i \\ \mathbf{E}_p^i \end{pmatrix} = \begin{pmatrix} r_{ss}\mathbf{E}_s^i + r_{sp}\mathbf{E}_p^i \\ r_{ps}\mathbf{E}_s^i + r_{pp}\mathbf{E}_p^i \end{pmatrix}$$

Either of the ratios r_{ps} to r_{ss} and r_{sp} to r_{pp} contains the Kerr rotation (θ_K) and Kerr ellipticity (ϵ_K), and can be expressed as:

$$\phi_s = \frac{r_{ps}}{r_{ss}} \approx \theta_K + i\epsilon_K \tag{3.11}$$

and

$$\phi_p = \frac{r_{sp}}{r_{pp}} \approx \theta_K + i\epsilon_K \tag{3.12}$$

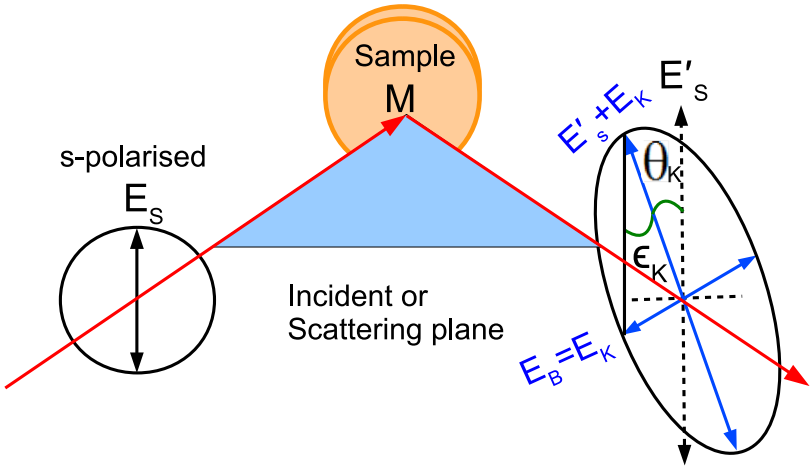

Figure 3.13: Schematic of MOKE principle. Without magnetization, $\mathbf{E}_s$ and $\mathbf{E}'_s$ are the electric field vectors of the incident and specularly reflected light beams, respectively. For magnetized sample, $\mathbf{E}_B$ ($\mathbf{E}_K$) is the electric field (Kerr) vector of the reflected light beam as described in the text. The θ_K (typically a fraction of a degree) and ϵ_K are the Kerr rotation and Kerr ellipticity, respectively. Note that the value of θ_K and ϵ_K is exaggerated in the sketch. In reality the Kerr ellipticity, the $\tan(\theta)$ (the ratio of shorter to larger axis of the ellipse) is close to zero.

MOKE can be described in the context of either macroscopic dielectric theory or microscopic quantum theory [113]. Macroscopically, magneto-optic effects arise from the antisymmetric, off-diagonal elements in the dielectric tensor. Microscopically, through the spin–orbit interaction coupling occurs between the electric field of the light and the electron spin within a magnetic medium. We restrict ourselves to the macroscopic description and formalism of the magneto-optic effect. The off-diagonal components of the dielectric tensor give the magneto-optic material an anisotropic permittivity which affects the speed of light $V_c = 1/\sqrt{\epsilon\mu}$ in a material, where ϵ is dielectric constant and μ is the material permeability. Linearly polarized light can be considered as a superposition of two (left and right) circularly polarized light. Two processes take place for light propagating in a magnetized medium. First, the two circularly polarized modes gain different phase shifts due to their different propagating velocities, resulting in a rotation of the polarization plane. Second, the different absorption rates of the medium for the two circularly polarized modes affects the ellipticity [113]. The macroscopic description of Kerr effects relies on the two modes having different refractive indices within the material. Therefore the two circular modes travel with different velocities and attenuate differently in the material. Upon reflection from the material, the two modes recombine to produce the Kerr rotation and ellipticity. Generally, the antisymmetric part of the dielectric tensor which represents the effects of a magnetic medium is given by [113, 115, 116]:

$$\epsilon = \epsilon_0 \begin{pmatrix} 1 & -iQ_z & iQ_y \\ iQ_z & 1 & -iQ_x \\ -iQ_y & iQ_x & 1 \end{pmatrix}.$$

where $\mathbf{Q}_{x,y,z}$ is the Voigt magneto optic constant which describes the magneto optical effect, and to the first order, proportional to the magnetisation of the material. The

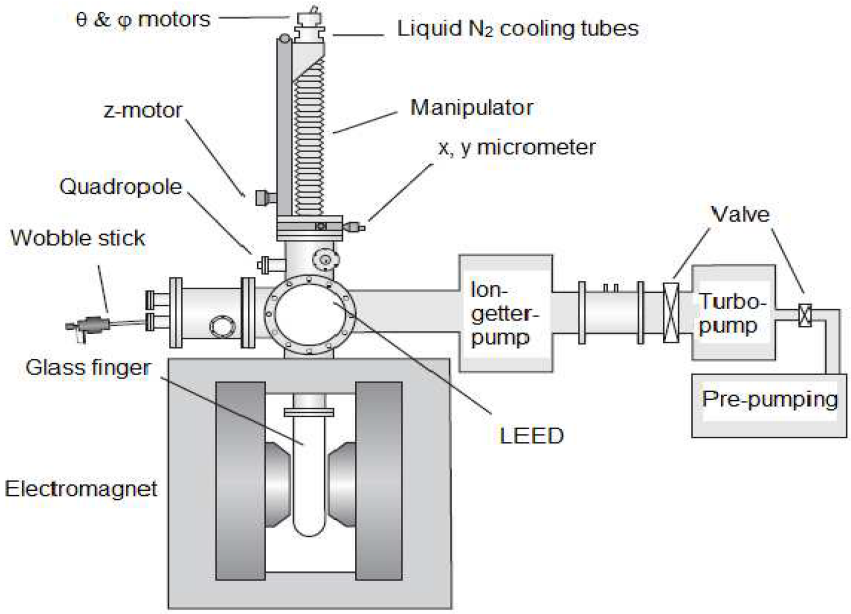

Figure 3.14: A side view of UHV compatible MOKE chamber.

two normal modes are left circularly polarized with $\epsilon_L = \epsilon(1 - \mathbf{Q}.\hat{k})$, right circularly polarized with $\epsilon_R = \epsilon(1 + \mathbf{Q}.\hat{k})$, and $\hat{k}$ is the unit vector along the light propagation direction. Hence, the Kerr effect originates from the off-diagonal antisymmetric elements of the dielectric tensor.

3.6.1 MOKE measurements and the UHV compatible MOKE set up

The UHV chamber is designed to prepare, analyze and measure the samples in *situ* using magneto-optical Kerr effect. This is necessary in order to minimize contamination or oxidation of the surface so that multiple layers can be deposited without influencing their physical properties by any foreign atoms. The experiments were performed in the UHV compatible MOKE set up as shown in Fig. 3.14. The sample mounted on a sample holder can adopt different positions being attached to the bottom part of the manipulator which has five degrees of movement (x, y, z, θ, and ϕ). The manipulator allows the movement of the sample $\pm$ 12.5 mm in the x- and y-direction, a vertical movement up to 480 mm, the polar rotation by 360^0, and the azimuth by about 110^0. The movement in the x and y direction can be manually performed via micrometer screws. The z, polar, and azimuth movements are possible manually as well as via programmable stepper motor controller. In addition to controlling the position of the sample, manipulator allows cooling, with a liquid nitrogen down to about 140 K, and heating of the sample with a resistance heater to about 1000 K. The sample temperature can be measured using K-type thermocouple attached to the sample holder. The samples are prepared in the upper part of the chamber. For measurement, the sample is moved downward in the glass finger between the magnetic-poles where the MOKE laser assembly is mounted aside outside the chamber. To generate the ultra high vacuum, the chamber consists of a multi-level pumping stages: the big turbo pump has a back-up of pre-vacuum created with another pumping unit of small turbo. Together

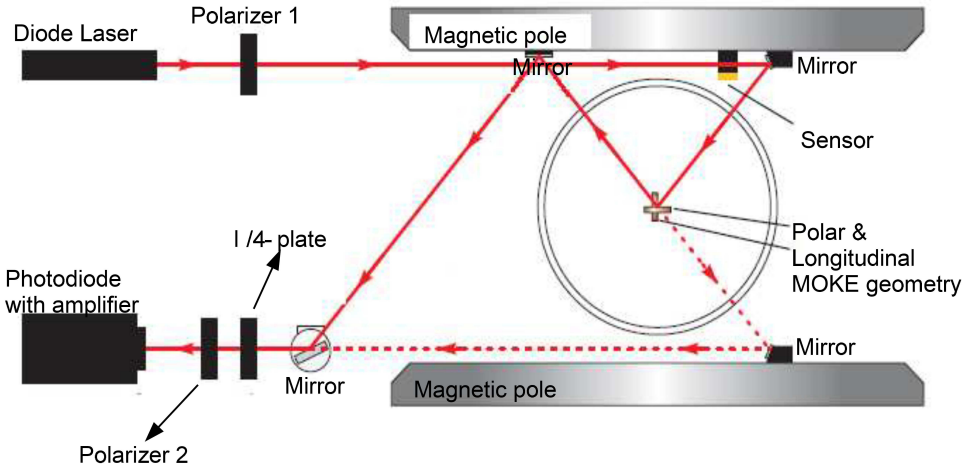

Figure 3.15: Schematic of the in *situ* MOKE set up capable of measuring hysteresis loops of magnetized samples in in-plane as well as in out-of-plane geometry. To make possible longitudinal and polar measurements, sample can be rotated by 90◦ and polarized laser light can be directed towards (analyser after reflection from) the sample.

with an ion-getter pump and a titanium sublimation pump inside the chamber, it is always possible to generate a base pressure of lower than 5×10^{-10} mbar. For a more detailed analysis of the residual gas and leak detection in the chamber, a quadrupole mass spectrometer is also ensembled.

Fig. 3.15 shows the experimental set up that involves laser light passing through a polarising filter and then reflecting the light off the sample. The glass-finger is set between the magnetic poles and its dimensions are such that the sample can be easily rotated by 90° so as to make possible both in-plane (IP) as well as out-of-plane (OoP) measurements. The laser beam can be directed onto the sample via a mirror which is attached to one of the magnetic pole. After reflecting from the sample, the elliptically polarized (slightly rotated) laser beam is again reflected once for longitudinal and twice for polar MOKE measurements. The combination of quarter-wave-plate and Glan-Thompson prism once again ensures the linear polarization of the reflected elliptically polarised laser beam which is finally collected by the photo-diode that is installed with an amplifier. Slight changes in the plane of polarisation cause variations in the detected light intensity which is proportional to the magnetization of the sample. MOKE measures the hysteresis loops of thin magnetic films (up to the laser penetration depth within metals at about ∼20 nm), by studying the slight changes in the laser light intensity at the photo-diode in terms of rotation or ellipticity (in our case rotation) as a function of applied magnetic field.

MOKE can be categorized by the direction of the magnetization vector with respect to the plane of incidence and the reflecting surface, i.e., (i) longitudinal MOKE, (ii) polar MOKE, and (iii) transverse MOKE. In the longitudinal MOKE, the magnetisation is in the plane of the sample and parallel to the incident plane. In the polar MOKE, the magnetisation is perpendicular to the sample plane and is parallel to the plane of incidence. These two are of our concern and are schematically shown in Fig. 3.16. When the magnetization is perpendicular to the plane of incidence and parallel to the surface it is said to be in the transverse configuration, which we did not use.

To address the magnetic properties of Ni_xMn_{1-x}/Ni/(Co/)Cu_3Au(001) bilayers and

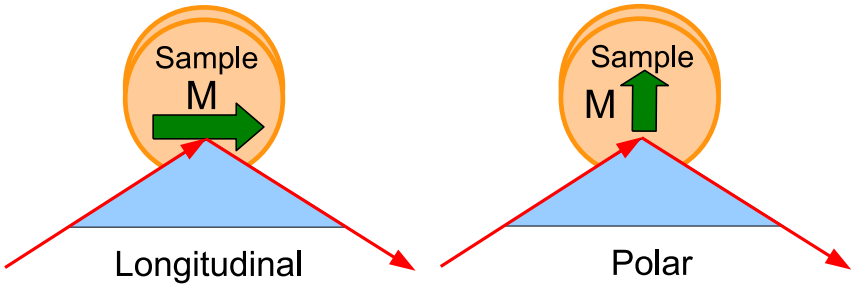

Figure 3.16: Longitudinal and polar MOKE geometries.

(Co/)Ni/Ni_xMn_{1-x}/Ni/(Co/)Cu_3Au(001 trilayers), we made use of longitudinal and polar MOKE geometries to study the IP and the OoP magnetization at the upper and the lower half of the sample, respectively. The schematic for the samples is shown in Fig. 1.2 of introduction. Linearly polarized laser light from a laser diode of 1 mW power and 635 nm wavelength was used. A field-cooling process was applied with the maximum available external magnetic field of ±200 mT.

Chapter 4

Growth and structure of epitaxial Ni_xMn_{100-x} single layers and magnetic properties of Ni_xMn_{100-x}/Ni(/Co) bilayers on $Cu_3Au(001)$

Using the techniques introduced in the previous chapter, the experimental results for growth, structure of epitaxial Ni_xMn_{100-x} and Ni single layers, and magnetic properties of Ni single layers and Ni_xMn_{100-x}/Ni(/Co) bilayers on $Cu_3Au(001)$ are presented here. In section 4.1.1 the growth of $Ni_xMn_{100-x}/Cu_3Au(001)$ alloy films and epitaxial growth of Ni films is characterized by recording the MEED intensity during film deposition. A layer-by-layer growth mode, monitored by oscillations in the MEED intensity, is observed for a broad range of alloy film composition. $Ni_xMn_{100-x}/Ni/Cu_3Au(001)$ does not show any MEED oscillations indicating a three-dimensional growth. On the other side, Ni always grows in a layer-by-layer growth mode on $Cu_3Au(001)$, $Ni_xMn_{100-x}/Cu_3Au(001)$, $Ni_xMn_{100-x}/Ni/Cu_3Au(001)$, $Mn/Cu_3Au(001)$, and $Co/Cu_3Au(001)$. The structure of $Ni_xMn_{100-x}/Cu_3Au(001)$ is studied by using, LEED, Reflection High-Energy Electron Diffraction (RHEED) for the lateral lattice constant, and LEED-I(V) for the vertical lattice constant. In section 4.2, thickness-dependent spin reorientation transition (SRT) of $Ni/Cu_3Au(001)$ is checked to be able to study the exchange coupling of $Ni_xMn_{100-x}/Ni/Cu_3Au(001)$ bilayers in in-plane and in out-of-plane direction. Antiferromagnetism in $Ni_{50}Mn_{50}/Ni/(Co/)Cu_3Au(001)$ bilayers is probed by the use of longitudinal and polar MOKE, and is discussed in section 4.3. Section 4.4 describes and discusses concentration-, and thickness-dependent magnetic properties of Ni_xMn_{100-x} in in-plane and out-of-plane magnetized epitaxially grown $Ni_xMn_{100-x}/Ni/(Co/)Cu_3Au(001)$.

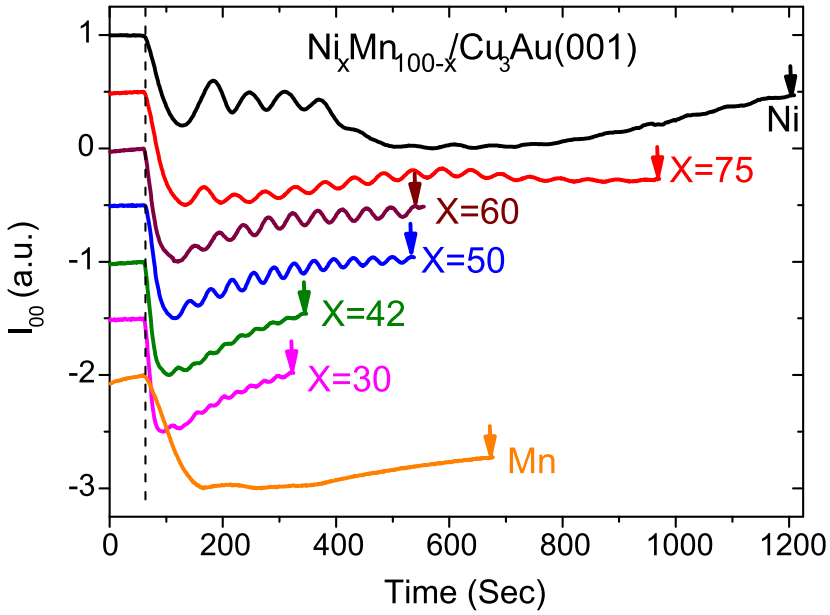

Figure 4.1: MEED (00)-spot oscillations recorded during the deposition of Ni_xMn_{100-x} films on $Cu_3Au(001)$ at T=300 K. The closing of the shutters is indicated by an arrow at each curve. The dashed vertical line at the time axis at 60 seconds represents the opening of the shutter. An oscillating MEED intensity is a fingerprint of a layer-by-layer growth mode.

4.1 Growth and structure of $Ni_xMn_{100-x}/Cu_3Au(001)$ and Ni films

4.1.1 Growth of Ni_xMn_{100-x} alloy films on $Cu_3Au(001)$

It is shown in the previous chapter that the presence of oscillations in the MEED intensity during the growth of Ni_xMn_{100-x} on $Cu_3Au(001)$ allows determining the thickness of the deposited film. During the simultaneous evaporation of Ni and Mn on $Cu_3Au(001)$, oscillations in the MEED intensity are observable. This is shown in Fig. 4.1 for a wide range of Ni concentrations (x) between 30 and 75%. The MEED intensity is displayed as a function of time during deposition of Ni_xMn_{100-x}. Each curve corresponds to a film with a different concentration as indicated. The arrows indicate the closing of the shutter in front of the evaporators. One can see that upon opening of the shutter represented by a vertical dashed line (at time 60 seconds) the MEED intensity drops down. This is a common feature of all the MEED intensity curves presented in this figure and is attributed to the initial increase of density of surface steps. An oscillatory behaviour of the MEED curves is related to the periodic variation of the average number of surface steps or, in other words, it is due to the layer-by-layer growth mode of the Ni_xMn_{100-x} alloy films on $Cu_3Au(001)$. The oscillation intensity is decreased for decreasing Ni concentration such that for the growth of pure $Mn/Cu_3Au(001)$, no MEED oscillations can be observed. One can see also that Ni grows layer-by-layer on $Cu_3Au(001)$.

Our collaborators in Brazil have monitored the growth of $Ni_xMn_{100-x}/Cu_3Au(001)$ using RHEED by employing a primary electron beam energy of 15 keV. The $Cu_3Au(001)$ substrate has been aligned to a grazing incidence of the electron beam with the [110]

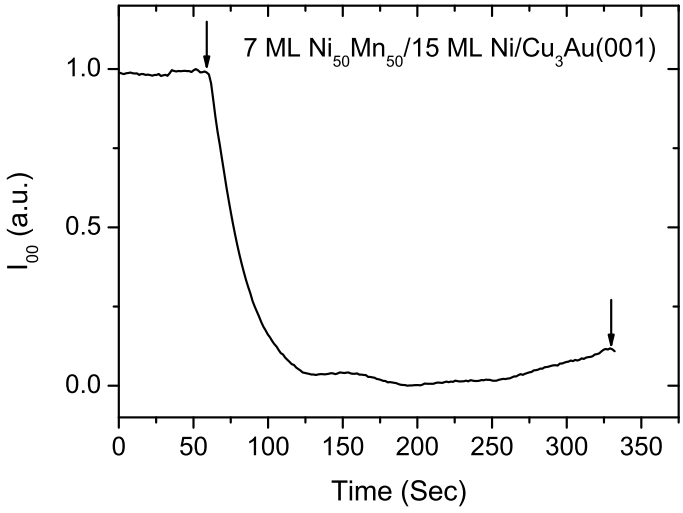

Figure 4.2: MEED (00)-spot intensity recorded during the deposition of 7 ML $Ni_{50}Mn_{50}/Cu_3Au(001)$ at T=300 K.

in-plane direction oriented parallel to the plane of incidence. They used a growth rate of around 2 ML/min, determined from the period of the RHEED oscillations. The evolution of the in-plane lateral spacing of an equiatomic NiMn film $Ni_{55}Mn_{55}$ with thickness during deposition at room temperature (RT) was determined from the RHEED line intensity profiles. Up to at least about 26 ML, the lateral spacing remains constant and, within the experimental precision, identical to the lattice parameter of the $Cu_3Au(001)$ substrate (3.75 Å).

Fig. 4.2 shows an example of $Ni_xMn_{1-x}/Ni/Cu_3Au(001)$, which illustrates that NiMn does not grow layer-by-layer on top of $Ni/Cu_3Au(001)$. It seems that simultaneously several layers of Ni_xMn_{1-x} film grow. Nevertheless we have adopted this system to study the Ni_xMn_{100-x} magnetic properties. The reason is mentioned in the previous chapter that for the case of $Ni/Ni_xMn_{100-x}/Cu_3Au(001)$, Ni exhibits a spin reorientation transition from OoP to IP at temperatures lower than the antiferromagnetic ordering temperatures of the Ni_xMn_{100-x} films.

The morphology of $Ni_{50}Mn_{50}$ is checked by using STM with a tungsten tip prepared by chemical etching. A topographic image of Ni_xMn_{100-x} on $Cu_3Au(001)$ is shown in Fig. 4.3(a). Fig. 4.3(b) shows a line scan profile of the area indicated by the dashed square in Fig. 4.3(a). The line scan profile indicates the presence of monolayer steps (roughly 1.86 Å) and some fractional height of roughly 0.80 Å which indicates the presence of a certain distorted structure, possibly related to a dislocation or a buckling of the $Ni_{50}Mn_{50}$ film.

4.1.2 Epitaxial growth and structure of Ni films

A number of MEED curves was recorded during Ni film growth using $Cu_3Au(001)$, $Ni_xMn_{100-x}/Cu_3Au(001)$ ($60 \geq x \geq 40$), $Mn/Cu_3Au(001)$, $Co/Cu_3Au(001)$, and $Ni/Ni_xMn_{100-x}/Ni/Cu_3Au(001)$ as substrates. Films were grown at deposition rates between 0.5 and 1 ML/min at 300 K. Fig. 4.4 shows two representative MEED oscillations for Ni growth on $Cu_3Au(001)$, and that on $Ni_{55}Mn_{45}/Cu_3Au(001)$. Both curves seem very similar to each other, indicating layer-by-layer growth of Ni due to similar morphology and lateral lattice constants provided by the two substrates. The similar

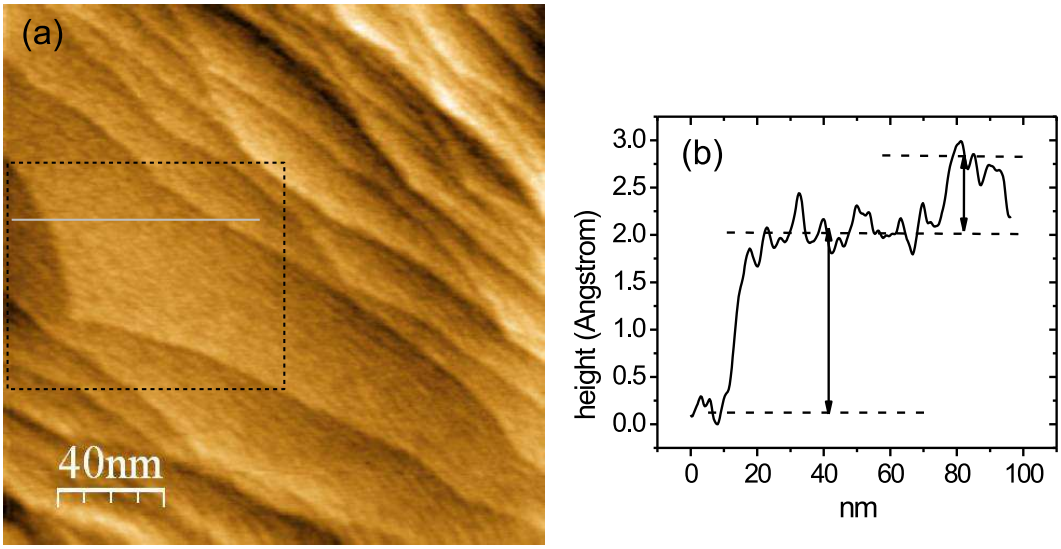

Figure 4.3: (a) STM constant-current image for 8 ML $Ni_{50}Mn_{50}/Cu_3Au(001)$. (b) line profile of the line shown in the area indicated by dashed-square of (a).

features of these two curves are regular intensity oscillations between 2 and 5 ML, the deep intensity minima at 5 ML, and after 7 ML decreased oscillation amplitude with increasing intensity. A small difference is that $Ni/Cu_3Au(001)$ has a deep minimum at 1 ML, whereas for $Ni/Ni_{55}Mn_{45}/Cu_3Au(001)$, there is a shoulder at 1 ML. Regular intensity oscillations are the characteristic feature of layer-by-layer growth [117, 118].

The intensity minimum at 1 ML for $Ni/Cu_3Au(001)$ can be attributed to a high step density due to which the Ni does not want to wet the $Cu_3Au(001)$ substrate as has been suggested previously [69]. Also the intensity minimum at 6–7 ML could be due to some structural changes (lattice relaxation). Such kind of intensity minimum at similar Ni thickness on $Cu_3Au(001)$ has been correlated to the spin reorientation transition of Ni from IP to OoP direction [69]. We think that this correlation could be just a coincidence, since OoP magnetization for Ni comes from volume magnetoelastic contribution which should be reduced if strain is reduced. Also the oscillation amplitude in the MEED curves is decreasing with increasing intensity as the film is made thicker than 7 ML. Braun *et al.* have found that substrate Au atoms segregate on Ni films as has been observed by Auger intensity at 69 eV which decreases with film thickness and vanishes at around 12 ML, and similar behaviour of $Ni/Cu_3Au(001)$ (after 7 ML) has been speculated to be due to substrate Au atoms segregation [69]. We do not think so. The reason is that a very similar behaviour is observed for $Ni/Ni_xMn_{100-x}/Cu_3Au(001)$ (not shown here) where there should not be any Au atoms segregation.

It is very important to mention that the growth mode of Ni on $Cu_3Au(001)$ and that on $Co/Cu_3Au(001)$ is very similar. For most of the work in this thesis, Ni_xMn_{100-x} is grown on out-of-plane magnetized Ni on one half, and on in-plane magnetized Ni/Co on the other half of $Cu_3Au(001)$ to make a comparative study of the magnetic properties of the bilayer (as well as trilayer) system when coupled in both directions. Careful analysis of the MEED oscillations for $Ni/Co/Cu_3Au(001)$ in the Fig. 4.4 (green line) reveals that after the rough surface of ∼2–3 ML Co is filled by Ni, its growth mode becomes very much similar to that on $Cu_3Au(001)$ (black line in Fig. 4.4). The increasing MEED intensity for the first monolayer of $Ni/Co/Cu_3Au(001)$ could be due to the filling of rougher surface of the Co film on which the growth starts. Also, from Fig.

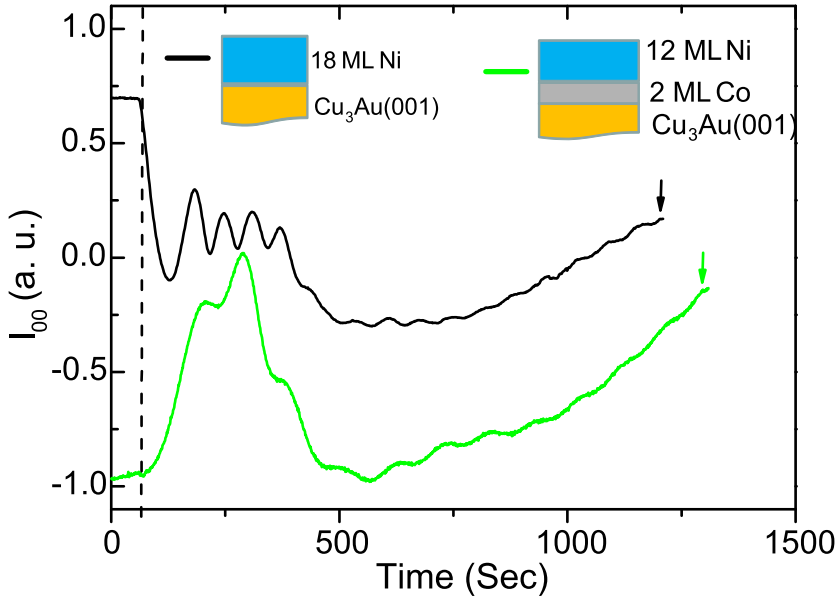

Figure 4.4: MEED (00)-spot intensity recorded during the deposition of 18 ML Ni/$Cu_3Au(001)$, and 12.7 ML Ni/2 ML Co/$Cu_3Au(001)$ at T=300 K.

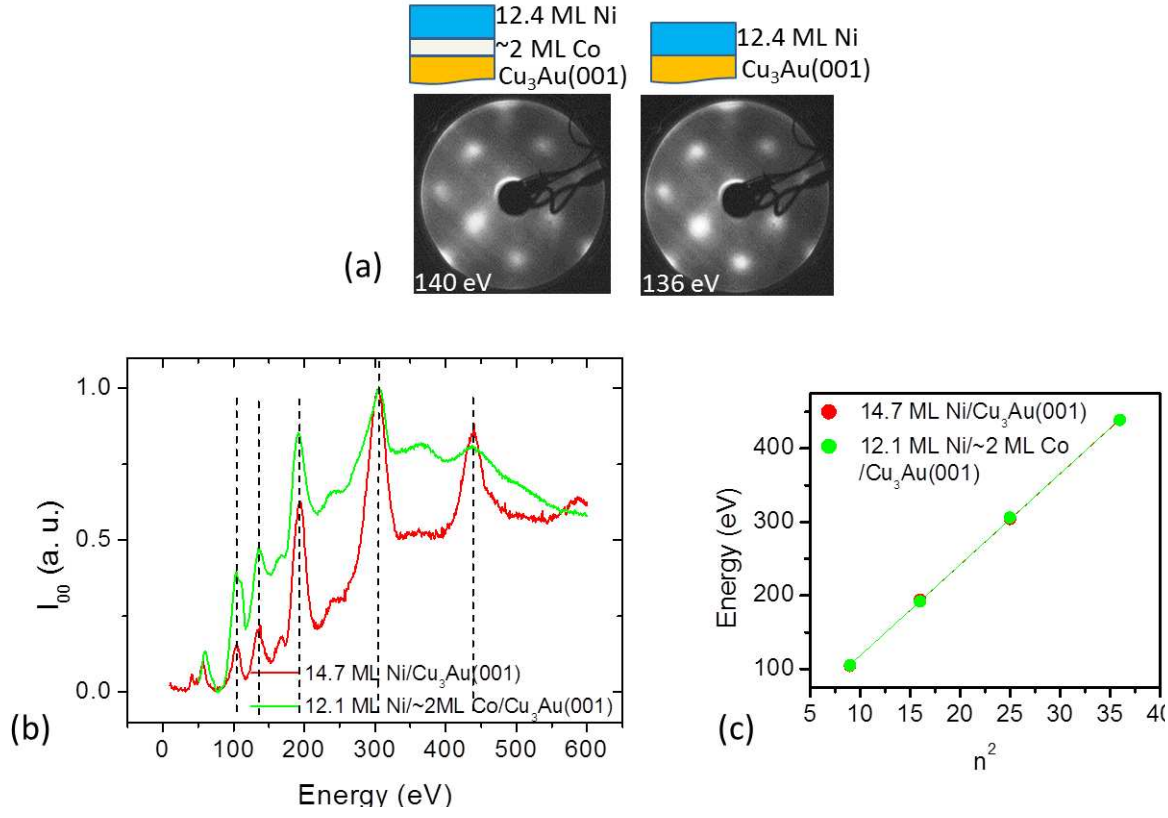

Figure 4.5: LEED pattern ($p(1\times1)$ unit cell) of (a) 12.4 ML Ni/∼2 ML Co/$Cu_3Au(001)$ for 140 eV and that of 12.4 ML Ni/$Cu_3Au(001)$ for 136 eV. (b) LEED I(V) curves for 14.7 ML Ni/$Cu_3Au(001)$ (red line) and 12.1 ML Ni/∼ ML Co/$Cu_3Au(001)$ (green line), and (c) Peak energy dependence of LEED I(V) curves on n^2 (n being Bragg differaction order) for 14.7 ML Ni/$Cu_3Au(001)$ (red symbols) and 12.1 ML Ni/∼ ML Co/$Cu_3Au(001)$ (green symbols). Note that data points in both cases overlap.

4.5(a), it is clear that the LEED pattern of 12.4 ML Ni/$Cu_3Au(001)$ and that of 12.4 ML Ni/∼2 ML Co/$Cu_3Au(001)$ is identical at similar energies. A linear fitting of the E_{kin} versus n^2 points extracted from the I(V) curves (Fig. 4.5(b)) gives the vertical interlayer distance d_p. The straight lines in Fig. 4.5(c) represent linear fittings based on the kinematic approximation of the (00) diffraction beam intensity, as described in section 3.2, and provide the perpendicular lattice constant of 14.7 ML Ni/$Cu_3Au(001)$ and that of 12.1 ML Ni/∼ ML Co/$Cu_3Au(001)$. The exactly matching d_p=1.74 Å indicates a very similar Ni structure for the both cases.

4.1.3 Structure of Ni_xMn_{100-x} alloy films on $Cu_3Au(001)$[1]

Fig. 4.6 shows the LEED patterns of the clean $Cu_3Au(001)$ substrate and of different Ni_xMn_{100-x} films deposited on $Cu_3Au(001)$ at 300 K, as indicated. The ordered $Cu_3Au(001)$ surface is characterized by the (1/2 1/2) spots of the c(2×2) superstructure, a pattern that is also observed for the Ni_xMn_{100-x} films, although with less intensity, in particular for x=10 and x=28. For NiMn, such a reconstruction is expected for a chemically ordered, bulklike, $Ni_{50}Mn_{50}$ epitaxial film grown with the a-axis along the film surface normal, when the Ni and Mn atoms are arranged in alternating atomic planes perpendicular to the c-axis [42], as observed for equiatomic NiMn on top of Cu(100) [58, 59, 60] but should not be the case for c-axis growth of this phase on a (100) fcc surface. The additional ordered structure at the surface of the NiMn films might just come from a reconstruction of NiMn atoms at the surface, or even be due to some Au segregation to the very first atomic layers of the NiMn surface, as already reported for thin Mn, as well as Co-Ni alloy films grown on top of $Cu_3Au(001)$ [119, 120, 121].

The presence of Au floating on top of the NiMn films was explored here by AES, from the evolution of the Ni, Mn, Cu, and Au Auger lines at low energy (∼30-100 eV) with increasing NiMn thickness. The results (not shown) indicate Au segregation in the first monolayers, but 11–12 ML NiMn suppresses completely the Au signal (at 69 eV). Therefore, the weak $c(2\times2)$ reconstruction at the surface NiMn films, which was still observed at thicknesses of 15 ML and more, seems not to be due to Au atoms segregated to the very surface of NiMn on $Cu_3Au(001)$.

The crystallographic structure of the $Ni_xMn_{100-x}/Cu_3Au(001)$ along the surface normal was determined from LEED I(V) curves. Only films grown at room temperature (RT) were investigated. The (00) diffraction beam intensity curves for different NiMn films were collected as a function of the electron energy (I_{00}(V) curves) after film deposition, and a kinematic approximation was used to calculate the average vertical interplanar distance of the top NiMn atomic layers in the films [122]. Considering that the electrons undergo only single scattering in the diffraction process (the kinematic approximation), the vertical (perpendicular) interlayer distance d_p can be evaluated by using the expression

$$d_p = \frac{n\pi\hbar}{sin(\theta)\sqrt{2m_e(E_{kin}(n) + (-V_0))}} \tag{4.1}$$

where the integer n is the order of the corresponding interference peak, E_{kin}(n) the primary kinetic energy of the electrons of that peak, V_0 the additional energy shift due

[1] taken from Ref. [132]

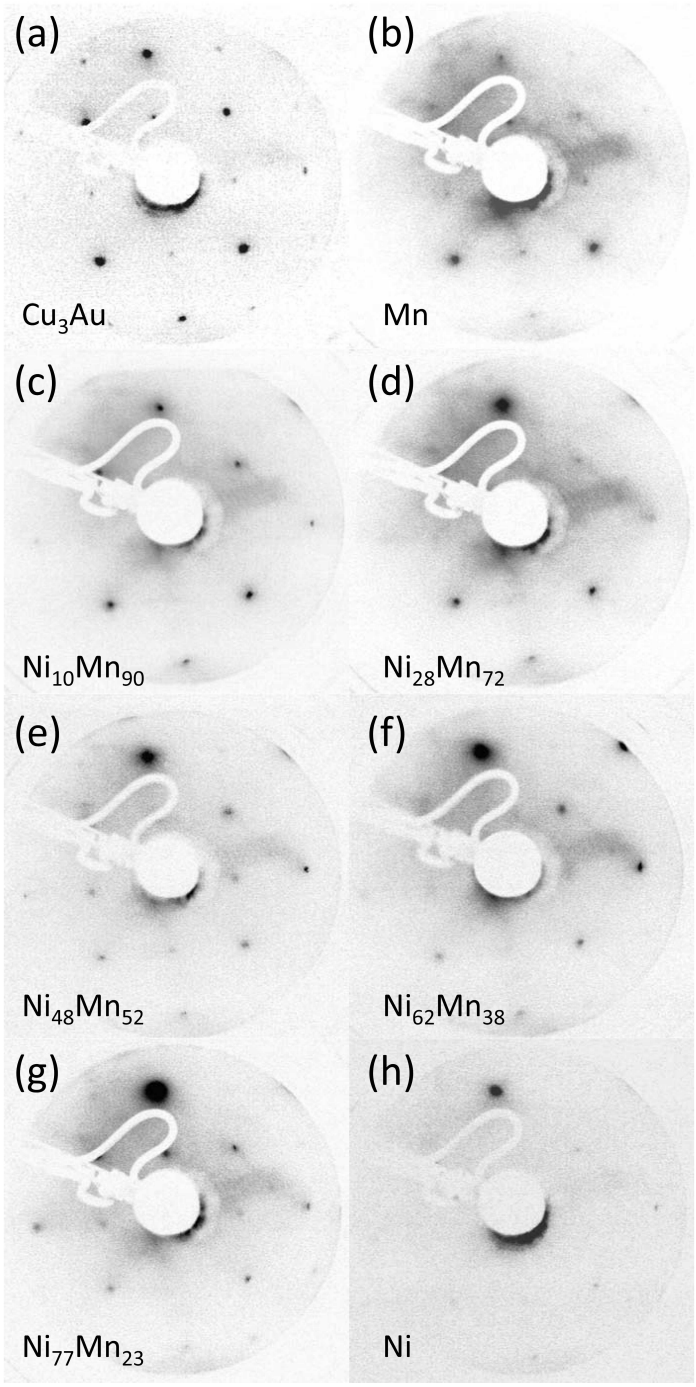

Figure 4.6: LEED pictures of the $Cu_3Au(001)$ substrate and Ni_xMn_{100-x} films of different composition x on $Cu_3Au(001)$.(a) $Cu_3Au(001)$, electron energy E=122 eV; (b) 8.5 ML $Mn/Cu_3Au(001)$, E=126 eV; (c) 8.0 ML $Ni_{10}Mn_{90}/Cu_3Au(001)$, E=120 eV; (d) 8.2 ML $Ni_{28}Mn_{72}/Cu_3Au(001)$, E=127 eV; (e) 8.8 ML $Ni_{48}Mn_{52}/Cu_3Au(001)$, E=123 eV; (f) 6.0 ML $Ni_{62}Mn_{38}/Cu_3Au(001)$, E=126 eV; (g) 6.8 ML $Ni_{77}Mn_{23}/Cu_3Au(001)$, E=121 eV; and (h) 7.5 ML $Ni/Cu_3Au(001)$, E=115 eV.

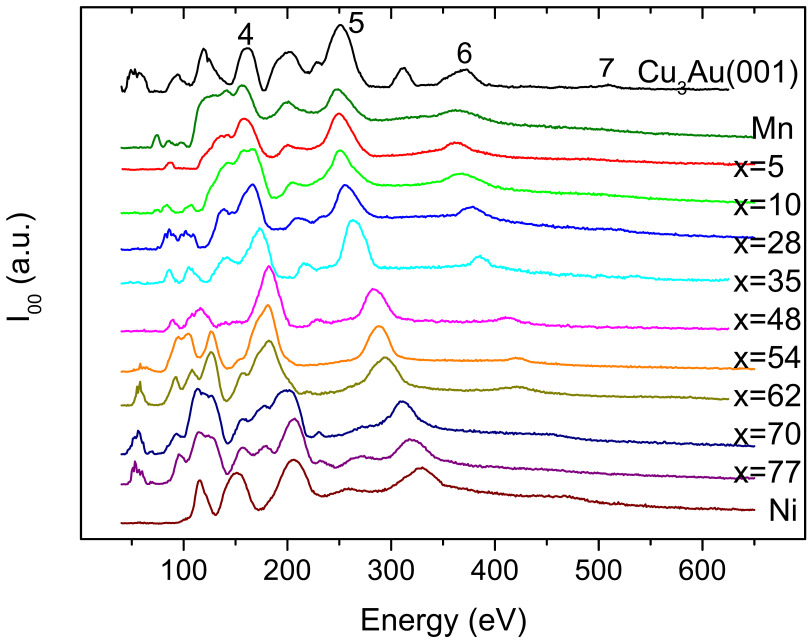

Figure 4.7: LEED I(V) curves for a series of different ∼8 ML thick Ni_xMn_{100-x} films (6 ML for x =62) deposited on the $Cu_3Au(001)$ substrate at RT, as indicated. The peaks above 150 eV are identified as the fourth-, fifth-, and sixth-order Bragg maxima.

to the average inner potential in the crystal, m_e the electron mass, and θ the incident angle with respect to the sample surface. A linear fitting of the E_{kin} versus n^2 points extracted from the I(V) curves gives the vertical interlayer distance d_p [122].

The LEED I(V) curves for NiMn films (∼8 ML thick) of different concentrations, from pure Mn to pure Ni, deposited at RT, are shown in Fig. 4.7, where the maxima above 150 eV were identified as the fourth-, fifth-, and sixth-order Bragg maxima. The determination of the perpendicular interlayer spacing d_p from the $E(n^2)$ curves is illustrated in Fig. 4.8 for the $Cu_3Au(001)$ substrate and for three epitaxially grown equiatomic NiMn films, $Ni_{45}Mn_{55}$, $Ni_{52}Mn_{48}$, and $Ni_{55}Mn_{45}$, 24, 12, and 26 ML thick, respectively. The straight lines represent linear regression fittings based on the kinematic approximation of the (00) diffraction beam intensity, as described above. For all NiMn films grown with near equiatomic composition and at a substrate temperature of 300 K, the average interlayer distance perpendicular to the sample surface is contracted relative to $Cu_3Au(001)$, as evidenced by the lower slope of the $E(n^2)$ curve for the substrate. The interlayer spacings were determined to be 1.78±0.02 Å for 24 ML $Ni_{45}Mn_{55}$ and 1.76±0.02 Å for both the 12 ML thick $Ni_{52}Mn_{48}$ and the 26 ML thick $Ni_{55}Mn_{45}$ films.

The average vertical interlayer spacing d_p obtained for Ni_xMn_{1-x} layers on $Cu_3Au(001)$ as a function of the Ni content x is shown in Fig. 4.9, where the dashed horizontal lines at 1.88 and 1.76 Å indicate the interlayer spacings of fcc $Cu_3Au(001)$, as experimentally obtained here, and in bulk $L1_0$ NiMn along the c-axis [42], respectively. The interlayer spacing of $Cu_3Au(001)$ coincides with the value of bulk $L1_0$ NiMn along the a-axis, as already mentioned, and the spacing along c in $L1_0$ NiMn coincides with the value of bulk fcc Ni. The average interlayer spacing of the NiMn alloy films decreases from 1.88(2) Å at x=10 to 1.69(2) Å at x=77. For pure Mn (x=0), our value of 1.91(2) Å is in good agreement with the value obtained by Lin *et al.* [119] for RT-grown Mn

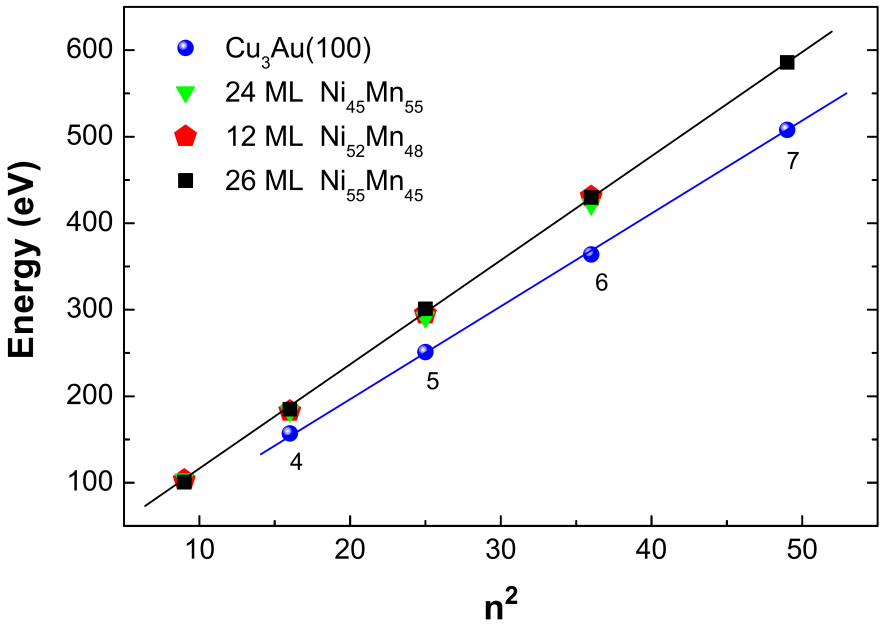

Figure 4.8: Energy dependence on n^2 for three different NiMn films near equiatomic concentration ($Ni_{45}Mn_{55}$, $Ni_{52}Mn_{48}$, and $Ni_{55}Mn_{45}$, 24, 12, and 26 ML thick, respectively) and for the $Cu_3Au(001)$ substrate. The contraction of the perpendicular interlayer distance in the NiMn films (of 5.3%) relative to the $Cu_3Au(001)$ substrate is evident. The full (blue) circles are for the $Cu_3Au(001)$ substrate, and the hexagons (red), squares (black), and triangles (green) are for the 24 ML $Ni_{45}Mn_{55}$, 12 ML $Ni_{52}Mn_{48}$, and $Ni_{55}Mn_{45}$, respectively. Please note that data points for the NiMn films overlap strongly.

films on $Cu_3Au(001)$ below 10–12 ML. For pure Ni (x=100), our value of 1.66(2) Å is smaller than the values of Ref. [69], indicating more strained films for equivalent thicknesses. As expected, the known tetragonal distortion of epitaxial ultrathin Ni films on Cu(001) [58, 59, 60, 123], characterized by an in-plane expansion of the fcc Ni lattice and a compression along the surface normal, is also observed here, as demonstrated by the lower average interlayer spacing in comparison to bulk Ni.

We have also determined the interlayer spacing d_p as a function of the film thickness for a $Ni_{40}Mn_{60}$ wedge. As plotted in Fig. 4.9 for the extreme values obtained (full blue triangles), d_p is equal to 1.90 Å up to 3 ML (where there should be a considerable signal from the substrate as well), and then starts to relax, decreasing linearly to reach 1.85 Å at 10 ML, remaining constant at that value until 13 ML $Ni_{40}Mn_{60}$. This observation is consistent with the results of Braun *et al.* for pure Ni films on $Cu_3Au(001)$ [69]. For pure Mn films on $Cu_3Au(001)$ at room temperature, Lin *et al.* observed an abrupt decrease in the interlayer distance at a critical thickness around 13 ML [119].

This perpendicular interlayer distance corresponds to a contraction of 5.3% relative to the in-plane spacing determined by RHEED for these films, and is in good agreement with the expected value of the interlayer distance along the c-axis in bulk $L1_0$ NiMn. Having in mind that we observe an in-plane interlayer distance that matches the $Cu_3Au(001)$ substrate, i.e., a value of 1.88±0.02 Å for the interlayer distance in the sample plane, our results are a clear indication of an fct structure with the c/a ratio compatible with the one expected for $L1_0$ NiMn, and with the a- and b-axes in

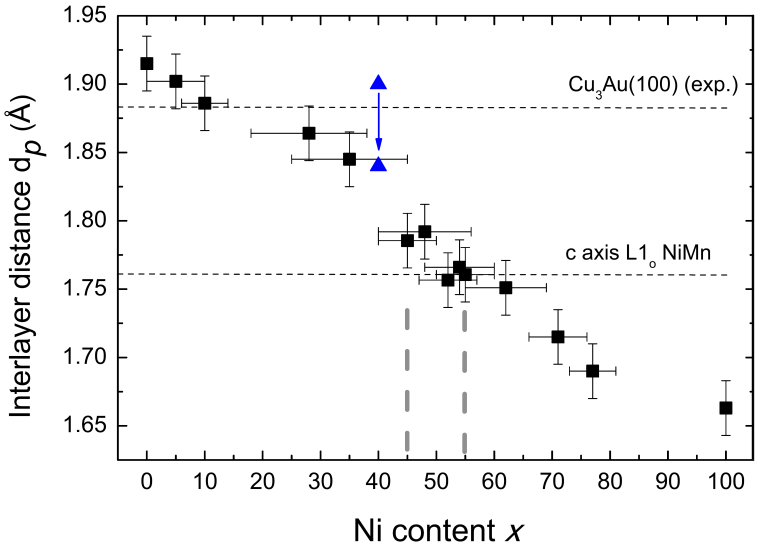

Figure 4.9: Perpendicular interlayer distance d_p vs Ni concentration in Ni_xMn_{1-x} on $Cu_3Au(001)$ at room temperature. The full triangles (blue points) limiting the arrow at x=40 represent the extreme values of d_p when the thickness of a $Ni_{40}Mn_{60}$ film increases from 3 to 10 ML (see text). The dashed horizontal lines at 1.88 and 1.76 Å indicate the interlayer spacings in fcc $Cu_3Au(001)$, as experimentally obtained here, and in bulk $L1_0$ NiMn along the c-axis [42], respectively. The dashed vertical (gray) lines indicate the $L1_0$ region for bulk NiMn. Note that for equiatomic NiMn films d_p coincides with the value of the c-axis in bulk $L1_0$ NiMn.

plane. In contrast to equiatomic NiMn on Cu(100) [58, 59, 60, 123], for NiMn films on $Cu_3Au(001)$ we observe a tetragonal distortion compatible with an epitaxial c-axis growth of fct NiMn(001).

4.2 Spin reorientation transition (SRT) of Ni on $Cu_3Au(001)$

To check the spin reorientation transition (SRT) of Ni/$Cu_3Au(001)$, hysteresis loops for different film thicknesses were recorded at room temperature (300 K). The thinnest studied film 4.2 ML Ni was measured at 150 K due to its lower T_C (∼230 K) (Fig. 4.10). Panel (a) and (b) show longitudinal and polar MOKE measurements, respectively. Longitudinal MOKE measurements show that the films have an in-plane magnetization in the thickness region from 4 to 7 ML, and for thicknesses ≥18 ML (Fig. 4.10(a)). At room temperature, the largest coercivity observed for IP magnetized 24.9 ML Ni/$Cu_3Au(001)$ film is 5.1 mT. Fot the films with thicknesses of 10 and 13.4 ML, the hysteresis loops have very large coercivities, ∼23 and ∼70 mT, respectively. The Zeeman energy is proportional to the product of magnetization and the applied field, thus for smaller magnetization, lager magnetic field is required to reverse it. This means that the larger coercivities of 10 and 13.4 ML Ni films actually arises from the small in-plane (IP) component of the out-of-plane (OoP) magnetized films during longitudinal MOKE measurements where the OoP component due to a small misalignment of the IP field reverses the OoP magnetization of the films.

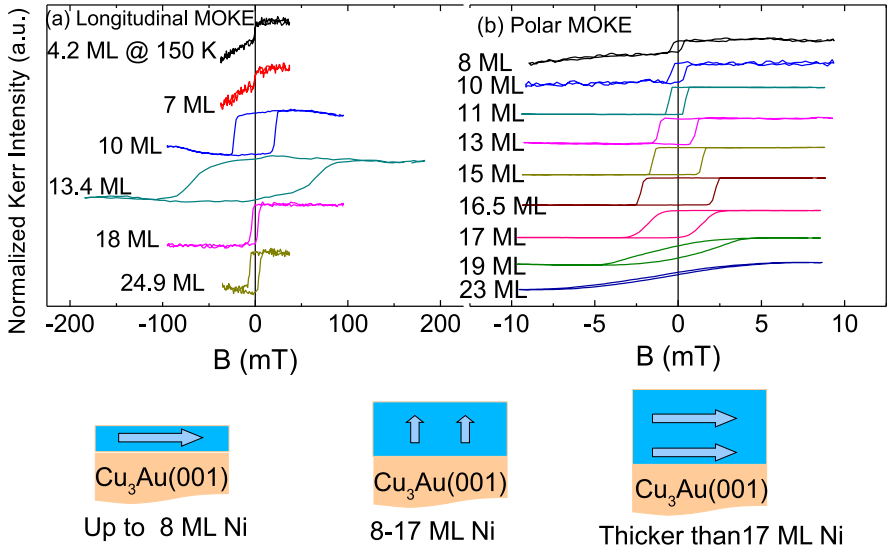

Figure 4.10: The spin reorientation transition (SRT) of Ni/$Cu_3Au(001)$: (a) Hysteresis loops measured in longitudinal MOKE geometry at 300 K, except the thinnest one, which measured at 150 K. Up to 7 ML, and at ≥18 ML Ni/$Cu_3Au(001)$, loops have small coercivities, showing IP easy axis of magnetization. Whereas thicknesses in-between have larger coercivities indicating a component of the out-of-plane loop. (b) Hysteresis loops measured in polar geometry at 300 K. From 8 to 16.5 ML Ni/$Cu_3Au(001)$, loops have smaller coercivities, showing OoP easy axis of magnetization, whereas for thicknesses of 17 ML and above, the loops are more tilted indicating hard axis of magnetization.

For Ni films with thickness between 8 and 17 ML, perpendicular hysteresis loops is observed using polar MOKE measurements (Fig. 4.10(b)). From 8 to 16.5 ML films, the polar MOKE loops are rectangularly shaped, showing a strong OoP anisotropy of the films. At 17 ML, the loop shows a tilt indicating some contribution from IP anisotropy. For thicker films the loops are much more tilted, which is due to the transition of magnetization from OoP to IP direction. This reorientation of the magnetization direction could be caused by a reduction of the strain in the Ni film on $Cu_3Au(001)$.

Previously, it has been shown that Ni/$Cu_3Au(001)$ films have OoP anisotropy between 5 and 12 ML and an IP magnetization below 5 and above 12 ML, [69]. Our finding can be compared with the behaviour of Ni films on Cu(001). For Ni/Cu(001), the first SRT from IP to OoP is observed for thicknesses between 10 and 12 ML [124, 125, 126]. The smaller lattice mismatch of 2.5% between Ni and Cu causes a smaller film strain which results in a larger reorientation thickness. It is known from theory that the smaller the lattice mismatch between the film and the substrate is, the larger magnetic reorientation thickness is required.

The ferromagnetic film magnetization easy axis depends on several energy terms, or, in other words, the thickness required for the reorientation transition of the ferromagnetic film's magnetization depends on the different contributions to magnetic anisotropy, such as magnetocrystalline, shape and magnetoelastic anisotropy. For these anisotropies, both bulk and surface contributions have to be distinguished. The former grow linearly with the film thickness, while the surface contributions are independent of film thickness. Some contributions may favour IP easy axis of the magnetization whereas the others may do OoP. There is a competition between these energy terms,

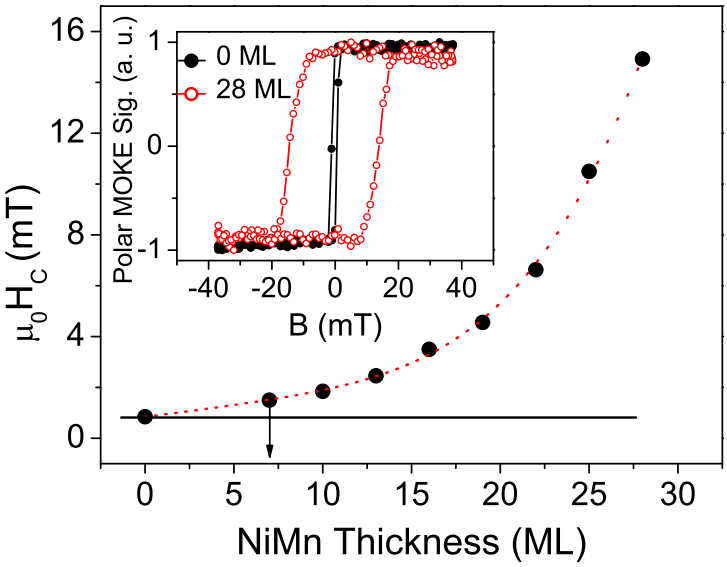

Figure 4.11: Coercivity (H_C) versus NiMn thickness for the bilayer system NiMn/9.3 ML Ni/Cu_3Au(001) measured by polar MOKE at 300 K. The red-dotted line is a guide to the eye. The black horizontal line passing through the first point of the curve (0 ML NiMn/9.3 ML Ni) shows the deviation of H_C due to NiMn. In the inset the normalized Kerr intensity is shown for (i) uncovered 9.3 ML Ni/Cu_3Au(001) (black loop with closed symbols) and (ii) the same film covered with $\sim$ 28 ML NiMn (red loop with open symbols).

and the magnetization easy axis is dictated by the winning one/s.

4.3 Antiferromagnetism in $Ni_{50}Mn_{50}$ thin films on Ni/(Co/)Cu_3Au(001)

In the following subsection, results for the antiferromagnetism of equiatomic single-crystalline NiMn thin film alloys grown on Ni/Cu_3Au(001) are described which are obtained by means of magneto-optical Kerr effect (MOKE). In the next subsection, these results are discussed to make some important conclusions regarding the spin structure of equiatomic single-crystalline NiMn thin films which are simultaneously in contact with IP and OoP magnetized Ni layers.

4.3.1 Results

Figure 4.11 shows our results measured at room temperature, for the coercivity of OoP magnetized Ni film versus the thickness of equiatomic NiMn for n ML NiMn/9.3 ML Ni/Cu_3Au(001), where $\sim 7 \leq n \leq \sim 28$. A steady increase of the coercivity of OoP magnetized 9.3 ML Ni/Cu_3Au(001) with NiMn thickness can be observed. With $\sim$7 ML of NiMn the bilayer has already a distinctly higher coercivity as compared to the Ni film alone. The inset of Fig. 4.11 shows as an example magnetization curves of 9.3 ML Ni without NiMn coverage (filled circles) and with $\sim$28 ML NiMn (open-circles), the latter exhibiting a much higher coercivity, but no exchange bias at 300 K.

An example of temperature-dependent hysteresis loops for both OoP as well as IP

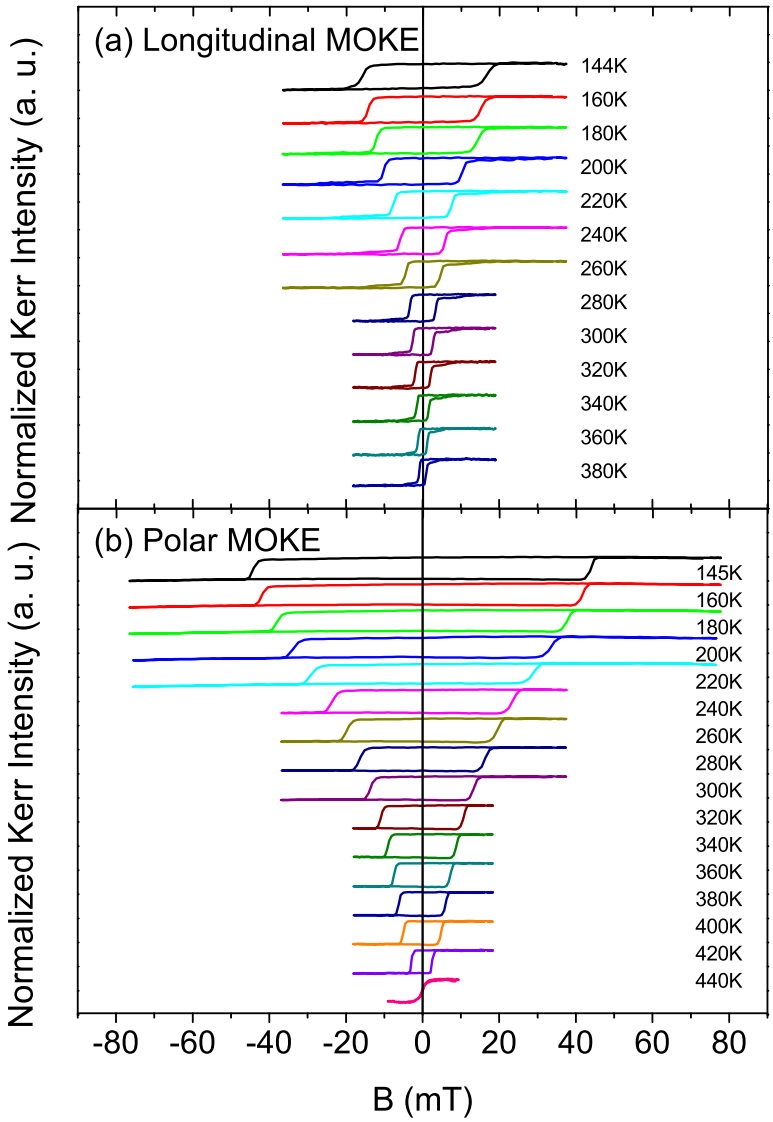

Figure 4.12: Normalized magnetic hysteresis loops for (a) 11.3 ML NiMn/12.5 ML Ni/∼2 ML Co/Cu_3Au(001) measured by longitudinal and (b) 11.3 ML NiMn/12.5 ML Ni/Cu_3Au(001) measured by polar MOKE at different temperatures.

magnetization is shown in Fig. 4.12. Here the sample is 11.3 ML NiMn/12.5 ML Ni with (Fig. 4.12(a)) and without ∼2 ML Co underneath (Fig. 4.12(b)), on Cu_3Au(001). Rectangularly shaped loops for both cases were obtained, where a coercivity enhancement with decreasing temperature can be observed. Although the general behaviour of the temperature-dependent hysteresis loops is similar for the IP and OoP cases, the details are different. The main differences between the two magnetization directions observed here are that the coercivity H_C for OoP magnetization is almost three times that for IP magnetization at low temperatures, and that the reduction of H_C to lower values occurs at higher temperatures for OoP magnetization of the Ni layer (loop at 440 K).

Fig. 4.13 shows the temperature-dependent coercivity for IP and OoP magnetized Ni films contacted to n ML NiMn film ($\sim 7 \leq n \leq \sim 35$) on the positive field axes. The insets of Fig. 4.13(a) and Fig. 4.13(b) show a zoom-in of H_C versus temperature curve for 7.4 ML NiMn in contact with IP and OoP Ni, respectively. The purpose

of these insets is to show how we determine the ordering temperature of AFM NiMn. If there were no exchange coupling between the AFM and the FM layers, the H_C of the FM layer alone would decrease monotonically as the temperature is increased, and would give rise to a certain slope of small steepness. We observe, in contrast, in Fig. 4.13(a) for all IP films a discontinuity in the slope of H_C versus temperature curves, which is typical for AFM/FM bilayer exchanged-coupled systems [37, 43, 127]. The point at which this discontinuity of temperature-dependent H_C occurs is considered as T_{AFM}. For its determination, we follow the procedure already used in Ref. [127], and fit a straight line to the high-temperature side of the $H_C(T)$ data to represent the behaviour of the uncoupled FM layer. The temperature at which the measured H_C significantly deviates from this line is defined as T_{AFM}, and marked by respective coloured arrows in Fig. 4.13. For the OoP magnetized Ni, this kind of discontinuity could only be seen for the thinnest (7.4 ML) studied NiMn film. For the thicker films up to 18 ML thickness, only lower limits for T_{AFM} (vertical arrows) can be given, it can be higher as indicated by horizontal arrows next to the vertical arrows in Fig. 4.13(b). For the three thickest NiMn films, it was not possible to get any information on T_{AFM}, since an easy-axis change of the Ni magnetization from OoP to IP occurs at a temperature lower than the ordering temperature (loop at 440 K in Fig. 4.12(b)).

From Fig. 4.13(a), one can see that for the IP samples the T_{AFM} value initially increases by 30 to 40 K every 3 to 4 ML of NiMn thickness. For the OoP part, a similar increment of T_{AFM} when increasing the NiMn thickness from 7.4 to 11.3 ML is observed. This increase of T_{AFM} with increasing AFM layer thickness is due to the well-known finite-size effect, and is in agreement with results for FeMn/Co/Cu(001) [37] and (Co/)Ni/FeMn/Cu(001) [43] for both, the IP and OoP cases. Like in Refs. [43, 44] for FeMn, we also found that the critical thickness of the NiMn films to form antiferromagnetic order at room temperature (300 K) varies with changing the magnetization direction of the FM layer from OoP to IP. Comparing the exchange-coupled AFM/FM samples shown in Fig. 4.13(a) and Fig. 4.13(b), one observes that the ordering temperature of the same NiMn thickness is distinctly higher for the OoP coupled part than for the IP one. This difference is 110 K for the thinnest film with 7.4 ML thickness.

The exchange coupling in the NiMn/Ni/(Co/)Cu_3Au(001) system also resulted in shifted loops with an exchange bias field (H_{eb}), but only at the thickest (35.7 ML) studied NiMn film as shown in Fig. 4.13(a) and Fig. 4.13(b) by black solid symbols on the negative side of the vertical axes for IP as well as OoP magnetized Ni, respectively. A common feature for both the IP and OoP exchange-biased systems is that the coercivity goes down with lower temperature as soon as exchange bias is established. This behaviour has been observed for several other systems [128, 129, 130, 131]. Both, the H_{eb} value and the blocking temperature T_b, the latter indicated by the black arrows in Fig. 4.13, are slightly higher in the case of NiMn coupled to OoP Ni than in the IP case. The ratio of the exchange bias field to the coercivity, however, is smaller for the OoP coupling compared to the IP one.

4.3.2 Discussion

In Ref. [132], no influence of NiMn layer with thickness up to 14.5 ML on the magnetic properties of a FM Co layer in Co/NiMn/Cu_3Au(001) was observed because of either chemical and/or crystallographic disorder, or because the NiMn spin order was

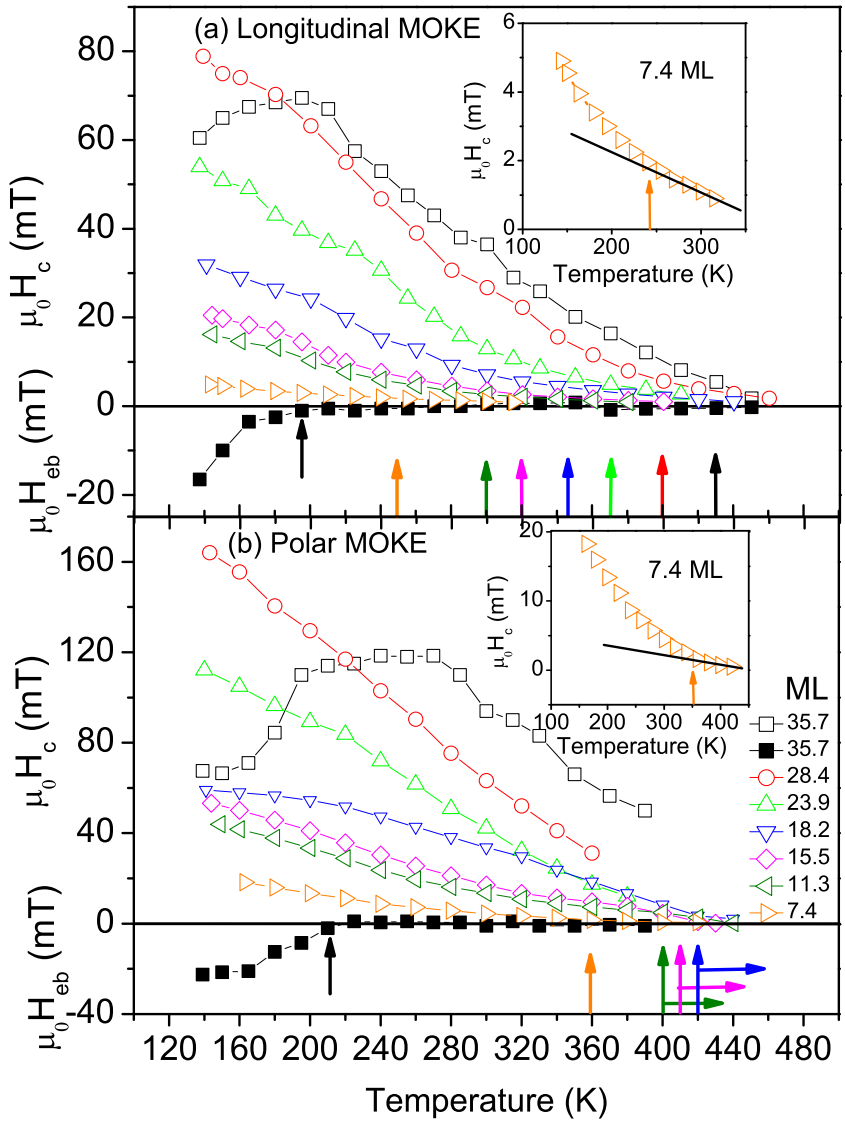

Figure 4.13: Temperature dependence of the coercivity (positive field axis) and the exchange bias field (negative field axis) for different thicknesses of NiMn grown on (a) in-plane-magnetized ∼12 ML Ni/∼2 ML Co/Cu_3Au(001) and (b) out-of-plane magnetized ∼12 ML Ni/Cu_3Au(001). In the respective insets, a zoom-in on the curve for 7.4 ML NiMn is presented to show how the antiferromagnetic ordering temperature is determined. The obtained antiferromagnetic ordering temperatures are indicated by coloured arrows, where the horizontal bars at 11.3, 15.5, and 18.2 ML NiMn in (b) denote that they just represent lower limits.

perpendicular to the Co magnetization. We will discuss the latter argument first. In FM/AFM bilayer systems, if the FM film thickness is kept constant, its coercivity increases with increasing thickness of the AFM thin film above the critical thickness for the onset of antiferromagnetic order. We observed this enhancement of coercivity in our bilayer system and found that its critical thickness is less than ∼7 ML for the OoP sample at room temperature. This is smaller than the one of 8 ML reported for NiMn/6 ML Co/Cu(001) [58, 59]. This could be due to the fact that the reported measurements have been done on an IP system whereas we performed it for the OoP one. Our result is similar to the observations in the system (Co/)Ni/FeMn/Cu(001), where the critical thickness is smaller for the case when the adjacent Ni is magnetized in the OoP direction than in IP [43, 44].

As mentioned in the introduction, one of the objectives of the present study was to check whether the spin structure of epitaxially grown NiMn thin films deviates from a simple collinear spin structure. The observed coupling of the NiMn layer to both IP and OoP magnetized adjacent FM layers (Figs. 4.12 and 4.13) is either a hint towards a non-collinear spin structure, or it shows that the NiMn spins can be tilted in either direction. Comparing the IP versus OoP samples for otherwise identical conditions, the striking difference is the T_{AFM}. The T_{AFM} for the OoP samples is as much as 110 K higher than for the IP samples. This can be attributed to the magnetic proximity effect in which the proximity of the magnetized FM layer raises the T_{AFM} of the AFM layer. The significance of this effect is that just by changing the magnetization direction of the adjacent FM layer, the very same NiMn film could be switched from the antiferromagnetic state to the paramagnetic one and vice versa. Our findings are similar to the ones reported for FeMn [43], where up to 60 K decrease of T_{AFM} is observed when the OoP Ni magnetization is switched to IP by deposition of a Co over-layer in the system (Co/)Ni/FeMn/Cu(001). The reason for the magnetic proximity effect leading to this difference in T_{AFM} has been related to the well-known three-dimensional bulk-like 3-Q spin structure of FeMn [35, 36]. This strengthens our assumption about a three-dimensional spin structure also in NiMn.

This magnetic proximity effect could be due to either a different coupling strength at the AFM/FM interface in the IP and the OoP direction and/or a different interfacial spin structure of NiMn. If a $3Q$-like three-dimensional spin structure of NiMn is assumed, a higher coupling strength in the OoP direction compared to IP could be one possible reason for the higher T_{AFM}. This higher coupling strength in the OoP direction could be justified under the assumption of large terraces of NiMn at the interface, as has been assumed for FeMn [43]. Assuming a $3Q$-like spin structure, the IP component of the NiMn spins should cancel each other, but not the OoP component. In the IP direction, uncompensated spins contribute only from the step edges [133], where their density would be smaller compared to OoP uncompensated spins at large terraces. Therefore the OoP uncompensated spins on the large terraces would lead to a higher coupling strength and hence a higher T_{AFM} as compared to the coupling strength from IP uncompensated spins at step edges. Recently, Stampe *et al.* [127] have reported that for OoP magnetization in FeMn/Ni/Cu(001), the interfacial coupling strength does not influence the T_{AFM} of FeMn. We do not exclude the contribution of the coupling strength towards the T_{AFM} of NiMn here. In the NiMn/Ni/(Co/)Cu_3Au(001) system we did not vary the AFM/FM interfacial coupling strength independently from the direction of easy axis of the FM, we therefore can not conclude whether in our system the coupling strength has a direct influence on T_{AFM}. But, besides the difference

in the lattice structural properties, the magnetic properties of both FeMn and NiMn might be also different. One considerable difference is that the Fe magnetic moment is comparable to that of Mn in FeMn, whereas in NiMn, the Ni magnetic moment is negligibly small as compared to the Mn moment [42, 46, 47]. Therefore, in spite of possibly having a similar spin structure, the coupling strength may have a different effect on T_{AFM} in both materials, such that we can not exclude the possibility that it could play a role. An alternative mechanism, not relying on the coupling strength, has been proposed to explain the different T_{AFM} when the adjacent FM layer magnetization is switched from OoP to IP [127]—the $3Q$ spin structure of the AFM layer could be differently distorted when coupled to an FM layer in IP and OoP direction. A different spin structure can result in different T_{AFM} if the average exchange coupling between the antiferromagnetic spins in the AFM layer depends on their relative orientations. In the assumed $3Q$-like spin structure of NiMn, the OoP AFM/FM coupling may lead to the rearrangement of NiMn spins towards a $1Q$-like OoP spin structure at and near the interface. The opposite situation may occur for the IP case, where the NiMn spins are rearranged towards a $2Q$-like IP spin structure. If the spin structure in the OoP coupling were more thermally stable than the IP one, this could give rise to a higher T_{AFM} in the former case.

When we compare our results to references [43, 44, 127], we can speculate that the spin structure of our studied NiMn films at the interface is either non-collinear, contrary to the reported collinear spin structure of bulk NiMn [42, 45], such that its spins make a very small angle with the OoP direction, where it has a large OoP (small IP) component and a small magnetic anisotropy, or that the spins of the NiMn layer acquire the respective directions of the adjacent FM Ni layer after the field cooling process. As a result the NiMn spin structure could be thermally more stable when coupled to OoP Ni than to IP.

In the light of our speculations about the mechanism for having different T_{AFM} of NiMn coupled to Ni magnetized along different axes, one can further speculate about the reason for the absence of any apparent coupling of 12 ML Co in contact with 14.5 ML NiMn/Cu_3Au(001), even at 190 K, as reported in Ref. [132]. A smaller coupling strength and/or differently distorted $3Q$-like spin structure of NiMn in contact to Co might result in a smaller T_{AFM} below the measured temperature range. Furthermore, the larger magnetization of Co, as compared to Ni, would certainly result in a reduced coercivity. Also, in Ref. [132], MOKE measurements have been performed only at two temperatures, with H_C for 190 K being slightly higher than for 300 K. Temperature-dependent MOKE measurements with smaller steps between these two temperatures might provide a more detailed picture.

We could only find exchange bias in the thickest NiMn film studied (35.7 ML), together with a peak in coercivity near T_b. The T_b and H_{eb} are also higher for the OoP case than for the IP. This could be directly related to the higher antiferromagnetic ordering temperature in the former case. At temperatures higher than T_b, all AFM spins reverse during the magnetization loop of the FM. While the FM spins are switched by the external magnetic field, they drag the AFM spins irreversibly, hence increasing the coercivity. For pinning of some fraction of AFM spins at lower temperatures (below T_b), the FM cannot drag as many AFM spins, consequently the exchange bias effect occurs, and H_C is reduced. This results in a peak in H_C at around T_b. For thinner NiMn layers, no stable pinning of AFM spins occurs in the studied temperature range to 'freeze' the AFM spins against being dragged by the FM magnetization. Therefore

no EB can be observed.

4.4 Exchange-biased bilayers: Ni_xMn_{100-x}/Ni/(Co/) $Cu_3Au(001)$

Magnetic proximity effects on concentration-, and thickness-dependent T_{AFM} and T_b along with H_{eb} of single crystalline thin films comprising of Ni_xMn_{100-x}/Ni/(Co/) $Cu_3Au(001)$ bilayers are investigated for IP and OoP directions by means of longitudinal and polar MOKE, respectively. First the results are described and then explained in the discussion part on the basis of an intuitive model which leads to some conclusions about the spin structure of Ni_xMn_{100-x} thin films in the system under study.

4.4.1 Results

Fig. 4.14 shows an example of temperature-dependent hysteresis loops for ∼35 ML $Ni_{30}Mn_{70}$ on IP and OoP magnetized Ni, measured by longitudinal and polar MOKE, respectively. exchange bias is observed for temperatures lower than 420 K for IP, and lower than 400 K for OoP magnetized Ni. This shows that the AFM/FM bilayer under study provides stronger exchange bias as compared to equiatomic NiMn concentrations where, as mentioned in the previous section, only a smaller EB has been observed for ∼ 35 ML $Ni_{50}Mn_{50}$/Ni(Co/)/$Cu_3Au(001)$ below 210 K and 195 K for OoP and IP magnetization, respectively. For example, for ∼35 ML $Ni_{30}Mn_{70}$ the H_{eb} is ∼-90 mT and ∼-6 mT, whereas for ∼ 35 ML $Ni_{50}Mn_{50}$/Ni(Co/)/$Cu_3Au(001)$, it is ∼-22 mT and 0 mT, in both cases at 140 K and 300 K for IP and OoP bilayers, respectively. The longitudinal MOKE measurements could be recorded down to the minimum available temperature (140 K), but polar MOKE measurements were only possible from 300 K upwards because of the high coercivities, higher than the maximum external magnetic field (±200 mT). From Fig. 4.14(a), one can see the temperature-dependent behaviour of H_C and H_{eb} for the IP sample. The loops are clearly shifted to the negative side of the magnetic field axis. The value of H_{eb} is more than twice to that of H_C at the minimum temperature (140 K). The IP exchange-biased loops are not of rectangular shape but rather tilted. At the blocking temperature (T_b), the temperature where EB finishes (here ∼420 K), the tilted shape of the hysteresis loops is changed to a more rectangular one. The reason for the tilted shape of the exchange-biased loops could be a locally different coupling strength at the interface of the bilayer. The higher the difference between the strength of the local uncompensated spins is, the more the loops are tilted. From a careful look at the IP loop of 400 K (dark green colour), one can see that it is slightly shifted to the right side, providing small positive EB. This kind of small positive EB just below T_b is observed for most of the IP samples with Ni concentration between ∼38% and ∼28%, which will be described and discussed later. As the temperature is increased, H_{eb} is decreased for both IP and OoP samples, as expected. For the same temperature, e.g., at 300 K, the value of H_C for the OoP case is much higher than for the IP one, while the H_{eb} values are comparable for both cases.

Fig. 4.15 shows the temperature-dependent evolution of H_C and H_{eb} for samples with different concentrations but similar thickness (∼32 ML) of Ni_xMn_{100-x} in contact with IP (Fig. 4.15(a)) and OoP magnetized Ni (Fig. 4.15(b)). For all IP samples, the H_C versus temperature curves exhibit a maximum which shifts towards higher

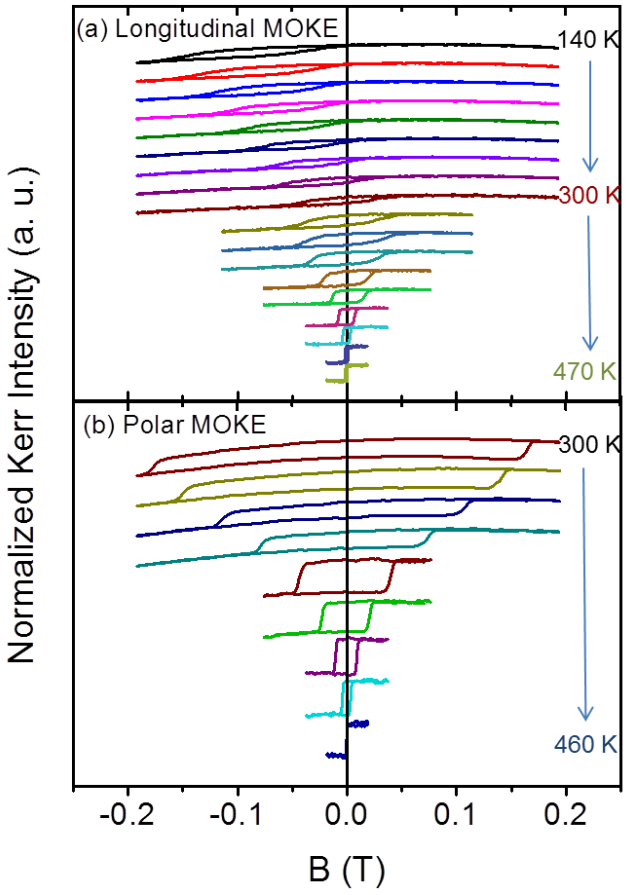

Figure 4.14: Normalized magnetic hysteresis loops for (a) ∼35 ML $Ni_{30}Mn_{70}$/12.3 ML Ni/∼2 ML Co/Cu_3Au(001) measured with longitudinal MOKE and (b) ∼35 ML $Ni_{30}Mn_{70}$/12.3 ML Ni/Cu_3Au(001) measured with polar MOKE at different temperatures.

temperatures with decreasing Ni concentration. All the IP samples with thicknesses from ∼16 to ∼50 ML for Ni ∼ 22%, including the one shown in Fig. 4.15(a), show two peaks in their $H_C(T)$ curves, one at lower temperature with a large H_C, and a second one at higher temperature with a smaller H_C. Due to the higher H_C with tilted loop shape, it was not possible to measure the IP $Ni_{22}Mn_{78}$ samples below 350 K with thickness smaller than ∼33 ML. The higher H_C could be suppressed by a larger thickness of $Ni_{22}Mn_{78}$, as observed for ∼50 ML $Ni_{22}Mn_{78}$. Also T_{AFM} is systematically shifted towards higher temperatures for decreasing Ni concentration, where a smaller difference between T_b and T_{AFM} is observed. This increase of T_{AFM} for the IP case is similar to the Fe concentration-dependent results found in the systems FeMn/Co/Cu(001) [37] and (Co)/Ni/FeMn/Cu(001) [43]. H_{eb} at fixed temperature as well as T_b increase with decreasing Ni concentration. The peak in $H_C(T)$ is close to T_b for $Ni_{49}Mn_{51}$, whereas T_b is related to the second, less prominent peak in $Ni_{22}Mn_{78}$. For $Ni_{28}Mn_{72}$ and $Ni_{38}Mn_{62}$, the peak in $H_C(T)$ occurs at lower temperatures than T_b. For 28 and 38% Ni in Ni_xMn_{1-x}, near the $H_C(T)$ peak, H_{eb} has small value for a few increasing temperature points and then switches through zero to small positive values just below T_b, where it vanishes to zero. This behaviour is shown in the inset, which is a zoom-in along the vertical axis for some temperature points of Fig. 4.15(a). The existence of positive EB just below T_b in a small temperature range is similar to the results found for $Ni_{81}Fe_{19}/Ir_{20}Mn_{80}$ bilayers [134]. For all IP samples, an abrupt increase in H_{eb} occurs at the peak in $H_C(T)$ (for $Ni_{22}Mn_{78}$, this peak is the prominent one).

For the OoP case (Fig. 4.15(b)), the peak in the $H_C(T)$ curves is only observed for equiatomic NiMn. For all other curves, H_C rises to values higher than the avail-

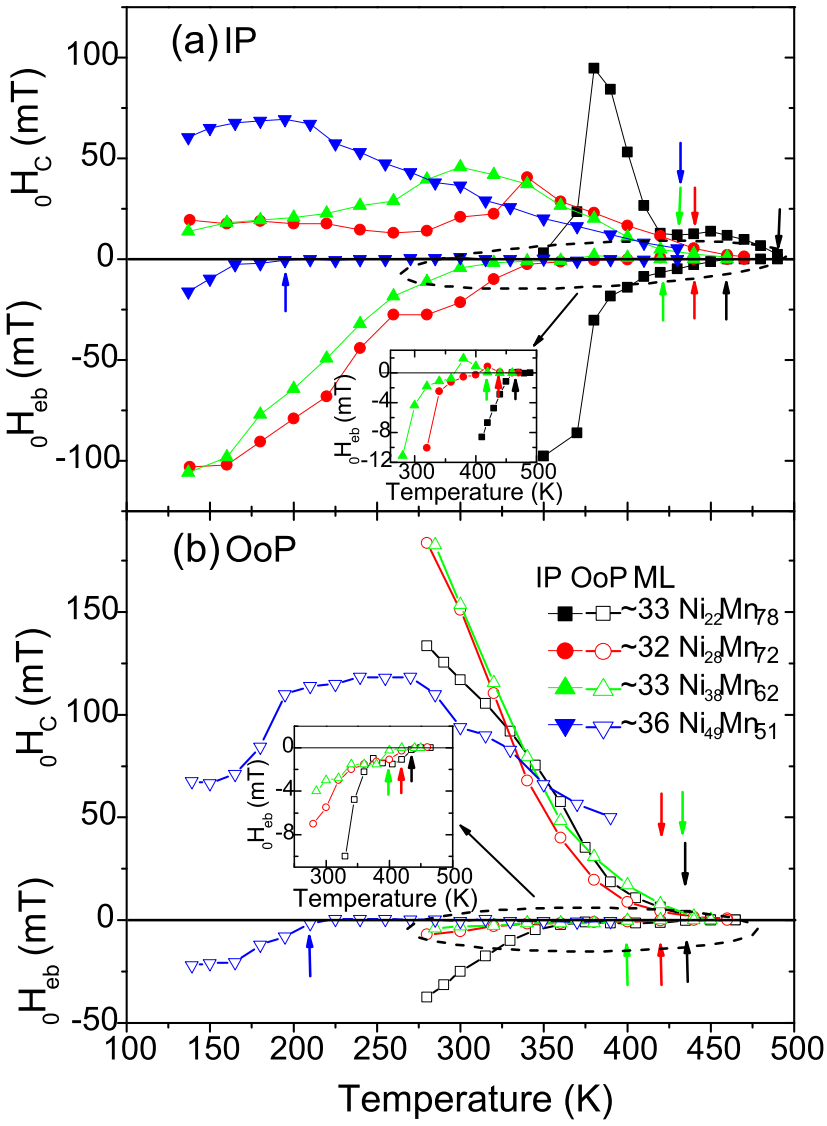

Figure 4.15: Temperature dependence of the coercivity (positive field axis) and the exchange bias field (negative field axis) for nearly equal thicknesses and different concentrations of Ni_xMn_{100-x} for (a) coupling with an in-plane magnetized ∼12 ML Ni/∼2 ML Co film on $Cu_3Au(001)$ and (b) coupling with an out-of-plane magnetized ∼12 ML Ni film on $Cu_3Au(001)$. The down arrows indicate T_{AFM}, and the up arrows T_b for the respectively coloured H_C and H_{eb} curves. For the determination of the blocking temperature, the two insets show a zoom-in of the three H_{eb} curves (a) for the IP and (b) for the OoP samples.

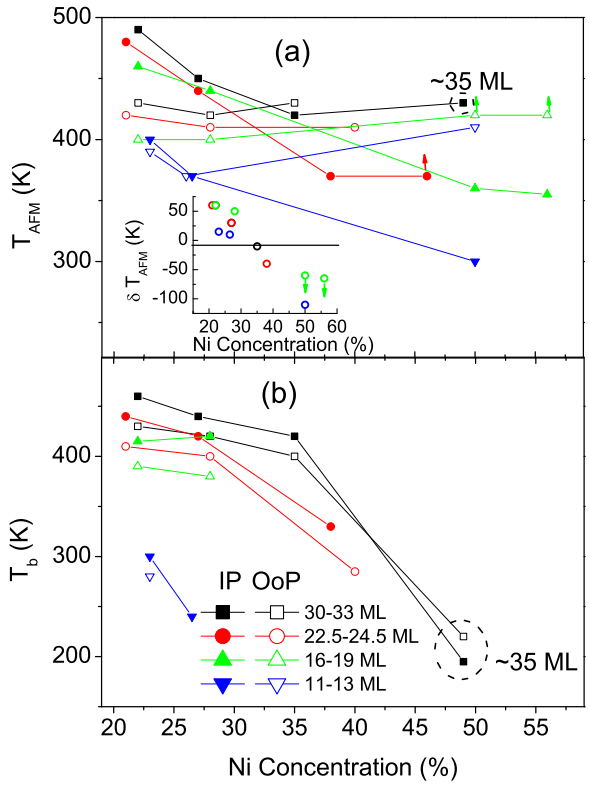

Figure 4.16: Concentration-dependence of (a) T_{AFM} and (b) T_b of Ni_xMn_{100-x} films of similar thicknesses coupled to IP and OoP Ni layers. The upward arrows indicate a higher value than shown of T_{AFM} which was not possible to determine due to a spin reorientation transition of Ni from OoP to IP direction for about equiatomic Ni_xMn_{100-x} films. The dashed circles around the black points for T_{AFM} and T_b shown in (a) and (b) respectively, just highlight that the Ni_xMn_{100-x} thickness is slightly higher than its other counterparts of the same group. The inset shows the difference between T_{AFM} of the Ni_xMn_{100-x} films coupled to IP and OoP magnetized Ni film (different colours represent the respective thickness of Ni_xMn_{100-x}, and the small green down arrows indicate higher than shown difference of T_{AFM}).

able magnetic field. T_{AFM} slightly changes by changing the Ni concentration. For equiatomic NiMn, the T_{AFM} for the three thickest NiMn films could not be determined because a spin reorientation transition of the under lying Ni film from OoP to IP occurs at about 410 K. For the OoP samples, T_b increases with decreasing Ni concentration. The small variation of T_{AFM} with Ni concentration for the OoP case is similar to the findings of Stampe *et al.* for the system Ni/FeMn/Cu(001) when the Fe concentration is changed in FeMn [127]. With decreasing temperature, the EB effect starts at a temperature T_b before the $H_C(T)$ peak is reached, if any, for all Ni_xMn_{100-x} films coupled to OoP magnetized Ni except for $Ni_{49}Mn_{51}$, where this effect is observed at about the maximum of H_C. Usually, EB starts at about the peak of $H_C(T)$ [49], but this is not always the case: for example, Maat *et al.* studied the IP and OoP EB in the system $(Co/Pt)_5$/(Co+CoO) and found that T_b occurs very close to T_{AFM} without any peak in $H_C(T)$ down to the minimum temperature of 10 K [135]. Like for the IP samples, also for the OoP samples H_{eb} very slowly decreases to zero with temperature. To demonstrate the determination of T_b, a zoom-in of $H_{eb}(T)$ on the vertical axis for the three samples above 250 K is shown in the inset of Fig. 4.15(b). Comparing the IP samples to OoP ones, one can see that at the same concentration and temperature, mostly higher values of H_{eb} and T_b are observed in the IP system except for the one sample with equiatomic concentration. Note that in Fig. 4.15(a), $Ni_{49}Mn_{51}$ has a slightly higher thickness (~36 ML) but is put together with the other films for the sake of completeness. Except for this film $Ni_{49}Mn_{51}$, the T_{AFM} of all the IP samples increases with decreasing the Ni concentration.

A systematic comparison of T_{AFM} and T_b versus Ni concentration for IP and OoP

samples of different Ni_xMn_{100-x} thicknesses is shown in Fig. 4.16(a) and (b), respectively. For all the studied Ni_xMn_{100-x} films with similar thicknesses, the T_{AFM} for the IP systems increases with decreasing Ni concentration, whereas only a slight change is observed for the OoP case. This is consistant with the reported study on FeMn coupled to IP [37], and OoP [127] FM layer when the Fe concentration is reduced. The lines connecting the T_{AFM}'s for several samples of similar thicknesses both in IP and in OoP directions cross each other. This crossing occurs for all samples of thicknesses ranged from ∼12 to ∼32 ML. In the inset of Fig. 4.16(a) the difference between the IP and the OoP T_{AFM} is shown. Same colours of the data points represent the corresponding thicknesses of Ni_xMn_{100-x}. It is clear from this inset that a transition in T_{AFM} for the IP and the OoP coupled systems occurs between Ni concentrations of ∼28% and ∼35%. Above ∼35% of Ni, T_{AFM} for the OoP samples is higher than for the IP samples, and below ∼28% of Ni, T_{AFM} for the IP samples is higher than for the OoP ones. This kind of crossing could not be observed for T_b except for the thickest NiMn films exhibiting EB with slightly higher T_b for the OoP sample than for the IP one at the equiatomic concentration (Fig. 4.16(b)). For all other Ni concentrations, T_b is always higher for the IP case than for the OoP one (Fig. 4.16(b)).

For the IP bilayers, the increase in T_{AFM} with decreasing Ni concentration is in line with the findings of Honda *et al.*, where an increased T_{AFM} (from 420 K to 470 K) is found for γ-Ni_xMn_{100-x} in bulk polycrystalline form when the Ni concentration is decreased from 40 to 10% [5]. Owing to its non-collinear $3Q$ spin structure [35, 36, 136], FeMn has similar properties as we found for Ni_xMn_{100-x}, which we assume to have a non-collinear spin structure similar to FeMn. In Refs. [37, 43], a similar increase in T_{AFM} by decreasing Fe concentration for IP measurements is also found for FeMn. Like in our result for Ni_xMn_{100-x}, only a small variation in T_{AFM} is observed for OoP coupling between Ni and FeMn when changing the Fe concentration in FeMn [127].

Fig. 4.17 shows temperature-dependent H_C and H_{eb} for different thicknesses of $Ni_{28}Mn_{72}$ in contact to Ni magnetized in IP (Fig. 4.17(a)) and OoP direction (Fig. 4.17(b)), respectively. To avoid an alloying of AFM and FM layers at the interface, we did not take measurements above 490 K in some IP samples, therefore only lower limits for T_{AFM} can be given. For the IP case, all the samples (except with the ∼13 ML $Ni_{28}Mn_{72}$) have a peak in their H_C versus temperature curves. Except for the thinnest sample (∼13 ML $Ni_{28}Mn_{72}$), only lower limit could be obtained for T_{AFM} (∼440 K), which is represented Fig. 4.17(a) by vertical down arrows to which horizontal arrows are connected indicating that the T_{AFM}'s of these samples could be higher. The peak temperature T_p (the temperature at which H_C has a peak) shifts towards higher temperatures as the $Ni_{28}Mn_{72}$ thickness is increased. For the thickest two samples, T_p occurs at similar temperatures. There seems to be no considerable relation between the H_C(T) peak width and the $Ni_{28}Mn_{72}$ thickness. The size (height) of the peak first increases and then decreases as the $Ni_{28}Mn_{72}$ layer is made thicker. The decrease in the $H_C(T)$ peak temperature, and increase (for the three thicker samples only) in the $H_C(T)$ peak height with increasing $Ni_{28}Mn_{72}$ thickness is similar to the results reported by Ali *et al.* for $Ir_{25}Mn_{75}$ [129]. The inset of Fig. 4.17(a) shows the magnified area of the figure indicated by the dashed ellipse for a closer look at H_{eb} close to T_b. A small positive EB just below T_b can be seen in all $H_{eb}(T)$ curves. T_b's are represented by respectively coloured up arrows. For $Ni_{28}Mn_{72}$, a comparison of thickness-dependent T_p's and T_b's curves for IP samples is given in the inset of Fig. 4.17(b). Nearly constant T_b for thicknesses ≥18 ML suggests that the T_b tends to saturate. The T_p is always

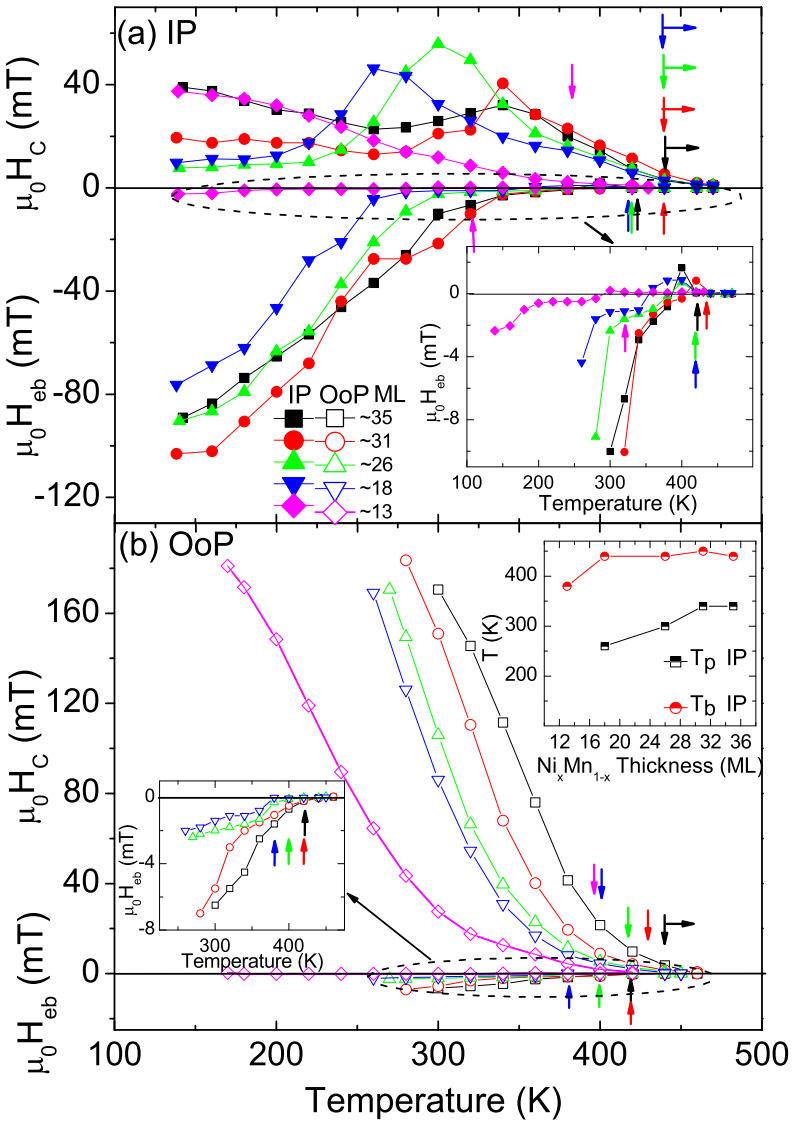

Figure 4.17: Temperature-dependent coercivity (positive field axis) and exchange bias field (negative field axis) for different thicknesses of (a) IP magnetized bilayer $\sim Ni_{28}Mn_{72}$/~12 ML Ni/~2 ML Co/$Cu_3Au(001)$, and (b) OoP magnetized bilayer $\sim Ni_{28}Mn_{72}$/~12 ML Ni/$Cu_3Au(001)$. The down and up arrows of respective colour represent T_{AFM} and T_b, respectively. The inset of (b) shows the Ni_xMn_{100-x} thickness-dependent peaking and blocking temperatures. The other two insets of (a) and (b) show a zoom-in of the H_{eb}(T) curves of the areas represented by ellipses.

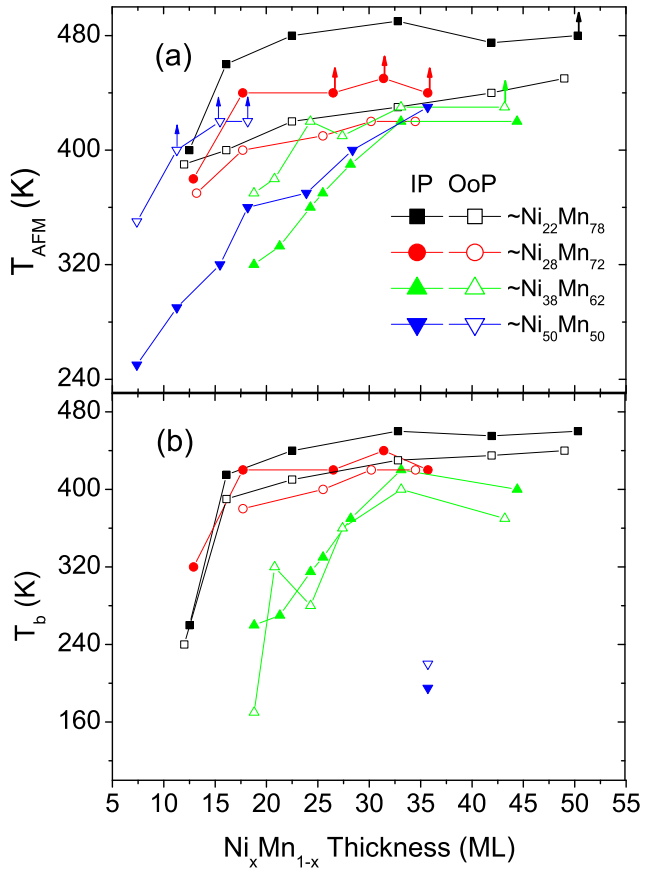

Figure 4.18: (a) T_{AFM} and (b) T_b for Ni_xMn_{100-x} thickness-dependent IP and OoP coupled samples. Small arrows in (a) indicate that the T_{AFM} could be higher than the shown value.

lower than the corresponding T_b. The difference between T_p and T_b decreases by increasing the thickness of $Ni_{28}Mn_{72}$. This is very similar to the results obtained by Ali *et al.* for $Ir_{25}Mn_{75}$ [129] and Leighton *et al.* for MnF_2/Fe [137].

For the OoP samples (Fig. 4.17(b)), again due to external magnetic field limitations and larger H_C's, lower temperature measurements were not possible except for the thinnest ∼13 ML $Ni_{28}Mn_{72}$ film. The T_{AFM} increases by increasing the $Ni_{28}Mn_{72}$ thickness. H_{eb} is observed with much higher H_C than in the IP case. No peak in the $H_C(T)$ curves is found for the studied temperature range. Perhaps the peaks occur at much lower temperatures out of our access. The difference between T_{AFM} and T_b is very small for the thicker samples. This is very similar to the results for AFM CoO in Ref. [135]. For IP and OoP samples, a very similar trend for H_C, H_{eb}, T_p (only fo IP), and T_b is observed for all thicknesses with Ni concentration of 38% (see appendix Fig. A.1). In Fig. 4.17, the main differences between the IP and the OoP samples are: (i) the H_C for the OoP samples is much larger than for the IP, (ii) the H_{eb} for the IP samples is much larger than for the OoP, and (iii) a peak in coercivity is observed for the IP samples which is absent for the OoP samples within the measured temperature range. Another inset of Fig. 4.17(b) gives a zoom-in to make visible the determination of T_b represented by the respectively coloured up arrows.

Fig. 4.18 shows a summary of Ni_xMn_{100-x} thickness-dependent T_{AFM}'s and T_b's of various Ni concentrations for IP versus OoP bilayers. Filled symbols are used for the IP, open symbols for the OoP bilayers. From the upper panel (Fig. 4.18(a)), it is evident that for Ni concentration of ∼22% and ∼28%, the IP samples have higher T_{AFM}'s than the OoP ones, whereas the reverse is true for ∼38% and ∼50% Ni. The arrows on some points indicate that these data points are only lower limits for T_{AFM}, which could be

even higher. A summary of T_b's is given in the lower panel (Fig. 4.18(b)). The T_b is generally higher for the IP samples than for the OoP, whereas for equiatomic NiMn, T_b is higher for the OoP sample than the IP ones.

4.4.2 Discussion

From the very similar features in the MEED oscillations, as well as identical LEED patterns and perpendicular lattice constants obtained from LEED I(V) for Ni when it is grown either directly on the bare substrate ($Cu_3Au(001)$) or on ∼2 ML Co/$Cu_3Au(001)$ (Fig. 4.4 and Fig. 4.5, it is very likely that Ni has a similar morphology in both cases. Therefore, any influence on the Ni_xMn_{100-x} structure due to the presence of the Co layer underneath the Ni film can be discarded. Our results for equiatomic NiMn films on $Cu_3Au(001)$ (section 4.1.3) showed a tetragonal distortion or strain (c/a ratio ∼5.3%) compatible with an epitaxial c-axis growth of fct bulk NiMn. Therefore, a similar strain is expected when Ni_xMn_{100-x} is grown on Ni/$Cu_3Au(001)$ or on Ni/∼2 ML Co/$Cu_3Au(001)$, which we associate with the observed change in the magnetic properties of Ni_xMn_{100-x} in our bilayers. It has been recently experimentally observed that there is a significant effect of strain on the magnetic properties of epitaxially grown antiferromagnetic Heusler alloy Fe_2VSi films [138] and $YMnO_3$ films [139]. A clear dependence of T_N on c/a has been observed when this ratio is varied from 0.987 to 0.998 at room temperature. The tensile epitaxial strain has been found to increase T_N to 193 K, 70 K higher than that of the unstrained bulk material [138]. Similarly, in Ref. [139], the variation of the lattice constant ratio c/a resulted in a marked shift in the T_N for $YMnO_3$. Thus it is plausible in our system that the concentration-induced strain in Ni_xMn_{100-x} grown on 12–13 ML Ni/∼2 ML Co/$Cu_3Au(001)$ plays a role in changing its magnetic properties.

Along with a brief calculation, Kawarazaki *et al.* have provided the first direct experimental evidence for a $3Q$ spin structure for an fcc antiferromagnetic $Ni_{28}Mn_{72}$ alloy [48]. Like in Ref. [48], it is very likely that some Mn moments, depending on their near-neighbor atomic configuration and the local concentration, deviate from the right directions of the $3Q$ alignment, since our sample is also a disordered alloy for other than equiatomic concentrations. However, based on the $3Q$-like spin structure of Ni_xMn_{100-x}, we propose the following model (shown in Fig. 4.19) to explain our results described above in this section: We suggest that the $3Q$-like spin structure of Ni_xMn_{100-x} deviates, driven by composition-dependent strain [132], from a more-OoP to a more-IP direction when decreasing the Ni concentration from ∼50 to ∼20%.

Fig. 4.19(a) shows a schematic illustration of the possible $3Q$-like spin structure of Ni_xMn_{100-x}. The in-plane component of the surface atom spins in extended flat terraces is compensated, whereas the OoP spin component is not. In the upper (lower) terrace of Fig. 4.19(a), the entire surface spins are pointing up (down), forming a layer-wise uncompensated spin component in the OoP direction. Depending upon the chemical composition of Ni_xMn_{100-x}, the spins could be along more-OoP or more-IP directions. Fig. 4.19(b) represents a possible spin configuration of the antiferromagnetic layer in a $3Q$-like spin structure at step edges viewed from the top. Light and dark coloured areas indicate the next-level atomic interface planes. Ellipses at the step edges represented by dashed lines indicate regions in which the IP components of the antiferromagnetic spins do not cancel. Fig. 4.19(c), which is the basis of the model, shows the situation when the spins are tilted towards more IP direction by decreasing the Ni concentration

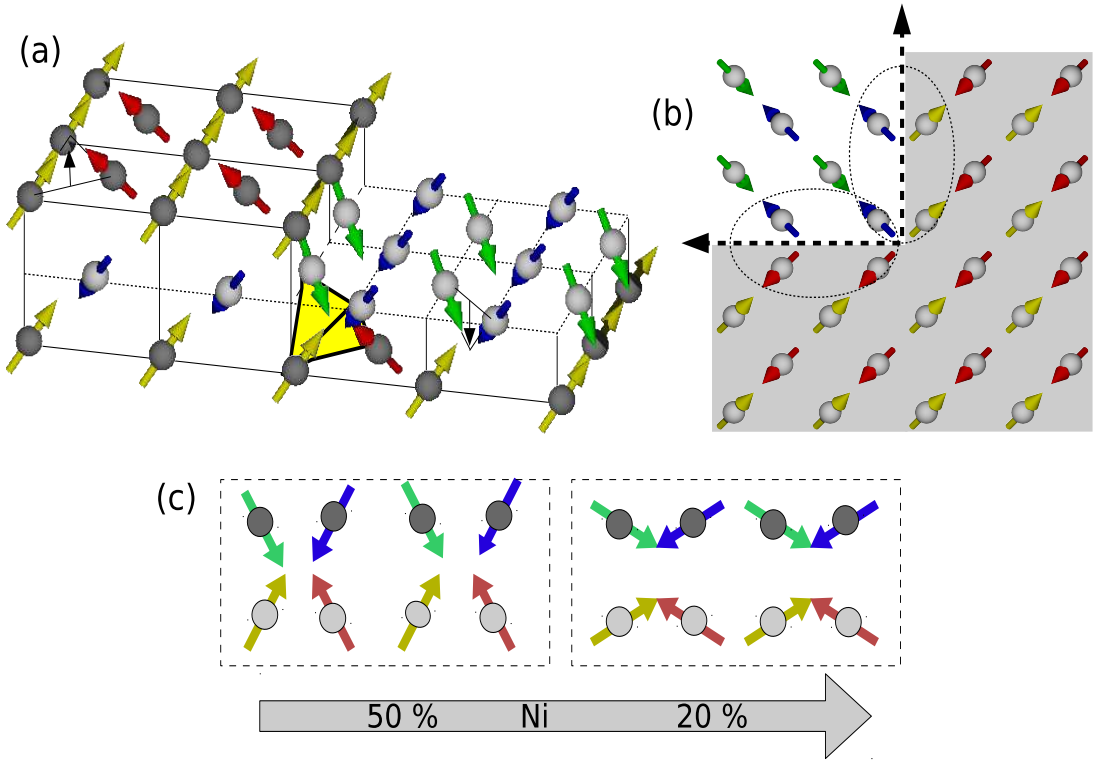

Figure 4.19: (a) Schematic drawing of a non-collinear 3-dimensional ($3Q$-like) spin structure of Ni_xMn_{100-x}. The different colours of spins only show their different orientations. The tetrahedron connected by dark lines and filled yellow space shows the magnetic unit cell of Ni_xMn_{100-x}. Within one layer, all the IP spin components are compensated along the extended terraces, but the OoP not. (b) Top view of the spin structure: the dashed ellipses show the uncompensated IP spin components at the step edges. (c) The proposed change of the non-collinear spin structure of Ni_xMn_{100-x} from more-out-of-plane to more-in-plane direction upon decreasing the Ni concentration from ∼50 to ∼20%. The dark gray (light gray) balls represent the top (second from top) layer atoms.

from ∼50 to ∼20%.

In the previous section, it is discussed that the equiatomic ordered state of NiMn has most probably a non-collinear spin structure such that its spins make a very small angle with the OoP direction, where it has a large OoP (small IP) component and a small magnetic anisotropy. Due to the latter, only an enhancement of H_C is observed which is almost twice for the OoP coupling than for the IP coupling for all temperatures and thicknesses, and therefore H_{eb} is only observed at the thickest equiatomic NiMn film (Fig. 4.13(b) and Fig. 4.15(b)). We suggest that decreasing the Ni concentration rotates the AFM spins from more-OoP towards more-IP direction associated with an increased magnetic anisotropy energy (MAE) (Fig. 4.19(c)). In the assumed $3Q$-like spin structure of Ni_xMn_{100-x}, a larger IP uncompensated spin component at the step edges of islands is expected compared to the OoP component in the flat terraces (Fig. 4.19(b)) with reduced Ni concentration along with increased MAE. Consequently, due to stronger coupling strength, higher values of T_{AFM}, H_{eb} and T_b are obtained for the

IP coupling than for the OoP at lower Ni concentrations (Fig. 4.15-Fig. 4.18).

Besides the interfacial coupling strength, from our proposed model, it is also possible to explain the reason for the concentration-dependent cross-over of the T_{AFM} of Ni_xMn_{100-x} for the IP versus OoP coupling (Fig. 4.16). At lower Ni concentrations the increased number of the nearest neighbour Mn atoms gives rise to stronger averaged Mn-Mn interaction (J_{AFM}) which should be responsible for the high T_{AFM} irrespective of the IP and OoP direction. An answer to the question why T_{AFM} is higher for the IP coupling than for the OoP at lower value of x in Ni_xMn_{100-x} can be simply given by the supposedly modified spin structure of Ni_xMn_{100-x} in our proposed model. That is by decreasing x, the intrinsically rotated spin structure of Ni_xMn_{100-x} (more-IP) becomes more thermally stable when coupled to an IP-magnetized Ni film than to an OoP one. By saying this, we mean that after coupling with the IP Ni layer, the intrinsically more-IP Ni_xMn_{100-x} spin structure is compelled to be further or even completely directed along the IP direction at the interface. Here Ni_xMn_{100-x} is thermally more stable compared to the case when it is coupled to the OoP Ni, where its spin structure deviates away from the intrinsic (more-IP) direction. A converse situation is supposed to occur for the equiatomic concentration where NiMn has higher T_{AFM} when coupled to the OoP FM layer than to the IP (Fig. 4.13 and Fig. 4.17(a)). After coupling with an OoP Ni layer, the intrinsically more OoP $Ni_{50}Mn_{50}$ spin structure is compelled to be further or even completely directed along the OoP direction. Here $Ni_{50}Mn_{50}$ is more thermally stable compared to the case when it is coupled to the IP Ni where its spin structure is deviated away from the intrinsic (more-OoP) direction. From this, we can speculate that Ni_xMn_{100-x} is thermally more stable when its spins are aligned along its intrinsic equilibrium spin structure. Our finding of higher T_{AFM} in OoP coupling than in the IP for equiatomic NiMn can be attributed to its distorted $3Q$ spin structure, as has been suggested in Ref. [127] for FeMn [43].

Our findings can be further discussed with the help of Refs. [43, 127]. Previously, for (Co/)Ni/FeMn/Cu(001) the higher value of T_{AFM} in the OoP direction than in the IP direction had been attributed to the higher coupling strength in the former case than in the latter [43]. However, in an experiment by Stampe *et al.*, the interface roughness of Ni/FeMn/Cu(001) bilayers has been modified by annealing the Ni layer before the FeMn layer deposition [127] which should have resulted in an increased number of OoP uncompensated spin components due to the extension of the flat terracess. This experiment has been performed only for equiatomic FeMn coupled in OoP direction with Ni/Cu(001) and resulted in enhancement of H_C and H_{eb}, whereas the T_{AFM} was found unchanged. Also, for $Ni_{50}Mn_{50}$/Ni/(Co/)/Cu_3Au(001) in the previous section, similar results as in Ref. [43] for (Co/)Ni/FeMn/Cu(001) are obtained and explained in terms of either a higher interfacial coupling strength or/and a more thermally stable $Ni_{50}Mn_{50}$ spin structure when coupled to Ni magnetized in OoP direction than in IP. An exchange coupling at the interface depends on the number of FM and AFM spins as well as the orientation between them, i.e., $E_{eff.} = -2\sum_{i<0}^{n} J_{ij} s_i.s_j$ [15], where J_{ij} is the exchange constant and s_i and s_j are the FM and AFM spins, respectively. This means that keeping fix the direction of the uncompensated spins and varying only their number, may not contribute to T_{AFM}, although it increases the interfacial coupling strength as has been observed in Ref. [127]. To see whether there is any influence of the interfacial coupling strength on T_{AFM}, we show in Fig. 4.20, the results for the thinnest studied samples for similar Ni_xMn_{100-x} thicknesses with no or very small EB.

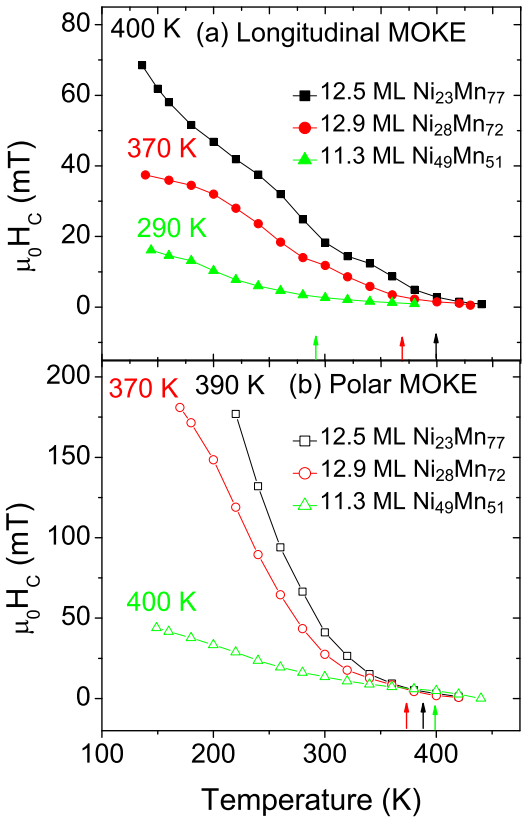

Figure 4.20: Temperature dependence of the coercivity for similar thicknesses of Ni_xMn_{100-x} grown on (a) in-plane-magnetized ∼12 ML Ni/∼2 ML Co/$Cu_3Au(001)$ and (b) out-of-plane magnetized ∼12 ML Ni/$Cu_3Au(001)$. The arrows represent the T_{AFM} of Ni_xMn_{100-x} given in the respectively coloured numbers.

Here the number as well as the direction of AFM spins (according to our proposed model) is changed by changing the AFM alloy composition. For IP case (Fig. 4.20(a)), H_C and T_{AFM} both increase with decreasing Ni concentration, whereas for the OoP case (Fig. 4.20(b)), $H_C(T)$ increases but T_{AFM} has no clear trend as the Ni concentration is decreased. This is apparently very similar to the results reported for FeMn coupled to OoP Ni [127]. But in our case (Fig. 4.20), along with the number and direction of the AFM spins, another factor, namely the magnetic anisotropy, also changes (increases) when decreasing Ni concentration. Therefore, the enhancement of coercivity in both IP and OoP direction could be either due to any or all of these three changed factors, i.e, the number and direction of AFM spins, and the magnetic anisotropy of the AFM. Similarly, we cannot conclusively say which of these three mentioned factors contribute to the differently changing behaviour of T_{AFM} in both IP and OoP coupling directions.

Our results seem to be the experimental verification of theoretical predictions by Mitsumata *et al.*, where they have investigated the spin structure of FM and Mn-based AFM bilayers, and proposed the mechanism of the exchange bias field within the framework of the classical Heisenberg model. A collinear spin structure formed in an ordered $L1_0$-type AFM Mn-based alloy has been reported to result in only the enhancement of coercivity of the ferromagnetic layer without any EB [66]. On the other hand, a Mn-based binary alloy composed of a disordered γ-phase antiferromagnetic layer showed a non-collinear spin structure, caused by the geometric frustrations in the AFM layer, which is responsible for the magnetization loop shift after coupling with an adjacent FM layer [66].

Within the domain of our model, we can discuss our data with the help of Malozemoff's perpendicular [26, 140] as well as Mauri's planar domain wall model [27] for the AFM layer in FM/AFM exchange-biased systems. At one side, in Mauri's domain wall model, the AFM layer thickness at which H_{eb} appears is said to be the point

where the AF layer is able to accommodate a planar domain wall of typical width ∼200 Å[141]. However, our results for the IP coupling show that the onset of biasing occurs at ∼12 ML (∼22 Å) below 260 K, which is too small to accommodate such a planar domain wall within the AFM layer. Therefore, it can be inferred that planar domain walls may not be responsible for exchange bias in our system; rather the perpendicular domain walls in the AFM layers seem to appear. This could be one of the plausible explanations as no such thickness restriction applies. This would be a similar explanation as has been reported for $Ir_{25}Mn_{78}$ [141]. However, on the other side, some of the thickness-, and concentration-dependent features of our system, e.g., saturation of T_b and T_{AFM} (Fig. 4.15–Fig. 4.18) favour the existence of Mauri's planar domain wall [27]. The planar domain wall width may not be considered constant (∼200 Å), as like any FM domain wall, it varies due to the two opposing energies that create it: the magnetocrystalline anisotropy energy and the exchange energy, both of which tend to be as low as possible so as to be in a more favourable energetic state. The anisotropy energy is lowest when the individual magnetic moments are aligned with the crystal lattice axes thus reducing the width of the domain wall. The exchange energy is reduced when the sublattice magnetic moments of an AFM are aligned parallel to each other, and thus makes the wall thicker. In the end an equilibrium is reached between the two, and the domain wall's width is set as such. In Malozemoff's perpendicular and in Mauri's parallel domain wall models, the critical thickness of the AFM layer for the onset of EB is determined by the magnetic anisotropy energy in the AFM layer. A large K_{AFM} directly reduces the critical thickness of AFM to establish EB. The well-known domain wall width is given by $\delta_w = \pi\sqrt{A_{AFM}/K_{AFM}}$ [26, 27, 28, 76], where A_{AFM} is the exchange stiffness and is given by $A_{AFM} \sim J_{AFM}/a_{AFM}$, where J_{AFM} and a_{AFM} are the exchange and lattice constants, respectively, in the AFM layer. Considering A_{AFM} as constant for both IP and OoP directions at constant Ni concentration in Ni_xMn_{100-x}, higher K_{AFM} will reduce the domain wall width, whether it is parallel or perpendicular. The reduction of the parallel domain wall width means that the thickness required to establish EB gets smaller. It has been reported that numerical calculations suggest that the reduction of critical thickness for the onset and saturation of H_{eb} is influenced by the spin structure in the AFM layer [67]. The critical thickness is proportional to the AFM domain wall width, and thinner AFM domain walls are obtained in the non-collinear spin structure of the Mn-based AFM layer as compared to ordered $L1_0$-type layer with the AF-I spin structure [67]. This very much supports our model since for the IP coupled part, for which we assume a more non-collinear $3Q$-like spin structure with larger IP component than the OoP one when lowering x in Ni_xMn_{100-x}, we get H_{eb} at smaller thicknesses of the AFM as compared to higher x values (see for example, Fig. 4.18). The only disagreement is that Mitsumata *et al.* assumed an AF-I spin structure (with spins along the c-axis) for the ordered $L1_0$-type AFM layer, whereas we suppose that this spin structure for our AFM film could be still three-dimensional, but with spins looking more towards the OoP direction. The OoP case may exhibit a similar behaviour of getting H_{eb} saturation with smaller Ni_xMn_{100-x} thickness but one cannot say this for sure as it was not possible to see EB at lower temperatures due to the external magnetic field limitations. Recently, Mitsumata *et al.* have generalized their work and theoretically proved that the case of an AFM domain wall might not be considered equivalent to that of the FM ones, and that the AFM domain wall width could possibly be significantly smaller than that of the FM [68]. The AFM thickness required to establish EB could be about $1/\sqrt{3}$ times smaller for

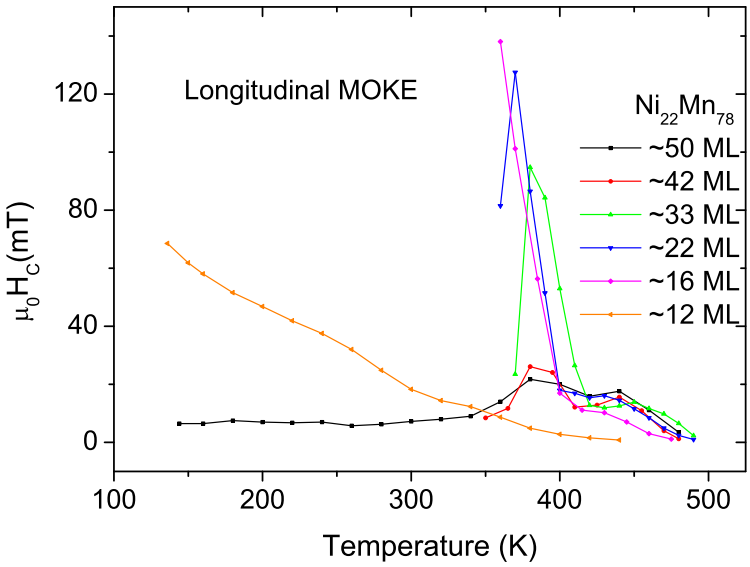

Figure 4.21: Temperature-dependent coercivity of $Ni_{22}Mn_{78}$ grown on in-plane-magnetized ∼12 ML Ni/∼2 ML Co/Cu_3Au(001).

any kind of AFM material having non-collinear spin structure as compared to the ones with collinear spin structure [68]. Also, for both IP and OoP cases in our study, the H_{eb} and T_b are saturated at much lower thicknesses of Ni_xMn_{100-x} with the smallest Ni concentration (∼ 20%) (Fig. 4.18(a) and (b)). For example, H_{eb} and T_b are both saturated at ∼32 ML $Ni_{22}Mn_{78}$ (∼6 nm), which is much smaller than the reported value of 25–35 nm [5] and >20 nm [55] (only for H_{eb} saturation) for polycrystalline equiatomic NiMn. The discussion above favours an idea of the coexistence of the perpendicular and the planar domain walls within the AFM layer.

It is important to mention that the planer domain wall does not need to be a complete "wall"like in ferromagnets; it could also describe the local twisting of a vertical spring connecting pinned uncompensated moments sitting in some depth in the AFM layer and rotating uncompensated moments at the interface to the FM layer.

The peak in coercivity close to the temperature where H_{eb} starts to increase significantly (Fig. 4.15(a)) is intuitively simple to understand. In the case of an AFM layer with small anisotropy, when the FM spins rotate, they drag most of the AFM spins, hence increasing the FM coercivity. For a large AFM anisotropy at lower temperatures and lower Ni concentrations in our proposed model, the FM layer decouples from the AFM layer because it cannot drag the AFM pinned spins, consequently an exchange bias effect comes into action on the cost of the reduction of H_C. A result of the influence of the anisotropy on H_C is the peak which is often found close to T_b [21]. This kind of peak is also observed in some other systems, for example in Refs. [128, 129, 130, 131]. In our system (Fig. 4.15(a)), as the anisotropy of the AFM decreases either due to increasing temperature or increasing the concentration of Ni in Ni_xMn_{100-x}, the FM is able to drag more and more AFM spins, thus increasing the coercivity. Just below T_b the pinning of the Ni_xMn_{100-x} pinned spins becomes very weak, therefore they can merely hinder the FM rotation, and hence the EB tends to vanish.

We studied six bilayer samples with different thicknesses of $Ni_{22}Mn_{78}$ varying from ∼50 to ∼12 ML. $H_C(T)$ of these samples for IP coupling is shown in Fig. 4.21. For the thickest five samples two peaks in $H_C(T)$ are observed. The one at higher tem-

peratures becomes less prominent as the thickness of $Ni_{22}Mn_{78}$ decreases from ∼50 to ∼16 ML, and completely disappears at ∼12 ML $Ni_{22}Mn_{78}$ (also shown in Fig. 4.20). This $Ni_{22}Mn_{78}$ thickness-dependence of the second $H_C(T)$ peak (at high temperatures) indicates the existence of a Mauri planar domain wall which could not be sustained due to decreased magnetic anisotropy at relatively low $Ni_{22}Mn_{78}$ thicknesses. For Ni concentrations of ∼28% and ∼38%, where the AFM layer has a smaller MAE compared to a Ni concentration of ∼22%, a kind of incomplete domain wall could be formed which could give rise to the small value of H_{eb} and its steady decrease to zero just below T_b. The small positive EB just below T_b in a small temperature range (Fig. 4.15(a) and Fig. 4.17(a)) can be explained by what has been speculated for $Ni_{81}Fe_{19}/Ir_{20}Mn_{80}$ bilayers by Mishra *et al.* [134], that there exist some unusual minority but strongly pinned species of spins in the opposite direction to that of the usual pinned spins. These minor species of strongly pinned spins remain pinned at higher temperatures than the usual pinned spins. This speculation can also explain the steady decrease of H_{eb} towards zero. Before switching to a small positive value, a small nearly constant or very slowly decreasing negative EB is observed for all IP samples with Ni concentrations of ∼38% and ∼28% (insets of Fig. 4.15 and Fig. 4.17), indicating a competition between the two opposite exchange biases. A corresponding small kink in the $H_C(T)$ curve, at least for ∼18 ML $Ni_{28}Mn_{72}$, can be observed (Fig. 4.15(a)). The increased MAE of Ni_xMn_{100-x} by decreasing x to ∼22% overcomes the pinning strength of the minority species of spins responsible for small positive EB just below T_b. Therefore, no such kind of small positive EB is observed for $Ni_{22}Mn_{78}$. This result, along with the other results mentioned in this chapter, shows that the Ni (Mn) concentration plays a very decisive role in determining all the magnetic properties of Ni_xMn_{100-x} including its crystalline and spin structure. This is consistent with the previous concentration-dependent studies on bulk Ni_xMn_{100-x} crystal [65] and spin structure [42, 48, 66].

In the light of the above discussion, we can say that our rotating spin model associated with changes in the magnetic anisotropy by changing Ni concentration in Ni_xMn_{100-x}, is able to explain all of our results.

Chapter 5

Magnetic coupling between ferromagnetic Ni layers across an antiferromagnetic Ni_xMn_{100-x} layer

In the section 4.4 of previous chapter, after finding the right concentration of Ni (∼20%) in Ni_xMn_{100-x} to get higher value of H_{eb} as well as higher T_b in both IP and OoP bilayers, in this chapter the Ni_xMn_{100-x} layer with similar lower Ni concentration and different thicknesses is sandwiched between two FM layers, of which magnetization can be manipulated from OoP to IP direction. The aim is to further investigate the complex nature of EB, particularly to look for the location of the pinned uncompensated moment within the AFM layer responsible for EB which is usually considered to be located at the interface of the FM/AFM bilayers.

5.1 Results

All the hysteresis loops are measured by longitudinal and polar MOKE for IP and OoP magnetized FM layers, respectively, at both interfaces coupled to sandwiched AFM Ni_xMn_{100-x}. Whether grown on $Cu_3Au(001)$ with thicknesses of 12–13 ML (FM1) at the lower or on top of Ni_xMn_{100-x} with thickness of 21–25 ML (FM2) at the upper interface, the Ni has always OoP magnetization. Therefore 2–3 ML Co was deposited either under the bottom or on top of the top FM Ni layer to switch its magnetization from OoP to IP direction, making the total number of layers more than three. Despite this, we shall call our system 'trilayer'. From now on, mostly the lower and the upper FM layers will be respectively called as FM1 and FM2. The bilayers without field-cooling as well as the trilayers which are field-cooled before but not after the second OoP or IP FM (FM2) layer, will be termed as as-grown samples. For a comparative study of IP versus OoP coupling, every film, unless otherwise stated, has been deposited on the two halves of the substrate such that one half has an IP magnetization (n ML Ni_xMn_{100-x}/12–13 ML Ni/∼2 ML Co/$Cu_3Au(001)$) and the other half has an OoP coupling (n ML Ni_xMn_{100-x}/12–13 ML Ni/$Cu_3Au(001)$). 21–25 ML Ni is then evaporated as FM2 over the whole sample. Now on one half, the Ni magnetization at the lower interface is IP and the upper one is OoP; whereas on the other half, it is in OoP direction at both interfaces. The FM2 was either left with OoP magnetization or turned in to the IP direction by the deposition of another ∼3 ML Co. The corresponding schematic drawing is shown in Fig. 5.1 for the trilayer to elaborate the situation.

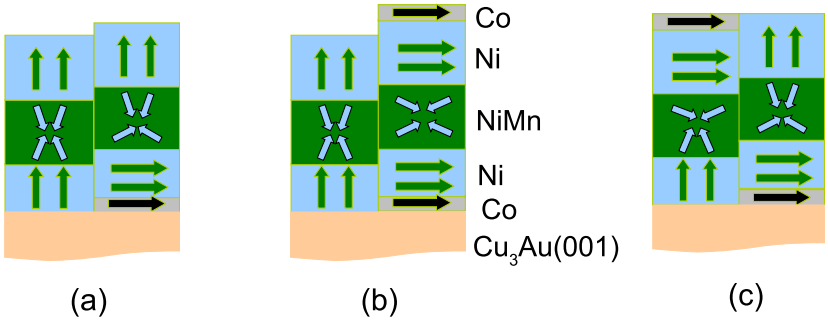

Figure 5.1: Schematic illustration of the three types of samples of FM2/AFM/FM1 trilayer system that have been prepared.

We will call the different configurations according to magnetization directions of the bottom and top FM layer: OoP-OoP (left part of Fig. 5.1(a) and (b)), IP-OoP (right part of Fig. 5.1(a)), IP-IP (right part of Fig. 5.1(b) and (c)), and OoP-IP (left part of Fig. 5.1(c)). All the measurements are done while increasing the temperature from lower to higher values (not the other way around). All the samples under study in this chapter were field-cooled (FC) (unless otherwise stated) in the FM layer magnetization direction of the respective probed interface. Samples were FC either in the presence of a positive or a negative external magnetic field to get parallel alignment of the two FM layers, or, where possible, in such a way that one of the layers is magnetized in the negative direction and the other in the positive (the upper and the lower FM layers are antiparallel to each other). Due to the limited external magnetic field and the large H_C of the OoP Ni layers, the loop of both FM layers in the OoP-OoP configuration could only be observed above a certain temperature. That is why OoP measurements are started from relatively higher temperatures compared to IP ones, where measurements are usually performed from the lowest available temperature (∼140 K). The accuracy for the thickness measurement of Ni_xMn_{100-x} is within the error of around ±1 ML, for that of Ni is sub-ML and, for concentration of Ni(Mn) in Ni_xMn_{100-x}, it is less than ±2%. In the following, the trilayer systems are first described with descending order of Ni_xMn_{100-x} thickness, and then discussed under topics of relevant physics involved.

5.1.1 Trilayer with thicker AFM (47 ML $Ni_{17}Mn_{83}$) layer

Fig. 5.2–Fig. 5.5 show the temperature-dependent hysteresis loops and the resultant H_C and H_{eb} curves for both FM1 and FM2 magnetized in IP and in OoP direction, respectively. The complete trilayer is grown before starting any measurements, no bilayer measurements are performed, i.e., no measurements are done until one half of the sample was prepared with AFM sandwiched between IP FM layers and the other half with OoP FM layers. All the times the sample is first heated up to above the T_{AFM} of the AFM layer and then field-cooled to minimum available temperature. The hysteresis loops are then measured from the minimum temperature for the IP case, whereas for the OoP case, from the temperature where the larger size of coercivity allowed to measure the loop with the available field of ± 200 mT. Fig. 5.2(a) shows the temperature-dependent normalized hysteresis loops when both FM layers are parallely magnetized in IP direction by the application of +10 mT external magnetic fields for FC to give a negative EB shift. With the application of -10 mT for FC, temperature-dependent hysteresis loops are also measured which provided positive EB shift (not

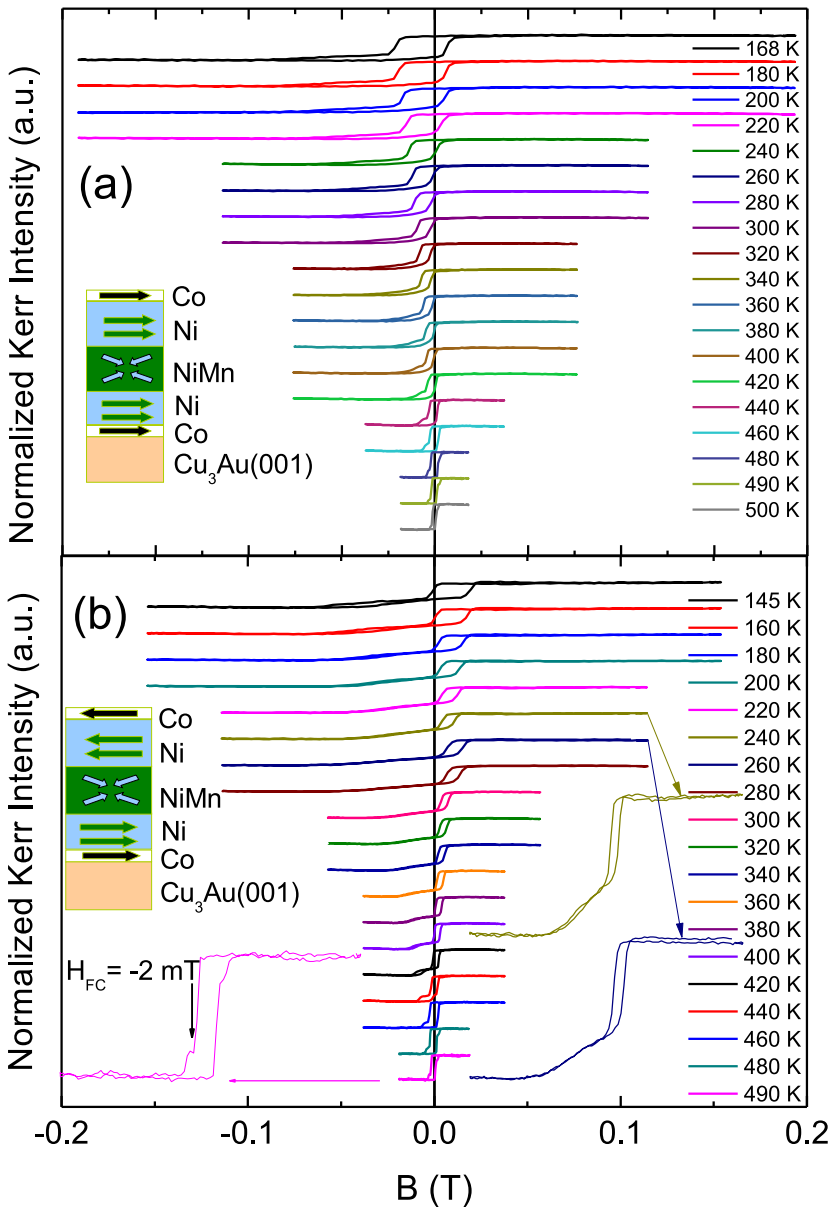

Figure 5.2: Normalized hysteresis loops for 3 ML Co/25 ML Ni/47 ML $Ni_{17}Mn_{83}$/12.9 ML Ni/2 ML Co/Cu_3Au(001) trilayer measured with longitudinal MOKE at different temperatures. (a) Both interfaces give negative exchange bias when field-cooled with +10 mT from 500 K, and (b) both interfaces give opposite exchange bias shifts: the lower one a negative due to previous field-cooling with +10 mT, and the upper one positive as it is field-cooled with -2 mT from 490 K. Zoom-in of two loops at the right bottom of (b) showing a small H_C at 240 K, and vanished H_C at 260 K. At the left bottom of (b) is shown a zoom-in of a loop taken at 490 K, indicating H_C value from where the sample was FC with -2 mT to get antiparallel alignment of the two FM layers.

shown). Fig. 5.2(b) is for the loops where a trick was applied such that both the FM layers were oppositely (antiparallely) magnetized during field-cooling, and provide one of the interfaces with a negative and the other with a positive EB shift. The FM2 had a smaller H_C (1.25 mT) than FM1 (2.6 mT); field-cooling was started from 490 K with -2 mT, only the FM2 is actually FC whereas the FM1 is already saturated from previous positive FC. Both the FM layers are now in antiparallel spin configuration, which by cooling through the T_b, gives opposite EB shift at both interfaces; positive at the upper interface and negative at the lower one. For the parallel spin configuration of both the FM layers, the EB shift towards negative field can be observed from the double loops (both loops in a double loop are shifted to the left side in Fig. 5.2(a)). Also, due to the antiparallel alignment of the FM layer's magnetization at both the interfaces, the negative (positive) shift due to EB at the lower (upper) interface is evident from the loops shown in Fig. 5.2(b). Because of the smaller (almost half) thickness of the FM2 layer, the EB and the H_C, both are larger for the lower interface than for the upper one in both cases.

If the two FM layers have parallel magnetization, the two loops arising from the lower and the upper interface are not well separated from each other for all temperatures below T_b (for example, Fig. 5.2(a)). For opposite FC (Fig. 5.2(b)), the two loops are very well separated. In the first case, the lower interface loops are more tilted with smaller signal and with higher H_C and H_{eb} than that of the upper one. In the case of oppositely magnetized FM layers, the lower FM layer (FM1) reduces its H_C to zero at 260 K till 280 K where the hysteresis curve looks like the one for any paramagnetic material but shifted towards negative field axis as shown in the zoomed-in (dark-blue) loop at the right bottom of Fig. 5.2(b). A zoomed-in loop at 240 K is also shown just above the 260 K loop, which has small coercivity. After 280 K till 400 K, a very slightly increased value of H_C (less than 1 mT) is somehow maintained constant, and then is slightly enhanced for a further few temperature points before it finally once again starts to decrease at 490 K (2.6 mT).

Fig. 5.3(a) shows the temperature-dependent curves for H_C's for the three cases. The H_C(T) and H_{eb}(T) curves look similar (within certain error) for the very same interface whether the system is FC with positive or negative magnetic field, giving rise correspondingly to negative or positive EB shift (parallel spin configuration at both interfaces). The lower interface exhibits almost twice the H_C than the upper one because it has half the thickness of FM1. Compared to the parallel spin configuration, the H_C is decreased for FM1 and FM2 as well as H_{eb}(T) is decreased for FM1 when they are oppositely magnetized with opposite EB (antiparallel spin configuration at the opposite interfaces). In Fig. 5.3(b), no clear peak in H_C(T) is observed for the upper as well lower interface. A very clear and relatively high peak in H_C(T) is observed for the IP magnetized bilayer system Ni_xMn_{100-x}/Ni/Co/Cu_3Au(001) with $\sim 20 \geq x \leq \geq 50$ as described and discussed in chapter 4. The AFM ordering temperature for all cases seems to be the same (around 500 K). H_{eb} is decreasing with increasing temperature and finishes at T_b but roughly remains very similar for the same interface (Fig. 5.3(b)). Because FM1 has half the thickness compared to FM2, the H_{eb} for the lower interface is almost twice to that of the upper interface as expected. T_b for the lower interface is ~30 K higher (~490 K) compared to the upper interface (~460 K). This could be due to either different roughness or slightly changed Ni (Mn) concentration at both interfaces.

Fig. 5.4(a) shows the temperature-dependent hysteresis loops when both FM layers

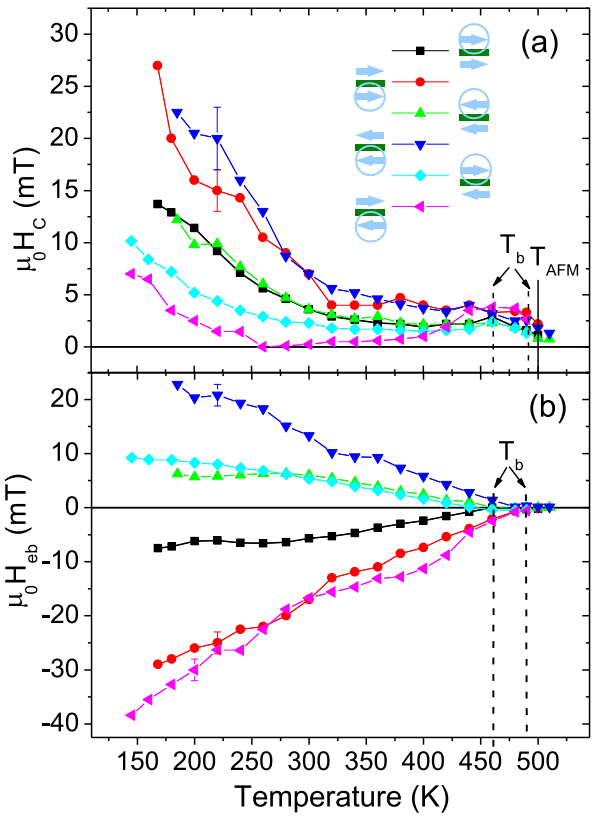

Figure 5.3: Temperature dependence of (a) coercivity and (b) exchange bias field for a 3 ML Co/25 ML Ni/47 ML $Ni_{17}Mn_{83}$/12.9 ML Ni/2 ML Co/Cu_3Au(001) trilayer measured with longitudinal MOKE. The different magnetization directions of the FM layers at the upper and at the lower interfaces are symbolically shown in front of the corresponding legend. The antiferromagnetic ordering temperature and the blocking temperature are indicated in (a) and (b), respectively. Note that for parallel magnetization of FM layers, there is an error in H_C and H_{eb} measurements of the lower interface as loops were not well separated below 400 K. Only one corresponding error bar per curve is shown to avoid overcrowd of the symbols.

are parallely magnetized in OoP direction by the application of +10 mT external magnetic field for FC to give a negative EB shift. With the application of -10 mT for FC, temperature-dependent hysteresis loops are also measured which provided positive EB shift (not shown). Fig. 5.4(b) is for the loops when both the FM layers are oppositely (antiparallely) magnetized to provide one of the interfaces with negative and the other one with positive EB shift. In all of the three cases, the H_C(T) and H_{eb}(T) decrease with the increase of temperature and the two coercivities in a loop are well separated from each other below and above 400 K (in case of -10 mT FC from 420 K). At 400 K (420 K), the H_C for both of the loops coincide with each other to give a single loop such that both of the FM layers are switching together with externally applied alternating magnetic field. Below (above) this temperature, the FM2 (FM1) switches before the FM1 (FM2) due to its smaller H_C.

Fig. 5.5(a) and Fig. 5.5(b) show the temperature-dependent H_C and H_{eb} curves for the three cases. The H_C(T) (H_{eb}(T)) curves clearly (nearly) overlap for the same interface in both cases of parallel and antiparallel alignment of the two FM layers magnetization. Again, the H_C(T) and H_{eb}(T) for lower interface (AFM/FM1) is about two times to that of the upper interface (FM2/AFM) because the thickness of FM1 is half that of FM2. The T_{AFM} is ∼440 K and ∼420 K for the upper and the lower interface interface, respectively. This is probably due to different morphology/roughness or slightly different Ni (Mn) concentration at both interfaces. The T_b (∼400 K) remains the same for both interfaces.

Summary: For IP-IP trilayer, H_C(T) and H_{eb}(T) are similar when FC with positive or negative fields to attain parallel magnetization for the two FM layers. Different

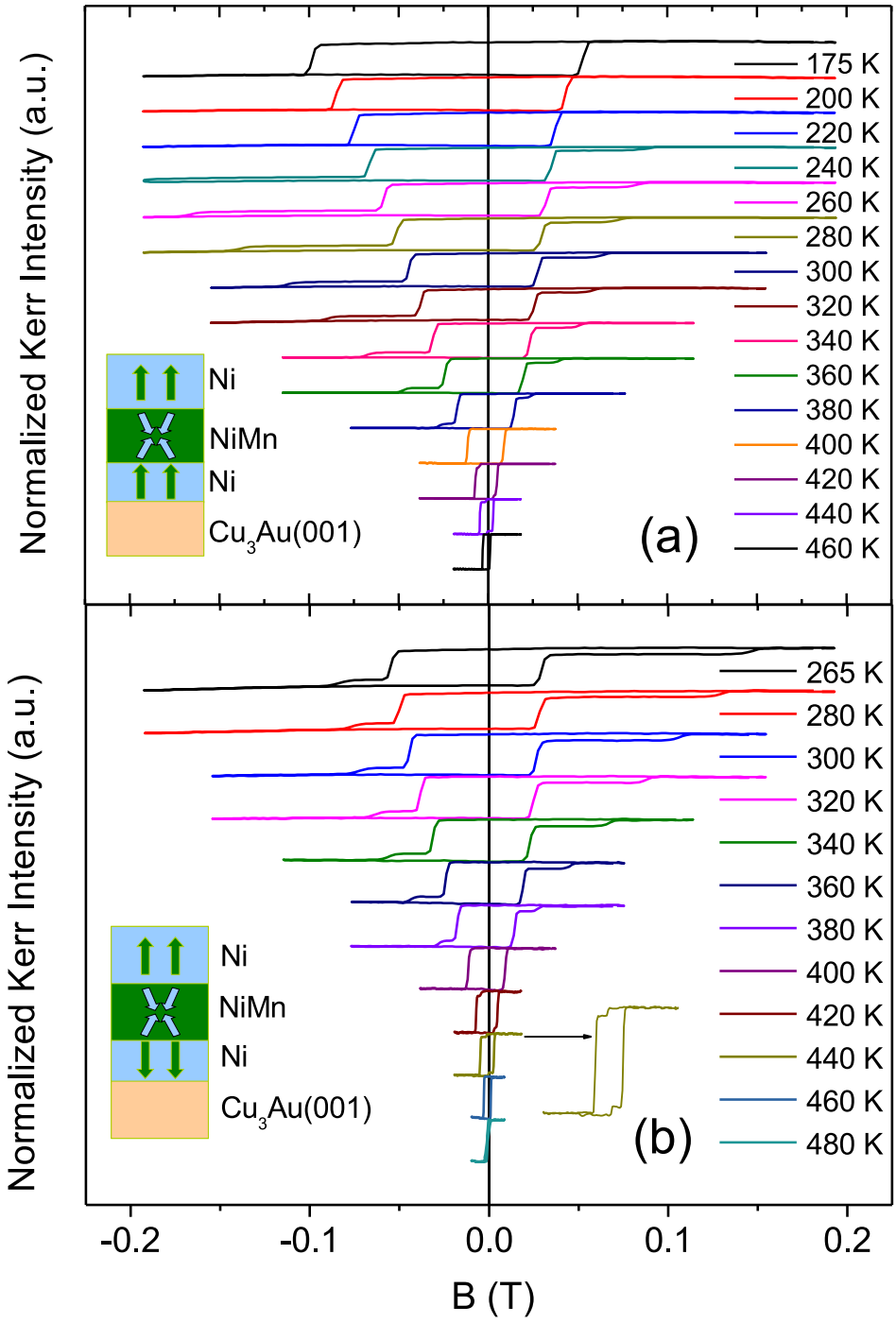

Figure 5.4: Normalized hysteresis loops for a 25 ML Ni/47 ML $Ni_{17}Mn_{83}$/12.9 ML Ni/Cu_3Au(001) trilayer measured with polar MOKE at different temperatures. (a) Both interfaces give negative exchange bias shift when field-cooled with +10 mT from 490 K, and (b) both interfaces give opposite exchange bias shifts: the lower one positive as it is field-cooled with -2 mT from 450 K (at similar temperature (440 K), a zoomed-in loop is shown), and the upper one a negative due to previous field-cooling with +10 mT.

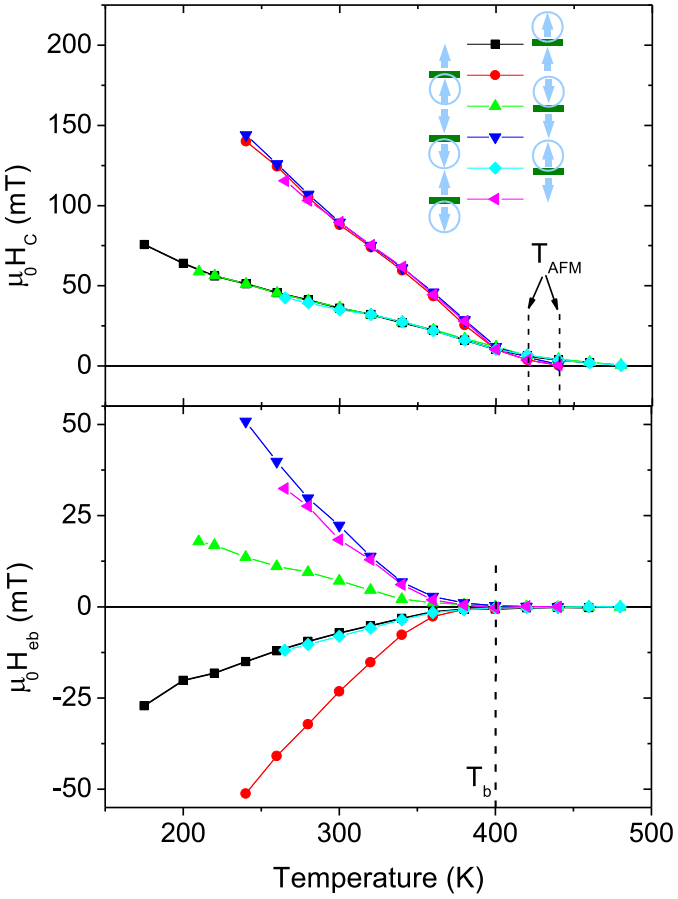

Figure 5.5: Temperature dependence of (a) coercivity and (b) exchange bias field for a 25 ML Ni/47 ML $Ni_{17}Mn_{83}$/12.9 ML Ni/Cu_3Au(001) trilayer measured with polar MOKE. The different magnetization directions of the FM layers at the upper and at the lower interfaces are symbolically shown in front of the corresponding legend. The antiferromagnetic ordering temperature and the blocking temperature are indicated in (a) and (b), respectively.

results are found when the two FM layers are oppositely magnetized to give opposite EB at both interfaces such that for the same lower interface H_C(T) (H_{eb}) has decreased (increased) values for most of the temperature range. However, for the OoP-OoP identical H_C/T) and H_{eb}(T) dependencies are observed. For both cases of the IP-IP and OoP-OoP trilayers with parallel and antiparallel magnetization configurations of the two FM layers, no change is seen in T_{AFM} and T_b for the same interface.

5.1.2 Trilayer with intermediate thickness of AFM layer (41 ML $Ni_{22}Mn_{78}$)

Along with some bilayer MOKE measurements at room temperature, temperature-dependent hysteresis loops for trilayer and the resultant H_C(T) and H_{eb}(T) curves are presented for both FM1 and FM2 magnetized in IP and OoP direction in Fig. 5.6–Fig. 5.11.

Longitudinal MOKE measurements are performed first for the bilayer 41 ML $Ni_{22}Mn_{78}$/12.5 ML Ni/2 ML Co/Cu_3Au(001) from 325 K up to 500 K and then 3 ML Co/22 ML Ni is evaporated on top of the bilayer to measure the hysteresis loops for the trilayer from 140 K to 515 K (Fig. 5.6(a)). For the trilayer IP measurements, there were two kind of spin configurations at both the interfaces of the two parts of the sample, that is, at the one half, both the upper and lower interfaces were magnetized in IP direction (IP-IP trilayer) whereas on the other half, the lower interface was magnetized in the OoP direction and the upper one in IP direction (OoP-IP trilayer). For FC, +20 mT external magnetic field was applied from 500 K. For the IP-IP configuration, the loops overlap each other and are more tilted (Fig. 5.6(a)) than the corresponding

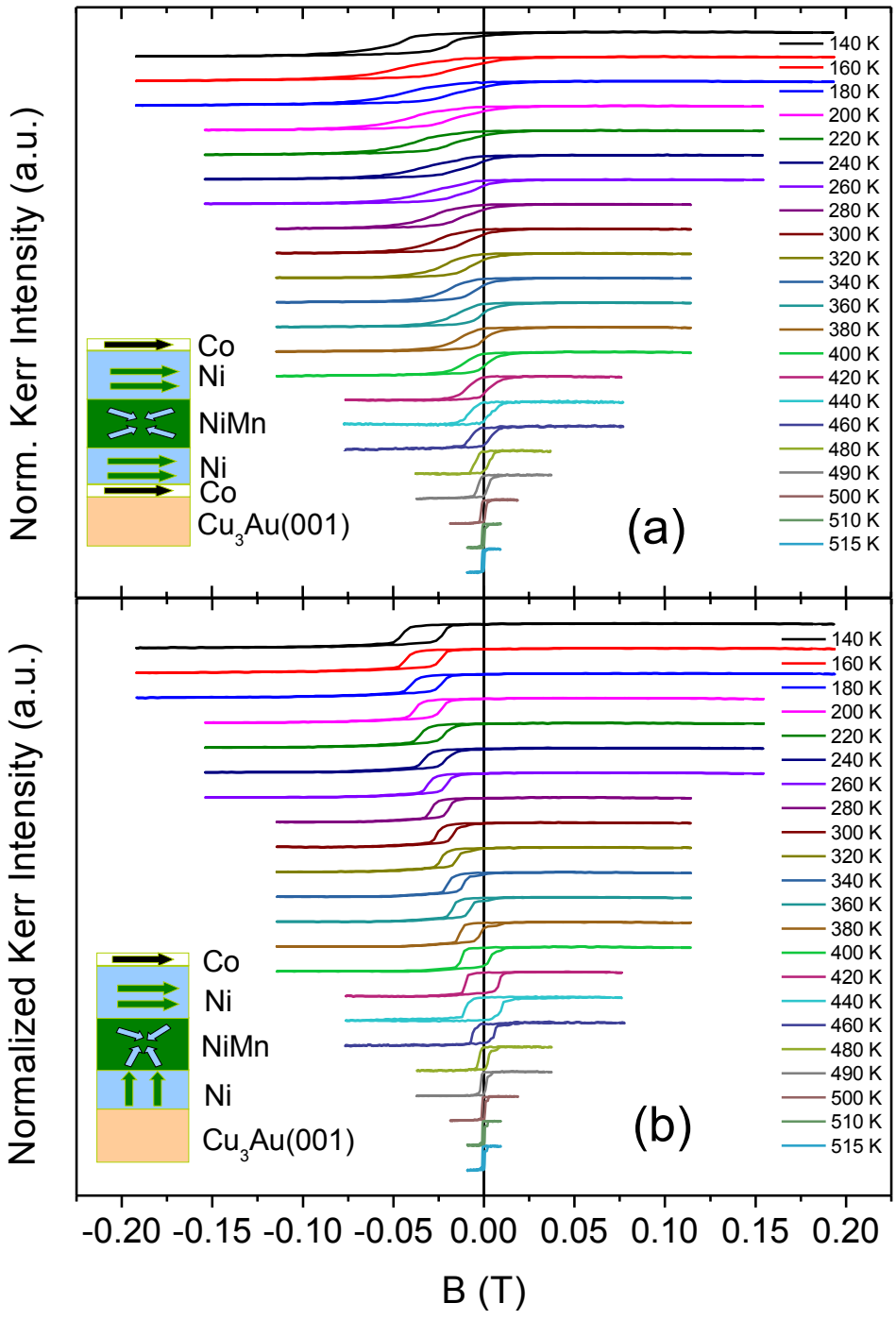

Figure 5.6: Normalized hysteresis loops for 3 ML Co/22 ML Ni/41 ML $Ni_{22}Mn_{78}$/12.5 ML Ni/(2 ML Co/)/Cu_3Au(001) trilayer measured with longitudinal MOKE at different temperatures. Both interfaces give a negative exchange bias shift when field-cooled with +20 mT from 500 K for (a) IP-IP trilayer, and (b) OoP-IP trilayer.

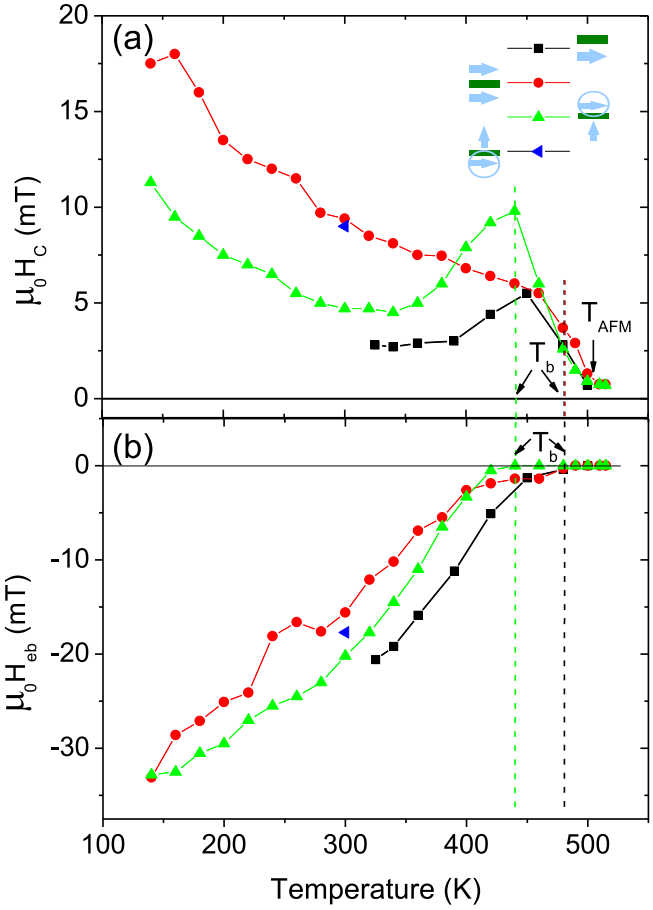

Figure 5.7: Temperature dependence of (a) coercivity and the (b) exchange bias field for 41 ML $Ni_{22}Mn_{78}$/12.5 ML Ni/(2 ML Co/)/Cu_3Au(001) bilayer and (3 ML Co/)22 ML Ni/41 ML $Ni_{22}Mn_{78}$/12.5 ML Ni/2 ML Co/Cu_3Au(001) trilayer measured with longitudinal MOKE. The different magnetization directions of the FM layers at the upper and at the lower interfaces are symbolically shown in front of the corresponding legend. The antiferromagnetic ordering temperature and the blocking temperature are indicated in (a) and (b), respectively. For the OoP-IP trilayer, the coercivity and exchange bias field values at 300 K are shown as blue triangles in (a) and (b), repectively.

bilayer loops (Fig. 5.8(a)). Fig. 5.6(b) shows the temperature-dependent loops for the case of OoP-IP coupling. In all the three cases (i.e., bilayer, IP-IP trilayer, and OoP-IP trilayer), the H_C, the H_{eb} and the tilt of the loops decrease with increasing temperature. The loops exhibit an almost rectangular shape near T_b.

The corresponding H_C(T) and H_{eb}(T) dependencies are presented in Fig. 5.7(a) and Fig. 5.7(b), respectively. The T_{AFM} remains almost constant (500 K), the T_b (∼480 K) for the IP bilayer and the IP-IP trilayer also do not change. However, T_b (∼440 K) is ∼40 K lower for the OoP-IP configuration than for the IP bilayer and IP-IP trilayer. There are considerable differences in the H_C(T) and H_{eb}(T) curves for the bilayer and the IP-IP trilayer. It is apparent that below T_b, the H_C (H_{eb}) of the IP-IP configuration is significantly higher (lower) than that of the bilayer. For example at 325 K, the H_C of the IP-IP trilayer is ∼3 times larger than the bilayer but the H_{eb} of the bilayer is ∼2 times larger than that of the IP-IP trilayer. Also, a peak in H_C(T) for the bilayer can be clearly seen, while there is no peak in the IP-IP trilayer.

The H_C(T) and the H_{eb}(T) curves also look different for the IP-IP configuration compared to that of the OoP-IP ones (Fig. 5.7(a) and Fig. 5.7(b)). Compared to the IP bilayer and the IP-IP trilayer, the H_C of the OoP-IP trilayer is higher in the temperature range of 360 K to 450 K where it has a peak, but it is lower for all other temperatures below 360 K. The H_{eb}(T) of the OoP-IP trilayer has values in between the bilayer and the IP-IP trilayer.

Fig. 5.8 shows hysteresis loops for the IP sample measured at room temperature for bilayer and trilayer with different FM magnetization configurations at the two interfaces. The red loops are measured when the sample is either as grown (bilayer) or

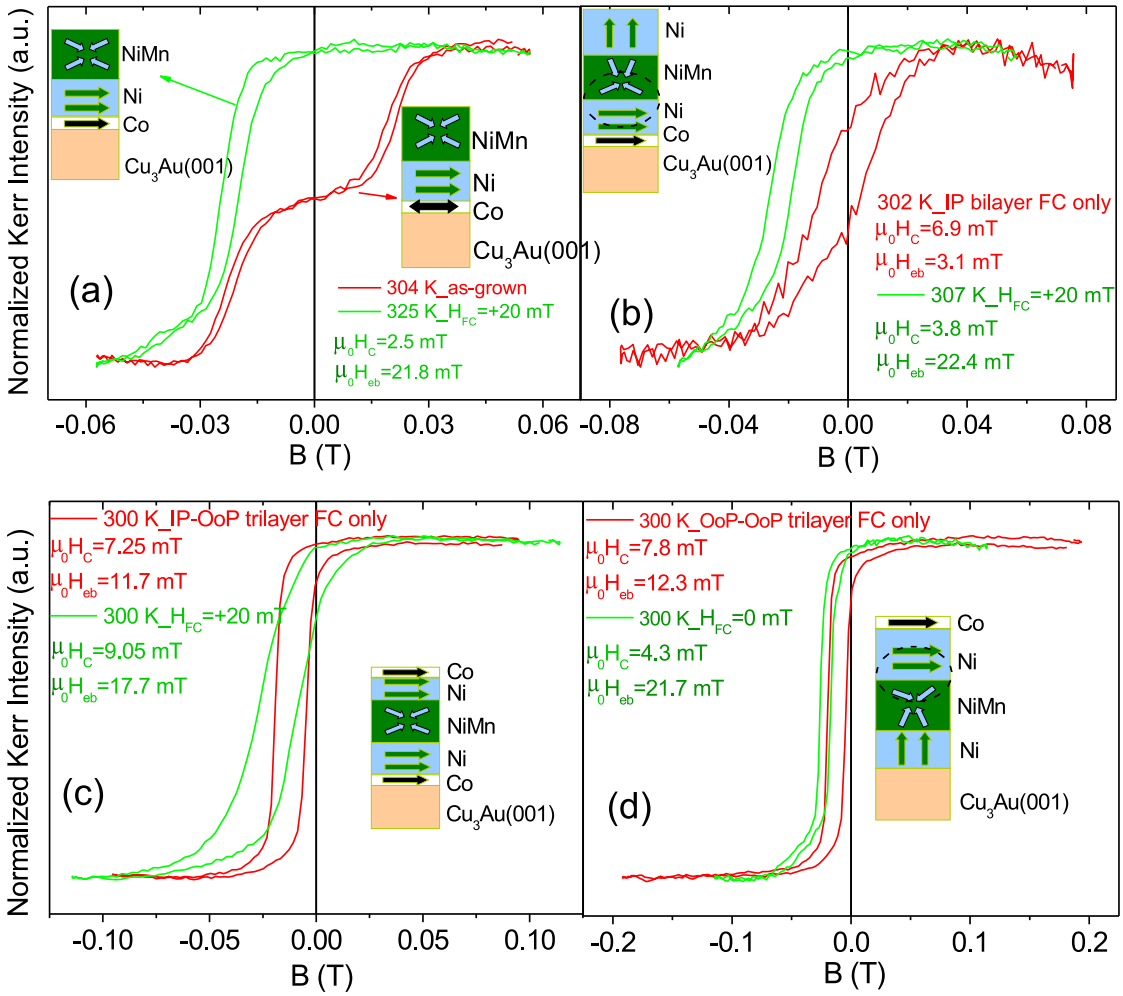

Figure 5.8: The as-grown (red loops), and field-cooled magnetization curves in positive field (green loops) measured with longitudinal MOKE at room temperature for (a) the bilayer, and for (b–d) the trilayer (3 ML Co/)22 ML Ni/41 ML $Ni_{22}Mn_{78}$/12.5 ML Ni/2 ML Co/Cu_3Au(001) with different magnetization configurations of the two FM layers indicated in the schematics of the corresponding plot.

is not FC for the particular FM magnetization configuration, and the green ones for the FC sample. The red double loop in Fig. 5.8(a) is measured for as-grown bilayer showing negative as well as positive EB shift. This is because the Co (and (Ni/Co)) layer exhibits domains with magnetization in different directions. This gives rise to the negative and to the positive shift simultaneously for the as-grown bilayer. The FC sample is measured at 326 K. Fig. 5.8(c) shows loops measured at 300 K for the IP-IP trilayer. The H_C is increased for the trilayer compared to the bilayer, but the H_{eb} of the bilayer is increased compared to the IP-IP trilayer. Note that they are measured at different temperatures, therefore the H_{eb} should be more smaller for the IP-IP trilayer compared to the bilayer. H_C (H_{eb}) is more than twice (smaller) for the IP-IP compared to that of the IP-OoP and OoP-IP configurations (Fig. 5.8 (b), (c) and (d)), and similar for the IP-OoP and OoP-IP configurations (Fig. 5.8 (b), and (d)).

The temperature-dependent hysteresis loops for the OoP-OoP and the IP-OoP configurations are shown in Fig. 5.9(a) and Fig. 5.9(b), respectively. The resultant curves for H_C(T) and H_{eb}(T) are presented in Fig. 5.10(a) and Fig. 5.10(b). Although measured one after the other at the same temperature, and having almost identical H_C values, the IP-OoP loops are more tilted than the OoP-OoP ones. This tilt is preserved by the loops until T_{AFM}. The OoP-OoP hysteresis contains two loops; the one originating from the lower interface with thinner FM layer is with larger H_C but with smaller magnetization (height of the loop), the other from the upper interface with thicker FM layer is with smaller H_C but with larger magnetization. Below 260 K, both of the loops are shifted to the left side providing usual and expected negative EB where both FM layers switch together at the negative fields. Between 280 and 300 K, the magnetization of FM1 switches before that of the FM2. Finally just below T_b (∼360 K), on the right hand side of both of the loops once again the two layers switch together and once again a negative H_{eb} results, although very small. This makes the situation unusual. The H_{eb} of the AFM/FM1 interface is very small compared to the FM2/AFM interface whether it is negative or positive. Let us analyze one of these loops, for example, the one measured at 280 K. At the maximum external magnetic field applied, the magnetization of both of the FM layers is parallel until the field sweeps to negative values to switch the FM1 magnetization first, making the spin configuration antiparallel at both interfaces. With further increase of the negative field, the magnetization of the FM2 eventually also switches in the direction of the field. Now the magnetization of both the FM layers is, again, parallel. Now, if the negative field is decreased towards positive values, the FM2 switches first, making the magnetization once again antiparallel to each other. By further increase of the positive field, the FM1 also switches in the field direction, turning the spin configuration once again to the initial parallel direction. Usually, as observed for the OoP-OoP coupling of ∼50 and 47 ML Ni_xMn_{100-x}, the FM layer with smaller H_C switches first at both sides of the loop, than the other FM with larger H_C. But here, we see that when a negative field is applied, the FM1 with larger H_C switches first, and then by the application of a positive field, the FM2 with smaller H_C switches first. More energy is required to turn the antiparallel alignment of the FM layers magnetization toward parallel alignment when the external field is negative, and less energy is required in the reverse case.

The switching of the sign of H_{eb} is evident from the temperature dependence of H_{eb} (Fig. 5.10(b)). Besides the sign change of EB from the AFM/FM1 interface in OoP-OoP trilayer, H_{eb} is also significantly reduced compared to the OoP bilayer and the OoP-IP trilayer. T_b also decreases to ∼360 K from ∼420 K compared to that of

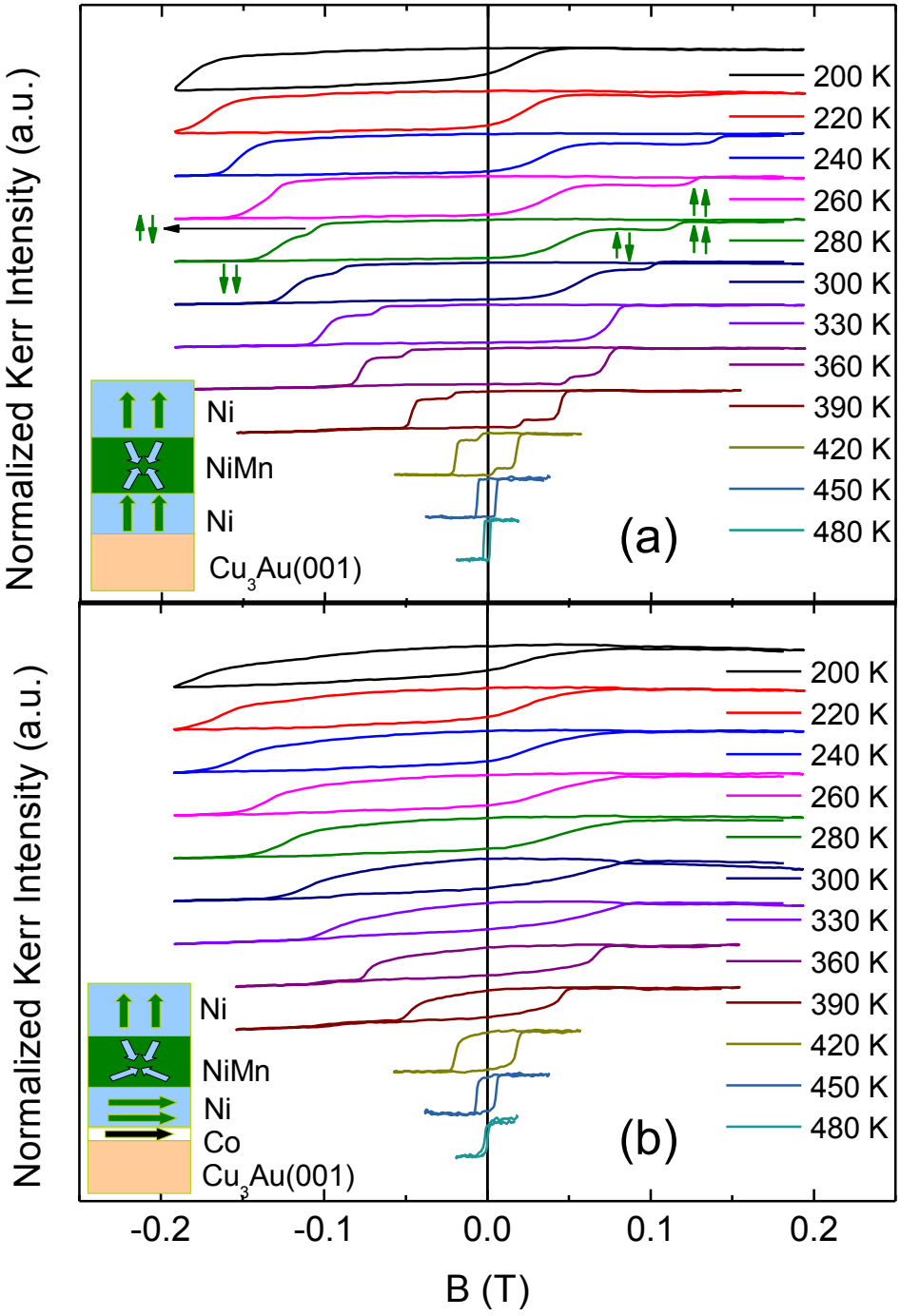

Figure 5.9: Normalized hysteresis loops for the 22 ML Ni/41 ML $Ni_{22}Mn_{78}$/12.5 ML Ni/(2 ML Co/)/Cu_3Au(001) trilayer measured with polar MOKE at different temperatures. (a) Both interfaces give a negative exchange bias shift below 260 K and above 340 K when field-cooled with +200 mT from 500 K for OoP-OoP coupled trilayer, and (b) negative exchange bias in the whole temperature range for the IP-OoP trilayer.

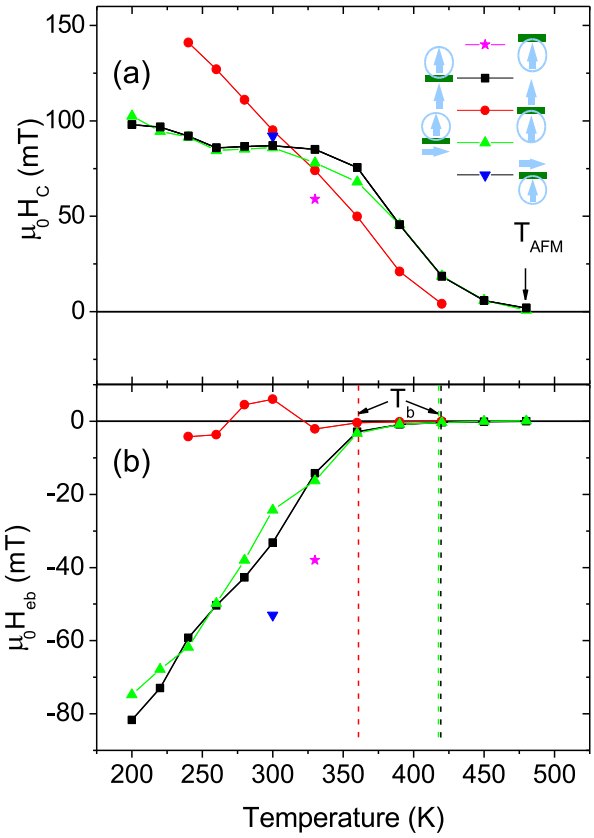

Figure 5.10: Temperature dependence of (a) coercivity and the (b) exchange bias field for the (3 ML Co/)22 ML Ni/41 ML $Ni_{22}Mn_{78}$/12.5 ML Ni/(2 ML Co/)/Cu_3Au(001) trilayer measured with polar MOKE. The different spin configurations of the FM layers at upper and lower interfaces are symbolically shown in front of the corresponding legend. A sign reversal of H_{eb} from negative to positive and then to small negative value just below T_b is observed for the OoP-OoP trilayer (b). The antiferromagnetic ordering temperature and blocking temperature are indicated in (a) and (b), respectively. For the OoP bilayer and OoP-IP trilayer, the coercivity and exchange bias field value at 300 K and 326 K, respectively, are also shown as pink stars and blue triangles, respectively.

the the upper ineterface (FM2/AFM) of the same trilayer. Also the H_{eb}(T) curves for the IP-OoP and OoP-OoP configurations show same T_b (420 K). While changing the FM2 direction from OoP to IP, at the lower interface (AFM/FM1) in the OoP-IP case (blue triangle in Fig. 5.10(a) and Fig. 5.10(b)), the H_C value nearly remains constant but the H_{eb} is now negative with much a larger value (∼9 times) compared to the OoP-OoP trilayer at the same interface. This means that the magnetization direction at one interface certainly plays a role to affect the H_{eb} or T_b of the very same AFM layer at the other one.

Some loops measured with polar MOKE at 300 K (except the one for the FC bilayer sample which is measured at 326 K) are presented in Fig. 5.11(a–d). These loops were measured only at room temperature after the sample is freshly field-cooled, i.e., they are not taken from temperature-dependent measurements. The red loops are measured for the as-grown sample (as-grown samples are defined in the beginning of the chapter (section 5.1)), and the green ones for the FC sample. The FC bilayer in Fig. 5.11(a) would have provided more EB than the one at 325 K, if it had been measured at 300 K. Compared to the bilayer (Fig. 5.10(b) and Fig. 5.11(a)), the reduced H_{eb} for the lower interface (AFM/FM1) of the OoP-OoP trilayer can clearly be seen from Fig. 5.10(b) and Fig. 5.11(b). The H_{eb} for the AFM/FM1 (FM2/AFM) interface is negative (positive) when the sample is either as-grown (field-cooled only for bilayer) (red loop) or field-cooled with negative field (black dashed loop), and is positive (negative) when it is field-cooled with positive field (green and blue loops, respectively). The EB changes its sign at both interfaces when the cooling field direction is changed from positive to negative or vice versa, as expected. Fig. 5.11(b) and (c) (green and blue loops) show

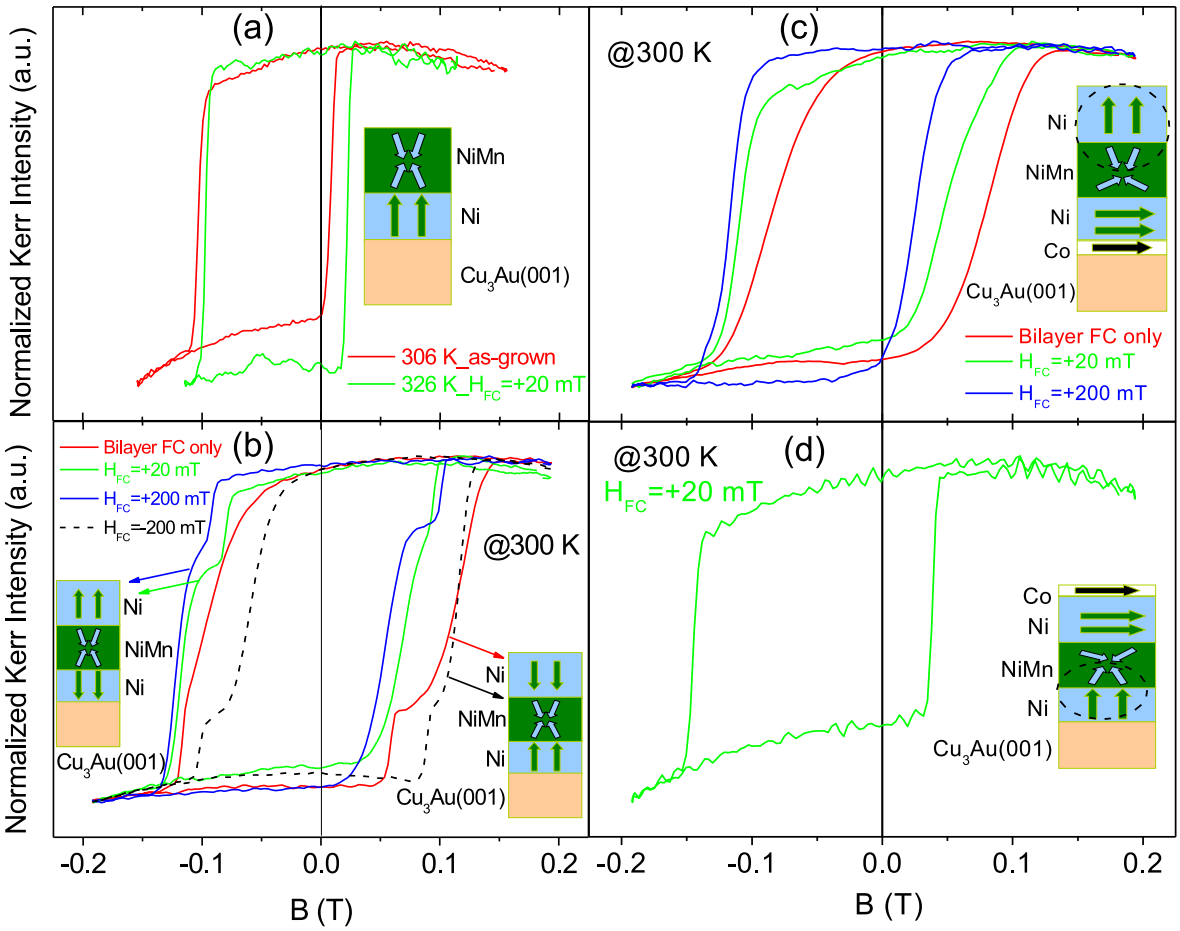

Figure 5.11: The as-grown (red loops) and field-cooled (green loops) polar MOKE measurements at room temperature for (a) the bilayer 41 ML $Ni_{22}Mn_{78}$/12.5 ML Ni/(2 ML Co/)/Cu_3Au(001) and (b–d) the trilayer of (3 ML Co/)22 ML Ni/41 ML $Ni_{22}Mn_{78}$/12.5 ML Ni/(2 ML Co/)/Cu_3Au(001) with different FM layer magnetization directions as shown schematically in the corresponding plot.

that the magnitude of the cooling field also affects the magnitude of the EB field: the higher cooling field results in a higher H_{eb}. The unusual behaviour of the OoP-OoP trilayer could not be correlated with the magnitude of the cooling field, as the same behaviour is observed whether cooling field was smaller (+20 mT) or larger (+200 mT). When the FM2 is made IP by deposition of a Co over layer, the OoP-IP trilayer regains its higher H_{eb} value which is similar as for the bilayer alone.

Summary: The IP-IP trilayer exhibits a single tilted hysteresis loop with no peak in H_C(T). Compared to the IP bilayer, the IP-IP trilayers has decreased H_{eb} but increased H_C, with no change in T_b and T_{AFM}. Compared to the IP bilayer, the OoP-IP trilayer has a peak in H_C(T) with decreased H_{eb} and decreased T_b but increased H_C with no change in T_{AFM}. The two interfaces provide opposite EB for the as-grown as well as for the positively or negatively FC OoP-OoP trilayer. A temperature-dependent sign reversal behaviour with much decreased value of H_{eb} is observed in the OoP-OoP trilayer compared to the OoP bilayer. By setting the top FM layer (FM2) IP, the OoP-IP trilayer somehow regains or even increases its H_{eb} as that for the OoP bilayer alone.

5.1.3 Trilayer with 32 ML $Ni_{18}Mn_{82}$

Bilayers are measured in IP and in OoP direction only at room temperature, whereas temperature-dependent measurements are performed only for the IP-IP configuration of the trilayer. The sample was FC from 500 K down to 300 K for the bilayer with +10 mT FC, and to 140 K for the trilayer with +10 mT and -10 mT. For the OoP-OoP trilayer some strange kind of triple-loop was obtained for all temperatures from 150 K to 450 K which could not be explained and is therefore not considered for description/discussion.

Fig. 5.12(a) and Fig. 5.12(b) show the temperature-dependent H_C and H_{eb} for the positively and negatively field-cooled IP-IP trilayer, respectively. The H_C and H_{eb} both decrease by increasing temperature. The H_C(T) for negative FC is slightly higher than for the positive FC at all temperatures (Fig. 5.12(a)), but with very similar T_{AFM} (∼500 K). The H_{eb}(T) remains almost the same for both FC directions with nearly equal T_b (490 K for the lower interface and 480 K for the upper interface) (Fig. 5.12(b)). The positive H_{eb} is mirrored on the negative axis (with open red symbols) to clearly see the equivalence of both cases.

The H_C and the H_{eb} measured only at room temperature (300 K) are reduced for the trilayer (blue loop) compared to the bilayer (green loop), as shown in Fig. 5.13. This reduction in H_C and H_{eb} is nearly 2 times and exactly 3 times, respectively. The double loop (red loop) is measured for bilayer without FC. This shows negative and positive H_{eb} at the same time as describe for 41 ML $Ni_{22}Mn_{78}$ in the previous section.

Summary: Whether FC with positive or negative field, the IP-IP trilayer exhibits a single hysteresis loop with no clear peak in H_C(T), and significantly reduces its H_{eb} compared to the IP bilayer.

5.1.4 Trilayer with thinner (27 ML $Ni_{25}Mn_{75}$) AFM layer

Fig. 5.14(a–d) shows the 300 K hysteresis loops measured with longitudinal MOKE for the bilayer and for the trilayer with IP-OoP, IP-IP, and OoP-IP configuration, respectively. The FC loop for the bilayer and that for IP-OoP trilayer is tilted (Fig.

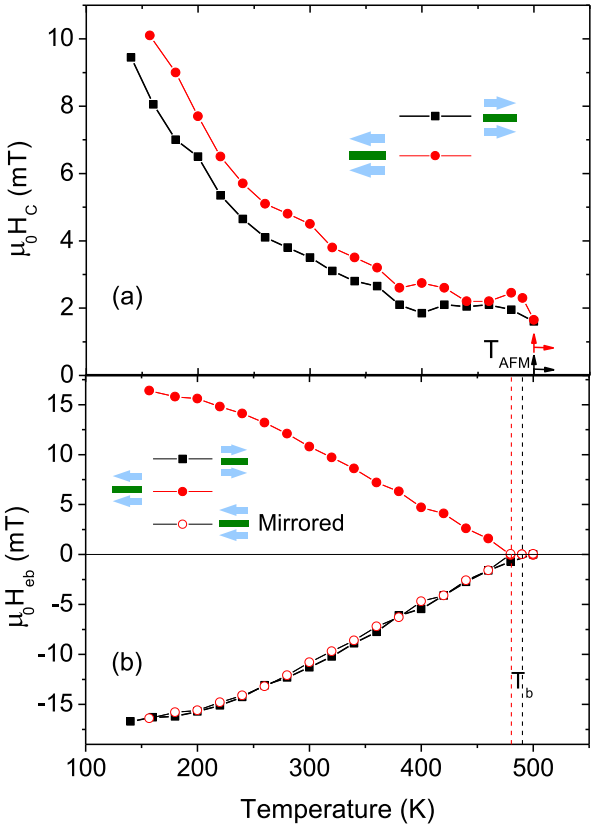

Figure 5.12: Temperature dependence of (a) coercivity and the (b) exchange bias field for the 3 ML Co/25 ML Ni/32 ML $Ni_{18}Mn_{82}$/12.8 ML Ni/2 ML Co/Cu_3Au(001) trilayer measured with longitudinal MOKE. The antiferromagnetic ordering temperature and blocking temperature are indicated in (a) and (b), respectively. The mirror image of the temperature-dependent H_{eb} curve for negative FC is also shown with open red circles in (b) overlapping the corresponding curve for positive FC, although there is a small difference in the coercivity curve shown in (a).

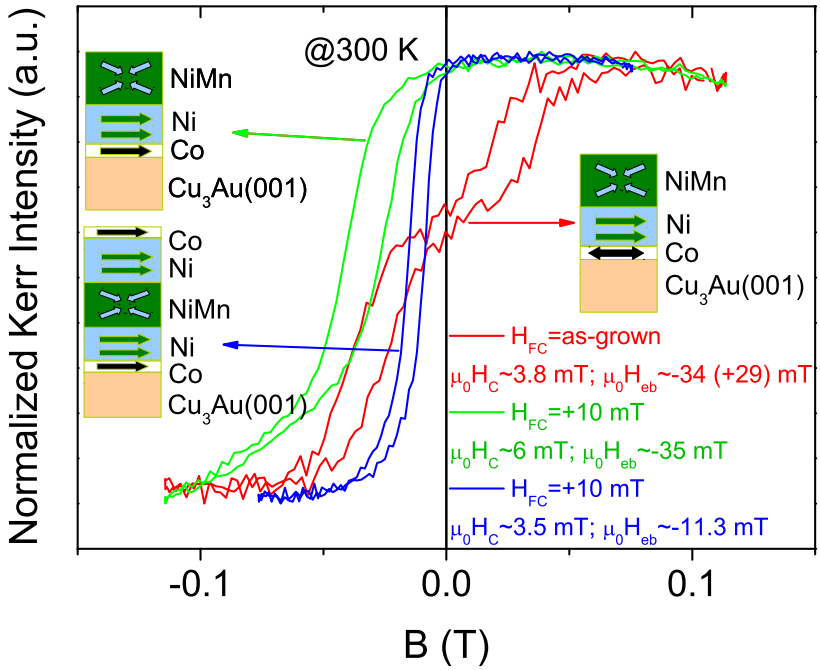

Figure 5.13: Exchange-biased loops for 32 ML $Ni_{18}Mn_{82}$/12.8 ML Ni/2 ML Co/Cu_3Au(001) bilayer and 3 ML Co/25 ML Ni/32 ML $Ni_{18}Mn_{82}$/12.8 ML Ni/2 ML Co/Cu_3Au(001) measured with longitudinal MOKE at 300 K. The red double coercivity loop for as-grown bilayer, green loop for field-cooled bilayer, and the blue one for field-cooled trilayer. The IP-IP trilayer significantly reduces the coercivity and EB of the bilayer.

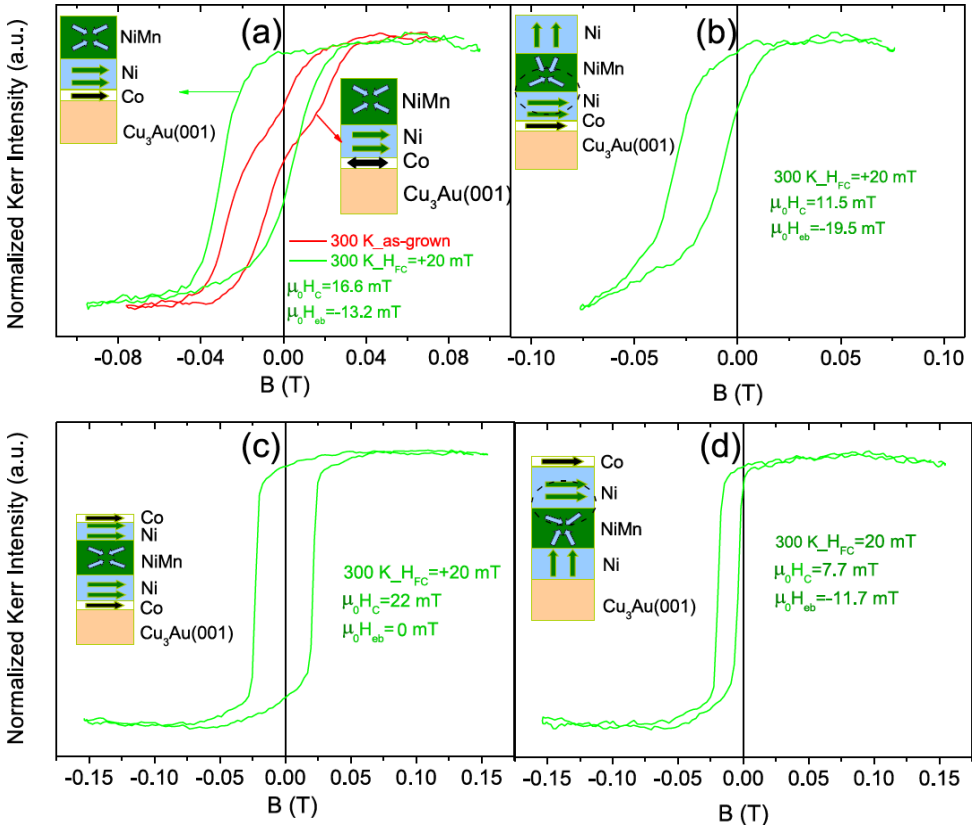

Figure 5.14: Normalized hysteresis loops at 300 K measured with longitudinal MOKE. (a) IP bilayer 27 ML $Ni_{25}Mn_{75}$/12 ML Ni/2 ML Co/Cu_3Au(001) (red double loop for as-grown, and green loop for FC sample), (b) IP-OoP trilayer 21 ML Ni/27 ML $Ni_{25}Mn_{75}$/11.9 ML Ni/2 ML Co/Cu_3Au(001), (c) IP-IP trilayer, and (d) IP-OoP trilayer (all FC). The easy axis of magnetization of the FM layers and the possible spin configuration of the AFM layer near the interface are also schematically shown within each plot.

5.14(a) and (b)) which shows that the magnetization reversal is not very abrupt. In the last two cases (IP-IP and OoP-IP), the loops are more rectangular although still with round corners (Fig. 5.14(c–d)). The corresponding H_C(T) and H_{eb}(T) curves for the bilayer and the trilayer are presented in Fig. 5.15.

The result of temperature-dependent MOKE measurements after FC with +20 mT in IP and in OoP direction is shown in Fig. 5.14 and Fig. 5.15, respectively. Filled symbols are used for H_C and open symbols for H_{eb}.

For all cases the T_{AFM} (∼460 K) does not change. For the bilayer (black symbols), the H_p (peak in H_C(T)) occurs at slightly smaller temperature compared to the trilayer with IP-OoP configuration (red symbols). This indicates a slightly higher H_{eb}(T) and higher T_b for the IP-OoP coupled trilayer than the bilayer, which is also seen from the corresponding H_{eb}(T) curves and T_b's in Fig. 5.15. T_b for the bilayer and trilayer is ∼430 K and ∼440 K, respectively. Due to the different thicknesses of FM2 and FM1, the H_C(T) and H_{eb}(T) (blue symbols) for the OoP-IP trilayer change differently than the IP-OoP trilayer, while the T_b remains the same. Interestingly, for the IP-IP trilayer the temperature dependence of H_C and H_{eb} (green symbols) is significantly different than that of the bilayer or the trilayer with IP-OoP or OoP-IP configuration. The peak in H_C(T) along with T_b occur at much lower temperatures. The H_C(T) and H_{eb}(T)

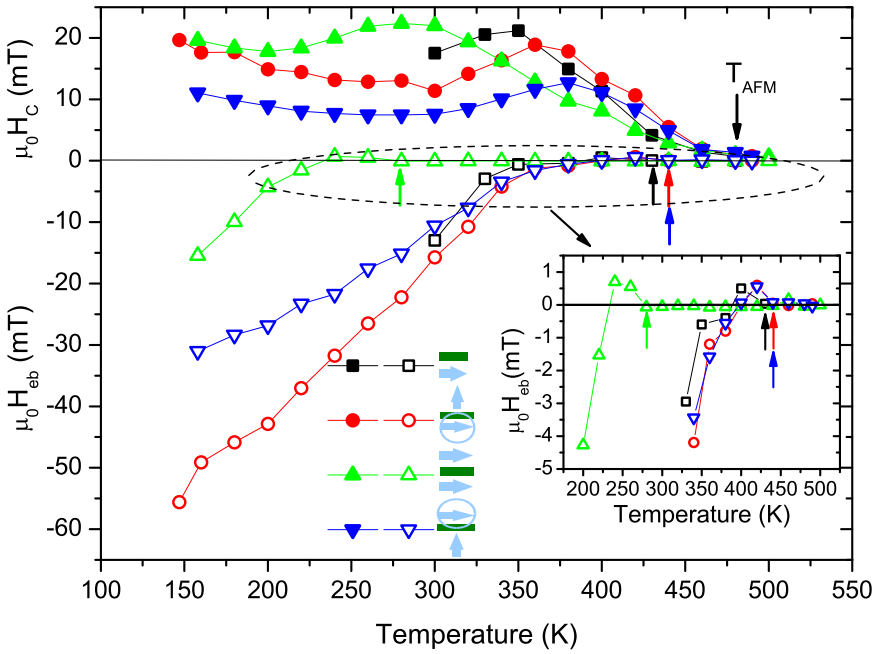

Figure 5.15: Temperature-dependence of coercivity (filled symbols on positive vertical axis), and exchange bias field (open symbols on negative vertical axis) for the IP bilayer 27 ML $Ni_{25}Mn_{75}$/11.9 ML Ni/2 ML Co/Cu_3Au(001) (black squares), the IP-OoP trilayer (red circles) 21 ML Ni/27 ML $Ni_{25}Mn_{75}$/11.9 ML Ni/2 ML Co/Cu_3Au(001), IP-IP trilayer (green up triangles), and (d) IP-OoP trilayer (blue down triangles). The antiferromagnetic ordering temperature (down arrow) and blocking temperatures (up arrows of the respective colour) are indicated,. The inset represents the dashed area with zoomed-in vertical axis to clearly show the small positive exchange bias just below T_b.

are smallest for the IP-IP trilayer compared to the bilayer or the IP-OoP and OoP-IP trilayers. The T_b=280 K for the IP-IP case is ∼150 K (∼160 K) smaller than that of the bilayer (IP-OoP and OoP-IP trilayer). Note that the small positive EB just below T_b is always there as shown in the inset with a zoom-in of the vertical axis for the dashed elliptical part of Fig. 5.15. This kind of small positive EB is not observed for other IP bi/trilayer samples with Ni concentration smaller than 24 %. This is attributed to an unusual minority species of spins but strongly pinned opposite to the majority pinned spins, and is consistent with the findings for $Ni_{81}Fe_{19}/Ir_{20}Mn_{80}$ bilayer [134].

There were seven polar MOKE measurements done for various spin configurations of the FM layers at the upper and lower interfaces. To avoid the crowd of plots, only four representative loops measured at 300 K for the OoP bilayer, OoP-OoP, OoP-IP, and IP-OoP trilayer are shown in Fig. 5.16. It is evident that the H_C and H_{eb} both are decreased—H_C from 136 to 110.3 mT, H_{eb} from -15 to -1.5 mT when second OoP FM2 is evaporated on top of the OoP bilayer. This decrease in H_{eb} is similar to the IP-IP trilayer of the same sample in Fig. 5.16 as well as to that of the IP-IP trilayers with 41 ML $Ni_{22}Mn_{78}$ (Fig. 5.8) and 32 ML $Ni_{18}Mn_{82}$ (Fig. 5.13). A similar decrease in H_{eb} is also observed for the OoP-OoP trilayer with 41 ML $Ni_{22}Mn_{78}$ (Fig. 5.8) but with temperature-dependent sign change.

The resulting H_C(T) and H_{eb}(T) for all seven measurements for different spin configurations of the FM layers at the upper and lower interfaces are shown in Fig. 5.17(a)

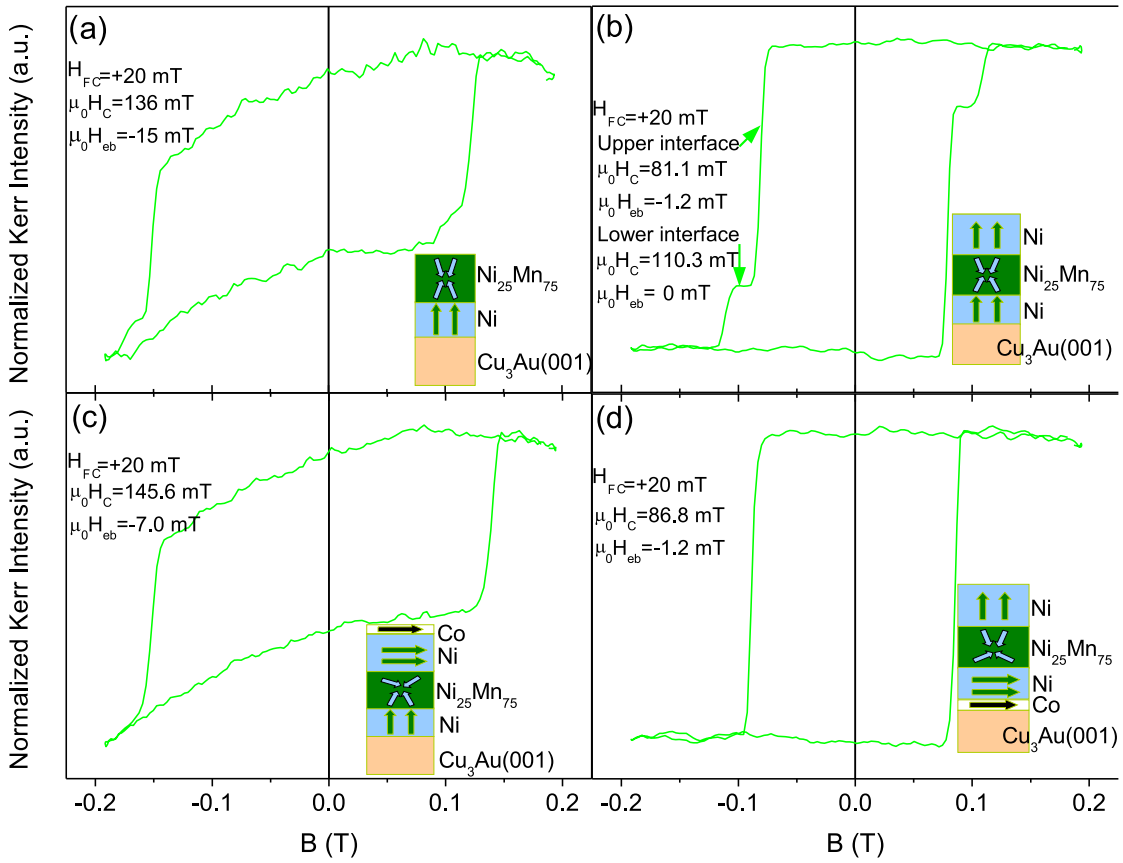

Figure 5.16: Normalized hysteresis loops at 300 K measured with polar MOKE. (a) OoP bilayer 27 ML $Ni_{25}Mn_{75}$/11.9 ML Ni/Cu_3Au(001), (b) OoP-OoP trilayer 21 ML Ni/27 ML $Ni_{25}Mn_{75}$/11.9 ML Ni/Cu_3Au(001), (c) OoP-IP trilayer, and (d) IP-OoP trilayer (all FC with +20 mT). The OoP-OoP trilayer (b) significantly reduces the coercivity and EB of the OoP bilayer (a). The easy axis of magnetization of the FM layers and the possible spin configuration of the AFM layer near the interface are also schematically shown within each plot.

and Fig. 5.17(b), respectively. Except for one case of OoP-IP trilayer, the H_C(T) as well as H_{eb}(T) for the same interface look very similar, irrespective of the magnetization directions of the FM layers, whether they are parallel, antiparallel or perpendicular to each other. The H_C(T) and H_{eb} for the upper interface (FM2/AFM with red, blue, and pink symbols) is always smaller than for the lower interface (AFM/FM1 with green and cyan symbols) due to the higher thickness of FM2.

The exceptional case, which triggers an interesting discussion, is the OoP-IP trilayer for which the H_C(T) and H_{eb}(T) (wine star symbol) are different/increased for the same (lower) interface compared to the other coupling configurations. With all spin configurations of the FM layers, the T_{AFM} for the upper interface also nearly remains unchanged (∼470 K). The smaller thickness of the FM1 (11.9 ML) does not allow to clearly determine the T_{AFM} for the lower interface because of its smaller Curie temperature ($T_C < T_{AFM}$). The T_b (∼360 K) for the exceptional OoP-IP trilayer is ∼40 K higher than all other spin combinations of the trilayer, however, it is still ∼30 K smaller than the T_b (∼390 K) of the bilayer sample.

Summary: The IP-IP trilayer exhibits a single hysteresis loop with a clear peak in H_C(T) at lower temperature, and not only significantly reduces H_{eb} but also markedly

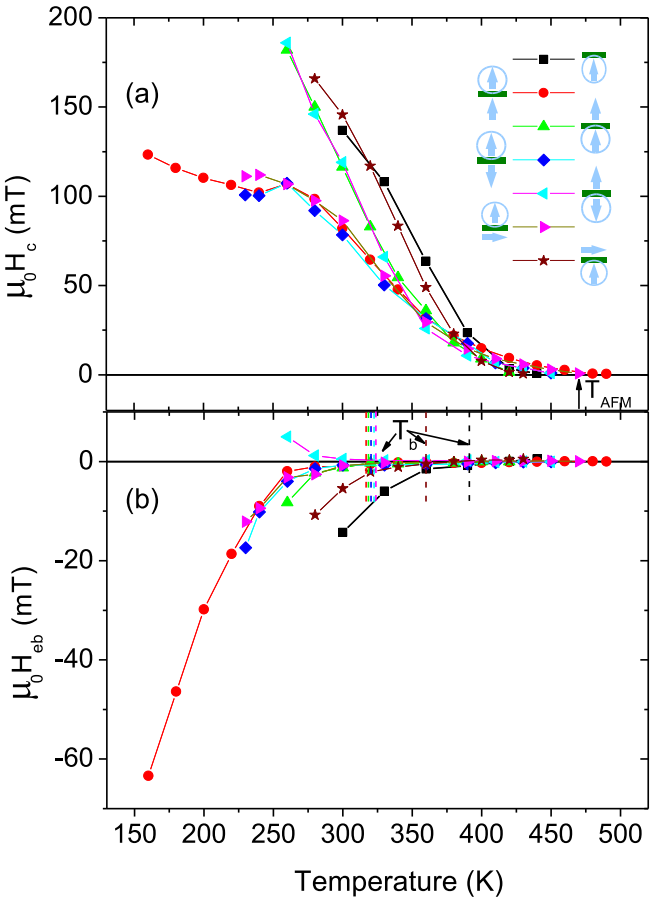

Figure 5.17: Temperature dependence of (a) coercivity and the (b) exchange bias field for the 27 ML $Ni_{25}Mn_{75}$/12 ML Ni/Cu_3Au(001) bilayer and (3 ML Co/)21 ML Ni/27 ML $Ni_{25}Mn_{75}$/11.9 ML Ni/Cu_3Au(001) trilayer measured with polar MOKE. The antiferromagnetic ordering temperature and the blocking temperature are indicated in (a) and (b), respectively. The magnetization directions of the FM layers at the upper and at the lower interfaces are schematically shown in front of the respective legend.

decreases T_b compared to the IP bilayer. The very same results are found for the OoP-OoP trilayer compared to the OoP bilayer but here, the coercivities of the two interfaces can be very clearly distinguished in the loop of the trilayer. Very similar results for $H_C(T)$, $H_{eb}(T)$, T_{AFM} and T_b are obtained for the trilayer when the two FM layers are oppositely FC to provide opposite EB shift at the two interfaces. However, the OoP-IP trilayer shows higher H_{eb} and T_b compared to the OoP-OoP trialyer but still smaller than the OoP bilayer.

5.1.5 Trilayer with thinnest (25 ML $Ni_{24}Mn_{76}$) AFM layer

For this sample more longitudinal MOKE measurements along with some polar ones are presented for the bilayer and the trilayer. In IP bilayer, a usual training effect at lower temperatures, and an unusual training effect leading to small positive EB shift for freshly cooled sample is observed just below T_b. In IP-IP trilayer, an unusual training effect is observed which leads to positive exchange bias shift. Therefore, a different hierarchy of describing the results is to be adopted because of the unusual results. The IP measurements are divided into three figures: Fig. 5.18 shows bilayer results, Fig. 5.19 and Fig. 5.20 describe observations of the trilayer when the FM2 is thinner, and Fig. 5.21 and Fig. 5.22 when the FM2 is thicker than FM1, respectively. The sample was FC in IP direction with +20 mT or -20 mT from 480 K. At the end, two polar MOKE loops are shown only for the OoP bilayr and OoP-OoP trilayer at 210 K in Fig. 5.23.

Fig. 5.18 shows the bilayer 25 ML $Ni_{24}Mn_{76}$/13.1 ML Ni/2 ML Co/Cu_3Au(001) loops measured at 300 K for as-grown sample (red double coercivity loop), at 300 K

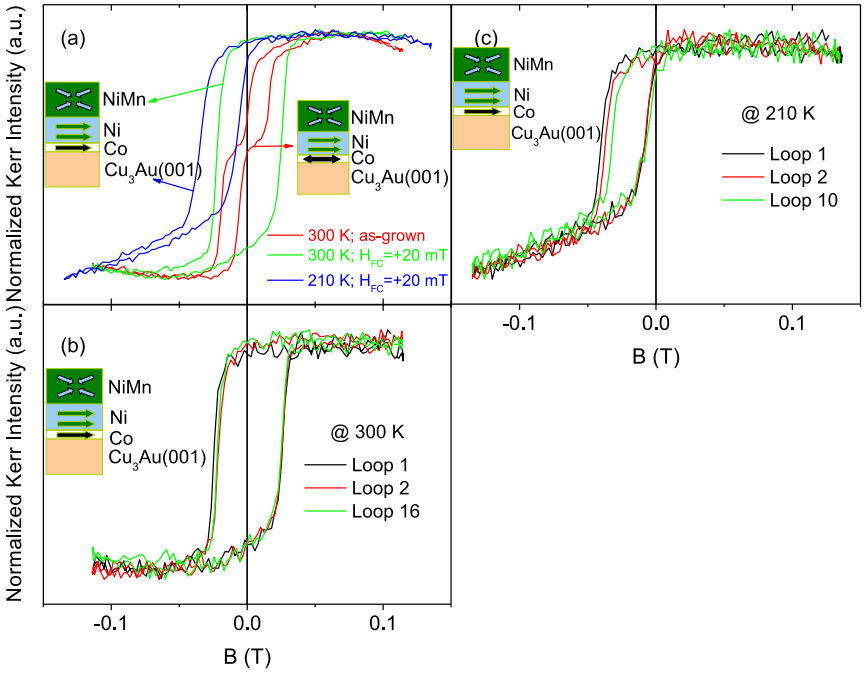

Figure 5.18: Normalized hysteresis loops measured with longitudinal MOKE for the 25 ML $Ni_{24}Mn_{76}$/13.1 ML Ni/2 ML Co/Cu_3Au(001) bilayer (a) red double loop for as-grown sample and green loop for freshly field-cooled sample at 300 K, the latter with small positive EB shift after training and is shown in (b), and (c) training effect at 210 K after previous measurement at 300 K, and then cooling down with out application of field. This training effect does not lead to positive EB.

(green loop) and 210 K (blue loop) each after fresh FC (Fig. 5.18(a)). The reason for the double loop for the as-grown sample, as mentioned before, are FM domains with oppositely magnetization giving rise to positive and negative EB shift simultaneously. When an external magnetic field is applied to the sample above the ordering temperature of the AFM layer, all the domains of the FM layer are saturated along the field direction, and unidirectional anisotropy is set after cooling down through the blocking temperature of the AFM layer. The magnitude of the EB of the as-grown sample suggests a higher or at least an equal EB for the FC sample at the same temperature (300 K) which is however, not the case. The loop is rather shifted a bit to the right hand side (green loop) with an enhanced H_C. Careful analysis reveals that it is due to a continuous decrease in H_C and in H_{eb} with increasing number of loops: the so called *training effect* occurs, where the left side of the loop moves towards the right side, and the right side of the loop always stays firm at its position (Fig. 5.18(b)). This leads to a small positive EB shift. It will be shown shortly that the T_b of this sample is just above 300 K and the small positive EB just below T_b is similar to our results presented in above subsection as well as in the bilayer results in chapter 4, section 4.4. Only the usual training effect is observed at lower temperature 210 K, Fig. 5.18(c), where the sample is not freshly field-cooled, it was cooled down to 210 K from 300 K without applying any external magnetic field. The training effect at both higher and lower temperatures is attributed to the presence of an unusual minority species of pinned spins which are strongly pinned in the opposite direction as the majority of pinned spins. They persist at higher temperatures than the usual pinned spins. This results is consistent with the findings for a $Ni_{81}Fe_{19}/Ir_{20}Mn_{80}$ bilayer [134].

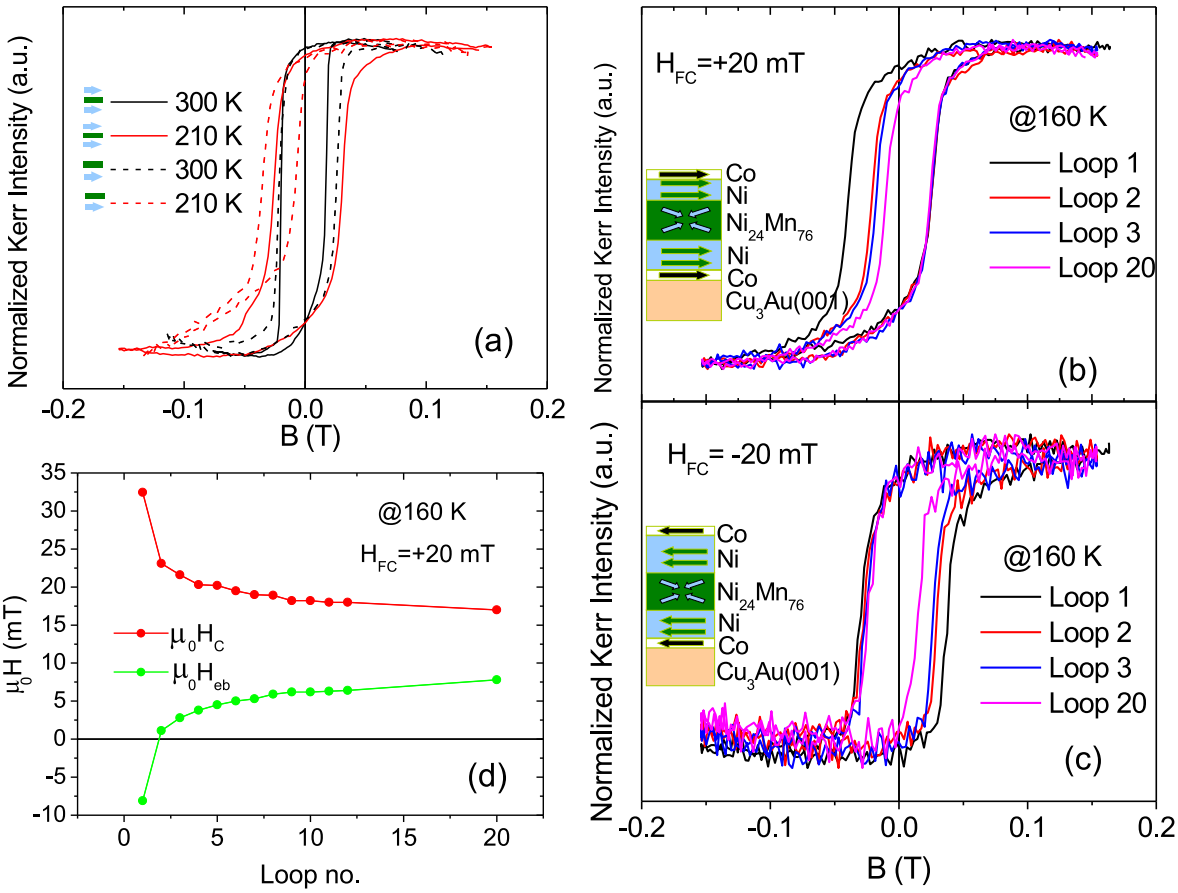

Figure 5.19: Longitudinal MOKE measurements for trilayer 2 ML Co/7 ML Ni/25 ML $Ni_{24}Mn_{76}$/13.1 ML Ni/3 ML Co/Cu_3Au(001). (a) The black loop exhibits negative EB at 300 K, red loop training-induced positive EB at 210 K, each measured after freshly field-cooling. The dashed two loops in the respective colours are for the bilayer (as shown in Fig. 5.18) at the same temperatures for comparison. (b) and (c) show the training effect leading to positive and negative exchange bias after field-cooling from 480 K with +20 mT and -20 mT, respectively. The evolution of coercivity and exchange bias field as a function of loop number is shown in (d).

A second thinner FM2 layer (2 ML Co/7 ML Ni which has similar magnetization as that of FM1) is evaporated on the bilayer and the hysteresis loop for the trilayer is measured using longitudinal MOKE at 300 K and 210 K after each time freshly field-cooling the sample in the presence of positive magnetic field. For comparison, the resultant loops for trilayer along with the loops for bilayer (dashed loops) are presented in Fig. 5.19(a). Each of the loops is an average of up to 20 loops and arises from indistinguishable contribution from the upper and the lower interface with approximately equal effective magnetization (13 ML Ni (FM1)$\simeq$ 7 ML Ni + 2 ML Co (FM2)). At 300 K, the small EB is similar in magnitude but with opposite sign for the bilayer (positive) and trilayer (negative), but the H_C of the trilayer is slightly smaller than that of the bilayer. At 210 K, a small positive EB is observed for the trilayer compared to a relatively larger negative EB of the trained loops for the bilayer. The H_C for the trilayer is almost twice that of the bilayer. Whenever there is a positive EB induced by the training effect, whether for the bilayer (measured only at 300 K) or the trilayer, the corresponding H_C is relatively larger. A careful look shows that the training effect for the trilayer at lower temperatures results in the positive EB; the training-induced positive EB is observed. This is similar to the one mentioned above for the bilayer or trilayer which is exhibited only for a short temperature range just below T_b, but now it is observed also at lower temperatures. Except for the OoP-OoP trilayer with 41 ML $Ni_{22}Mn_{78}$, only a reduced EB without any significant training effect, has been observed in almost all of the other trilayer samples described before. To see more details of this training effect, the sample was field-cooled to 160 K and then the loops were measured. Four loops are shown in Fig. 5.19(b). Clearly, loop number 20 leads to a positive EB after the left side of every previous loop moved towards the right, reducing H_C and H_{eb}, while the right side of all loops stayed fixed. The difference in H_C and H_{eb} of the first and the second loop is dominant compared to the difference between the rest of the successive loops. Again, without any external field applied, the sample was cooled to 145 K. Still some training effect was observed, leading to a further increase of the positive EB (not shown), which means that the sample needs more than 20 reversals of magnetization at that temperature to completely release the magnetic frustration within it.

To be further convinced that this effect is not an artifact, the sample was FC in a negative magnetic field and then measured at the same temperature (160 K). The same effect is found but with an opposite sign (Fig. 5.19(c)): the training-induced positive EB is now observed as a shift to the left. This confirms that the effect is real. Fig. 5.19(d) shows the evolution of H_C and H_{eb} with an increasing number of loops at 160 K like in Fig. 5.19(b). After the first loop, the EB abruptly changes sign from negative to positive and then slowly enhances its positive value with increasing loop number. The H_{eb} value for the untrained loop (loop number 1) and trained loop (loop number 20) is very similar in magnitude, i.e., $\sim$ -8 mT and $\sim$ +8 mT, respectively. The coercivity (H_C) after training is reduced to half of its untrained value (from $\sim$ 33 mT to $\sim$ 17 mT).

The temperature-dependent behaviour of H_C and H_{eb} was checked by first field-cooling the sample to 160 K and then taking measurements by increasing the temperature up to 400 K (Fig. 5.20(a)). The corresponding H_C(T) and H_{eb}(T) curves are shown in Fig. 5.20(b). It was found that after a total of 40 hysteresis loops (20 loops at 160 K and 20 loops at 180 K), the sample was fully trained to give a maximum positive EB. By further increasing the temperature, the sample starts to exhibit a decrease in

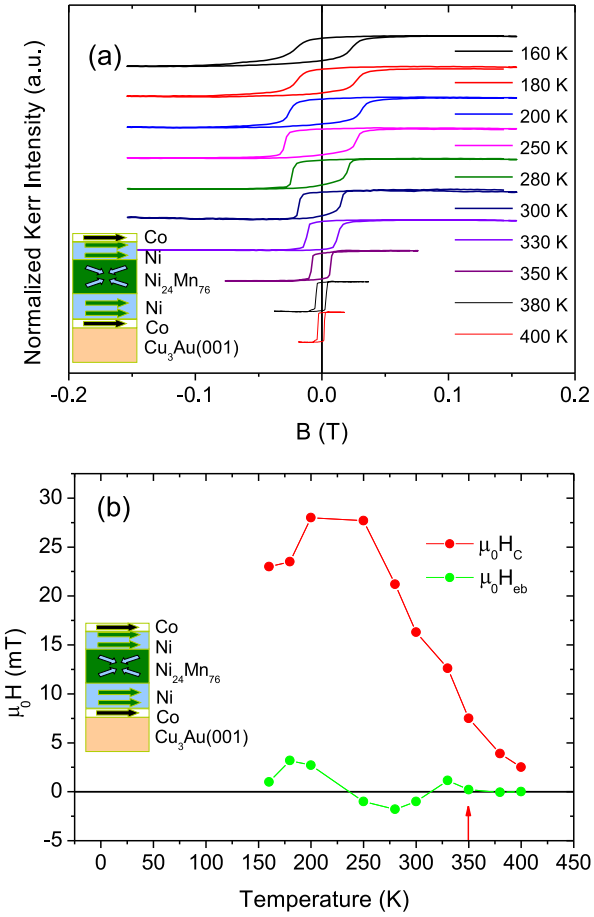

Figure 5.20: (a) Fully trained normalized hysteresis loops for the IP-IP trilayer 2 ML Co/7 ML Ni/25 ML $Ni_{24}Mn_{76}$/13.1 ML Ni/2 ML Co/Cu_3Au(001) (with thinner FM2) measured with longitudinal MOKE at different temperatures, and (b) temperature dependence of coercivity and exchange bias field for the same trilayers with the blocking temperature indicated. The sign reversal of exchange bias as a function of temperature can be seen from (b).

positive EB, going to negative H_{eb} values. In between 205 K and 250 K (near 250 K), the EB has switched its sign from positive to negative. Still at 300 K, the EB is negative but at 330 K, the sign of the EB is once again changed to small positive value (as was observed for the bilayer but only checked at 300 K) and then finally vanishes to zero at 350 K. The H_C(T) has its main peak at about 220 K and a small kink at ∼330 K where small positive EB is observed.

For the bilayer system only a small reduction of H_{eb} is observed after usual training effect at lower temperatures. A small positive EB just below T_b at 300 K is also observed, which is consistent with the observation for the bilayer system with similar Ni concentration of Ni in Ni_xMn_{100-x} as discussed in chapter 3, section 4. Therefore, the unusual training effect leading to positive EB in the trilayer at lower temperatures should come from the upper interface. To check whether only one of the interfaces is contributing to the training-induced positive EB, or whether it is a combined effect of both interfaces, the coercivities of both interfaces have to be compared. For that the thickness of the upper FM2 layer was increased by evaporating (3 ML Co/15 ML Ni) on its top. Now the effective thickness of the FM2 is (22 ML Ni + 5 ML Co). It is evident from Fig. 5.21(a) that only the upper interface is responsible for this effect, as the lower one does not show any clear training effect. The H_{eb} values for the untrained loop (loop number 1) and the trained loop (loop number 20) are ∼ -10 mT and ∼ +2.5 mT, respectively. The H_C after training is reduced from ∼30 mT to ∼12 mT as expected due to the increased thickness of FM2. A kink between the double loop in Fig. 5.20(a) could be due to some contamination at the upper interface, as the top second FM layer was evaporated after two days. The temperature-dependent loops and the

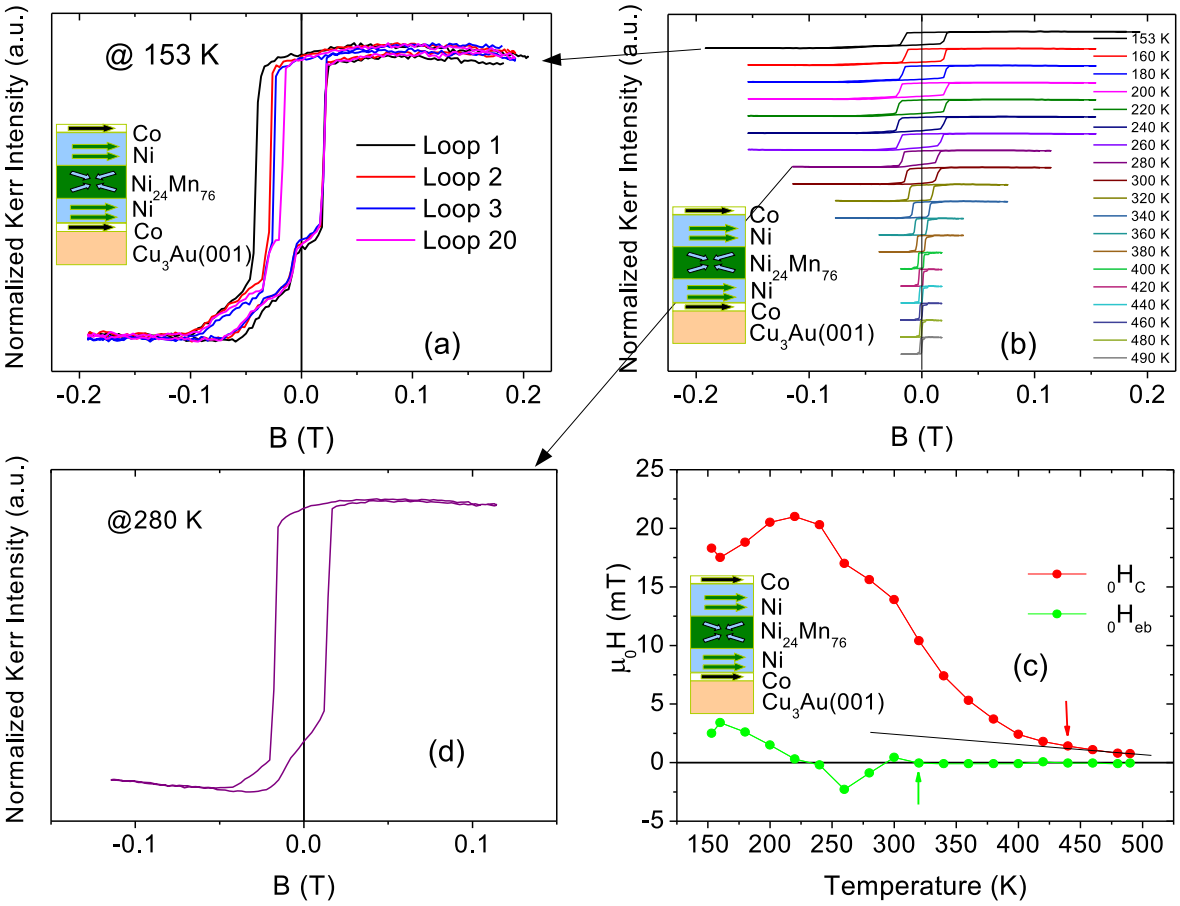

Figure 5.21: (a) Training effect leading to positive exchange bias measured with longitudinal MOKE at 153 K for the IP-IP trilayer $(7\ \mathrm{ML})_{eff}$ Co/$(22\ \mathrm{ML})_{eff}$ Ni/25 ML $Ni_{24}Mn_{76}$/13.1 ML Ni/2 ML Co/Cu_3Au(001) (with thicker FM2). (b) Temperature-dependent fully trained normalized hysteresis loops for the trilayer, and (c) the corresponding temperature dependence of coercivity and exchange bias field for the upper interface with the antiferromagnetic ordering and the blocking temperatures indicated by down and up arrow, respectively. The sign reversal of exchange bias as a function of temperature can be seen from (c). (d) The loop measured at 280 K is a zoom-in of the one in (b) and indicates that as the temperature is increased, the lower FM layer coercivity decreases faster and tries to drag the upper one to develop a negative exchange bias in the latter. Note that due to two times evaporation, the $(7\ \mathrm{ML})_{eff}$ Co and the $(22\ \mathrm{ML})_{eff}$ Ni are the effective thicknesses in the top FM layer (FM2).

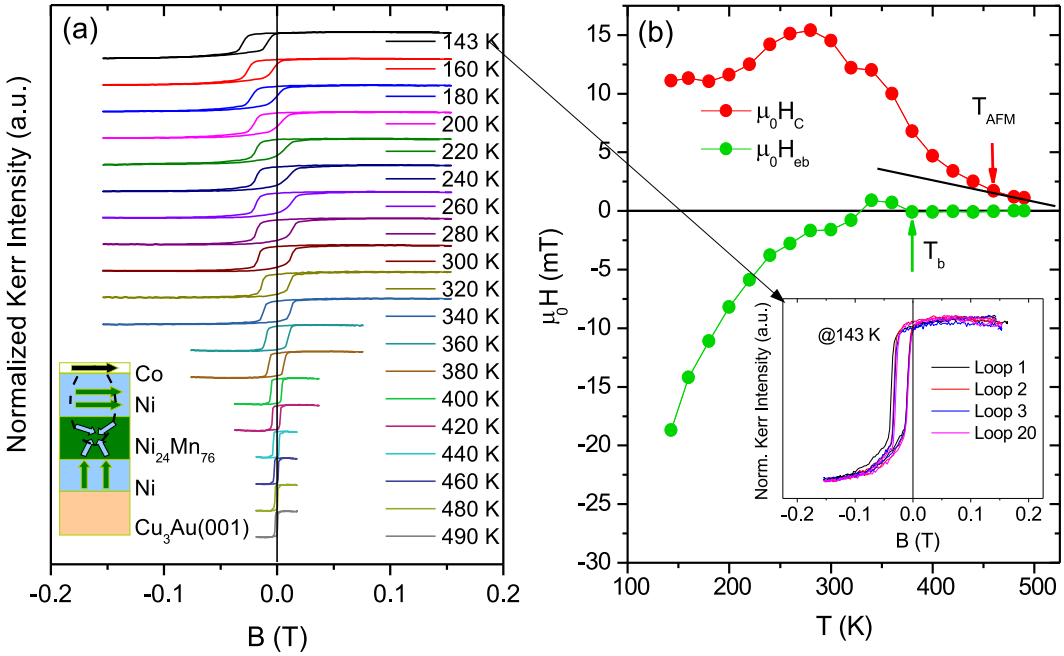

Figure 5.22: (a) Normalized hysteresis loops for the OoP-IP trilayer (7 ML)$_{eff}$ Co/(22 ML)$_{eff}$ Ni/25 ML $Ni_{24}Mn_{76}$/13.1 ML Ni/Cu_3Au(001) measured with longitudinal MOKE at different temperatures, and (b) temperature dependence of coercivity and exchange bias field for the same trilayers with the antiferromagnetic ordering and the blocking temperatures indicated. Inset: A zoomed-in loop of (a) measured at 143 K after freshly field-cooling, providing only a usual training effect. Note that due to two times evaporation, the (7 ML)$_{eff}$ Co and the (22 ML)$_{eff}$ Ni are the effective thicknesses in the top FM layer (FM2).

corresponding H_C(T) and H_{eb}(T) curves only for the upper interface are shown in Fig. 5.21(b) and Fig. 5.21(c), respectively. From 150 K to 220 K, EB is positive, in between 220 K and 240 K, the sign is changed from positive to negative, and again at 300 K it becomes positive, finally at 320 K it reduces to zero (Fig. 5.21(c)). This behaviour of EB and H_C is qualitatively very similar as observed for the trilayer with thinner FM2, except for the relatively smaller H_C for the thicker FM2, which is expected. The change of sign for EB occurs at slightly higher temperature for the upper interface with thinner FM2 (Fig. 5.20(b)) than with thicker one (Fig. 5.21(c)). Correspondingly the T_b is also slightly higher (∼350 K) for the former case than for the latter one (∼320 K). At 220 K, when the EB of the upper interface (FM2/AFM) reaches zero, some of the lower interface (AFM/FM1) spins seem to drag (switch) the spins of the upper interface (FM2/AFM) to produce negative EB at the upper interface. This can be seen from the right side of the lower interface switching which is getting closer and closer to the respective side of the upper interface at increasing temperature (Fig. 5.21(d)). At 300 K the magnetization of the FM1 (right side switching of the lower interface) switches at larger field with some negative EB than the magnetization of FM2 with no EB, and can no more drag the upper interface spins, therefore the EB at the upper interface gets vanished. Just below T_b (∼350 K), a small positive EB at 330 K along with a kink in H_C is also observed, as noted for the same interface with thinner FM2 at 300 K.

In the sample under study a very similar positive EB just below T_b was also ob-

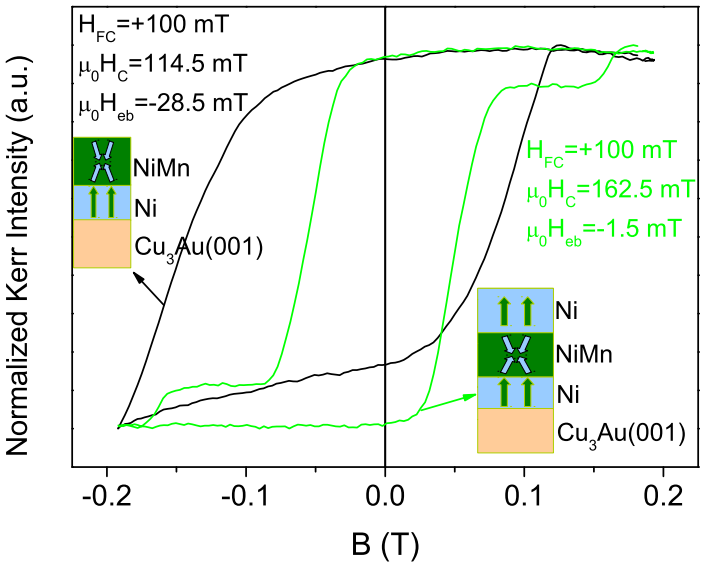

Figure 5.23: Normalized hysteresis loops at 210 K measured with polar MOKE. (a) OoP bilayer 25 ML $Ni_{24}Mn_{76}$/13.1 ML Ni/Cu_3Au(001), (b) OoP-OoP trilayer 22 ML Ni/25 ML $Ni_{24}Mn_{76}$/13.1 ML Ni/Cu_3Au(001). In both cases sample is FC with +100 mT. The OoP-OoP trilayer (smaller height/magnetization in the green loop) significantly reduces EB compared to that of the OoP bilayer (black loop). The easy axis of magnetization of the FM layers and the possible spin configuration of the AFM layer near the interface are also schematically shown indicated for each loop.

served for OoP-IP magnetization of FM1 and FM2. The corresponding temperature-dependent hysteresis loops measured with longitudinal MOKE, as well as their H_C(T) and H_{eb}(T) curves are shown in Fig. 5.22(a) and Fig. 5.22(b), respectively. A prominent peak in H_C(T) at 280 K is clearly seen from where the H_{eb} starts to increase drastically by decreasing temperature, whereas a small peak in H_C(T) at ∼350 K corresponds to the temperature range of the small positive EB shift. A relatively high blocking temperature of 380 K is observed. The usual training effect of the same interface (OoP-IP coupling) is also shown in the inset of Fig. 5.22(b). The existence of a training effect along with positive EB just below T_b in a small temperature range is similar to the case of IP-IP trilayers and is consistent with our bilayer results presented in chapter 3, section 4, for similar Ni concentration in Ni_xMn_{100-x}, and the ones found for $Ni_{81}Fe_{19}/Ir_{20}Mn_{80}$ bilayer [134]. Speculation about the presence of minority species which are strongly pinned in opposite direction to that of the regular pinned spins has been put forward to explain this behaviour [134].

Some polar MOKE measurements are also performed for the bilayer and OoP-OoP trilayer with 25 ML $Ni_{24}Mn_{76}$. The room temperature H_{eb} for the OoP bilayer is only ∼-3 mT which is hard to realize in the plot because of relatively very high H_C(T) of ∼96 mT, and for the OoP-OoP trilayer it is completely vanished. Therefore, to clearly see the difference between H_{eb} for the OoP bilayer and OoP-OoP trilayer, measurements taken only at 210 K are presented in Fig. 5.23. The -28.5 mT H_{eb} of the OoP bilayer (black loop) is decreased to -1.5 mT for the OoP-OoP trilayer (with smaller height/magnetization in the green loop). This decrease in H_{eb} is consistent with the other OoP-OoP and IP-IP trilayers studied in this chapter.

Summary: When the FM2 is thinner, the IP-IP trilayer exhibits a single hysteresis

loop with a clear peak in H_C(T) and sign reversal of H_{eb}(T). In IP bilayer, a usual training effect at lower temperatures, and an unusual training effect leading to a small positive EB shift for freshly cooled sample is observed just below T_b. In the IP-IP trilayer, an unusual training effect is observed whenever the sample is freshly FC in positive or negative field which leads to positive or negative exchange bias shift, respectively, below certain temperature. When the FM2 is made thicker, the loop could be splitted to provide two coercivities. It is observed that the positive EB contribution comes from the upper interface. The OoP-OoP trilayer significantly reduces the H_{eb} compared to the OoP bilayer.

5.2 Discussion

5.2.1 Field-cooling geometry in OoP-OoP trilayers does not affect the exchange bias

For the three trilayers with 27, 47, and 50 ML Ni_xMn_{100-x}, with OoP-OoP configuration, H_C(T) and H_{eb}(T) as well as T_{AFM} and T_b all are the same no matter whether the system is field-cooled such that both the FM layers are either parallel or antiparallel to each other (Fig. A.3, Fig. A.4, Fig. 5.4(b), Fig. 5.4(b), and Fig. 5.17(b)). From the identical H_C(T) and H_{eb}(T) as well as from the identical T_{AFM} and T_b of these three trilayers, it is evident that the trilayer system is independent of the field-cooling configuration. For the OoP-OoP trilayer with 27 ML AFM thicknesses, the H_{eb} and T_b were found significantly changed compared to the OoP-IP trilayers, and to that of the OoP bilayers. This is attributed to the interlayer coupling between the two OoP magnetized FM layers. For the thickest AFM films of 50 and 47 ML, no measurements have been performed for the OoP bilayer and OoP-IP trilayer, however, the existence of interlayer coupling can not be excluded due to the limited thicknesses of AFM layers and due to similar results as obtained for the trilayer with 27 ML $Ni_{25}Mn_{75}$. Therefore, in contrast to our observations, H_{eb} is expected to depend on the field-cooling configuration in all the three cases.

One can explain the results for two thicker samples with 47 and 50 ML Ni_xMn_{100-x} by considering that the AFM layer is treated by the two FM layers as if it (AFM layer) had provided two separate exchange-biased bilayer systems (AFM/FM1 and FM2/AFM) such that the AFM layer is somehow equally shared by the two FM layers. In this case, probably the Mauri planar domain wall width or a twist within the AFM layer from each side of the interfaces, which could be considered as one possible source for establishing EB, is smaller than half of the AFM thickness. Although, the AFM layer's spins at the interface should be polarized by the exchange coupling with the OoP magnetized FM layer, the magnetic/spin structure of the AFM layer away from the interface/s is not changed as it is insensitive to the interfacial coupling. Or in other words there is no coupling between the two FM layers through the AFM layer. However, if we exclude the interlayer coupling then the decrease in the H_{eb} and that in the T_b for the OoP-OoP trilayer with 27 ML $Ni_{25}Mn_{75}$ compared to the OoP bilayer can not be explained. Therefore, at the moment, we do not have any satisfactory explanation for these results. These results are contrary to the findings of Morales *et al.* [142] who have shown that in the trilayer system 50 nm Ni/200 nm FeF_2/50 nm Py, the magnitude of pinned uncompensated interfacial AFM moments that gives rise to EB depends not only on the interfacial spins but also on the entire bulk AFM magnetic structure.

Their conclusion is based on the result that compared to the parallel alignment of the FM layers, only by making both of them antiparallely aligned, the EB field value is significantly reduced. This is, according to the authors, due to the changed magnetic structure of the bulk AFM which exhibits its effect through the interface, and could be explained by the domain state model [143]. The Mauri model can not explain this work as the planar domain wall width for FeF_2 is only a few monolayers due to the strong FeF_2 uniaxial magnetic anisotropy [144]. Furthermore, the changed magnetic structure within the bulk of the AFM (FeF_2) has been attributed to the changed/tilted shape of the hysteresis loops of the reported system on changing the configuration of the two FM layers from parallel to antiparallel [142]. This is indeed not the case in our study, as very similar rectangularly shaped double coercivity loops can be seen for both the FM layers configuration. For the above discussion, one can say that the effect of the bulk AFM magnetic structure, as observed in Ref. [142], may not be generalized for all EB systems.

5.2.2 Non-collinear coupling between two FM layers in FM/AFM/FM trilayer

The results for the IP-IP configuration of trilayer 3 ML Co/25 ML Ni/47 ML $Ni_{17}Mn_{83}$/12.9 ML Ni/2 ML Co/Cu_3Au(001) are not the same for the case of the parallel spins alignment of the two FM layers to that of the antiparallel ones. In the case of oppositely magnetized FM layers (Fig. 5.3), H_C reduces to zero at 260 K till 280 K for FM1, where the corresponding hysteresis loop is no more a loop but a curve, and looks similar to the one for any paramagnetic material which is shifted towards negative field axis. H_C of FM1 then keeps very small values from 280 K to 380 K with tilted shape. This indicates a 90° or non-collinear coupling between the two FM layers. As mentioned in chapter 2, subsection 2.9.1, besides the collinear FM coupling across a spacer layer in a trilayer system where either parallel or antiparallel spin configuration of the top and bottom FM layer is preferred depending on the sign of the exchange coupling constant, also a non-collinear or even 90° coupling between the two FM layers is also possible because of the roughness-induced thickness fluctuations of the spacer layer, especially when the spacer layer is an AFM [145, 146, 147]. This is consistent with the Slonczewski or torsion model [96, 148] where a competition between parallel and antiparallel magnetic interlayer coupling on a length scale smaller than the typical magnetic length scale due to thickness fluctuations within the AFM layer leads to the occurrence of 90° coupling. Within this model, Pierce *et al.* have shown in Ref. [91] how the roughness can strongly influence the short-period coupling strength. The normalized short-period bilinear coupling J_1 decreases from 1 for ideal surfaces to 0.014 for an interface roughness $\sigma_t = 1$ ML. For the different behaviour of the IP-IP sample compared to the OoP-OoP one, the same reasoning as stated above (interfacial roughness) can be used because Ni is grown on 2 ML Co in the former case which might have provided rougher surface for its growth and then for the $Ni_{17}Mn_{83}$ growth compared to the case where $Ni_{17}Mn_{83}$/Ni grows directly on Cu_3Au(001). The $Ni_{17}Mn_{83}$ growth on Ni/Co certainly should have induced more thickness fluctuations in the AFM layer resulting in the 90° coupling between the two FM layers.

The temperature-dependent change in interlayer coupling is not unique as a transition from parallel to antiparallel coupling has been observed for $[Pt/Co]_4$ /MgO/ $[Co/Pt]_2$ multilayers and has been mainly attributed to the temperature-dependent

enhancement of the magnetization of the ferromagnetic layers due to dipolar coupling across the insulating MgO [149]. Also, in order to study the exchange coupling of Fe films across Cr interlayers, Fe/Cr/Fe structures have been investigated by Wolf *et al* [150]. In addition to a long range (1.8 nm) oscillation as a function of interlayer thickness, a short-period oscillation with a period of two ML and an appreciable contribution of 90°-type coupling have been reported, but no clear argument has been given for the 90° coupling [150]. In our case, it is not clear whether a non-collinear (bi-quadratic) coupling exists alone or it is there along with collinear (bilinear) coupling. For the antiparallel FM layers compared to the parallel one in the trilayer, H_C is decreased and H_{eb} increased. This favours the argument of 90°-type coupling because, a collinear coupling, as we shall see later, has an opposite effect: it increases H_C and decreases H_{eb}. In case of the co-existence of both of the couplings, we can speculate some argument for the transition from parallel to perpendicular coupling. As stated in chapter 2, subsection 2.9.1, thickness fluctuations lead to variations of the coupling strength on different terraces. The fluctuations lower the energy the most when the two magnetizations are perpendicular to each other. It seems that there is a competition between the antiparallel and the perpendicular coupling of the two FM layers across the AFM layer, and that the antiparallel spin configuration is not a favoured one. Therefore, the further increase of temperature increases the thickness fluctuations which results in a perpendicular (non-collinear) coupling at 260 K (higher temperatures).

Also the T_{AFM} and T_b are higher for the IP-IP sample than for the OoP-OoP one. This is an indication towards the possibility that the coupling strength at both interfaces is higher in the former case than in the latter—both interfaces feel the effect of each other in the IP-IP case but less in the OoP-OoP one. Therefore, we can say that due to a smaller coupling strength besides a relatively smaller interfacial roughness, no such kind of non-collinear coupling is observed for the OoP-OoP case.

5.2.3 Comparison between OoP bilayers, OoP-OoP, and IP-OoP trilayers

At 300 K, H_{eb} for the OoP-OoP trilayer 22 ML Ni/41 ML $Ni_{22}Mn_{78}$/12.5 ML Ni/Cu_3Au(001) is +6 mT. The most important point in this configuration that supports the $3Q$-like AFM spin structure as well as the interlayer exchange coupling is that when the FM2 is made IP by deposition of a Co overlayer, the OoP-IP trilayer somehow regained its higher H_{eb} at 300 K as for the bilayer alone. At 300 K, the H_{eb}=-53 mT, Fig. 5.10(b) and Fig. 5.11(a) for OoP-IP trilayer seems even higher than H_{eb}=-38 mT for the bilayer at 326 K, Fig. 5.10(b) and Fig. 5.11(d). This means that the spin orientation on the other interface significantly affects the H_{eb} of the lower interface in this trilayer system. In the OoP-IP trilayer, the lower interface (AFM/FM1) is left to couple to pinned spins with OoP component in the whole AFM layer (which we assume to have a $3Q$-like spin structure), because the top IP FM2 layer does not influence this component. Therefore, to the OoP FM1, the AFM layer is no more or very slightly shared by the top IP FM2 layer, and thus the AFM/FM1 interface gives larger EB. This also provides an indirect proof of the interlayer coupling between the two FM layers across the AFM layer and the $3Q$-like spin structure of $Ni_{22}Mn_{78}$. If there were no interlayer coupling, the reduction in H_{eb} for the OoP-OoP trilayer would not have occurred.

Some remarkable results are obtained from polar MOKE measurements for the lower interface in the trilayer with 27 ML $Ni_{25}Mn_{75}$ and 25 ML $Ni_{24}Mn_{76}$ (Fig. 5.17(a)

and (b), and Fig. 5.23). Compared to the OoP bilayer (black square symbols in Fig. 5.17), there is a clear reduction in H_C (from 136 to 145.6 mT) and H_{eb} (from -15 to -1.5 mT) at 300 K as well as in the T_b (∼70 K) for the OoP-OoP trilayer (green and cyan symbols for H_C(T) and H_{eb}(T) in Fig. 5.17(a) and (b), respectively). At 210 K, a similar decrease is observed in H_{eb} (from -28.5 to -1.5 mT) for the OoP-OoP trilayer with 25 ML $Ni_{24}Mn_{76}$ in comparison to the OoP bilayer. For the trilayer with 27 ML $Ni_{25}Mn_{75}$, when the top FM2 layer is made IP, the OoP-IP trilayer exhibits an increase in H_C and H_{eb} as well as in the T_b by ∼60 K (wine star symbols for H_C(T) and H_{eb}(T) in Fig. 5.17(a) and (b), respectively). This clearly indicates the significance of the FM layer magnetization direction in the interlayer exchange coupled trilayer through an AFM layer, as is discussed above for a similar trilayer system with 41 ML $Ni_{22}Mn_{78}$. The increase in the mentioned H_C and H_{eb} of the trilayer when the magnetic configuration is switched from OoP-OoP to OoP-IP can be explained by the very same reasoning as for the system with 41 ML $Ni_{22}Mn_{78}$. That means that the FM layer's spin orientation on the opposite interfaces not only significantly affects the H_{eb} but also the T_b of the lower interface due to change in the AFM spin structure which itself could be changed due to interfacial/interlayer coupling. In the OoP-IP trilayer, the lower interface (AFM/FM1) is left to couple to pinned spins in the whole AFM layer through the OoP uncompensated AFM spins components and is not influenced by the top layer. The top IP FM2 layer couples only to the IP spin component. That means that the AFM spin structure is non-collinear, and allow independent setting of IP and OoP spin components, as for example the $3Q$ spin structure. Therefore, to the OoP FM1, the AFM layer is no more shared by the top IP FM2 layer, and thus the AFM/FM1 interface gives a relatively larger H_{eb}(T) and T_b compared to the OoP-OoP trilayer. In the same trilayer, the relatively small reduction in T_b (∼80 K) for the OoP-OoP trilayer than for the IP-IP (∼150 K) could be due to smaller interlayer exchange coupling in the former case compared to the latter. This explanation for the reduction of H_C, H_{eb}, and T_b by the AFM spin structure change due to interlayer coupling in the trilayer is supported by results of Mitsumata *et al.* Recently, Mitsumata *et al.* have generalized their work and theoretically proved that the case of an AFM planar domain wall might not be considered equivalent to that of the FM ones, and that the AFM domain wall width could possibly be significantly smaller than that of an FM wall [68]. The AFM domain wall width depends on the spin structure. The antiferromagnetic wall width is $\sqrt{|cos\theta|}$ times smaller than the ferromagnetic one since the factor $|cos\theta| \leq 1$. The AFM thickness required to establish EB could be about $1/\sqrt{3}$ times smaller for any kind of AFM material having a non-collinear spin structure as compared to the ones with collinear spin structure [68]. Therefore, keeping in view the reduction in H_{eb}(T) and T_b, one can say that the $3Q$-like spin structure in ∼$Ni_{25}Mn_{75}$ could be modified to $1Q$ and $2Q$ in OoP-OoP (will be discussed shortly) and IP-IP trilayers, respectively.

We discuss now the remaining results of the polar MOKE measurements for the the IP-OoP trilayer. The less rectangular EB polar loops of the IP-OoP trilayer (Fig. 5.9(b)) could also be due to the same reason mentioned in section 5.2.4 for the longitudinal MOKE measurements of the IP-OoP trilayer. In the *Slonczewski torsion* model, the non-collinear coupling between FM1 and FM2 could lead to a gradual approach of the saturation magnetization of the FM layers. Here, the OoP FM2 layer seems to be slightly tilted, and exhibits slightly tilted exchanged biased loops.

Taking into account the stronger anisotropy of the IP (Ni/Co) FM layer compared

to the OoP Ni, the difference in T_b for the OoP bilayer and for the same interface of the OoP-IP trilayer can be discussed (Fig. 5.17(b)). In the polar MOKE measurements at the lower interface of the OoP-IP trilayer, the AFM spin structure could be changed from $3Q$ to $2Q$ at the upper interface (FM2/AFM). This is due to the stronger anisotropy of the IP FM2 layer, and now the system offers a smaller effective AFM thickness for the OoP lower interface (AFM/FM1). This would explain why the value of H_{eb}(T) and T_b for the OoP-IP trilayer is smaller (∼360 K) than for the bilayer (FM1/AFM) with larger H_{eb}(T) and T_b (∼390 K). This situation is exactly converse to that of the longitudinal MOKE measurements at the lower interface of the IP-OoP coupled trilayer (Fig. 5.15(b)) where due to the stronger anisotropy of the IP magnetized FM1 layer, it could transmit its coupling through larger length scales within the AFM layer, therefore gaining larger thickness contribution from the AFM compared to the OoP FM2 which is much softer. Therefore, the upper interface does not significantly influence the magnetic properties at the lower interface of the IP-OoP trilayer.

5.2.4 Comparison between IP bilayers, IP-IP, and IP-OoP trilayers

A double coercivity is observed in the as-grown IP bilayer samples when measured along one of the two axes where Co exhibits magnetic domains in opposite directions, Fig. 5.7, Fig. 5.13, Fig. 5.14, and Fig. 5.18. Therefore, the FM layer domains of which magnetization is parallel (antiparallel) to the AFM layer spins components provide negative (positive) loops shift due to EB. This kind of simultaneous negative and positive shift has been also reported for a CrMn/Co bilayer [151]. Another experimental evidence for two different types of interfacial uncompensated Fe moments in exchange-biased Co/FeF_2 bilayer has been reported where some moments are pinned and coupled parallel and some antiparallel to the FM layer [152].

The IP-IP trilayer 3 ML Co/22 ML Ni/41 ML $Ni_{22}Mn_{78}$/12.5 ML Ni/2 ML Co/Cu_3Au(001) exhibits smaller H_{eb} and different H_C than the bilayer 41 ML $Ni_{22}Mn_{78}$/12.5 ML Ni/2 ML Co/Cu_3Au(001) (Fig. 5.7). This decrease in H_{eb} (-4 mT) could be more as the bilyer is measured at 325 K whereas the trilayer at 300 K. The difference in the H_C(T) and H_{eb} of the IP bilayer and the IP-IP trilayer could be attributed in the latter case, to the thickness of the AFM layer, which could not be sufficient to provide complete planar domain walls from both interfaces. The two AFM planar domain walls penetrate into each other making most of the uncompensated pinned spins rotatable due to interlayer exchange coupling and diluting their pinning strength, even at low temperatures. This would explain that by decreasing temperature, why the H_C (H_{eb}) relatively increases (decreases) for the IP-IP trilayer compared to that of the IP bilayer. This is contrary to the bilayer, where H_C(T) exhibits a peak nearby T_b, because more and more uncompensated spins are strengthened by decreasing temperature which results in increased H_{eb} but decreased H_C. By considering different roughness in the OoP-OoP case, and a slightly varied chemical composition of the $Ni_{22}Mn_{78}$ alloy at both halves of the sample, the difference in T_b (∼60 K) for the OoP-IP trilayer compared to the IP bilayer and the IP-IP trilayer (Fig. 5.7) might be explained. This is supported by the different temperature-dependent behaviour of the corresponding H_C(T) and the H_{eb}(T) curves. Furthermore, there could exist a non-collinear interlayer coupling in the OoP-IP trilayer which may be responsible for the ∼60 K higher value of T_b, as is

observed for the trilayer with ∼47 ML $Ni_{17}Mn_{83}$ in Fig. 5.3(b).

Fig. 5.13 shows that for 32 ML $Ni_{18}Mn_{82}$, H_{eb} is 3-times decreased for the IP-IP trilayer compared to the IP bilayer at 300 K. This decrease in H_{eb} (from -35 to -11 mT at 300 K) is more compared to the IP-IP trilayer sample with 41 ML $Ni_{22}Mn_{78}$. Similar to the above argument for the IP-IP trilayer with 41 ML $Ni_{22}Mn_{78}$, we explain this by interlayer exchange coupling between the two FM layers through the AFM layer. The reason is that the IP-IP trilayer should have provided a double hysteresis loop for the two interfaces as the thickness of the FM1 is almost half that of the FM2. This is not the case for all the IP-IP trilayer samples, the double loop is compressed to a single one as the AFM thickness is decreased. For 47 ML $Ni_{17}Mn_{83}$ thickness (Fig. 5.2(a)), the loops are not well separated, and then for 41 ML $Ni_{22}Mn_{78}$ (Fig. 5.6(a) and Fig. 5.8), the double loop is converted to a single one but is more tilted. Even this tilt in the single loop is reduced when the Ni_xMn_{100-x} thickness is further reduced to the samples under discussion here, with 32 ML (Fig. 5.13), and 27 ML (Fig. 5.14(c)), where the combined loop from both interfaces becomes a more rectangular single loop. The 3-fold reduction of H_{eb} for the IP-IP trilayer with 32 ML $Ni_{18}Mn_{82}$ is because now the AFM thickness is reduced and can not provide complete domain walls between the pinned spins and both of the interfaces. Only an incomplete twist in the AFM spin structure is then possible from the both interfaces which tries to suppress the $3Q$-like AFM spin structure towards $2Q$-like. This will lead to smaller H_{eb}, as the twist (Mauri spring [27]) is actually responsible for the EB. The decrease of the AFM thickness will also strengthen the interlayer exchange coupling between the two FM layers through the sublattice magnetization of the AFM layer which will then force the AFM spins towards more IP direction near both interfaces to get $2Q$ spin structure from the $3Q$ one. This will result in decreased H_{eb} because the $2Q$ spin structure of the AFM might need larger Mauri domain wall compared to the $3Q$ one [68]. For the IP-IP trilayer with 32 ML $Ni_{18}Mn_{82}$, it seems that although the twist in the AFM spins is considerably reduced to decrease H_{eb}, some of the AFM layer still consists of the $3Q$ spin structure except at and nearby the interfaces where it has $2Q$ spin structure. If the AFM thickness is further reduced, due to enhanced interlayer coupling the twist in the AFM spins will be further decreased along with increased number of $2Q$ spins deeper inside the AFM layer from both interfaces. This kind of situation is observed for IP-IP trilayer with 27 ML $Ni_{25}Mn_{75}$, where the changed ($2Q$ from $3Q$-like) AFM spin structure not only considerably reduces the H_{eb} (from -13 to -1 mT at 300 K), but also the T_b is decreased markedly (∼150 K).

We discuss now the rest of the longitudinal MOKE measurements of bilayer with 27 ML $Ni_{25}Mn_{75}$, IP-OoP trilayer 21 ML Ni/27 ML $Ni_{25}Mn_{75}$
/12 ML Ni/2 ML Co/Cu_3Au(001). The tilt in the EB loops of the IP bilayer (Fig. 5.14(a)) is due to the different pinning strength of the local AFM frozen/pinned spins. The reason for the tilted loops of the IP-OoP trilayer may not be the same. The interlayer coupling can not only be observed through a non-magnetic spacer layer such as Cu but also through an AFM spacer layer such as Cr, Mn and FeMn. The latter with non-collinear spin structure can transmit this coupling through its thicknesses up to at least 24 ML [153]. The AFM sublattice magnetization provides an additional third degree of freedom for the interlayer coupling besides dipolar and RKKY coupling. Although this makes the situation difficult to analyze, one can still qualitatively discuss it. In an FM/AFM/FM trilayer the interlayer coupling is different from the non-magnetic spacer layers because of the magnetic state of the AFM layer especially at

the interfaces has to be taken into account. For an AFM as a spacer layer, each atom has a magnetic moment which is exchange coupled to other AFM atoms and across the interface to the ferromagnet. As a spacer layer, an AFM can no longer be considered a "passive" medium transmitting the indirect exchange coupling, rather it very actively participates in the coupling through exchange coupling at the interface as well as through the exchange coupling within itself. Therefore, for the IP-OoP trilayer (Fig. 5.14(b)), the reason for the tilted or less rectangularly shaped loops below as well as above T_b could be explained by taking into account the interlayer non-collinear coupling similar to the one discussed for the IP-IP trilayer with ∼47 ML $Ni_{17}Mn_{83}$ in Fig. 5.3(b).

Second reason for the tilt in the IP-OoP trilayer could be that when the perpendicular magnetization of the FM2 couples to IP FM1, the perpendicular anisotropy of the Ni layer (FM2) tends to orient the Ni magnetization OoP, the interlayer coupling tries to align it parallel with the IP FM1 (Ni/Co) moment because of the stronger Co anisotropy, thus leading to a canted Ni (FM2) spin configuration. Although, due to the Co underneath, the Ni (FM1) IP anisotropy should be stronger than that of the OoP Ni (FM2, still it will have some small effect on the FM1 magnetization direction—deviating it slightly from completely IP direction which will lead to the tilt in the loops shapes.

In the trilayer with 47 ML $Ni_{17}Mn_{83}$, perpendicular or non-collinear coupling was observed to provide more EB as compared to parallel coupling (Fig. 5.3(b)). The above discussion about the tilted loops of the IP-OoP trilayer suggests a non-collinear coupling between the two FM layers as well. Therefore, the increased value of H_{eb} for the IP-OoP trilayer (Fig. 5.14(b)) compared to the IP bilayer (from -13 to -19.5 mT) can be attributed to the same argument (non-collinear coupling).

5.2.5 Training-induced positive exchange bias, and temperature dependent sign reversal of exchange bias in OoP-OoP trilayer

In the OoP-OoP trilayer 22 ML Ni/41 ML $Ni_{22}Mn_{78}$/12.5 ML Ni /Cu_3Au(001), for parallel spin configuration of the two FM layers, a positive EB shift for the lower interface is observed in a certain temperature range below the blocking temperature (Fig. 5.10). This could be either a "real" EB arising due to different arrangement of the pinning cites at the interface or inside the AFM layer which changes the AFM spin structure at the interface, or an "artificial" EB arising from an antiparallel magnetic coupling between the two FM layers through the AFM layer, or even borh of them together.

For discussing the different arrangement of the pinning cites as a reason for the positive EB shift, the loops measured with polar MOKE at room temperature are important (Fig. 5.11(a–d)). These loops are measured only at room temperature after the sample is freshly field-cooled, i.e., they are not taken from temperature-dependent measurements. The decrease in H_{eb} for the OoP-OoP trilayer at the lower interface compared to the OoP bilayer could be expected by arguing that the AFM layer is shared by the two interfaces. The main point of the OoP-OoP trilayer is that both interfaces are antiparallely coupled whether they are as-grown or FC with either positive or negative field. This anomalous behaviour of the OoP-OoP trilayer, especially at the lower interface, could be discussed with the help of Fig. 5.24, where the OoP-OoP

sample (before deposition of a Co over-layer) is field-cooled with +200 mT from 500 K to 300 K, and then the hysteresis loop is measured. It was surprising to see that the positive EB at 300 K is actually induced by a training effect. Due to the FC, the AFM spins are frozen at room temperature in the bilayer AFM/FM1 to give negative EB: both the FM1 magnetization and the OoP uncompensated spin's component of the AFM layer are in upward direction. An addition of one or two effective AFM layers provides a net AFM spin component which leads to either a parallel or an antiparallel interlayer coupling [133]. This could be one possible reason that just by co-incidence the condition for the antiparallel coupling in the OoP-OoP coupled trilayer is fulfilled and thus for the as-grown sample opposite EB shift is observed at both interfaces. The same argument for the antiparallel coupling could answer the question why we could not observe this antiparallel coupling for the other trilayer samples except the IP-IP trilayer with 25 ML $Ni_{24}Mn_{76}$. For large thickness to grow so smooth is less likely but not impossible. Probably the 41 ML $Ni_{22}Mn_{78}$ film growth is very smooth, it provides an effective odd number of atomic monolayers with OoP uncompensated spins component looking down at the top interface. Therefore, when the top OoP magnetized FM2 layer is deposited, it also gets parallel (downward) direction with the uncompensated AFM spins components such that the as-grown sample provides a negative EB shift for the AFM/FM1 interface, and positive for the FM2/AFM (Fig. 5.11(b)). When the sample is positively FC, at both interfaces the uncompensated OoP AFM spins components follow the FM spins in the direction of the applied field. The coupling through the AFM layer is then frustrated. During the hysteresis loop measurement at room temperature, this frustrated effective AFM atomic mono layer is pushed to the lower interface while rearranging the AFM spins so as to release the frustration. This resulted in the training-induced positive EB at the lower interface of the OoP-OoP coupled trilayer (Fig. 5.24).

By the application of positive and negative field for FC, the frustrated region within the AFM could be moved back and forth between the two interfaces which correspondingly changes the direction of EB, as is evident from Fig. 5.11(b). The interlayer coupling is mediated by the antiparallel nearest-neighbour exchange interaction in the AFM layer, which has the ability to transfer any local modification of the spin structure at one interface to the other. Magnetization loops of Co/FeMn/Co trilayer have been reported to reveal a direct interlayer magnetic coupling across the FeMn antiferromagnetic layer for different thicknesses of the Co bottom layer and the FeMn antiferromagnetic layer [133]. The common feature between this reported work and that of the recent one is the magnetic coupling between the two FM layers through the AFM layer. The main differences are the thickness of the AFM layer and the magnetization direction of the FM layers. Kuch *et al.* [133] have used smaller thicknesses of AFM layer (13–14 ML FeMn) and IP magnetization of the FM (Co) layers compared to our thicker AFM layer (41 ML $Ni_{22}Mn_{78}$) and OoP magnetization of the FM (Ni) layers. Also, the thicknesses of the FM and AFM layers are very precisely controlled in the referred work which, in our case, was possible only with certain error as mentioned in the beginning of this chapter.

Or, another explanation could be that there exist some "pinning species" or "pinning domains" in the AFM layer, as has been proposed in domain state model [143]. It is possible to strongly influence EB by replacing magnetic atoms by nonmagnetic ones or by defects not at the FM/AFM interface, but rather throughout the volume of the AFM. This could lead to form domains with net magnetic moment within the AFM

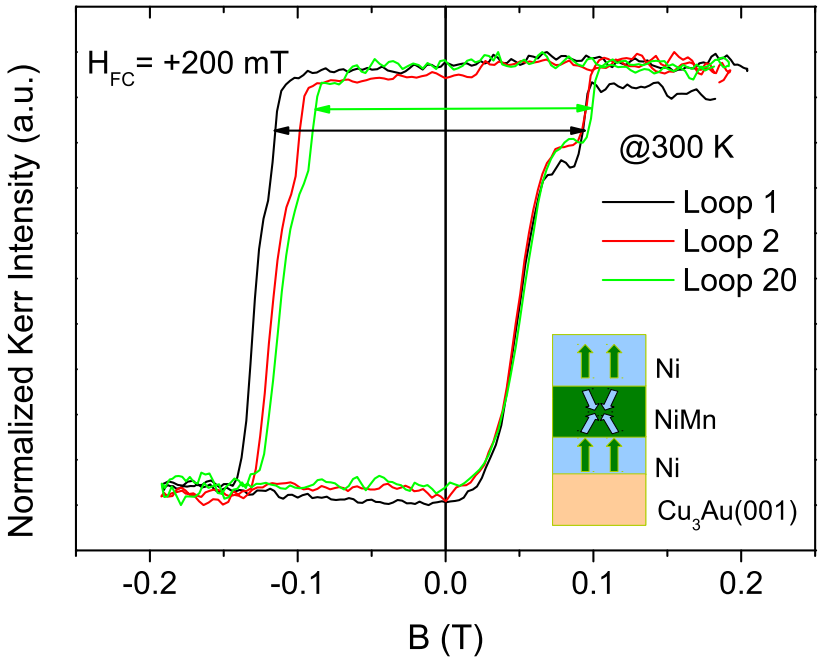

Figure 5.24: Training-induced positive exchange bias at the lower interface of the OoP-OoP trilayer 22 ML Ni/41 ML $Ni_{22}Mn_{78}$/12.5 ML Ni/Cu_3Au(001) measured with polar MOKE at 300 K. For lower interface, before training, H_C=105 mT, H_{eb}=-11.5 mT, and after training (20th loop), H_C=94 mT, H_{eb}=+5.5 mT. For upper interface, before training, H_C=90 mT, H_{eb}=-41.5 mT, and after training (20th loop), H_C=81.5 mT, H_{eb}=-31.5 mT.

which can affect the spin arrangement and the FM/AFM exchange interaction at the interface. If the average number of these domains or pinning centres is in the same direction, EB will be more, and less in the opposite case. Also, if these domains are near to the interface, the twist in the AFM spins would be smaller, and consequently smaller EB will be observed. In our case, these kind of domains can favour the upper and lower interfaces to provide opposite EB shift. This could be the reason for the smaller opposite EB in the OoP-OoP trilayer, Fig. 5.10(b) and Fig. 5.11(b). This kind of small positive EB has been reported by Radu *et al.* [154] and Mishra *et al.* [134] for different FM/AFM bilayer systems. Usually for high cooling fields, positive exchange bias is obtained [86, 155] when the external field exceeds the interfacial coupling, changing the parallel alignment between the FM and AFM spins to antiparallel. In our case, during the field cooling procedure a minority species of the uncompensated interfacial AFM spin's component might have preferred to align antiparallel to the direction of the FM layer. This could result in a typical negative EB but with small positive EB field contributed by the antiparallely aligned uncompensated spin's component of this spin fraction. Such a small number of very strongly pinned spins could manifest themselves in a positive EB at higher temperatures near T_b, where the majority of parallely aligned spins responsible for the usual negative EB have lost their pinning strength and are dragged by the adjacent FM layer irreversibly. When the sample is freshly FC only to room temperature where positive EB is observed, it is found that an associated training effect led to the positive EB due to the assumed strongly anchored AFM spin components. A similar training effect has been reported for an IP coupled bilayer $Ni_{81}Fe_{19}/Ir_{20}Mn_{80}$ [134]. This supports the assumption of a strongly anchored

minority species of spins. The weak point is that we have to ignore the small negative EB at 330 K by considering this temperature as T_b, and also, importantly it can not explain the significant reduction of H_{eb} of the OoP-OoP trilayer compared to the OoP bilayer and OoP-IP trilayer. This kind of small positive EB just below T_b is found to be a feature of only IP samples (not for OoP samples) with Ni concentration above 22% in Ni_xMn_{100-x} as is discussed in chapter 3, section 4 as well as bi/trilayer with 25 ML $Ni_{24}Mn_{76}$ in this chapter. Therefore the interlayer coupling has to be considered the preferred reason for this effect and we can can exclude that this positive EB shift could be due to this kind of unusual strongly pinned species in opposite direction.

The temperature-dependent sign reversal of EB can be discussed by taking into account the interlayer exchange coupling mediated by the sublattice magnetization of the AFM layer. Since the thicknesses of both FM layers are different, the $H_C(T)$ behaviour is also different. Still the coercivities of both of the loops can coincide by coincidence (Fig. 5.9(a)). When the magnetizations of the two FM layers happen to switch at the same field, the interfacial coupling favours this together switching and resists if one of the FM layers wants to change its coercivity by changing temperature, thus creating an "artificial"EB at the interface of which magnetization is resisted from changing. In this case, the sign of EB is dictated by the interface which requires more energy to be switched. This is apparent from the left sides of the loops at and below 260 K, and the right side of the loop at 330 K, where for the lower interface a small negative EB is artificially created in spite of positive one. In other words, the small negative EB just below T_b and below 260 K can be explained by speculating that there exists some competition between the positive EB due to the interlayer coupling and the negative EB due to intelfacial coupling. At lower temperatures, the latter overcomes the former. While increasing the temperature, a similar interlayer coupling transition but from FM to AFM has been recently observed for $[Pt/Co]_4$ /MgO/ $[Co/Pt]_2$ multilayers. This has been mainly attributed to the temperature-dependent enhancement of the magnetization of the ferromagnetic layers by taking into account dipolar coupling across the insulating MgO [149]. Here, in our case, we cannot omit the possibility of having this kind of coupling.

5.2.6 Training-induced positive exchange bias, and temperature dependent sign reversal of exchange bias in IP-IP trilayer

The possible reasons for the training-induced positive EB in the IP-IP trilayer 3–8 ML Co/7–25 ML Ni/25 ML $Ni_{24}Mn_{76}$/13.1 ML Ni/2 ML Co/Cu_3Au(001) are discusses in the following. As mentioned before, by making the FM2 layer thicker to distinguish between the coercivities arising from the lower and upper interfaces, it was observed that the origin of the training-induced positive EB is the upper interface Fig. 5.21. The intefacial roughness or thickness fluctuations within this sample seem to be significantly different from the other studied IP samples presented in this chapter which resulted in anomalous behaviour of the system. Otherwise, it should have provided with reduction in EB along with reduced T_b as observed for similar sample discussed above, and should not have resulted in training-induced positive EB. It is possible that due to the roughness or thickness fluctuations in the AFM/FM1 bilayer, the effective thickness of the AFM is such that the AFM spins make a kind of Mauri's spring and, after FC, the AFM is ferromagnetically coupled to the FM1 at the lower interface but at the upper

interface it has an antiparallel spin configuration to that of FC direction. Let us assume that for our system a parallel spin configuration is favoured at the interface, that is, the FM and the AFM spins like to be aligned parallel to each other. When the second FM (FM2) is evaporated on top of the AFM/FM1 bilayer, the unfavoured (antiparallel) spin configuration is attained at the upper interface (FM2/AFM). When the trilayer system (FM2/AFM/FM1) is field-cooled, both interfaces get a parallel spin configuration. If now the effective AFM thickness corresponds to an odd number of monolayers, corresponding to antiparallel coupling the two FM layers, there should be a frustration within the AFM layer at somehow equal distance from both interfaces, leading to a kind of domain wall parallel to the interfaces [97, 98, 156]. In our case, these spins stay frustrated waiting for an opportunity to release their frustration. During the hysteresis loop measurement the domain wall due to the frustrated effective mono-layer's spins is removed to relieve the frustration such that the upper interface is "compelled"to get an unfavoured antiparallel (antiferromagnetic) spin configuration which should give positive H_{eb}. Now there is a competition between negative and positive H_{eb} from the lower and the upper interface, respectively. In units of Ni magnetization, the effective thicknesses for the FM2 and FM1 are: t_{FM2}=16 ML and t_{FM1}=19 ML, respectively. Thus intuitively, one can think that as both of the FM layers are having similar effective thicknesses and similar coercivities, therefore they should switch together during hysteresis loop measurement, and the contribution towards EB from both the interfaces should be similar but with opposite sign to give zero net H_{eb}. But this is not the case, as positive EB is finally obtained after training although both of the FM layers switch together. This cannot be simply due to a slightly smaller thickness of the FM2 compared to that of the FM1, as we know that H_{eb} is inversely proportional to the FM layer thickness.

Apparently, it seems that the upper interface provides a larger positive EB compared to the negative EB of the lower interface; which along with a rearrangement of the frustrated spins during the hysteresis loop measurement leads to the training-induced positive EB of the whole system. The trilayer with thicker FM2 (40 ML in units of Ni magnetization) provides two coercivities such that at 160 K, H_{eb} of ∼+2.5 mT is obtained for the upper interface after training and ∼-55 mT for the lower interface, which does not show any training effect. Before second time evaporation of the FM2, the trained loop of the trilayer with thinner FM2 (16 ML in units of Ni magnetization) provides an H_{eb} of +8 mT at a similar temperature (∼160 K). Since the thickness of the FM1 (19 ML in units of Ni magnetization) remains constant all the times, which should provide the same H_{eb} (-55 mT), no matter whether the FM2 is thinner or thicker (by considering the same anisotropy for both FM layers). Therefore an H_{eb} shift of roughly ∼+83 mT and ∼+30 mT is expected for the upper interface when the FM2 is thinner and thicker, respectively. Correspondingly this should lead to the training induced positive ∼+28 mT and negative ∼-20 mT EB for the respective two thicknesses of FM2. This is of course not the case. This certainly suggests that some other mechanisms than the higher positive EB field value at the upper interface that induces the net positive EB after training should be effective.

It could be that the ferromagnetic interlayer coupling strength is playing a key role, i.e., it is different when the magnetization of both FM layers switches together than in the other case; being stronger in the former situation than in the latter one. This statement is supported by Fig. 5.21(a) where, if the interlayer coupling had the same strength for the ferromagnetically coupled two FM layers during loops measurement

of different coercivities, then due to the upper interface an associated positive training is expected in the negatively shifted loop of the lower interface, which is not observed. As the antiparallel spin alignment at the upper interface is not a favoured situation and was only formed to release the frustration, therefore it is in a high energy state, and a smaller field is required to overcome the hindering of the uncompensated pinned spins at the upper interface. Due to the identical coercivity for the thinner FM2, the stronger interlayer coupling overcomes the interfacial coupling and makes it favourable for all spins of the lower interface to follow the easy switching of the upper interface spins, thus training-induced positive EB is established.

The two times temperature-dependent sign reversal of EB can also be discussed in terms of the assumptions made above. With increasing temperature, the trilayer system (with thinner as well as thicker FM2) first changes sign for EB from positive to negative just below 250 K (Fig. 5.20(b) and Fig. 5.21(c)). There is a competition between the positive EB of the upper interface favoured by the interlayer exchange coupling and the negative EB of the lower interface, which is finally won by the latter. During the training effect leading to the positive EB, the antiparallel alignment of the AFM spins should have needed more energy as compared to its parallel alignment with the FM magnetization set by field-cooling. Therefore even in this antiparallel spin configuration, the upper interface is not in its minimum energy state, and smaller thermal energy (temperature) compared to the lower interface is required to cancel the EB. Though being larger in combined effect with the interlayer exchange coupling, the upper interface positive H_{eb} decreases faster compared to the negative H_{eb} of the lower interface. On the other hand the lower interface being in its minimum energy state set by FC, is more stable and still has pinned spins giving rise to negative EB even after the positive EB of the upper interace is vanished. The second sign reversal for H_{eb} between 300 K and 330 K (280 K and 300 K) for the trilayer with thinner (thicker) FM2 respectively, could originate from a different reason. This could be attributed to a strongly pinned minority species of spins deep inside the AFM layer. These kind of spins are reported to be the cause of positive EB nearby (just below) T_b in a small temperature range [134].

For the trilayer $(7\ \text{ML})_{eff}$ Co/$(22\ \text{ML})_{eff}$ Ni/25 ML $Ni_{24}Mn_{76}$/13.1 ML Ni/2 ML Co/Cu_3Au(001), one possible reason for higher T_b (∼380 K in Fig. 5.22) for the OoP-IP compared to IP-IP coupling (∼350 K or ∼320 K in Fig. 5.20 and Fig. 5.21), for otherwise identical conditions, could be a different morphology. This difference of T_b can also be discussed in terms of the interlayer IP-IP and OoP-IP coupling on the AFM spin structure. In chapter 3, section 4, for the concentration-dependent study of the bilayer system Ni_xMn_{100-x}/Ni(Co)/Cu_3Au(001), a deviation of Ni_xMn_{100-x} $3Q$-like spin structure was speculated to explain the results: the three-dimensional non-collinear spin structure of Ni_xMn_{100-x} rotates from ordered and more-OoP to disordered and more-IP direction when the Ni concentration in Ni_xMn_{100-x} is decreased from ∼50 to ∼20%, which is associated with increased magnetic anisotropy as well. Therefore, for the IP-IP spin configuration of FM1 and FM2, the interfacial AFM spins most probably are inclined towards more IP or completely IP direction from their intrinsic non-collinear $3Q$-like spin structure (with IP spin component larger than OoP) at both interfaces.

For the OoP-IP trilayer, the AFM spin structure is changing from more-IP towards slightly OoP direction to get its intrinsic spin structure while moving from the upper interface (FM2/AFM) towards the lower interface (AFM/FM1) as schematically shown

in Fig. 5.11(c) and (d). After field-cooling in IP direction, most likely, the AFM spin structure cannot be considerably influenced by the OoP magnetized FM1 at the lower interface because of the smaller magnetic anisotropy of Ni (FM1) compared to that of (Co/Ni) (FM2). In other words, a larger effective thickness of the AFM is coupled to the IP magnetized FM2, and a smaller one stays coupled with the OoP magnetized FM1 which results in a higher value of H_{eb} and T_b compared to IP-IP trilayer.

Chapter 6

Summary and conclusions

The antiferromagnetism of Ni_xMn_{100-x} films has been probed contacted with ferromagnetic Ni in exchange-biased bilayers and trilayers on $Cu_3Au(001)$. For that, the growth and structure of single crystalline Ni_xMn_{1-x} ultrathin films on $Cu_3Au(001)$ are investigated first. For the Ni_xMn_{1-x} films ($10 \leq x \leq 77$), our results revealed epitaxial, layer-by-layer growth at a substrate temperature of 300 K. A weak signal of a c (2×2) superstructure was observed at the surface of the NiMn films for all the investigated concentrations. The average perpendicular interlayer distance of the NiMn alloy films decreases from 1.88 Å at x=10 to 1.69 Å at x=77. The lattice parameters of equiatomic NiMn films were determined to be 3.52 Å perpendicular to the sample surface and 3.76 Å in the sample plane, indicating an fct structure as expected for the $L1_0$ NiMn phase, which has its c-axis along the film normal, i.e., c-axis growth.

Thickness-dependent H_C of polar MOKE measurements on OoP magnetized NiMn/ 9.3 ML Ni/$Cu_3Au(001)$ showed that ∼7 ML of equi-atomic single-crystalline NiMn order antiferromagnetically at room temperature. It is further observed that NiMn thin films as an AFM material can couple to both OoP as well as IP magnetized ferromagnetic Ni films. The finite-size effect of T_{AFM} for NiMn is observed both in IP and OoP cases. The ordering temperature of NiMn is much higher when coupled to Ni magnetized in OoP than in IP direction. This shift of ordering temperature (as high as 110 K), while switching the interfacial coupling from perpendicular to in-plane by manipulating the Ni magnetization direction, is the result of a magnetic proximity effect which in turn is either due to (i) a different interface coupling strength in the two cases or/and (ii) the NiMn spin structure itself, which is distorted in such a way that it is thermally more stable when coupled to OoP magnetized Ni compared to IP one. An exchange-bias effect is only observed for the thickest NiMn film studied (35 ML), where slightly higher T_b and H_{eb} values for OoP samples than for IP ones are observed and attributed to the influence of T_{AFM}. On the basis of these findings, it can be concluded that the spin structure of equi-atomic NiMn thin film alloys epitaxially grown on Ni/(Co/)$Cu_3Au(001)$ is either non-collinear, at variance from its collinear bulk spin structure [42, 45], or that the NiMn spins follow the spin orientation of the adjacent Ni layer under the respective field-cooling directions.

The concentration-, thickness-, and temperature-dependent magnetic properties of Ni_xMn_{1-x}/Ni/(Co/)$Cu_3Au(001)$ bilayers coupled in IP and OoP direction have been investigated. For T_{AFM} of Ni_xMn_{1-x}, the Ni concentration between ∼35% and ∼28% is critical, above (below) which T_{AFM} for the OoP (IP) samples is higher than for the IP (OoP). Another important result is that both IP and OoP samples show larger

H_{eb}, and that T_{AFM} and T_b saturate at much smaller thicknesses of Ni_xMn_{1-x} for smaller x compared to larger x. In the exchange-biased bilayer system, the supposedly non-collinear $3Q$-like spin structure of Ni_xMn_{1-x} is found to be very sensitive on the concentration which results in different magnetic properties when coupled to IP or OoP magnetized adjacent Ni layer. An intuitive model is proposed that is able to explain our results. It correlates different magnetic anisotropy energies with different spin structures of Ni_xMn_{1-x}, which change as a function of x. According to this model, the three-dimensional non-collinear spin structure of Ni_xMn_{1-x} deviates from more-OoP, to more-IP direction when x is decreased from ∼50 to ∼20%. At the same time the magnetic anisotropy energy (MAE) increases. The enhanced MAE leads to smaller domain wall widths within the Ni_xMn_{1-x} films. Our results suggest that the disordered AFM Ni_xMn_{1-x} alloys with smaller x, having a non-collinear spin structure and increased MAE, are favourable for the for reducing the critical thickness for the onset of EB, and saturation of T_{AFM} and T_b.

To further explore the subtle nature of EB, trilayers of Ni/Ni_xMn_{1-x}/Ni on $Cu_3Au(001)$ are studied in detail, while manipulating the easy axis of magnetization of one or both of the FM Ni layers by the deposition of an adjacent Co layer. Several trilayer samples have been measured by longitudinal and polar MOKE. The thickness of the Ni_xMn_{1-x} films ranged from 25 to 50 ML and $17 \leq x \leq 25$. In this composition range, the T_b's and the T_{AFM}'s for the IP samples are always higher than for the OoP ones. The reason for choosing this thickness and composition range of Ni_xMn_{1-x} is the respective study of bilayers, where a stronger H_{eb} and higher T_b as well as higher T_{AFM} were found as stated above. The following results for the trilayers are observed which are mainly attributed to an interlayer exchange coupling between the two FM (Ni) layers across the supposedly $3Q$-like spin structure of the AFM (Ni_xMn_{1-x}) layer.

1. There is no significant difference observed in T_b for the trilayers and the corresponding bilayers. However, H_{eb} is always found smaller for IP-IP and OoP-OoP configuration of FM layers magnetization in an FM/AFM/FM trilayer compared to the corresponding AFM/FM bilayer with IP and OoP magnetization. This difference of H_{eb} increases as the thickness of the Ni_xMn_{1-x} layer decreases. When the AFM layer thickness is reduced to 27 ML, a significant reduction in H_{eb} is observed along with markedly reduced T_b of ∼150 K and ∼90 K for trilayers with IP-IP and OoP-OoP configurations of FM layers, respectively, compared to the corresponding bilayer. Besides a distortion of the spin structure of Ni_xMn_{1-x} due to an interlayer exchange coupling, these results are attributed to an incomplete planar domain wall within the AFM layer. The AFM layer can not provide a complete planar domain wall to each of the two interfaces when its thickness is reduced, and from both interfaces the AFM planar domain walls penetrate into each other to dilute the EB strength.

2. H_{eb} is always smaller for IP-IP and OoP-OoP trilayers compared to IP-OoP and OoP-IP trilayers, repectively, at similar temperatures. This can be explained by a non-collinear spin structure of Ni_xMn_{1-x}. The IP and OoP components of such a spin structure of Ni_xMn_{1-x} independently couple to the FM layers in the corresponding direction. This way the AFM layer is not completely shared any more by the two interfaces and thus H_{eb} is increased. This means that for a specific system, H_{eb} can be switched on and off just by manipulating the magnetization direction of the top FM layer. This result also justifies the assumption of a non-collinear spin structure of Ni_xMn_{1-x}.

3. A training-induced positive EB shift, and a sign reversal of EB with increasing

temperature are two other interesting results for the thinnest studied IP-IP trilayer with 25 ML $Ni_{24}Mn_{76}$ as well as for OoP-OoP trilayer with 41 ML $Ni_{22}Mn_{78}$. In both cases, the two interfaces of the trilayers provide opposite EB shift, one is favoured by the system and the other not. This results in frustration of AFM spins when the system is field-cooled, which is released in the form of training-induced positive EB during the reversal of magnetization while measuring the loops. The temperature-dependent sign change of EB could be due to the interplay between interlayer and interfacial coupling.

4. No difference is observed in $H_C(T)$ and $H_{eb}(T)$ as well as in T_{AFM} and T_b for three OoP-OoP trilayers with 27, 47, and 50 ML Ni_xMn_{1-x} when the samples are field-cooled either in positive field direction, negative field direction, or in such a way that one of the interfaces is set to give a positive exchange bias shift and the other one a negative. Since both bilayer as well as trilayer measurements have been performed for the thinner sample with 27 ML Ni_xMn_{1-x} (not for the thicker two samples) which showed different results from each other due to interlayer coupling, therefore the identical magnetic properties for the opposite FC geometries for all the three cases seem to be independent of the interlayer coupling.

5. Some signs of perpendicular interlayer coupling are also observed, particularly for the IP-IP coupled trilayer with ∼47 ML $Ni_{17}Mn_{83}$, when the two FM layers have opposite magnetization which can be attributed to thickness fluctuations of the AFM layer.

In summary, the concentration-dependent lattice structural changes in single crystalline Ni_xMn_{1-x} on $Cu_3Au(001)$ seem to be strongly correlated with changes in its spin structure which offers it to exhibit interesting magnetic properties in IP and OoP direction in exchange-biased bi- and trilayers. Besides its technological relevance, an interesting and rich physics lies in the study of single crystalline Ni_xMn_{1-x} which could be be further explored by means of other techniques like X-ray magnetic circular dichroism-photoelectron emission microscopy (XMCD-PEEM) to get layer/element-resolved magnetic domain images in exchange-biased system, and spin-polarized scanning tunnelling microscopy (SP-STM) in order to further elucidate its non-collinear spin structure.

Bibliography

[1] G. A. Prinz, Science **282**, 1660 (1998)

[2] *Special issue on magnetoelectronics*, Phys. Today (1995)

[3] J. F. Gregg, I. Petej, E. Jouguelet, and C. Dennis, J. Phys. D: Appl. Phys. **35**, 121 (2002)

[4] *Spin Electronics*, Ed. by M. Ziese and M. J. Thornton, (Springer, Berlin, 2001)

[5] Y. Wu, Nano Spintronics for Data Storage in *Encyclopedia for Nanoscience and Nanotechnology, vol.7*, Ed. by H. S. Nalwa (American Scientific Publishers, Valencia, CA, 2003), p. 493

[6] J. M. Dauton, Thin Solid Films **216**, 162 (1992)

[7] J. M. Dauton, J. Appl. Phys. **81**, 3758 (1997)

[8] S. S. P. Parkin, K. P. Roche, M. G. Samant, P. M. Rice, R. B. Beyers, R. E. Scheuerlein, E. J. O'Sullivan, S. L. Brown, J. Bucchigano, D. W. Abraham, Yu Lu, M. Rooks, P. L. Trouilloud, R. A. Wanner, and W. J. Gallagher, J. Appl. Phys. **85**, 5828 (1999)

[9] S. Tehrani, E. Chen, M. Durlam, M. Deherrera, J. M. Slaughter, J. Shi, and G. Kerszkowski, J. Appl. Phys. **85**, 5822 (1999)

[10] *Molecular Beam Epitaxy*, Ed. by A. Cho, (AIP, New York, 1994)

[11] L. L. Chang, L. Esaki, W. E. Howard, and R. Ludeke, J. Vac. Sci. Technol. **10**, 11 (1973)

[12] T. Shinjo and T. Takada, *Ferromagnetic Materials*, Ed. by E. P. Wohlfarth, (Elsevier, Amsterdam, **3**, 1987)

[13] G. Binasch, P. Grunberg, F. Saurenbach, W. Zinn, Phys. Rev. B **39**, 4828 (1989)

[14] M. N. Baibich, J. M. Broto, A. Fert, F. Nguyen van Dau, F. Petroff, P. Etienne, G. Creuzet, A. Friederich, and J. Chazelas, Phys. Rev. Lett. **61**, 2472 (1988)

[15] J. Stöhr, H. C. Siegmann, *Magnetism From Fundamentals to Nanoscale Dynamics*, (Springer Series in solid state sciences **152**, Berlin Heidelberg, 2006)

[16] X. Wang and A. M. Taratorin, *Magnetic Information Storage Technology*, (Academic, New York, 1999)

[17] H. N. Bertram, *Theory of Magnetic Recording*, (Cambridge University Press, Cambridge, 1994)

[18] J. C. Mallinson, *Magneto-Resistive Heads: Fundamentals and Applications*, (Academic, New York, 1996)

[19] E. M. Williams, *Design and Analysis of Magnetoresistive Recording Heads*, (Wiley, New York, **161**, 2001)

[20] W. H. Meiklejohn and C. P. Bean, Phys. Rev. **102**, 1413 (1956)

[21] J. Nogués and I. K. Schuller, J. Magn. Magn. Mater. **192**, 203 (1999)

[22] A. E. Berkowitz and K. Takano, J. Magn. Magn. Mater. **200**, 552 (1999)

[23] R. L. Stamps, J. Phys. D: Appl. Phys. **33**, 247 (2000)

[24] M. Kiwi, J. Magn. Magn. Mater. **234**, 584 (2001)

[25] L. Néel, Ann. Phys. Paris **2**, 61(1967)

[26] A. P. Malozemoff, Phys. Rev. B **35**, 3679 (1987)

[27] D. Mauri, H. C. Siegmann, P. S. Bagus, and E. Kay, J. Appl. Phys. **62**, 3047 (1987)

[28] N. C. Koon, Phys. Rev. Lett. **78**, 4865 (1997)

[29] T. C. Schulthess and W. H. Butler, Phys. Rev. Lett. **81**, 4516 (1998).

[30] T. C. Schulthess and W. H. Butler, J. Appl. Phys. **85**, 5510 (1999)

[31] M. Kiwi, J. Mejía-López, R. D. Portugal, and R. Ramírez, Appl. Phys. Lett. **75**, 3995 (1999)

[32] S. Zhang, D. Dimitrov, G. C. Hadjipanayis, J. W. Cai, and C. L. Chien, J. Magn. Magn. Mater. **198-199**, 468 (1999)

[33] M. Lederman, IEEE Trans. Magn. **35**, 794 (1999)

[34] T. Lin, C. Tsang, R. E. Fontana, and K. K. Howard, IEEE Trans. Magn. **31**, 2585 (1995)

[35] W. Kuch, L. I. Chelaru, F. Offi, J. Wang, M. Kotsugi, and J. Kirschner, Phys. Rev. Lett. **92**, 017201 (2004)

[36] C. H. Marrows, Phys. Rev. B **68**, 012405 (2003)

[37] F. Offi, W. Kuch, and J. Kirschner, Phys. Rev. B **66**, 064419 (2002)

[38] A. J. Devasahayam and M. H. Kryder, IEEE Trans. Magn. **35**, 649 (1999)

[39] G. W. Anderson, Y. Huai, and M. Pakala, J. Appl. Phys. **87**, 5726 (2000)

[40] E. Krén, E. Nagy, I. Nagy, L. Pál, and P. Szabó, J. Phys. Chem. Solids **29**, 101 (1968)

[41] B. Dai, J. W. Cai, W. Y. Lai, F. Shen, Z. Zhang, and G. H. Yu, Appl. Phys. Lett. **82**, 3722 (2003)

[42] J. S. Kasper and J. S. Kouvel, J. Phys. Chem. Solids **11**, 231 (1959)

[43] K. Lenz, S. Zander, and W. Kuch, Phys. Rev. Lett. **98**, 237201 (2007)

[44] J. Wang, W. Kuch, L. I. Chelaru, F. Offi, and M. Kotsugi, Appl. Phys. Lett. **86**, 122504 (2005)

[45] L. Pál, E. Krén, G. Kádár, P. Szabó, and T. Tarnóczi, J. Appl. Phys. **39**, 538 (1968)

[46] D. Spišák and J. Hafner, J. Phys. Condens. Matter **11**, 6359 (1999)

[47] A. Sakuma, J. Magn. Magn. Mater. **187**, 105 (1998)

[48] S. Kawarazaki, K. Fujita, K.Yasuda, Y. Sasaki, T. Mizusaki, and A. Hirai, Phys. Rev. Lett. **61**, 471 (1988)

[49] J. Nogués, T. J. Moran, D. Lederman, I. K. Schuller, and K. V. Rao, Phys. Rev. B **59**, 6984 (1999)

[50] F. Nolting, A. Scholl, J. Stöhr, J. W. Seo, J. Fompeyrine, H. Siegwart, J.-P. Locquet, S. Anders, J. Lüning, E. E. Fullerton, M. F. Toney, M. R. Scheinfein, and H. A. Padmore, Nature **405**, 767 (2000)

[51] H. Ohldag, A. Scholl, F. Nolting, S. Anders, F.U. Hillebrecht, and J. Stöhr, Phys. Rev. Lett. **86**, 2878 (2001)

[52] L. Ding, P. F. Ladwig, X. Yan, and Y. A. Chang, Appl. Phys. Lett. **80**, 1186 (2002)

[53] T. Lin, D. Mauri, N. Staud, C. Hwang, J. K. Howard, and G. L. Gorman, Appl. Phys. Lett. **65**, 1183 (1994)

[54] Z. Qian, J. M. Sivertsen, J. H. Judy, B. A. Everitt, S. Mao, and E. S. Murdock, J. Appl. Phys. **85**, 6106 (1999)

[55] M. F. Toney, M. G. Samant, T. Lin, and D. Mauri, Appl. Phys. Lett. **81**, 4565 (2002)

[56] C. Loch, W. Maass, B. Ocker, and K. Röll, J. Appl. Phys. **85**, 4460 (1999)

[57] M. S. Lund, M. R. Fitzsimmons, S. Park, and C. Leighton, Appl. Phys. Lett. **85**, 2845 (2004)

[58] C. Tieg, W. Kuch, S. G. Wang, and J. Kirschner, Phys. Rev. B **74**, 094420 (2006)

[59] M. Reinhardt, J. Seifert, M. Busch, and H. Winter, Phys. Rev. B **81**, 134433 (2010)

[60] C. L. Gao, A. Ernst, A. Winkelmann, J. Henk, W. Wulfhekel, P. Bruno, and J. Kirschner, Phys. Rev. Lett. **100**, 237203 (2008)

[61] N. Cheng, J.-P. Ahn, and K. M. Krishnan, J. Appl. Phys. **89**, 6597 (2001)

[62] R. F. C. Farrow, R. F. Marks, M. F. Toney, S. David, A. J. Kellock, J. A. Borchers, K. V. ÓDonovan, and D. Smith, Appl. Phys. Lett. **80**, 808 (2002)

[63] F. Bruno, D. Cvetkob,L. Floreano, R. Gotter, C. Mannori, L. Mattera, R. Moroni, S. Prandi, S. Terreni, A. Verdini, and M. Canepa, Appl. Surf. Sci. **162-163**, 340 (2000)

[64] W. A. A. Macedo, W. Keune, and R. D. Ellerbrock, J. Magn. Magn. Mater. **93**, 552 (1991)

[65] N. Honda, Y. Tanji and Y. Nakagawa, J. Phys. Soc. Jpn. **41**, 1931 (1976)

[66] C. Mitsumata, A. Sakuma and K. Fukamichi, Phy. Rev. B **68**, 014437 (2003)

[67] C. Mitsumata, A. Sakuma, K. Fukamichi, M. Tsunoda, and M. Takahashi, J. Phys. Soc. Jpn. **77**, 044602 (2008)

[68] C. Mitsumata and A. Sakuma, IEEE Trans. Magn. **47** 3501, (2011)

[69] A. Braun, B. Feldmann, M. Wuttig, J. Magn. Magn. Mater. **171**, 16 (1997)

[70] W. H. Meiklejohn and C. P. Bean, Phys. Rev. **102**, 1413 (1956)

[71] W. H. Meiklejohn and C. P. Bean, Phys. Rev. **105**, 904 (1957)

[72] E. C. Stoner and E. P. Wohlfarth, Nature **160**, 650 (1947)

[73] W. H. Meiklejohn, J. Appl. Phys. **33**, 1328 (1962)

[74] H. Ohldag, T. J. Regan, J. Stöhr, A. Scholl, F. Nolting, J. Lüning, C. Stamm, S. Anders, and R. L. White, Phys. Rev. Lett. **87**, 7201 (2001)

[75] H. Ohldag, A. Scholl, F. Nolting, E. Arenholz, S. Maat, A.T. Young, M. Carey, and J. Stöhr, Phys. Rev. Lett. **91**, 17203 (2003)

[76] M. D. Stiles and R. D. McMichael, Phys. Rev. B **59**, 3722 (1999)

[77] A. Scholl, M. Liberati, E. Arenholz, H. Ohldag, and J. Stöhr, Phys. Rev. Lett. **92**, 247201 (2004)

[78] A. P. Malozemoff, Phys. Rev. B **37**, 7673 (1988)

[79] J. Stöhr, A. Scholl, T. J. Regan, S. Anders, J. Lüning, M. R. Scheinfein, H. A. Padmore, and R. L. White, Phys. Rev. Lett. **83**, 1862 (1999)

[80] A. Scholl, J. Stöhr, J. Lüning, J. -P. Locquet, J. Fompeyrine, J. W. Seo, H. Siegwart, F. Nolting, S. Anders, E. Fullerton, M. R. Scheinfein, H. A. Padmore, Science **287**, 1014 (2000)

[81] A. Scholl, F. Nolting, J. W. Seo, H. Ohldag and J. Stöhr, S. Raoux, J.-P. Locquet and J. Fompeyrine, Appl. Phys. Lett. **85**, 4085 (2004)

[82] W. Kuch, F. Offi, L. I. Chelaru, M. Kotsugi, K. Fukumoto, and J. Kirschner, Phys. Rev. B **65**, 140408 (2002)

[83] M. Bode, E. Y. Vedmedenko, K. von Bergmann, A. Kubetzka, P. Ferriani, S. Heinze and R. Wiesendanger, Nature Materials **5**, 477 (2006)

[84] D. Paccard, C. Schlenker, O. Massenet, R. Montmory, and A. Yelon, Phys. Stat. Sol. **16**, 301 (1966)

[85] C. Binek, Phys. Rev. B. **70**, 014421 (2004)

[86] J. Nogués, D. Lederman, T. J. Moran, I.K. Schuller, Phys. Rev. Lett. **76**, 4624 (1996)

[87] L. Néel, Comp. Rend. Acad. Sci. France **255**, 1545 (1962)

[88] M. A. Ruderman and C. Kittel, Phys. Rev. **96**, 99 (1954)

[89] T. Kasuya, Prog. Theor. Phys. **16**, 45 (1956)

[90] K. Yosida, Phys. Rev. **106**, 893 (1957)

[91] D. T. Pierce, J. Unguris, R. J. Celotta, M. D. Stiles, J. Magn. Magn. Mater. **200**, 290 (1999)

[92] A. Vega, D. Stoeffler, H. Dreysse, C. Demangeat, Europhys. Lett. **31**, 561 (1995)

[93] D. Stoeffler, F. Gautier, J. Magn. Magn. Mater. **147**, 260 (1995)

[94] A. Berger, H. Hopster, Phys. Rev. Lett. **73**, 193 (1994)

[95] A. Schreyer, C. F. Majkrzak, T. Zeidler, T. Schmitte, P. Bödeker, K. Theis-Bröhl, A. Abromeit, J.A. Dura, T. Watanabe, Phys. Rev. Lett. **79**, 4914 (1997)

[96] J. C. Slonczewski, J. Magn. Magn. Mater. **150**, 13 (1995)

[97] E. E. Fullerton, C. H. Sowers, S. D. Bader, Phys. Rev. B **56**, 5468 (1997)

[98] E. E. Fullerton, K. T. Riggs, C. H. Sowers, S. D. Bader, A. Berger, Phys. Rev. Lett. **75**, 330 (1995)

[99] H. Hopster, Phys. Rev. Lett. **83**, 1227 (1999)

[100] M. Rührig, R. Schäfer, A. Hubert, R. Mosler, J.A. Wolf, S. Demokritov, P. Grünberg, Phys. Stat. Sol. (a) **125**, 635 (1991)

[101] B. Heinrich, J.F. Cochran, M. Kowalewski, J. Kirschner, Z. Celinski, A.S. Arrott, K. Myrtle, Phys. Rev. B **44**, 9348 (1991)

[102] M. Freyss, D. Stoeffler, H. Dreysse, Phys. Rev. B **54**, 12667 (1996)

[103] M. Freyss, D. Stoeffler, H. Dreysse, J. Appl. Phys. **81**, 4363 (1997)

[104] see for example *Practical Surface Analysis*, D. Briggs and M. P. Seah eds., (Wiley, Chichester, 1990)

[105] J. B. Pendry, Low Energy Electron Diffraction, Academic Press, New York, 1974

[106] B. Feldmann, B. Schirmer, A. Sokoll, and M. Wuttig, Phys. Rev. B **57**, 1014 (1998)

[107] C. Mannori, T. Scimia, P. Cantini, S. Terreni, M. Canepa, L. Mattera, Surf. Sci. **433**, 307 (1999)

[108] F. Offi, *Magnetic interaction between antiferromagnetic and ferromagnetic films*: Co/$Fe_{50}Mn_{50}$ *bilayers on* Cu(001), PhD thesis Halle/Saale, 2002

[109] J. Kerr, Philos. Mag. **3**, 339 (1877)

[110] J. Kerr, Philos. Mag. **5**, 161 (1878)

[111] M. Faraday, Diary, 13 September 1845, Vol. 4, p. 7504

[112] *Molecular Electro-Optics, Part I, Theory and Methods*, C. T. O'Konski (Dekker, New York, 1976), 517

[113] Z. Q. Qiu, and S. D. Bader, Rev. Sci. Instrum. **71**, 1243 (2000)

[114] J. A. C. Bland, M. J. Padgett, R. J. Butcher, N. Bett, J. Phys. E. Sci. Inst. **22**, 308 (1989)

[115] J. Zak, E.R. Moog C. Liu, S.D. Bader, J. Appl. Phys. **68**, 4203 (1990)

[116] Z.Q. Qiu, S.D. Bader, J. Magn. Magn. Mater. **200**, 664 (1999)

[117] J. M. V. Hove, C. S. Lent, P. R. Pukite, P. I. Cohen, J. Vac. Sci. Technol. B **1**, 741 (1983)

[118] J. H. Neave, B. A. Joyce, P. J. Dobson, N. Norton, Appl. Phys. A **47**, 100 (1985)

[119] W. C. Lin, T. Y. Chen, L. C. Lin, B. Y. Wang, Y. W. Liao, Ker-Jar Song, and Minn-Tsong Lin, Phys. Rev. B **75**, 054419 (2007)

[120] Y. Wang, W. C. Lin, Y. W. Liao, Ker-Jar Song, and Minn-Tsong Lin, Surf. Sci. **600**, 4517 (2006)

[121] W. C. Lin, B. Y. Wang, Y. W. Liao, Ker-Jar Song, and Minn-Tsong Lin, Phys. Rev. B **71**, 184413 (2005)

[122] J. B. Pendry, *Low Energy Electron Diffraction* (Academic, New York, 1974)

[123] B. Schirmer, B. Feldmann, A. Sokoll, Y. Gauthier, and M. Wuttig, Phys. Rev. B **60**, 5895 (1999)

[124] W. E. O'Brien and B. P. Tonner, Phys. Rev. B **49**, 15370 (1994)

[125] B. Schulz and K. Baberschke, Phys. Rev. B **50**, 13467 (1994)

[126] G. Bochi, C. A. Ballentine, H. E. Inglefield, S. S. Bogomolov, C. V. Thompson, R. C. O'Handley, Mater. Res. Soc. Symp, Proc. **313**, 309 (1993)

[127] M. Stampe, P. Stoll, T. Homberg, K. Lenz, and W. Kuch, Phys. Rev. B **81**, 104420 (2010)

[128] M. Ali, P. Adie, C. H. Marrows, D. Greig, B. J. Hickey, and R. L. Stamps, Nat. Mater. **6**, 70 (2007)

[129] M. Ali, C. H. Marrows, M. Al-Jawad, B. J. Hickey, A. Misra, U. Nowak, and K. D. Usadel, Phys. Rev. B **68**, 214420 (2003)

[130] H. C. N. Tolentino, M. D. Santis, J. M. Tonnerre, A. Y. Ramos, V. Langlais, S. Grenier, and A. Bailly, Braz. J. Phys. **39**, 150 (2009)

[131] W. Pan, N. Y. Jih, C. C. Kuo, and M. T. Lin, J. Appl. Phys. **95**, 7297 (2004)

[132] W. A. A. Macedo, P. L. Gastelois, M. D. Martins, W. Kuch, J. Miguel, and M. Y. Khan, Phys. Rev. B **82**, 134423 (2010)

[133] W. Kuch, L. I. Chelaru, F. Offi, J. Wang, M. Kotsugi, and J. Kirschner, Nature Mater. **5**, 128 (2006)

[134] S. K. Mishra, F. Radu, H. A. Dürr, and W. Eberhardt, Phys. Rev. Lett. **102**, 177208 (2009)

[135] S. Maat, K. Takano, S. S. P. Parkin, and E. E. Fullerton, Phys. Rev. Lett. **87**, 087202 (2001)

[136] Y. Endoh and Y. Ishikawa, J. Phys. Soc. Jpn. **30**, 1614 (1971)

[137] C. Leighton, M. R. Fitzsimmons, A. Hoffmann, J. Dura, C. F. Majrkzak, M. S. Lund, and I. K. Schuller, Phys. Rev. B **65**, 064403 (2002)

[138] N. Fukatani, K. Ueda, and H. Asano, J. Appl. Phys. **109**, 073911 (2011)

[139] K. H. Wu, H.-J. Chen, Y. T. Chen, C. C. Hsieh, C. W. Luo, T. M. Uen, J. Y. Juang, J.-Y. Lin, T. Kobayashi, and M. Gospodinov, Eurphys. Lett. **94**, 27006 (2011)

[140] A. P. Malozemoff, J. Appl. Phys. **63**, 3874 (1988)

[141] M. Ali, C. H. Marrows, and B. J. Hickey, Phys. Rev. B **67**, 172405 (2003)

[142] R. Morales, Zhi-Pan Li, J. Olamit, Kai Liu, J. M. Alameda, and I. K. Schuller, Phys. Rev. Lett. **102**, 097201 (2009)

[143] U. Nowak, K. D. Usadel, J. Keller, P. Miltényi, B. Beschoten, and G. Güntherodt, Phys. Rev. B **66**, 014430 (2002)

[144] D. Lederman, R. Ramírez, and M. Kiwi, Phys. Rev. B **70**, 184422 (2004)

[145] M. Rührig, R. Schäfer, A. Hubert, R. Mosler, J.A. Wolf, S. Demokritov, P. Grünberg, Phys. Stat. Sol. (a) **125**, 635 (1991)

[146] A. Schreyer, J. F. Ankner, T. Zeidler, H. Zabel, M. Schäfer, J. A. Wolf, P. Grünberg, and C. F. Majkrzak, Phys. Rev. B **52**, 16066 (1995), and references therein

[147] Shi-shen Yan, R. Schreiber, F. Voges, C. Osthöver, and P. Grünberg, Phys. Rev. B **59**, R11 641 (1999)

[148] J. C. Slonczewski, Phys. Rev. Lett. **67**, 3172 (1991)

[149] L. Li, F. Zhang, N. Wang, Y. F. Lv, X. Y. Han, and J. J. Zhang, J. Appl. Phys. **108**, 073908 (2010)

[150] J. A. Wolf, Q. Leng, R. Schreiber, P. Grünberg, W. Zinn, J. Magn. Magn. Mater. **121**, 253 (1993)

[151] N. N. Phuoc, N. P. Thuy, N. A. Tuan, L. T. Hung, N. T. Thanh, N. T. Nam, J. Magn. Magn. Mater. **43**, 298 (2006)

[152] H. Ohldag, H. Shi, E. Arenholz, J. Stöhr, D. Lederman, Phys. Rev. Lett. **96**, 027203 (2006)

[153] L. I. Chelaru, *Microscopic studies of interlayer magnetic coupling across non-magnetic and antiferromagnetic spacer layers*, PhD thesis Halle/Saale, 2003

[154] F. Radu, M. Etzkorn, R. Siebrecht, T. Schmitte, K. Westerholt, and H. Zabel, Phys. Rev. B **67**, 134409 (2003)

[155] T. M. Hong, Phys. Rev. B **58**, 97 (1998)

[156] E. E. Fullerton, S. D. Bader, J. L. Robertson, Phys. Rev. Lett. **77**, 1382 (1996)

Appendix A

Appendix

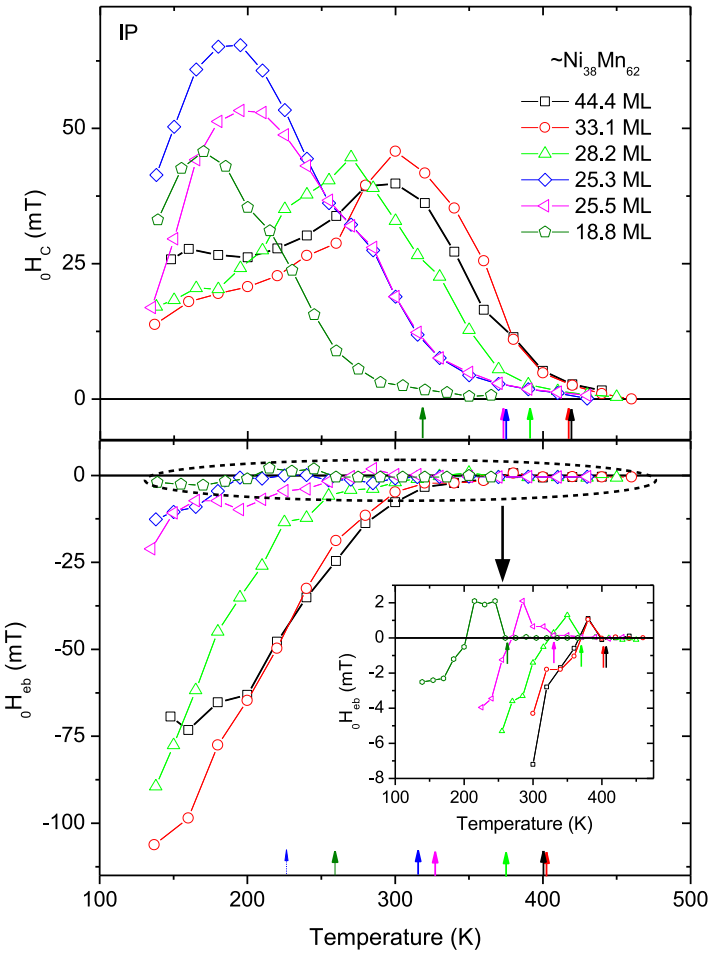

Figure A.1: Temperature-dependent coercivity (positive field axis) and exchange bias field (negative field axis) for different thicknesses of IP magnetized bi-layer $\sim Ni_{38}Mn_{62}$/$\sim$12 ML Ni/$\sim$2 ML $Co/Cu_3Au(001)$. The down and up arrows of respective colour represent T_{AFM} and T_b, respectively. The inset shows zoom-in of the area indicated by a dashed-ellipse to magnify a small positive exchange bias just below T_b.

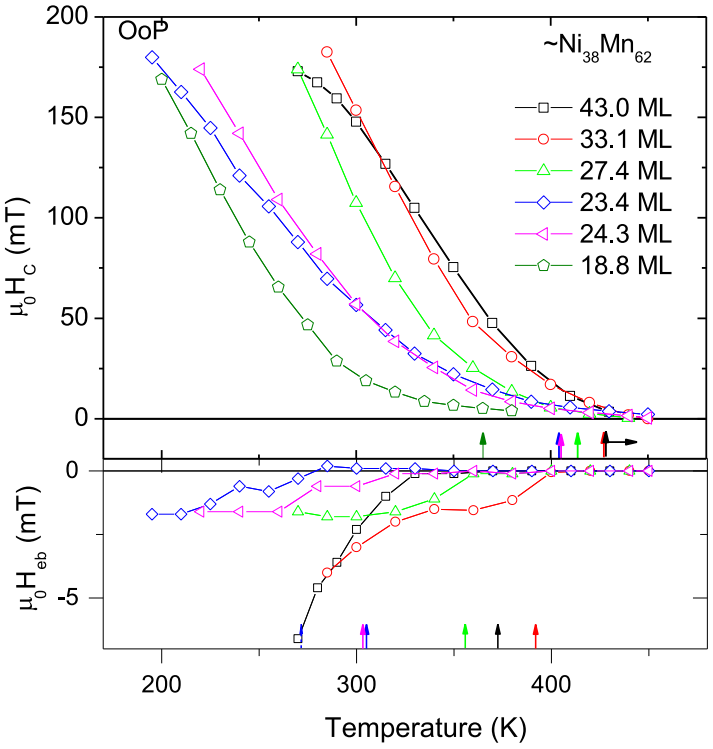

Figure A.2: Temperature-dependent coercivity (positive field axis) and exchange bias field (negative field axis) for different thicknesses of OoP magnetized bi-layer $\sim Ni_{38}Mn_{62}$/$\sim$12 ML Ni/$\sim$2 ML $Co/Cu_3Au(001)$. The down and up arrows of respective colour represent T_{AFM} and T_b, respectively.

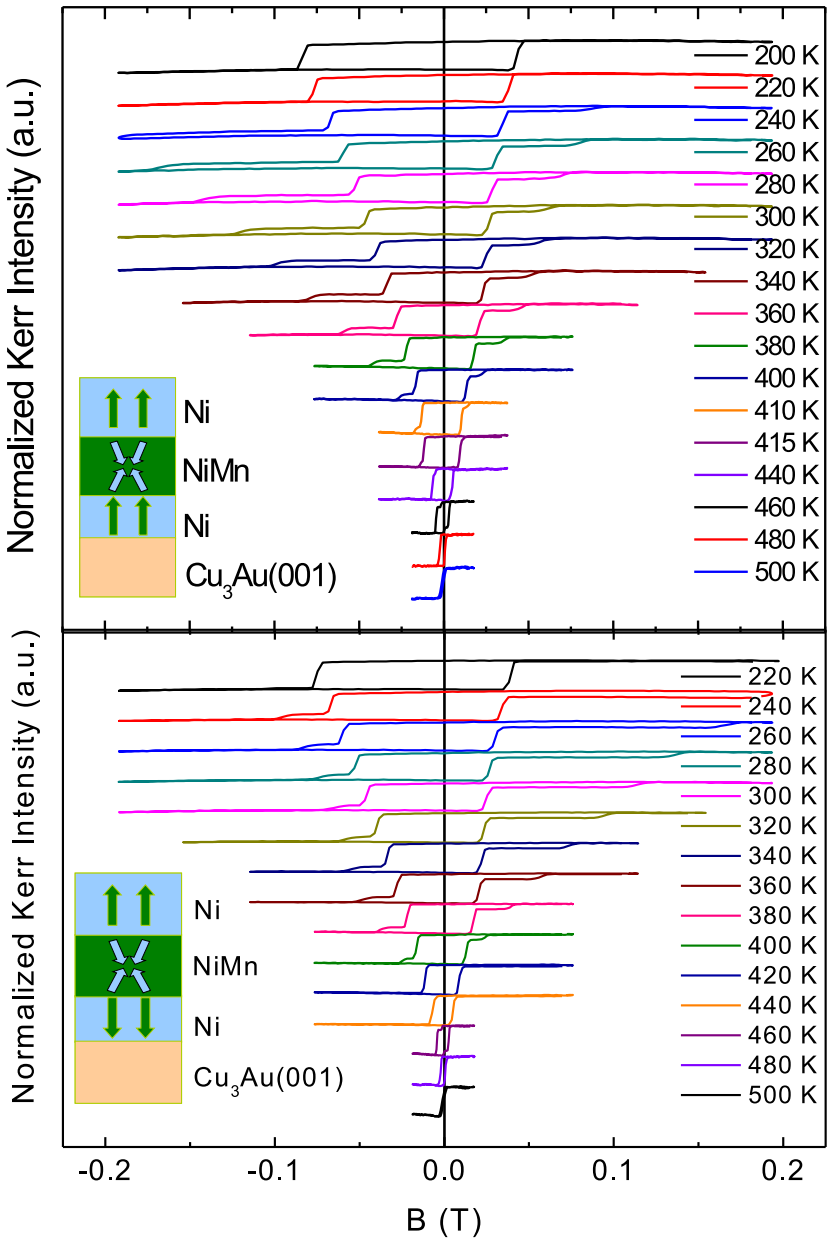

Figure A.3: Normalized hysteresis loops for ∼25 ML Ni/∼50 ML $Ni_{21}Mn_{79}$/12.9 ML Ni/Cu_3Au(001) trilayer measured with polar MOKE at different temperatures. (a)Both interfaces give negative exchange-bias in the magnetic field direction when field-cooled with +10 mT from 510 K, and (b) both interfaces give opposite exchange-bias: the upper one along positive field as it is field-cooled with -2 mT from 460 K, and the lower one along negative field due to previous field-cooling with +10 mT.

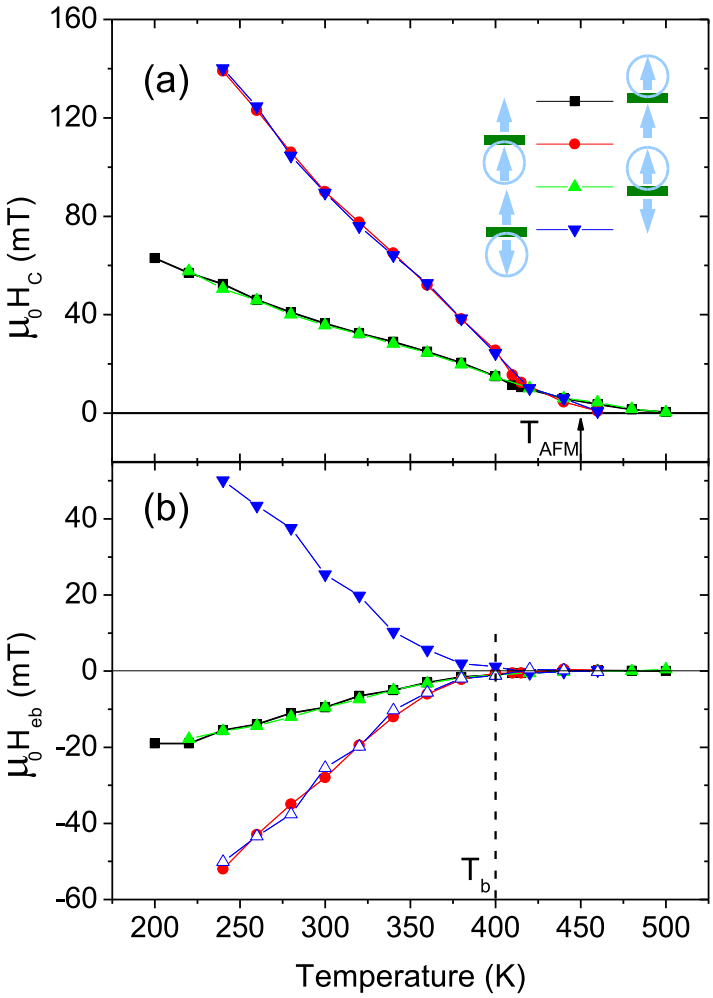

Figure A.4: Temperature dependence of (a) coercivity and (b) exchange-bias field for the ∼25 ML Ni/∼50 ML $Ni_{21}Mn_{79}$/12.9 ML Ni/Cu_3Au(001) trilayer measured with polar MOKE. The different spin configurations of the FM layers at upper and lower interfaces are symbolically shown in front of the corresponding legend. The antiferromagnetic ordering temperature and blocking temperature are indicated in (a) and (b), respectively. Open blue symbols in (b) is a mirror of the same coloured filled symbols in (a).

List of publications

1. Growth, structure, and magnetic properties of epitaxial Ni_xMn_{100-x} single layers and Co/Ni_xMn_{100-x} bilayers on $Cu_3Au(001)$. W. A. A. Macedo, P. L. Gastelois, M. D. Martins, W. Kuch, J. Miguel, and M. Y. Khan, Phys. Rev. B **82**, 134423 (2010)

2. Probing antiferromagnetism in $NiMn/Ni/(Co/)Cu_3Au(001)$ single-crystalline epitaxial thin films. M. Yaqoob Khan, Chii-Bin Wu, and Wolfgang Kuch (in preparation), 2012

3. Concentration-, and thickness-dependent magnetic properties of Ni_xMn_{1-x} in in-plane and out-of-plane exchange-coupled epitaxially grown $Ni_xMn_{1-x}/Ni/(Co/)Cu_3Au(001)$. M. Yaqoob Khan, Chii-Bin Wu, and Wolfgang Kuch (in preparation), 2012

Acknowledgements

First of all, I wish to express my immense gratitude to my PhD supervisor Prof. Wolfgang Kuch for providing me an opportunity to do my PhD work in his research group. He always provided me professional guidance and encouragement throughout this research work. The readily supporting attitude from Wolfgang was not limited to the academic and professional life, he always proved to be helpful in resolving my social problems as well. Without his valuable help, it would have been almost impossible for me to accomplish this job. Really I do not find words to thank him.

I thank Prof. Dr. Robert Bittl for his willingness to co-assess this thesis.

I am also very much grateful to Dr. Chii-Bin Wu for sharing his excellent knowledge and experience on different aspects of my work. He always helped me in the experimental work as well as provided me all other professional support. While sharing the same office, I learnt from him a lot by making use of valuable discussion. I cordially acknowledge the help of my fiends and lab fellows Dr. Mustafa Erkovan and Yasser Shokr. I can not forget a very friendly behaviour and selfless help from Dr. Matthias Bernien. I shall always remember the affection and cooperation of Prof. Dr. Barbara Sandow. Many thanks to Bin Zhang for being always helping. I am thankful to Dr. Yin-Ming Chang, Alex Krüger, Felix Hermanns, Jiaming Song, Oliver Sandig, Lili Sun, and all other members of AG Kuch for providing me a cooperative and memorable company as well as healthy working environment. Special thanks to the AG Kuch secretary Marion Badow and engineer Uwe Lipowski. I must thank to our former group fellows for their cooperation: Dr. Kilian Lenz, Dr. Julia Kurde, Dr. Miriam Stampe, Dr. Jeorge Miguel, and Dr. Cristina.

I am very much thankful to my country fellow friends, their company provided me a very memorable time during my stay in Berlin.

I am also thankful to cryogenic laboratory, electronics and machine-parts repairing workshops for assisting me having working lab.

I am grateful to the Higher Education Commission (HEC) of Pakistan through Kohat University of Science & Technology (KUST), Kohat (K.P.K.), Pakistan, and Freie Universität Berlin, for their financial support during my stay in Berlin.

At the end, I consider it obligatory to acknowledge and thank all members of my family, my parents, and my brothers and sisters. The prayers and moral support of my parents always strengthened me whenever I felt my self weak and alone being thousands of kilometres away from them. I dedicate my thesis to my wife Asma, her love and care always encouraged me to do my best, and to my little son Haider, to whom I love the most!